UNIVERSITY of KASDI MERBAH OUARGLA
Faculty of Applied Sciences
Department of Electrical Engineering

Thesis
Presented for the purpose of obtaining the LMD DOCTORAT degree
Domain : Science and technology
Field: Electrotechnics
Specialty : Electrical Machines
Presented by:
BENZAOUI Khaled Mohammed Said

Theme:

Multilevel direct torque control of sensorless two five-phase induction machines connected in parallel

Publicly defended on 01/12/2025, before the jury composed of:

Mr Djafour Ahmed	Pr	President	UKM Ouargla
Mr Benyoussef Elakhdar	Pr	Thesis supervisor	UKM Ouargla
Mr Tabbache Bekheira	Pr	Examiner	EMP Algiers
Mr Bourek Yacine	Pr	Examiner	UKM Ouargla
Mr Khettache Laid	MCA	Examiner	UKM Ouargla
Mr Rouibah Tahar	MCA	Examiner	UKM Ouargla

Academic year 2025/2026

Acknowledgement

First of all, we would like to thank ALLAH, who helped us and gave us the patience and courage to finish this small and modest work. "During the preparation of this thesis, I received a lot of support and encouragement."

First, I would like to thank my thesis advisor, Pr Benyoussef, whose experience has been invaluable to me. I am indebted to him, Dr. Guedida, and Pr Tabbache for highlighting my research strengths and patiently encouraging me to improve my weaknesses. Your insightful comments encouraged me to improve my ideas and my work.

I would like to express my sincere thanks and deep gratitude to the members of the jury for agreeing to evaluate this work. Not only for their time and extreme patience, but also for their intellectual contributions, Pr. Benyoussef, Professor at the University of Ouargla, for providing me with the opportunity to pursue a doctoral thesis under their guidance. I would also like to express my heartfelt thanks to Pr. Djafour Ahmed, Professor at the University of Ouargla, who honored me by presiding over the defense jury of this thesis and Pr. Bourek Yacine, Professor at the University of Ouargla, and Pr. Tabbache Bekheira, Professor at the Ecole Militaire Polytechnique, Dr. Khettache Laid and Dr. Rouibah Tahar, lecturer at the University of Ouargla, who honored us by accepting to participate in the jury as examiners of this thesis.

I would like to thank my parents, my sisters, and my entire family in particular. My family has always encouraged me throughout my PhD. I thank you for your constant support throughout the ups and downs of my academic career. It has sometimes been difficult, but the trust you have shown me has strengthened my ability to overcome all of this and succeed in the end. Without your support, I wouldn't be here. Your encouragement has always pushed me to redouble my efforts to accomplish my work and move forward.

Finally, but not least, I express my most sincere thanks to all my teachers who contributed to my education throughout my scientific journey. Thank you to my colleagues and friends and to everyone who helped me, directly or indirectly, in the completion of this work.

Khaled Mohammed Said Benzaoui

Dedication

To my beloved parents,

To my beloved sisters and their families,

To my sweet nephews and niece,

To my friends,

And last but not least me, myself and I.

KHALED MOAMMED SAID BENZAOUI

List of content

Acknowledgement i
Dedication ii
List of content iii
List of abbreviations viii
List of symbols x
List of figures xiii
List of tables xviii
Abstract xx

General introduction

1. Introduction 1
2. Control methods 2
3. Sensorless control 3
4. The concept of multi-machine drive 4
5. The proposed concept of multiphase multi-machine drive 5
6. Aims of the thesis 7
8. Thesis's organization 7
   8.1. Chapter 1 7
   8.2. Chapter 2 8
   8.3. Chapter 3 8
   8.4. Chapter 4 8
   8.5. Chapter 5 8

Chapter 1 Modelling of two parallel-connected machine drive

1.1. Introduction 9
1.2. Multi-phase machines 10
   1.2.1. Type 1 multi-phase AC machines 10
   1.2.2. Type 2 multi-phase AC machines 10
   1.2.3. Multi-phase AC machines' merits and demerits 11
      1.2.3.1. Multi-phase AC machines merits 12
      1.2.3.2. Multi-phase AC machines demerits 12
1.3. Modelling of the FPIM 13

1.3.1. FPIM electrical equations 13
1.3.2. FPIM mechanical equations 15
1.3.3. Decoupling transformation 16
1.3.4. The FPIM's model in the arbitrary reference frame 16
1.4. Drive's power supply modelling 19
1.4.1 Rectifier modelling 19
1.4.2 RLC filter modelling 21
1.4.3 Modelling of n-level five-phase VSI 21
1.4.3.1. Two-level five-phase VSI 22
1.4.3.2. Three-level five-phase NPC VSI 25
1.5. Modeling of the two parallel-connected multi-phase machines drive 28
1.5.1. Introduction 28
1.5.2. parallel-connected multi-phase machines drive's advantages 29
1.5.2. multi-phase machines parallel- connectivity 30
1.5.3. Two parallel-connected FPIMs' modelling 32
1.6. Simulation results 35
1.7. Conclusion 37

Chapter 2 Multi-level DTC of two-machine drive

2.1. Introduction 39
2.2. Conventional DTC 40
2.2.1. DTC's principals 40
2.2.1.1. Stator flux control 41
2.2.1.2. Electromagnetic torque control 43
2.2.2. DTC's merits and demerits 45
2.2.2.1. DTC's merits 45
2.2.2.2. DTC's demerits 45
2.3. Two-machines drive's DTC 45
2.3.1. Variable state estimation 46
2.3.1.1. Stator flux estimation 46
2.3.1.2. Electromagnetic torque estimation 47
3.2.2. State variables controller 47
3.2.2.1. Two-level stator flux HC 47
2.3.2.2. Seven-level electromagnetic torque HC 48

2.3.3. VV's selection 49
2.3.3.1. Two-level DTC's ST 50
2.3.3.2. Three-level DTC's ST 51
2.3.4. Logic selection 52
2.4 Simulation results 52
2.4.1. First simulation scenario 52
2.4.1. Second simulation scenario 55
2.4.3. Results interpretation 57
2.4.4. Comparative study 57
2.5. Conclusion 57

Chapter 3 Multi-level intelligent DTC of two-machine drive

3.1. Introduction 59
3.2. Artificial neural networks 60
3.2.1. Biological neuron 60
3.2.2. Formal neuron 61
3.2.3. ANNs architecture types 62
3.2.3.1. Feedforward ANNs 62
3.2.3.2. Recurrent ANNs 63
3.2.3.3. Convolutional ANNs 64
3.2.3.4 Generative adversarial ANNs (GAN) 65
3.2.4. ANNs learning 66
3.2.4.1. Supervised learning 66
3.2.4.2. Unsupervised leaning 67
3.3. ANN based DTC 67
3.3.1. Two-level DTC-ANN 69
3.3.2. Three-level DTC-ANN 70
3.4. Simulation results 72
3.4.1. First simulation scenario 72
3.4.2. Second test scenario 75
3.4.3. Results interpretation 77
3.4.4. Comparative study 77
3.5. Conclusion 77

Chapter 4 Sensorless multi-level intelligent DTC of two-machine drive

4.1. Introduction 79
4.2. MM sensorless control 80
4.2.1. Estimators 80
4.2.2. Observers 80
4.3. Sensorless DTC-ANN based on MRAS 81
4.3.1. Model Reference Adaptive System (MRAS) 81
4.3.1.1. Estimation of the rotor flux 82
4.3.1.2. The rotor's speed estimation 82
4.3.1.3. Stator flux and electromagnetic torque estimation 83
4.3.2. Simulation results 84
4.3.2.1. Test one 84
4.3.2.2. Test two 86
4.3.2.3. Results discussion 88
4.4. Sensorless DTC-ANN based on SMO 88
4.4.1. Sliding Mode Observer (SMO) 88
4.4.1.1. Stator flux and electromagnetic torque estimation 89
4.4.1.2. The rotor's mechanical speed estimation 94
4.4.2. Simulation results 94
4.4.2.1. Test one 94
4.4.2.2. Test two 97
4.4.2.3. Results discussion 98
4.5. Sensorless DTC-ANN based on stator currents reconstruction 99
4.5.1. Introduction 99
4.5.2. Virtual Current Sensor (VCS) 99
4.5.3. Stator flux and electromagnetic torque estimation 100
4.5.4. Simulation results 101
4.5.4.1. Test one 101
4.5.4.2. Test two 104
4.5.4.3. Results discussion 105
4.6. Comparative study 105
4.7. Conclusion 106

Chapter 5 Multi-level DTC with CMV mitigation for two-machine drive

5.1. Introduction 108
5.2. Common-Mode Voltage 108
5.2.1. Definition of CMV 109
5.2.2. Impact of CMV 109
5.2.3. CMV mitigation techniques 112
5.2.3.1. Corrective methods 112
5.2.3.2. Preventive methods 117
5.3. Preventive DTC method (DTC_{CMV}) 117
5.3.1. Step 1 117
5.3.1.1. Three-level DTC's CMV status 118
5.3.1.2. Status of CMV for the mitigation technique DTC_{CMV} 119
5.3.2. step 2 119
5.3.3. step 3 120
5.3.4. Step 4 121
5.4. Simulation results 122
5.5. Conclusion 126

General conclusion

conclusion 128
References

List of abbreviations

Abbreviations	
2L-DTC	Two level direct torque control
2L-DTC-ANN	Two level artificial neural network based direct torque control
2L-HC	Two-level HC
3L-DTC	Three level direct torque control
3L-DTC-ANN	Three level artificial neural network based direct torque control
7L-HC	Seven-level HC
AC	Alternative current
AI	Artificial intelligence
AJA	Adjustable speed applications
ANN	Artificial neural network
ANN-DTC	Artificial neural network Direct torque control
$ANN-HC_{\phi_s}$	Artificial neural network stator flux hysteresis controller
$ANN-HC_{T_{em}}$	Artificial neural network electromagnetic torque hysteresis controller
$ANN-ST$	Artificial neural network switching table
ASD	Adjustable speed drives
CMV	Common-Mode Voltage
CS	Current sensor
DC	Direct current
DOF	Degrees of freedom
DSP	Digital signal processors
DTC	Direct Torque Control
DTC_{CMV}	Direct torque control based on CMV mitigation approach
EMI	Electromagnetic interference
EV	Electrical vehicle
FOC	Field Oriented Control
FPIM	Five-phase induction machine
FP-VSI	Five-phase voltage source inverter
FTC	Fault-tolerant control
GAN	Generative adversarial ANN

HB	Hysteresis band
HC	Hysteresis controllers
HEV	Hybrid electrical vehicle
HVAC	Heat Ventilation Air Conditioner
IGBT	Insulated gate bipolar transistors
IM	Induction machines
MM	Machine-model-based methods
MMF	Magneto-motive force
MRAS	Model reference adaptive system
NN	Neural network
NPC	Neutral point clamped
PBC	Passivity-based control
PI	Proportional Integrator
PMSM	Permanent magnet synchronous machine
PWM	Pulse width modulation
SMC	Sliding Mode Control
SMO	Sliding mode observer
ST	Switching table
THD	Total harmonic distortion
THL-FP-VSI	Three-level five-phase NPC VSI
VC	Vector control
VCS	Virtual current sensor
VFD	Variable frequency drives
VSI	Voltage source inverter
VV	Voltage vectors
VVV	Virtual voltage vectors

List of symbols

Symbol	
q	Phase number.
V_{sabcde}	Stator voltages vector.
I_{sabcde}	Stator currents vector.
I_{rabcde}	Rotor currents vector.
ϕ_{sabcde}	Stator flux vector.
ϕ_{rabcde}	Rotor flux vector.
R_{sabcde}	Stator resistance matrix.
R_{rabcde}	Rotor resistance matrix.
L_{ss}	Stator inductances matrix.
L_{rr}	Rotor inductance matrix.
M_{sr}, M_{rs}	Mutual inductances.
σ	Coefficient of dispersion.
T_r	Rotor's time constant.
θ	Electrical angel between stator and rotor phases.
J	Moment of inertia.
f	Fraction coefficient.
T_L	Load torque.
T_{em}	Electromagnetic torque.
[C_s]	Stator co-ordinate transformation matrix.
[C_r]	Rotor co-ordinate transformation matrix.
ω_m	Rotor's mechanical speed.
ω	Rotor's instantaneous electrical angular speed.
$\alpha\beta_1$	Fundamental subspace.
$\alpha\beta_2$	Harmonic subspace.
$V_{s\alpha\beta}$	Stator voltages in the arbitrary reference frame.
$V_{r\alpha\beta}$	Rotor voltages in the arbitrary reference frame.

$i_{s\alpha\beta}$	Stator currents in the arbitrary reference frame.
$i_{r\alpha\beta}$	Rotor voltages in the arbitrary reference frame.
$\phi_{s\alpha\beta}$	Stator flux in the arbitrary reference frame.
$\phi_{r\alpha\beta}$	Rotor flux in the arbitrary reference frame.
f_c	Cut-off frequency.
T_{ks}	Transistor.
D_{ks}	Diode.
S_i	Bi-directional switch.
B_{ks}	Control signal.
$[S_A, S_B, S_C, S_D, and\ S_E]$	Switching states.
V_{dc}	DC-link voltage.
Ts	Sampling time.
$\phi_{s\alpha\beta 0}$	Stator flux at instant (t=0).
$\left\|\overrightarrow{\phi_{s\alpha\beta}}\right\|, \left\|\overrightarrow{\phi_{r\alpha\beta}}\right\|$	Stator rotor flux module.
δ	Angle between the stator rotor flux.
ϕ_{sj}^{*}	Stator rotor flux reference value.
$\hat{\phi}_{sj}$	Stator rotor flux estimated value.
$\varepsilon_{\phi sj}$	Stator flux HC response.
$HB_{\phi s1}$	hysteresis band for the flux HC.
T_{emj}^{*}	Electromagnetic torque reference value.
$\hat{T}_{emj}$	Electromagnetic torque estimated value.
HB_{Tem3}	Hysteresis band for the torque HC.
ε_{Temj}	Torque HC response.
θ_{sj}	Stator flux position.
S	Sector number.
x_i	Formal neurons inputs.
w_{ij}	Weighting parameters.

$netj$	Formal neuron output.
ε_{estj}	Estimation error of the MRAS.
$\hat{\phi}_{rj\alpha j}$, $\hat{\phi}_{rj\beta j}$	Estimated rotor flux components.
$\otimes$	Cross product.
$\hat{i}_{s\alpha}$, $\hat{i}_{s\beta}$	Estimated stator currents components.
$\hat{\phi}_{s\alpha}$, $\hat{\phi}_{s\beta}$	Estimated stator flux components.
A_{ij} , $A_{\phi j}$	SMO's gains.
S1, S2	Sliding surfaces.
I_s	Sign vector of the chosen sliding vector.
εi	Current's observation error.
$\varepsilon\phi$	Flux observation error.
q_1, q_2	Positive constants.
$U_{CM}(t)$	Generated CMV.

List of figures

Introduction

Figure 1: AC machines' control schemes. 3
Figure 2: Sensorless techniques. 4

Chapter 1 Modelling of two parallel-connected drive

Figure 1.1: Type 1 multi-phase AC machines: (a) FP machine, (b) seven-phase machine. 11
Figure 1.2: Type 2 multi-phase AC machines: (a) symmetrical machines, (b) asymmetrical machines. 11
Figure 1.3: Schematic representation of the FPIM. 13
Figure 1.4: Schematic representation of the FPIM in the arbitrary reference frame. 19
Figure 1.5: Schematic diagram of VSI fed FPIM. 19
Figure 1.6: Rectifier's power circuit. 20
Figure 1.7: RLC filter. 21
Figure 1.8: Simplified approximation of transistor-diode group. 22
Figure 1.9: Power circuit of FP-VSI. 22
Figure 1.10: Mapping of the VVs: (a) $\alpha\beta_1$ plane, (b) $\alpha\beta_2$ plane. 24
Figure 1.11: Possible connections of the FP-VSI to the load. 25
Figure 1.12: Switching configuration of the THL-FP-VSI. 25
Figure 1.13: Power circuit of THL-FP-VSI. 26
Figure 1.14: Mapping of the VVs: (a) $\alpha\beta_1$ plane, (b) $\alpha\beta_2$ plane. 27
Figure 1.15: Possible configurations of ASD: (a) independent one machine drive, (b) multiple VSI with shared DC-link, (c) parallel-connected multi-machine drive, and (d) series-connected multi-machine drive. 29
Figure 1.16: Schematic diagram of two-machine drive. 32
Figure 1.17: Two parallel-connected FPIMs drive response's fed by FP-VSI: (a) mechanical rotor speed, (b) electromagnetic torque, and (c) stator current. 36
Figure 1.18: Two parallel-connected FPIMs drive response's fed by THL-FP-VSI: (a) mechanical rotor speed, (b) electromagnetic torque, and (c) stator current. 37

Chapter 2 Multi-level DTC of two-machine drive

Figure 2.1: MAK DE502 introduced by ABB and controlled by DTC scheme. 40
Figure 2.2: Block diagram of DTC. 41
Figure 2.3: stator flux control: (a) VV applied to reduce the flux amplitude, (b) VV applied to increase the flux amplitude. 42
Figure 2.4: Stator flux circular trajectory. 42
Figure 2.5: Electromagnetic torque: (a) torque variation for a positive change in the speed, (b) torque variation for a negative change in the speed. 45
Figure 2.6: Schematic diagram of the two-machine drive's multi-level DTC. 46
Figure 2.7: (a) Two-level HC's structure (b) flux behaviour. 48
Figure 2.8: Seven-level HC's structure. 49
Figure 2.9: Selection rules of the VVs in the first sector. 50
Figure 2.10: Logic selection block's structure. 52
Figure 2.11: Two-level DTC's response: (a) mechanical rotor speed, (b) electromagnetic torque, (c) stator flux, and (d) stator currents. 53
Figure 2.12: Two-level DTC's currents THD: (a) FPIM1 and (b) FPIM2. 54
Figure 2.13: Three-level DTC's response: (a) mechanical rotor speed, (b) electromagnetic torque, (c) stator flux, and (d) stator currents. 54
Figure 2.14: Three -level DTC's currents THD: (a) FPIM1 and (b) FPIM2. 55
Figure 2.15: Two-level DTC's response: (a) mechanical rotor speed, (b) electromagnetic torque, and (c) stator flux. 56
Figure 2.16: Three-level DTC's response: (a) mechanical rotor speed, (b) electromagnetic torque, and (c) stator flux. 56

Chapter 3 Multi-level intelligent DTC of two-machine drive

Figure 3.1: The neuron cell. 60
Figure 3.2: Mac Culloch and Pitts' model of the artificial neuron. 61
Figure 3.3: The most selected activation functions. 62
Figure 3.4: Feedforward ANNs. 63
Figure 3.5: Recurrent ANNS. 64
Figure 3.6: Convolutional ANNs. 65
Figure 3.7: Generative adversarial ANNs structure. 66
Figure 3.8: Supervised learning. 67
Figure 3.9: Unsupervised learning. 67

Figure 3.10: Training process flowchart. 68
Figure 3.11: Off-line training technique. 69
Figure 3.12: Two-level DTC-ANN ANNs controllers: (a) $ANN-HC_{\phi_s}$, (b) $ANN-HC_{T_{em}}$, and (c) $ANN-ST$. 69
Figure 3.13: Three-level DTC-ANN ANNs controllers: (a) $ANN-HC_{\phi_s}$, (b) $ANN-HC_{T_{em}}$, and (c) $ANN-ST$. 71
Figure 3.14: Multi-level DTC-ANN of the two parallel-connected FPIMs' drive. 72
Figure 3.15: Two-level DTC-ANN's response: (a) rotor's mechanical speed, (b) electromagnetic torque, (c) stator flux, (d) stator current. 73
Figure 3.16: Two-level DTC-ANN's currents' THD: (a) FPIM1, (b) FPIM2. 74
Figure 3.17: Three-level DTC-ANN's response: (a) rotor's mechanical speed, (b) electromagnetic torque, (c) stator flux, (d) stator current. 74
Figure 3.18: Three-level DTC-ANN's currents' THD: (a) FPIM1, (b) FPIM2. 75
Figure 3.19: Two-level DTC-ANN's response: (a) rotor's mechanical speed, (b) electromagnetic torque, (c) stator flux. 76
Figure 3.20: Three-level DTC-ANN's response: (a) rotor's mechanical speed, (b) electromagnetic torque, (c) stator flux. 76

Chapter 4 Sensorless multi-level intelligent DTC of two-machine drive

Figure 4.1: Basic structure of estimators. 80
Figure 4.2: Basic structure of observer. 81
Figure 4.3: The structure of the MRAS observer. 81
Figure 4.4: The schematic diagram of the MRAS observer. 83
Figure 4.5: Sensorless DTC-ANN based on MRAS. 84
Figure 4.6: Sensorless DTC-ANN based on MRAS: (a) mechanical rotor speed, (b) electromagnetic torque, (c) stator flux, (d) stator current, (e) estimated rotor speed, and (f) estimation error of rotor speed. 86
Figure 4.7: Sensorless DTC-ANN based on MRAS: (a) mechanical rotor speed, (b) electromagnetic torque, (c) stator flux, (d) estimated rotor speed, and (e) estimation error of rotor speed. 87
Figure 4.8: Basic structure of SMO. 89
Figure 4.9: Schematic diagram of SMO. 94
Figure 4.10: Sensorless DTC-ANN based on SMO. 95

Figure 4.11: Sensorless DTC-ANN based on SMO: (a) mechanical rotor speed, (b) electromagnetic torque, (c) stator flux, (d) stator current, (e) estimated rotor speed, and (f) estimation error of rotor speed. 96

Figure 4.12: Sensorless DTC-ANN based on SMO: (a) mechanical rotor speed, (b) electromagnetic torque, (c) stator flux, (d) estimated rotor speed, and (e) estimation error of rotor speed. 98

Figure 4.13: Schematic diagram of VCS. 101

Figure 4.14: Sensorless DTC-ANN based on VCS. 102

: (a) mechanical rotor speed, (b) electromagnetic torque, (c) stator flux, (d) stator current, (e) estimated stator current 103

Figure 4.16: Sensorless DTC-ANN based on VCS: (a) mechanical rotor speed, (b) electromagnetic torque, (c) stator flux. 104

Chapter 5: Multi-level DTC with CMV mitigation for two-machine drive

Figure 5.1: The path of the CMV in generalized schematic of the multi-phase VSI. 109

Figure 5.2: EMI's sources in the ASD. 110

Figure 5.3: the effect of the voltage surge on the machine's windings insulation. 110

Figure 5.4: voltages generated in the AC machines due to the parasitic capacitances and the simplified equivalent circuit. 111

Figure 5.5: paths of the bearing's currents. 111

Figure 5.6: (a) Causes of the CMV, effects and their respective solutions, (b) the solution location on the drive. 112

Figure 5.7: (C1) Faraday shielding. 113

Figure 5.8: (C2) Insulated bearings. 113

Figure 5.9: (C3) Ceramic or hybrid bearings. 114

Figure 5.10: (C4) Conductive grease. 114

Figure 5.11: (C5) Insulated mechanical load coupling. 115

Figure 5.12: (C6) Shielded cables. 115

Figure 5.13: (C7) Grounding cables. 116

Figure 5.14: (C8) Brushes. 116

Figure 5.15: (C9) Shaft grounding ring. 117

Figure 5.16: The path of CMV in the two-machine drive. 118

Figure 5.17: Mapping of the VVs: (a) $\alpha\beta_1$ plane, (b) $\alpha\beta_2$ plane. 119

Figure 5.18: (a) VVs peculiarities, (b) VVVs mapping. 120
Figure 5.19: Schematics of DTC_{CMV} for the two-machine drive. 122
Figure 5.20: Three-level DTC-ANN response: (a) rotor's mechanical speed, (b) electromagnetic torque, (c) stator flux, (d) stator currents. 123
Figure 5.21: Stator currents' THD of Three-level DTC-ANN: (a) FPIM1, (b) FPIM2. 123
Figure 5.22: Generated CMV in three-level DTC-ANN. 124
Figure 5.23: Response Of DTC_{CMV}: (a) rotor's mechanical speed, (b) electromagnetic torque, (c) stator flux, (d) stator currents. 124
Figure 5.24: Stator currents' THD of DTC_{CMV}: (a) FPIM1, (b) FPIM2. 124
Figure 5.25: Generated CMV in DTC_{CMV}. 125

List of tables

Chapter 1 Modelling of two parallel-connected drive

Table 1.1: The switching states of the FP-VSI. 23
Table 1.2: The amplitudes of the FP-VSI's VVs. 24
Table 1.3: The switching states of THL-FP-VSI. 26
Table 1.4: Vertex VVs amplitudes. 28
Table 1.5: Non-vertex VVs amplitudes. 28
Table 1.6: Phase transposition rules for even phase number. 31
Table 1.7: Phase transposition rules for odd phase number. 32
Table 1.8: Phase transposition rules. 33
Table 1.9: Parameters of the two FPIMs. 35
Table 1.10: Testing scenario. 35

Chapter 2 Multi-level DTC of two-machine drive

Table 2.1: Sector numbers and boundaries. 49
Table 2.2: Two-level DTC's ST. 51
Table 2.3: Three-level DTC's ST. 51
Table 2.5: First test scenario of the FPIM1. 53
Table 2.6: First test scenario of the FPIM2. 53
Table 2.7: Second test scenario. 55
Table 2.8: Comparative study between the 2L-DTC and 3L-DTC techniques. 58

Chapter 3 Multi-level intelligent DTC of two-machine drive

Table 3.1: Two-level DTC-ANN 's controllers characteristics. 70
Table 3.2: Three-level DTC-ANN 's controllers characteristics. 71
Table 3.3: First test scenario. 73
Table 3.4: Second test scenario. 75
Table 3.5: Analytical study between the 2L-DTC and 2L-DTC-ANN. 78
Table 3.6: Analytical study between the 3L-DTC and 3L-DTC-ANN. 78

Chapter 4 Sensorless multi-level intelligent DTC of two-machine drive

Table 4.1: First test scenario for the FPIM1. 85
Table 4.2: First test scenario for the FPIM2. 85
Table 4.3: Second test scenario for the two machines. 86

Table 4.4: First test scenario for the FPIM1. 95
Table 4.5: First test scenario for the FPIM2. 95
Table 4.6: Second test scenario for the two machines. 97
Table 4.7: First test scenario for the FPIM1. 102
Table 4.8: First test scenario for the FPIM2. 102
Table 4.9: Second test scenario for the two machines. 104
Table 4.10: Comparative analysis of the performance of DTC and DTC-ANN. 106
Table 4.11: Performance comparison of the three MM sensorless methods. 106

Chapter 5 Multi-level DTC with CMV mitigation for two-machine drive

Table 5.1: Peak-to-peak CMV and the theoretical waveforms. 118
Table 5.2: The ST of VVVs. 121
Table 5.3: Actual VV’s ST. 121
Table 5.4: First test scenario for the FPIM1. 122
Table 5.5: First test scenario for the FPIM2. 122
Table 5.6: Comparative analysis. 126

Abstract

Multilevel direct torque control of sensorless two five-phase induction machines connected in parallel

Railway traction, naval propulsion, and robotics are just a few examples of numerous industrial sectors that exploit the multi-machine drive, more than one electrical machine drive. Which is currently comprising n three-phase machines parallel-connected in different configurations. However, it lacks the means of independent control of each machine in the drive due to the Master-Slave and Averaging control schemes utilized in the three-phase system.

Therefore, this thesis considers the concept of an independently controlled two-machine drive constituted of two multiphase induction machines (IM) parallel-connected to a single multi-level multiphase voltage source inverter (VSI), to enhance the concept of multi-phase multi-machine drive when compared to its three-phase counterpart. Where the five-phase IM (FPIM) topology is proposed based on a cost-effective technique study, by exploiting the additional degrees of freedom (DOF) offered by this topology. The fundamentals of the independent control concept of the parallel operation of the two-machine drive is derived from the fact that the AC machines, disregarding the phase number, require the control of only one set of current components. Thus, the extra current set can be exploited to control independently the other machines in the drive with the proper stator phase connection. Nevertheless, this concept faces numerous challenges due to the inherited control difficulties of the IM and the multi-level topologies of the VSI, the parallel operation complexity, and the poor performance of the traditional control strategies, especially during the low-speed operation.

For this reason, the direct torque control (DTC) technique presents an interesting solution to overcome the aforementioned challenges, offering robust and dynamic performance. Nevertheless, every technique has its pros and cons; for instance, it presents a high content of flux/torque ripples, in addition to the size and complexity of the switching table (ST), which reduces the performance of the suggested concept of the two-machine drive. For this reason, an AI-based DTC technique, exploiting the artificial neural networks (ANN) benefits, to improve

the robustness and enhance the performance of the drive resulting in the reduction of the developed flux/torque ripples. This latter is achieved by replacing the hysteresis controllers (HC) and the ST of the conventional method by ANNs-based controller; thus, resulting in a simple yet more robust structure.

Moreover, to further optimize the performance, size and improve the aforementioned cost-effective technique study based two-machine drive's fault-tolerant capability, Machine Model-based (MM) sensorless methods are investigated to observe and estimate the machine's critical state variables to achieve the optimum performance of the DTC technique and the drive by addressing the drawback of the utilized open-loop estimator especially during the low-speed operation. Where the three proposed MM techniques based on Model reference adaptive system (MRAS), Sliding mode observer (SMO), and Virtual current sensor (VCS) results in higher performance regarding the speed tracking during the transient and steady state operation, negligible estimation error, and better rejection of external disturbances in different operating scenarios.

On the other hand, a preventive mitigation approach to tackle the Common-Mode Voltage (CMV) generated by the PWM-controlled VSI's discrete voltages is considered. For this reason, a modified DTC is discussed, utilizing the concept of virtual voltage vector (VVV). These VVVs are synthesized based on a selected switching states capable of reducing the CMV peak-to-peak values. Thus, improving the drive's reliability and reducing the maintenance's time and cost by addressing the inherited drawback of the multi-level VSI from its roots.

Keywords: Five-phase induction machine (FPIM), Direct torque control (DTC), two-machine drive parallel-connected, Multi-level voltage source inverters (VSI), Artificial neural network (ANN), Sensorless control, Model reference adaptive system (MRAS), Sliding mode observer (SMO), Current reconstruction, Virtual current sensor (VCS), Common-Mode Voltage (CMV), Virtual voltage vectors (VVV).

Résumé

Commande directe de couple multiniveaux sans capteur de deux machines à induction penta-phasées connectées en parallèle

La traction ferroviaire, la propulsion navale et la robotique ne sont que quelques exemples parmi les nombreux secteurs industriels qui exploitent l'entraînement multi-machines, c'est-à-dire l'entraînement de plusieurs machines électriques. Celui-ci comprend actuellement trois machines triphasées connectées en parallèle selon différentes configurations. Cependant, il ne permet pas de contrôler indépendamment chaque machine de l'entraînement en raison des schémas de contrôle maître-esclave et de moyennage utilisés dans le système triphasé.

Par conséquent, cette thèse examine le concept d'un entraînement à deux machines à commande indépendante constitué de deux machines à induction multi phasés (IM) connectées en parallèle à un seul onduleur à tension multi phasé à plusieurs niveaux (VSI), afin d'améliorer le concept d'entraînement multi phasé à plusieurs machines par rapport à son équivalent triphasé. La topologie IM à cinq phases (FPIM) est proposée sur la base d'une étude technique rentable, en exploitant les degrés de liberté supplémentaires (DOF) offerts par cette topologie. Les principes fondamentaux du concept de contrôle indépendant du fonctionnement en parallèle du système à deux machines découlent du fait que les machines à courant alternatif, quel que soit le nombre de phases, ne nécessitent le contrôle que d'un seul ensemble de composants de courant. Ainsi, l'ensemble de courants supplémentaire peut être exploité pour contrôler indépendamment les autres machines de l'entraînement avec la connexion de phase statorique appropriée. Néanmoins, ce concept se heurte à de nombreux défis en raison des difficultés de contrôle héritées de l'IM et des topologies à plusieurs niveaux du VSI, de la complexité du fonctionnement en parallèle et des performances médiocres des stratégies de contrôle traditionnelles, en particulier lors du fonctionnement à basse vitesse.

Pour cette raison, la technique de contrôle direct du couple (DTC) présente une solution intéressante pour surmonter les défis susmentionnés, offrant des performances robustes et dynamiques. Néanmoins, chaque technique a ses avantages et ses inconvénients ; par exemple,

elle présente un contenu élevé d'ondulations de flux/couple, en plus de la taille et de la complexité de la table de commutation (ST), ce qui réduit les performances du concept proposé d'entraînement à deux machines. C'est pourquoi une technique DTC basée sur l'IA, exploitant les avantages des réseaux neuronaux artificiels (ANN), a été mise au point afin d'améliorer la robustesse et les performances de l'entraînement, ce qui a permis de réduire les ondulations de flux/couple développées. Ce dernier objectif a été atteint en remplaçant les contrôleurs d'hystérésis (HC) et la ST de la méthode conventionnelle par un contrôleur basé sur les ANN, ce qui a permis d'obtenir une structure simple mais plus robuste.

De plus, afin d'optimiser davantage les performances, la taille et d'améliorer la capacité de tolérance aux pannes de l'entraînement à deux machines basé sur l'étude technique rentable susmentionnée, des méthodes sans capteur basées sur le modèle de machine (MM) sont étudiées pour observer et estimer les variables d'état critiques de la machine afin d'obtenir les performances optimales de la technique DTC et de l'entraînement en remédiant à l'inconvénient de l'estimateur en boucle ouverte utilisé, en particulier pendant le fonctionnement à basse vitesse. Les trois techniques MM proposées, basées sur le système adaptatif de référence de modèle (MRAS), l'observateur en mode glissant (SMO) et le capteur de courant virtuel (VCS), permettent d'obtenir des performances supérieures en termes de suivi de la vitesse pendant le fonctionnement transitoire et en régime permanent, une erreur d'estimation négligeable et un meilleur rejet des perturbations externes dans différents scénarios de fonctionnement.

D'autre part, une approche préventive d'atténuation visant à lutter contre la tension en mode commun (CMV) générée par les tensions discrètes du VSI contrôlé par PWM est envisagée. Pour cette raison, un DTC modifié est envisagé, utilisant le concept de vecteur de tension virtuel (VVV). Ces VVV sont synthétisés sur la base d'états de commutation sélectionnés capables de réduire les valeurs crête à crête de la CMV. Ainsi, la fiabilité du variateur est améliorée et le temps et le coût de maintenance sont réduits en remédiant à l'inconvénient inhérent au VSI à plusieurs niveaux.

Mots clés : Machine à induction penta-phasé (FPIM), Commande directe de couple (DTC), Deux machines connectées on parallèle, Onduleurs multi-niveaux (VSI), Réseaux neurones artificiel (ANN), Commande sans capteur, Model reference adaptive system (MRAS), Observateur en mode glissant (SMO), Reconstruction des courants, Capteur du courant virtuel (VCS), Tension en mode commun (CMV), Vecteur de tension virtuel (VVV).

ملخص

التحكم المباشر متعدد المستويات في عزم الدوران لماكنتين حثيّتين خماسيتي الطور بدون مستشعرات متصلتين على التوازي

تعد قوة الجر للسكك الحديدية والدفع البحري والروبوتات مجرد أمثلة قليلة من بين العديد من القطاعات الصناعية التي تستفيد من متعدد الماكنات، أي أكثر من ماكينة كهربائية واحدة. والذي يتألف حاليًا من ثلاث ماكينات ثلاثية الطور متصلة بشكل متوازٍ في تكوينات مختلفة. ومع ذلك، فإنه يفتقر إلى وسائل التحكم المستقل لكل ماكينة في المحرك بسبب أنظمة التحكم Master-slave وAveraging المستخدمة في النظام ثلاثي الطور.

لذلك، تتناول هذه الأطروحة مفهوم نظام ثنائي الماكنات يتم التحكم فيه بشكل مستقل ويتكون من آلتين حثيتين متعددتي الطور (IM)متصلتين بشكل متوازٍ بمموج جهد متعدد المستويات متعدد الطور (VSI) واحد، وذلك تحسين أداء نظام متعدد الماكنات متعددة الأطور مقارنة بنظيره ثلاثي الطور. حيث يتم اقتراح طوبولوجيا IM خماسية الطور (FPIM) بناءً على دراسة تعتمد على المقارنة بين فعالية تقنية و التكلفة، من خلال استغلال درجات الحرية الإضافية (DOF) التي توفرها هذه الطوبولوجيا. تستمد أساسيات مفهوم التحكم المستقل للتشغيل المتوازي لنظام ثنائي الماكنات من حقيقة أن الآلات التي تعمل بالتيار المتردد، بغض النظر عن عدد الأطوار، تتطلب التحكم في مجموعة واحدة فقط من مكونات التيار. وبالتالي، يمكن استغلال مجموعة التيار الإضافية للتحكم بشكل مستقل في الآلات الأخرى في النظام مع توصيل المناسب لأطور الجزء الثابت. ومع ذلك، يواجه هذا المفهوم العديد من التحديات بسبب صعوبات التحكم الموروثة في IM والطوبولوجيات متعددة المستويات لـVSI ، وتعقيد التشغيل المتوازي، والأداء الضعيف لاستراتيجيات التحكم التقليدية، خاصة أثناء التشغيل بسرعة منخفضة.

لهذا السبب، تقدم تقنية التحكم المباشر في عزم الدوران (DTC) حلاً مثيراً للاهتمام للتغلب على التحديات المذكورة أعلاه، حيث توفر أداءً قوياً وديناميكياً. ومع ذلك، لكل تقنية مزاياها وعيوبها؛ على سبيل المثال، فهي تتميز بمحتوى عالٍ من تموجات التدفق/عزم الدوران، بالإضافة إلى حجم وتعقيد جدول التبديل (ST)، مما يقلل من أداء المفهوم المقترح لنظام الماكينتين. لهذا السبب، تستخدم تقنية DTC القائمة على الذكاء الاصطناعي مزايا الشبكات العصبية الاصطناعية (ANN) لتحسين المتانة وتعزيز أداء المحرك، مما يؤدي إلى تقليل تموجات التدفق/العزم الناتجة. ويتحقق هذا الأخير عن طريق استبدال وحدات التحكم في التباطؤ (HC) وجدول التبديل (ST) في الطريقة التقليدية بوحدة تحكم قائمة على الشبكات العصبية الاصطناعية (ANNs)؛ مما ينتج عنه هيكل بسيط ولكنه أكثر متانة.

علاوة على ذلك، من أجل تحسين الأداء والحجم وتحسين الدراسة الفنية المذكورة أعلاه المتعلقة بالقدرة على تحمل الأعطال لنظام ثنائي الآلة، تمت دراسة الطرق غير المستندة إلى أجهزة الاستشعار القائمة على نموذج الآلة (MM) لمراقبة وتقدير المتغيرات الحرجة للآلة من أجل تحقيق الأداء الأمثل لتقنية DTC والنظام من خلال معالجة عيوب مستشعر الحلقة المفتوحة

المستخدم خاصة أثناء التشغيل بسرعة منخفضة. حيث تؤدي التقنيات الثلاث المقترحة MM القائمة على نظام التكيف المرجعي للنموذج (MRAS) ومراقب الوضع المنزلق (SMO) ومستشعر التيار الافتراضي (VCS) إلى أداء أعلى فيما يتعلق بتتبع السرعة أثناء التشغيل العابر والحالة المستقرة، وخطأ تقدير ضئيل، ورفض أفضل للاضطرابات الخارجية في سيناريوهات التشغيل المختلفة.

من ناحية أخرى، يتم النظر في نهج التخفيف الوقائي لمعالجة الجهد المشترك (CMV) الناتج عن الجهد الغير مستمر لـ VSI الذي يتم التحكم فيه بواسطة PWM. لهذا السبب، تتم مناقشة DTC المعدلة، باستخدام مفهوم متجه الجهد الافتراضي (VVV). يتم توليف هذه VVVs بناءً على حالات التبديل المحددة القادرة على تقليل قيم CMV من الذروة إلى الذروة. وبالتالي، يتم تحسين موثوقية النظام وتقليل وقت الصيانة وتكلفتها من خلال معالجة العيب الموروث من VSI متعدد المستويات من جذوره.

كلمات مفتاحية : آلة الحث الخماسية الطور (FPIM)، التحكم المباشر في عزم الدوران (DTC)، نظام ثنائي الآلة, محركان متصلان بالتوازي، مموج متعدد المستويات (VSI)، الشبكة العصبية الاصطناعية (ANN)، التحكم بدون مستشعرات، نظام التكيف المرجعي النموذجي (MRAS)، مراقب الوضع المنزلق (SMO)، إعادة بناء التيار، مستشعر التيار الافتراضي (VCS)، الجهد المشترك (CMV)، متجهات الجهد الافتراضي (VVV).

Chapter 1

Modelling of two parallel-connected machine drive

1.1. Introduction

Numerous industrial sectors, such as EVs, for example, rely on AC machines for adjustable speed drives (ASD) [2]. The multiphase machines, namely the FPIMs, are the best candidates for such applications since they have the benefit of a fair balance between the system advantages, cost, and size compared to their complexity. These advantages are increased torque per ampere ratio, reduced EMI, and better MMF waveforms, to name a few [29].

To ensure a wide speed range and four quadrants of drive operation, multi-level multiphase voltage source inverters (VSI) are used. Because additional phases are available, these inverters decrease the current rating per phase and reduce the stress on the semiconductors and the machine's windings [43].

Furthermore, the FPIMs offer additional degrees of freedom (DOF) that further enhance the potential use of these machines, such as fault-tolerant operation, torque enhancement, and single VSI fed parallel/series connected multiphase multi-machine drive, for example [29].

The independent multiphase multi-machine drive parallel/series connected has a high potential in the industrial sector. The cornerstone of this latter application is based on the fact that the VC of any AC machine requires only the control of two of the current components. Nevertheless, such control requires the performance of a determined phase transposition for the stator phase connection.

Thus, this chapter details the multiphase machine types and merits/demerits in the second section. The FPIMs are modeled in section three by five sets of electrical and magnetic equations and one mechanical equation in the natural frame. Nevertheless, these sets of equations require simplification process for easy study of the machine's performance for a four-phase system $(\alpha_1, \beta_1, \alpha_2, \beta_2)$ through a transformation matrix in the fourth section. The different parts of the VFD are modeled with special focus on the multi-level VSIs. In section

five, the working principle of the two-machine parallel-connected to a single VSI, advantages, and modeling are discussed.

1.2. Multi-phase machines

The AC machines with a phase number higher than three-phases are recognized as a potential solution for specific ASDs, namely the hybrid and full EVs, naval propulsion, and aerospace applications [42, 44 - 47].

The multi-phase machine solution can be categorized into two types according to the multiple of three-phase or the number of the stator phases referred to as type 1 or type 2, respectively.

1.2.1. Type 1 multi-phase AC machines

The type 1 multi-phase AC machines are characterized by a multiple of three stator phases number and further grouped in n (n=1,2,3…n) stator three-phase machine (multi-star three-phase machine). Nevertheless, based on the angle α for a given phase number between the two adjacent phases, several configurations are possible. For instance, for the dual star AC machine (q=6), two different configurations are possible as follows [42, 44 - 47]:

- Asymmetrical dual-star AC machine, where the two-star points are shifted by an angle of 30°, as shown in Figure 1.1.a.
- Symmetrical dual-star AC machine, where the two-star points are shifted by an angle of 60°, as shown in Figure 1.1.b.

Figure 1.1 presents the type 1 multi-phase AC machines.

1.2.2. Type 2 multi-phase AC machines

The type 2 multi-phase AC machines are characterized by stator phases of an odd number (q) as shown in Figure 1.2, where α is the angle between the two adjacent stator phases windings [42, 44 - 47].

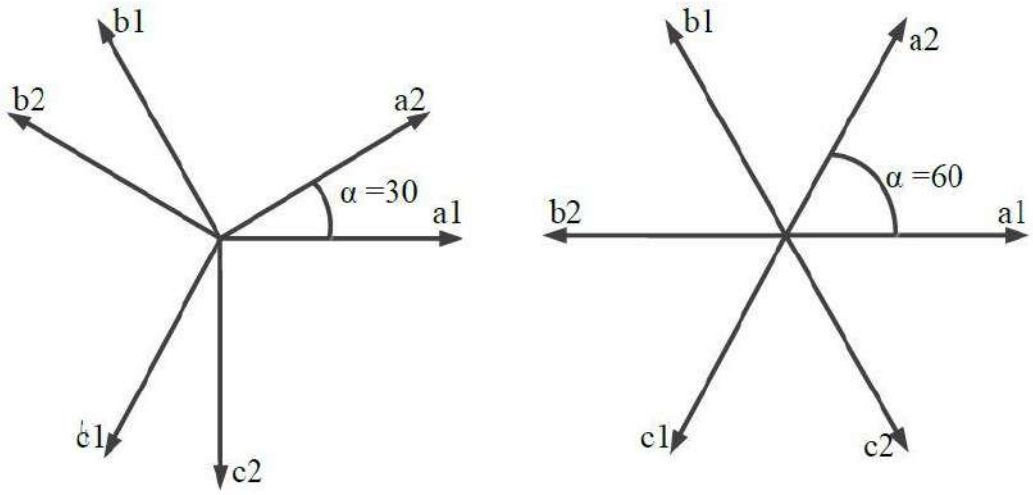

(a) (b)

Figure 1.1: Type 1 multi-phase AC machines: (a) symmetrical machines, (b) asymmetrical machines.

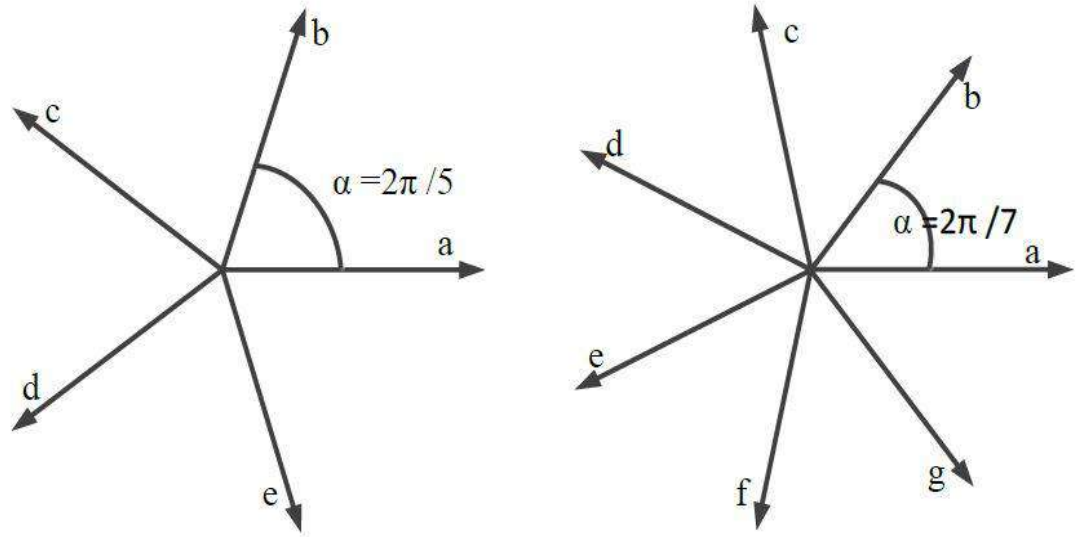

(a) (b)

Figure 1.2: Type 2 multi-phase AC machines: (a) FP machine, (b) seven-phase machine.

1.2.3. Multi-phase AC machines' merits and demerits

Since the introduction of multiphase AC machines, a special interest has been trigged due to their capability to reduce electromagnetic pulsations [42]. However, every solution has some downsides, too, as follows:

1.2.3.1. Multi-phase AC machines merits

- **Torque ripples reduction:** The multi-phase AC machines have a potent signature of reducing the developed torque ripples, especially in the era of the PWM drive rating from the low to medium power levels. Thus, optimize the noise-vibration levels of the drive [44].
- **Power segmentation:** This type of machine possesses a key factor in the high-power industries, in contract with the three-phase machine, which is that for a given machine's power rating, the additional phases available enable the reduction of the power level per phase; hence, current, which in turn is translated in the semiconductor's switches rating [32, 48]
- **Additional DOF:** In the multi-phase topology, in contrast to the three-phase topology, not only is the fundamental component used to generate the torque, but also the third current harmonic component. For instance, in the five-phase topology, the torque can be generated both by the fundamental and the third current harmonic components. By exploiting this feature, the developed torque can be enhanced through the injection of harmonic currents.
- **Fault-tolerant:** The foremost reason to consider multi-phase machines in critical applications is their ability to operate under a faulty condition, such as an open-phase fault. These machines can produce a rotating MMF in the case of an open-phase fault without any modification in either the control scheme or the wiring of the drive. However, the performance degrades, and the power level is reduced [48].

1.2.3.2. Multi-phase AC machines demerits

- **Current harmonics:** Specific harmonic components (stator harmonics) are trapped in the stator windings due to the fact that they contribute to the generation of a rotating MMF. Where the impedance presented by these harmonic spaces is low, which results in a high harmonic current [49].
- **High cost and complexity of the drive:** The additional phases in use imply the use of additional semiconductor switches, which in turn increase the cost of the drive. Moreover, the additional switches in use implies a complex control scheme.

1.3. Modelling of the FPIM

Figure 1.3 shows a schematic representation of the FPIMs. Where these latter have five symmetrical distributed windings star-connected with 72 electrical degrees between any two consecutive phases and a squirrel cage rotor.

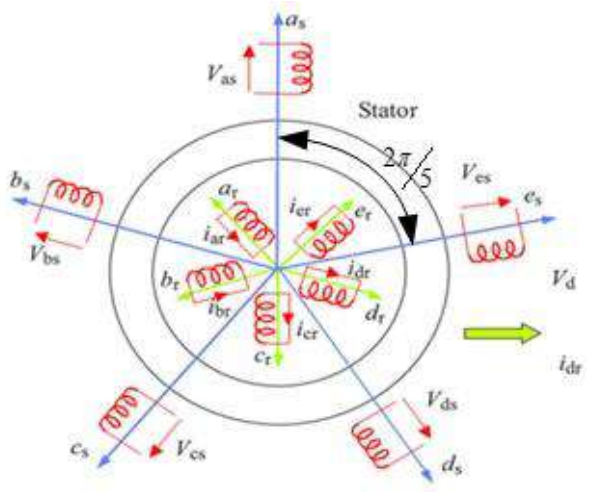

Figure 1.3: Schematic representation of the FPIM.

The modeling approach of the FPIMs considers the same simplifying hypothesis as for the three-phase machines as follows [50]:

- A uniform air gap.
- Sinusoidal distribution of MMF in the airgap.
- Neglected skin effect, temperature effect, and core losses.
- The notch effect is neglected.
- Constant inductances and resistances.
- The magnetic saturation effect is neglected.
- The stator and rotor have the same phase order.

1.3.1. FPIM electrical equations [51]

The stator and rotor's five-phase voltage equations are given as follows:

$$\begin{cases} V_s = R_s I_s + d\phi_s / dt \\ 0 = R_r I_r + d\phi_r / dt \end{cases} \quad (1.1)$$

The stator and rotor's flux expression are as follows:

$$\begin{cases} \phi_s = L_{ss} I_s + M_{sr} I_r \\ \phi_r = L_{rr} I_r + M_{rs} I_s \end{cases} \quad (1.2)$$

By substituting (1.2) in (1.1):

$$\begin{cases} V_s = R_s I_s + d(L_{ss} I_s)/dt + d(M_{sr} I_r)/dt \\ 0 = R_r I_r + d(L_{rr} I_r)/dt + d(M_{rs} I_s)/dt \end{cases} \quad (1.3)$$

Where:

$V_s = \left[V_{as}\ V_{bs}\ V_{cs}\ V_{ds}\ V_{es} \right]^T$: stator voltages vector.

$I_s = \left[I_{as}\ I_{bs}\ I_{cs}\ I_{ds}\ I_{es} \right]^T$: stator currents vector.

$I_r = \left[I_{ar}\ I_{br}\ I_{cr}\ I_{dr}\ I_{er} \right]^T$: rotor currents vector.

$\phi_s = \left[\phi_{as}\ \phi_{bs}\ \phi_{cs}\ \phi_{ds}\ \phi_{es} \right]^T$: stator flux vector.

$\phi_r = \left[\phi_{ar}\ \phi_{br}\ \phi_{cr}\ \phi_{dr}\ \phi_{er} \right]^T$: rotor flux vector.

$R_s = diag\left[R_{as}\ R_{bs}\ R_{cs}\ R_{ds}\ R_{es} \right]$: stator resistance matrix.

$R_r = diag\left[R_{ar}\ R_{br}\ R_{cr}\ R_{dr}\ R_{er} \right]$: rotor resistance matrix.

L_{ss} : stator inductances matrix.

L_{rr} : rotor inductance matrix.

$$L_{ss} = \begin{bmatrix} L_s & M_s & M_s & M_s & M_s \\ M_s & L_s & M_s & M_s & M_s \\ M_s & M_s & L_s & M_s & M_s \\ M_s & M_s & M_s & L_s & M_s \\ M_s & M_s & M_s & M_s & L_s \end{bmatrix} \quad (1.4)$$

$$L_{rr}=\begin{bmatrix} L_r & M_r & M_r & M_r & M_r \\ M_r & L_r & M_r & M_r & M_r \\ M_r & M_r & L_r & M_r & M_r \\ M_r & M_r & M_r & L_r & M_r \\ M_r & M_r & M_r & M_r & L_r \end{bmatrix} \tag{1.5}$$

$M_{sr}=M_{rs}$: mutual inductances.

$$M_{sr}=M_{rs}=M\begin{bmatrix} \cos(\theta) & \cos(\theta+\alpha) & \cos(\theta+2\alpha) & \cos(\theta+3\alpha) & \cos(\theta+4\alpha) \\ \cos(\theta+4\alpha) & \cos(\theta) & \cos(\theta+\alpha) & \cos(\theta+2\alpha) & \cos(\theta+3\alpha) \\ \cos(\theta+3\alpha) & \cos(\theta+4\alpha) & \cos(\theta) & \cos(\theta+\alpha) & \cos(\theta+2\alpha) \\ \cos(\theta+2\alpha) & \cos(\theta+3\alpha) & \cos(\theta+4\alpha) & \cos(\theta) & \cos(\theta+\alpha) \\ \cos(\theta+\alpha) & \cos(\theta+2\alpha) & \cos(\theta+3\alpha) & \cos(\theta+4\alpha) & \cos(\theta) \end{bmatrix} \tag{1.6}$$

θ: electrical angel between stator and rotor phases and $\alpha=2\pi/5$.

1.3.2. FPIM mechanical equations

The developed electromagnetic torque is expressed as:

$$\begin{cases} T_{em}=pI_s\,{}'d(M_{rs}I_s)/dt \\ T_{em}-T_L=J\,d\omega_m/dt+f\,\omega_r \end{cases} \tag{1.7}$$

Where:

J: moment of inertia.

f: fraction coefficient.

T_L: load torque.

T_{em}: electromagnetic torque.

ω_m: rotor's mechanical speed.

The model in (1.3) describing the FPIMs is highly complex, containing coupled and time-varying coefficients depending on the rotor's instantaneous position. Therefore, a coordinate transformation is applied to simplify the obtained model in (1.3).

1.3.3. Decoupling transformation

The power invariant co-ordinate transformation matrix to the arbitrary reference frame is applied to the five-phase machine equations as follows [52]:

$$[C_s]=\begin{bmatrix} V_{s\alpha 1} \\ V_{s\beta 1} \\ V_{s\alpha 2} \\ V_{s\beta 2} \\ V_{s0} \end{bmatrix} = \sqrt{2/5}\begin{bmatrix} \cos(\theta) & \cos(\theta+\alpha) & \cos(\theta+2\alpha) & \cos(\theta+3\alpha) & \cos(\theta+4\alpha) \\ -\sin(\theta) & -\sin(\theta+\alpha) & -\sin(\theta+2\alpha) & -\sin(\theta+3\alpha) & -\sin(\theta+4\alpha) \\ 1 & \cos(\theta+2\alpha) & \cos(\theta+4\alpha) & \cos(\theta+\alpha) & \cos(\theta+3\alpha) \\ 0 & \sin(\theta+2\alpha) & \sin(\theta+4\alpha) & \sin(\theta+\alpha) & \sin(\theta+3\alpha) \\ \sqrt{1/2} & \sqrt{1/2} & \sqrt{1/2} & \sqrt{1/2} & \sqrt{1/2} \end{bmatrix} \quad (1.8)$$

The machine's rotor variables are transformed using the same co-ordinate transformation matrix while taking into consideration the instantaneous angular position of the α axis of the common reference frame with respect to the rotor's phase 'a' magnetic axis [52]:

$$[C_r]=\begin{bmatrix} V_{r\alpha 1} \\ V_{r\beta 1} \\ V_{r\alpha 2} \\ V_{r\beta 2} \\ V_{r0} \end{bmatrix} = \sqrt{2/5}\begin{bmatrix} \cos(\beta) & \cos(\beta+\alpha) & \cos(\beta+2\alpha) & \cos(\beta+3\alpha) & \cos(\beta+4\alpha) \\ -\sin(\beta) & -\sin(\beta+\alpha) & -\sin(\beta+2\alpha) & -\sin(\beta+3\alpha) & -\sin(\beta+4\alpha) \\ 1 & \cos(\beta+2\alpha) & \cos(\beta+4\alpha) & \cos(\beta+\alpha) & \cos(\beta+3\alpha) \\ 0 & \sin(\beta+2\alpha) & \sin(\beta+4\alpha) & \sin(\beta+\alpha) & \sin(\beta+3\alpha) \\ \sqrt{1/2} & \sqrt{1/2} & \sqrt{1/2} & \sqrt{1/2} & \sqrt{1/2} \end{bmatrix} \quad (1.9)$$

The two transformations matrices $[C_S]$ and $[C_r]$ angles are selected based on the common reference frame's arbitrary speed as follows:

$$\theta_s = \int \omega_s dt; \quad \beta = \theta_s - \theta = \int (\omega_s - \omega) dt \quad (1.10)$$

With ω is the rotor's instantaneous electrical angular speed.

1.3.4. The FPIM's model in the arbitrary reference frame [51]

The relationship between the machine's original state variables and newly transformed variables is as follows:

Voltages' equations:

$$\begin{cases} V_{s\alpha\beta} = [C_s] V_{sabcde} \\ V_{r\alpha\beta} = [C_s] V_{rabcde} \end{cases} \quad (1.11)$$

Currents' equations:

$$\begin{cases} i_{s\alpha\beta} = [C_s] i_{sabcde} \\ i_{r\alpha\beta} = [C_s] i_{rabcde} \end{cases} \quad (1.12)$$

Fluxes equations

$$\begin{cases} \phi_{s\alpha\beta} = [C_s] \phi_{sabcde} \\ \phi_{r\alpha\beta} = [C_s] \phi_{rabcde} \end{cases} \quad (1.13)$$

Where:

$V_{s\alpha\beta}$: stator voltages in the arbitrary reference frame.

$V_{r\alpha\beta}$: rotor voltages in the arbitrary reference frame.

$i_{s\alpha\beta}$: stator currents in the arbitrary reference frame.

$i_{r\alpha\beta}$: rotor voltages in the arbitrary reference frame.

$\phi_{s\alpha\beta}$: stator flux in the arbitrary reference frame.

$\phi_{r\alpha\beta}$ rotor flux in the arbitrary reference frame.

By the application of (1.8) and (1.9) to (1.1), (1.2), and (1.3), the machine's mathematical model is given as:

The stator voltages equations:

$$\begin{cases} V_{s\alpha1} = R_s i_{s\alpha1} - \omega_a \phi_{s\alpha1} + d\phi_{s\alpha1}/dt \\ V_{s\beta1} = R_s i_{s\beta1} + \omega_a \phi_{s\beta1} + d\phi_{s\beta1}/dt \\ V_{s\alpha2} = R_s i_{s\alpha2} + d\phi_{s\alpha2}/dt \\ V_{s\beta2} = R_s i_{s\beta2} + d\phi_{s\beta2}/dt \\ V_{s0} = R_s i_{s0} + d\phi_0/dt \end{cases} \quad (1.14)$$

The rotor voltages equations:

$$\begin{cases} V_{r\alpha1} = R_r i_{r\alpha1} - (\omega_a - \omega)\phi_{r\alpha1} + d\phi_{r\alpha1}/dt \\ V_{r\beta1} = R_r i_{r\beta1} + (\omega_a - \omega)\phi_{r\beta1} + d\phi_{r\beta1}/dt \\ V_{r\alpha2} = R_r i_{r\alpha2} + d\phi_{r\alpha2}/dt \\ V_{r\beta2} = R_r i_{r\beta2} + d\phi_{r\beta2}/dt \\ V_{r0} = R_r i_{r0} + d\phi_{r0}/dt \end{cases} \quad (1.15)$$

The stator flux linkage equation:

$$\begin{cases} \phi_{s\alpha1} = L_s i_{s\alpha1} + M_{sr} i_{r\alpha1} \\ \phi_{s\beta1} = L_s i_{s\beta1} + M_{sr} i_{r\beta1} \\ \phi_{s\alpha2} = L_s i_{s\alpha2} \\ \phi_{s\beta2} = L_s i_{s\beta2} \\ \phi_{s0} = L_s i_{s0} \end{cases} \quad (1.16)$$

The rotor flux linkage equation:

$$\begin{cases} \phi_{r\alpha1} = L_r i_{r\alpha1} + M_{rs} i_{s\alpha1} \\ \phi_{r\beta1} = L_r i_{r\beta1} + M_{rs} i_{s\beta1} \\ \phi_{r\alpha2} = L_r i_{r\alpha2} \\ \phi_{r\beta2} = L_r i_{r\beta2} \\ \phi_{r0} = L_s i_{r0} \end{cases} \quad (1.17)$$

The developed electromagnetic torque and mechanical equation are described as follows:

$$\begin{cases} T_{em} = p(\phi_{s\alpha1} i_{s\beta1} - \phi_{s\beta1} i_{s\alpha1}) \\ J\, d\omega_m/dt = T_{em} - T_L - f\,\omega_m \end{cases} \quad (1.18)$$

Figure 1.4 illustrates the schematic diagram of the FPIM in the arbitrary reference frame.

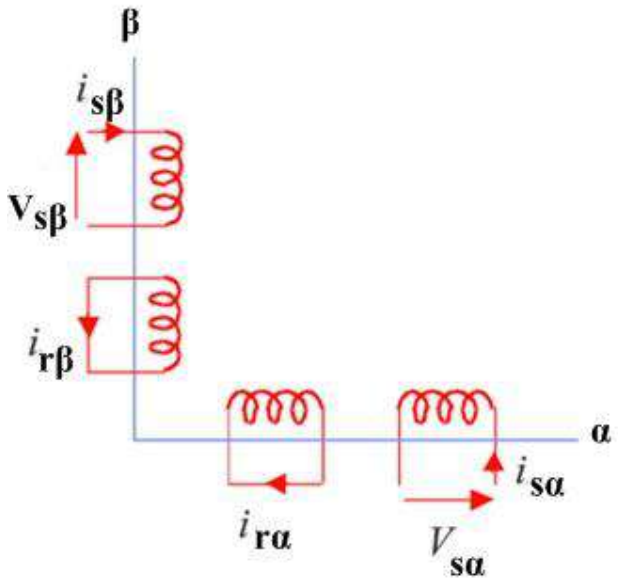

Figure 1.4: Schematic representation of the FPIM in the arbitrary reference frame.

1.4. Drive's power supply modelling

The VFSs, illustrated in Figure 1.5, can be divided into three subsystems as follows:

- The AC/DC converter.
- RLC filter to reduce the DC-link voltage/current ripples.
- The DC/AC converter.

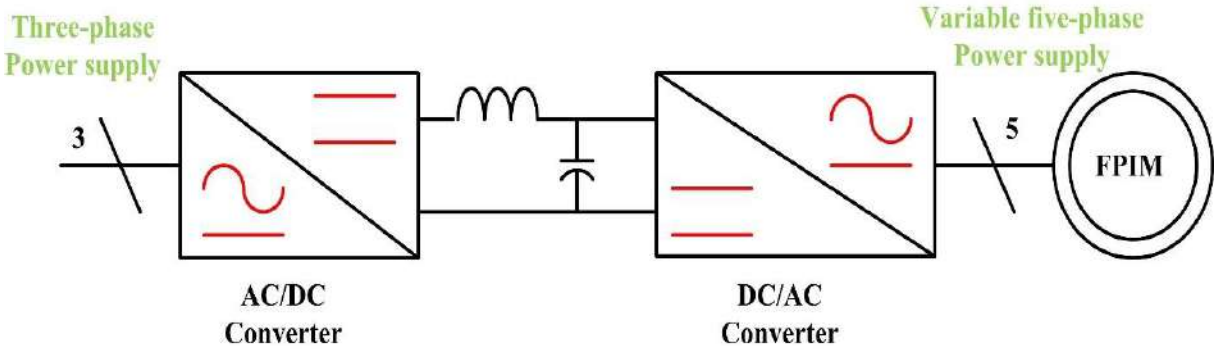

Figure 1.5: Schematic diagram of VSI fed FPIM.

1.4.1 Rectifier modelling

The rectifiers are AC-to-DC converters, and their main purpose in the ASD is to supply a constant DC voltage to power the DC link. Furthermore, the use of the rectifier enables

enhancing the power factor and the current/voltage distortion. Figure 1.6 illustrates the schematics of the rectifier's power circuit.

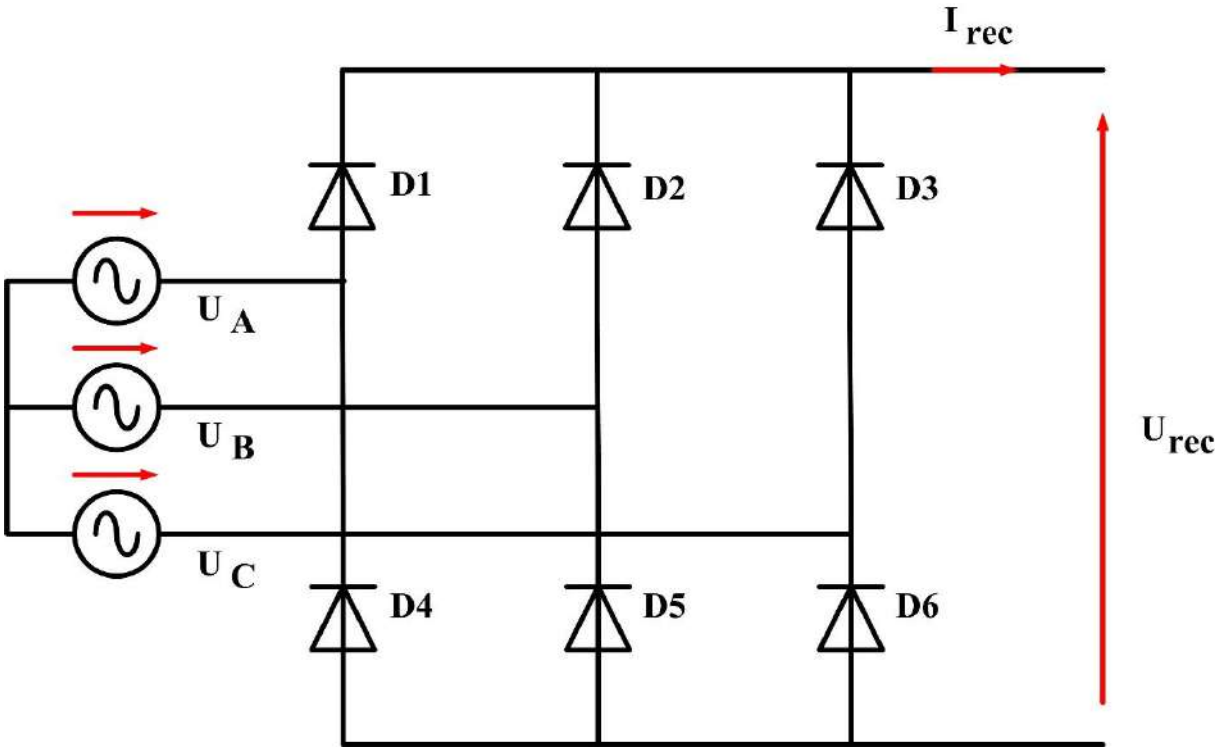

Figure 1.6: Rectifier's power circuit.

Considering a balanced three-phase power supply, with a constant voltage's amplitude and frequency, in addition to an ideal diode and neglecting the power losses. Thus, the rectifier's input voltages are expressed as follows:

$$\begin{cases} U_A(t) = V_m \sin(\omega t) \\ U_B(t) = V_m \sin\left(\omega t - 2\pi/3\right) \\ U_C(t) = V_m \sin\left(\omega t - 4\pi/3\right) \end{cases} \quad (1.19)$$

The output voltage of the rectifier is given as:

$$U_{rec}(t) = \max\left[U_A(t), U_B(t), U_C(t)\right] - \min\left[U_A(t), U_B(t), U_C(t)\right] \quad (1.20)$$

The average voltage of the rectifier is expressed as follows:

$$\overline{U_{rec}} = 3\sqrt{3}/\pi V_m \quad (1.21)$$

The rectifier's ripple rate is expressed as follows:

$$k = {U_{rec(\max)} - U_{rec(\min)}}\Big/{2\overline{U_{rec}}} \tag{1.22}$$

1.4.2 RLC filter modelling

A low-pass filter (RLC) is used to reduce the rectifier's output voltage ripples and ensure a constant DC-link. Figure 1.7 illustrates the schematic diagram of the RLC filter.

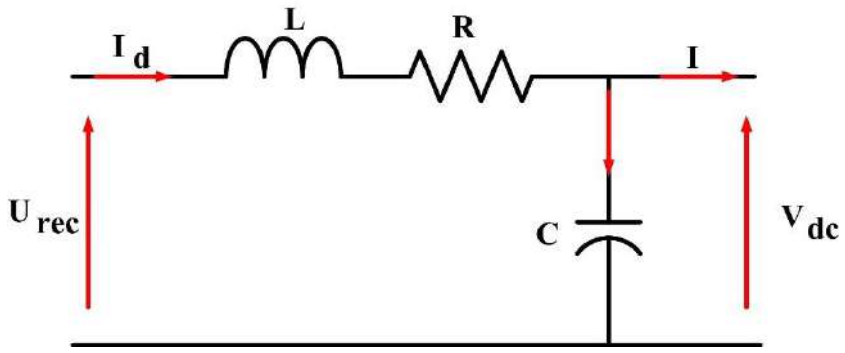

Figure 1.7: RLC filter.

The filter equations are as follows:

$$\begin{cases} U_{rec}(t) = L\,{dI_d(t)}\Big/{dt} + RI_d(t) + V_d(t) \\ {dV_d(t)}\Big/{dt} = \dfrac{1}{C}\left(I_d(t) - I(t)\right) \end{cases} \tag{1.23}$$

The filter's transfer function is expressed as follows:

$$\begin{cases} F(s) = {V_d(s)}\Big/{U_{rec}(s)} = \dfrac{1}{LCs^2 + RCs + 1} \\ \omega_c = \dfrac{1}{\sqrt{LC}} = 2\pi f_c \end{cases} \tag{1.24}$$

With: f_c is the cut-off frequency.

1.4.3 Modelling of n-level five-phase VSI

The VSIs are DC to AC converters, where their main purpose in the ASD is to supply a q-phase voltage with a controllable frequency and amplitude.

To simplify the study and modeling of the multi-level VSI, some hypothesises are made [53]:

- Instant switching between the semiconductor's switches.
- A balanced neutral point potential.

- Neglecting the voltage drop across the switches.
- Star-connected load with isolated neutral point.

Based on the aforementioned hypothesis, the power semiconductor's switches (transistor (T_{ks})-diode (D_{ks}) group) can be approximated to a controllable bi-directional switch (S_i) as shown in Figure 1.8, with B_{ks} is the control signal.

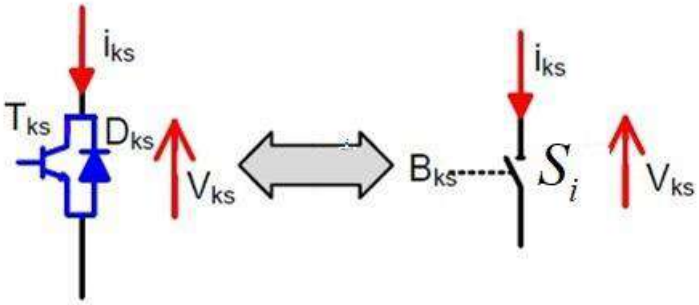

Figure 1.8: Simplified approximation of transistor-diode group.

1.4.3.1. Two-level five-phase VSI

Figure 1.9 depicts the power circuit configuration of the two-level five-phase VSI (FP-VSI). This topology has 2^5 voltage vectors (VV), which are defined using the switching states of the FP-VSI [$S_A, S_B, S_C, S_D, and\ S_E$], as described in Table 1.1 [42].

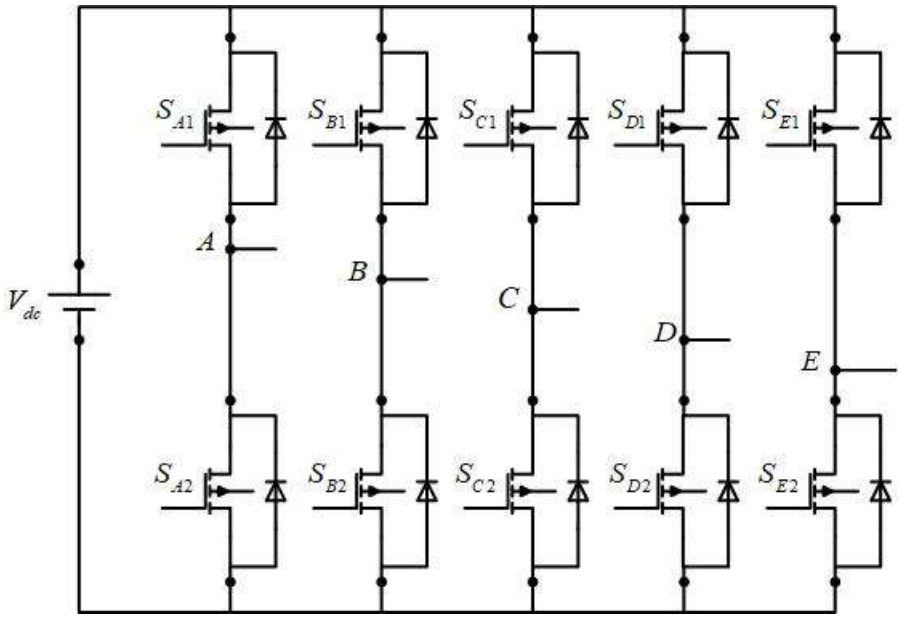

Figure 1.9: Power circuit of FP-VSI.

Table 1.1: The switching states of the FP-VSI.

Switch	Switching function	State of the upper switch	The output voltage
S_{i1}	1	On	V_{dc}
S_{i1}	0	OFF	$-V_{dc}$

Where: $i=[A,B,C,D,E]$ and V_{dc} is the DC-link voltage.

The FP-VSI line-to-line voltages are expressed as follows:

$$\begin{cases} V_{AB}^{inv}=V_{A}^{inv}-V_{B}^{inv} \\ V_{BC}^{inv}=V_{B}^{inv}-V_{C}^{inv} \\ V_{CD}^{inv}=V_{C}^{inv}-V_{D}^{inv} \\ V_{DE}^{inv}=V_{D}^{inv}-V_{E}^{inv} \\ V_{EA}^{inv}=V_{E}^{inv}-V_{A}^{inv} \end{cases} \tag{1.25}$$

The relationships between the FP-VSI's leg voltages and phase voltages are expressed as follows:

$$\begin{cases} V_{A}^{inv}=V_{AO}^{inv}-V_{NO}^{inv} \\ V_{B}^{inv}=V_{BO}^{inv}-V_{NO}^{inv} \\ V_{C}^{inv}=V_{CO}^{inv}-V_{NO}^{inv} \\ V_{D}^{inv}=V_{DO}^{inv}-V_{NO}^{inv} \\ V_{E}^{inv}=V_{EO}^{inv}-V_{NO}^{inv} \end{cases} \tag{1.26}$$

Considering a star-connected load with an isolated neutral point.

$$V_{A}^{inv}+V_{B}^{inv}+V_{C}^{inv}+V_{D}^{inv}+V_{E}^{inv}=0 \tag{1.27}$$

Based on (1.26), the summation of the FP-VSI's phase voltages in (1.27) yields:

$$V_{NO}^{inv}=\left(V_{A}^{inv}+V_{B}^{inv}+V_{C}^{inv}+V_{D}^{inv}+V_{E}^{inv}\right)/5 \tag{1.28}$$

Thus, the FP-VSI output phase voltage can be computed from the VVs switching states and the DC-link voltage, as given in (1.29) [42].

$$\begin{bmatrix} V_{AN}^{inv} \\ V_{BN}^{inv} \\ V_{CN}^{inv} \\ V_{DN}^{inv} \\ V_{EN}^{inv} \end{bmatrix}=\frac{V_{dc}}{5}\begin{bmatrix} 4 & -1 & -1 & -1 & -1 \\ -1 & 4 & -1 & -1 & -1 \\ -1 & -1 & 4 & -1 & -1 \\ -1 & -1 & -1 & 4 & -1 \\ -1 & -1 & -1 & -1 & 4 \end{bmatrix}\begin{bmatrix} S_{A1} \\ S_{B1} \\ S_{C1} \\ S_{D1} \\ S_{E1} \end{bmatrix} \tag{1.29}$$

The inverter's phase voltages are transformed to the arbitrary reference frame by the use of the $[C_S]$ matrix described in equation (1.8) as follows:

$$[V_{\alpha\beta 1\alpha\beta 20}] = [C_s][V_{ABCDE}] \tag{1.30}$$

The 32 VVs space vector representation in $\alpha\beta_1$ and $\alpha\beta_2$ planes using (1.31) is as follows:

$$\begin{cases} v_{\alpha\beta_1} = \dfrac{2}{5}(v_A + v_B\, e^{(j2\pi/5)} + v_C\, e^{(j4\pi/5)} + v_D\, e^{(j6\pi/5)} + v_E\, e^{(j8\pi/5)}) \\ v_{\alpha\beta_2} = \dfrac{2}{5}(v_A + v_C\, e^{(j2\pi/5)} + v_E\, e^{(j4\pi/5)} + v_B\, e^{(j6\pi/5)} + v_D\, e^{(j8\pi/5)}) \end{cases} \tag{1.31}$$

The 32 VVs space vector mapping in $\alpha\beta_1$ and $\alpha\beta_2$ planes are given in Figure 1.10:

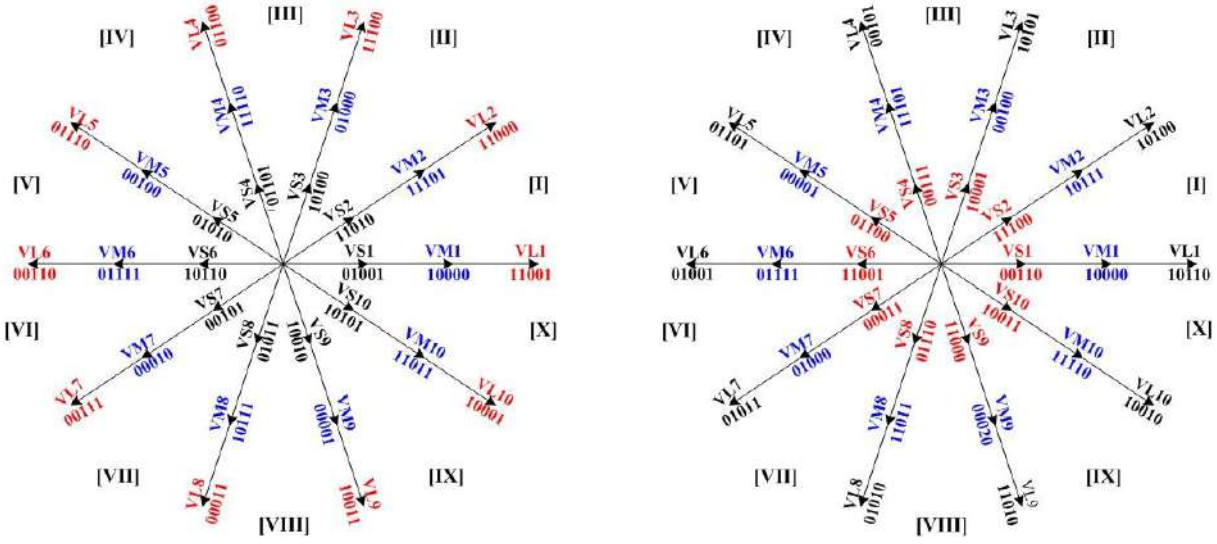

Figure 1.10: Mapping of the VVs: (a) $\alpha\beta_1$ plane, (b) $\alpha\beta_2$ plane.

The amplitudes of the FP-VSI's VVs are given in Table 1.2 in both $\alpha\beta_1$ and $\alpha\beta_2$ planes.

Table 1.2: The amplitudes of the FP-VSI's VVs.

VVs	$\alpha\beta_1$ plane	$\alpha\beta_2$ plane
VL1 – VL10	$0.6472V_{dc}$	$0.2472V_{dc}$
VM1 – VM10	$0.4V_{dc}$	$0.4V_{dc}$
VS1 – VS10	$0.2472V_{dc}$	$0.6472V_{dc}$
V0	$0V_{dc}$	$0V_{dc}$

Figure 1.11 illustrates the six possible connections of the five-phase load to the FP-VSI.

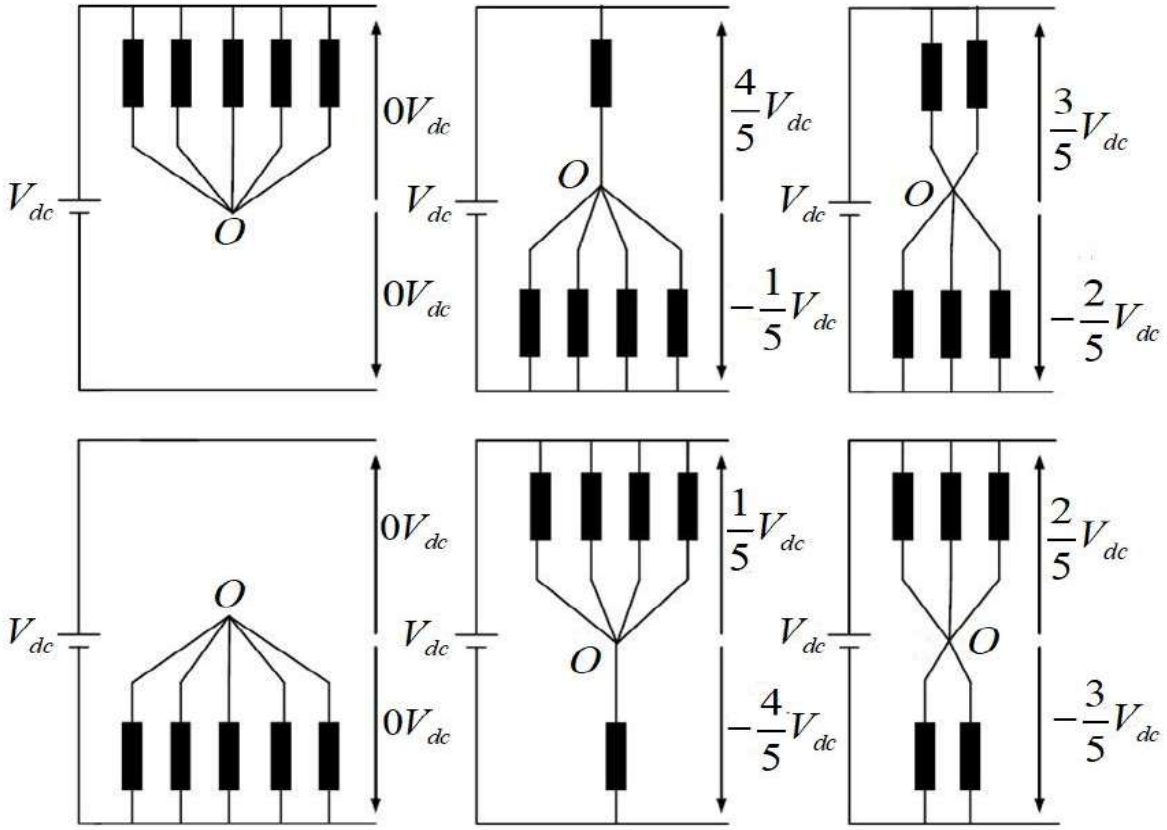

Figure 1.11: Possible connections of the FP-VSI to the load.

1.4.3.2. Three-level five-phase NPC VSI

The three-level five-phase NPC VSI (THL-FP-VSI) topology provides different switching configurations, as illustrated in Figure 1.12 [54].

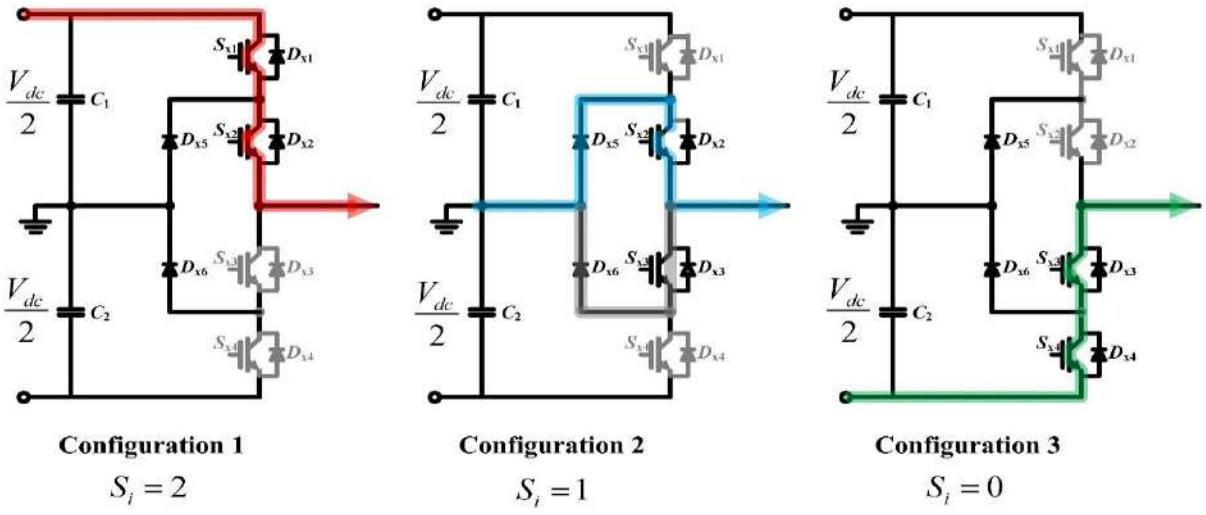

Figure 1.12: Switching configuration of the THL-FP-VSI [54].

Figure 1.13 depicts the power circuit topology of the THL-FP-VSI having 3^5 VVs defined by the switching states of the five legs of the inverter $[S_A, S_B, S_C, S_D, and\ S_E]$, Table 1.3, according to the aforementioned configuration.

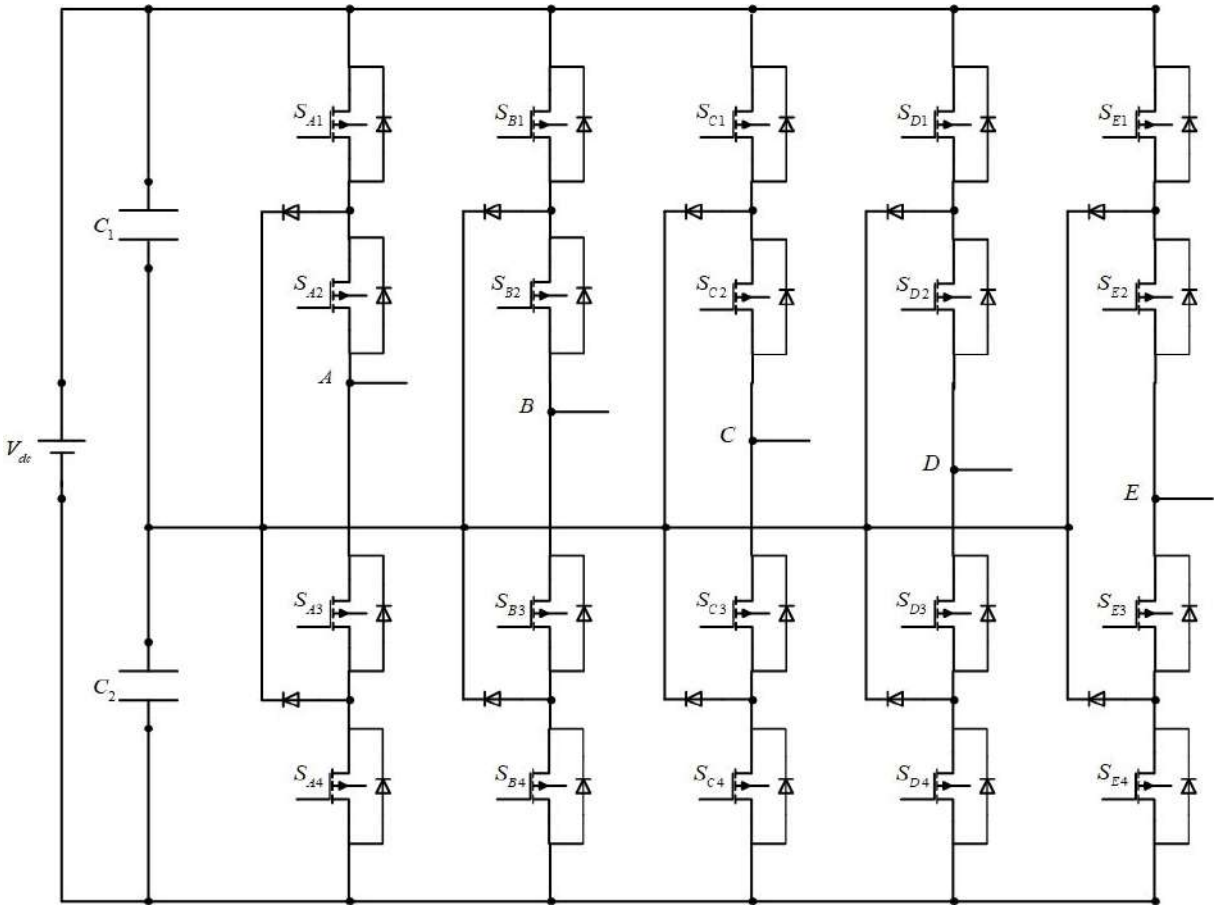

Figure 1.13: Power circuit of THL-FP-VSI.

Table 1.3: The switching states of THL-FP-VSI.

Switch	Switching state	Output voltage	Conducting switches
S_i	Configuration 1	V_{dc} / 2	Two upper switches
S_i	Configuration 2	$0V_{dc}$	Two middle switches
S_i	Configuration 3	$-V_{dc}$ / 2	Two lower switches

Where: $i = [A, B, C, D, E]$ and V_{dc} is the DC-link voltage.

The pole voltage of THL-FP-VSI with respect to the middle point of the DC-link is expressed as [55]:

$$V_{iZ} = \frac{S_i - 1}{2} V_{dc} \tag{1.32}$$

The THL-FP-VSI five-phase voltage expression with respect to the middle point of the DC-link is given as:

$$\begin{bmatrix} V_{AN}^{inv} \\ V_{BN}^{inv} \\ V_{CN}^{inv} \\ V_{DN}^{inv} \\ V_{EN}^{inv} \end{bmatrix} = \frac{2}{5} \begin{bmatrix} 4 & -1 & -1 & -1 & -1 \\ -1 & 4 & -1 & -1 & -1 \\ -1 & -1 & 4 & -1 & -1 \\ -1 & -1 & -1 & 4 & -1 \\ -1 & -1 & -1 & -1 & 4 \end{bmatrix} \begin{bmatrix} V_{AZ} \\ V_{BZ} \\ V_{CZ} \\ V_{DZ} \\ V_{EZ} \end{bmatrix} \tag{1.33}$$

Using the transformation matrix $[C_S]$ defined in (1.8), the THL-FP-VSI's phase voltages can be expressed in the arbitrary reference frame.

$$[V_{\alpha\beta 1 \alpha\beta 20}] = [C_s][V_{ABCDE}] \tag{1.34}$$

The space vector mapping of the 243 VVs of the THL-FP-VSI in the two planes, $\alpha\beta_1$ and $\alpha\beta_2$, is shown in Figure 1.14 using equation (1.31).

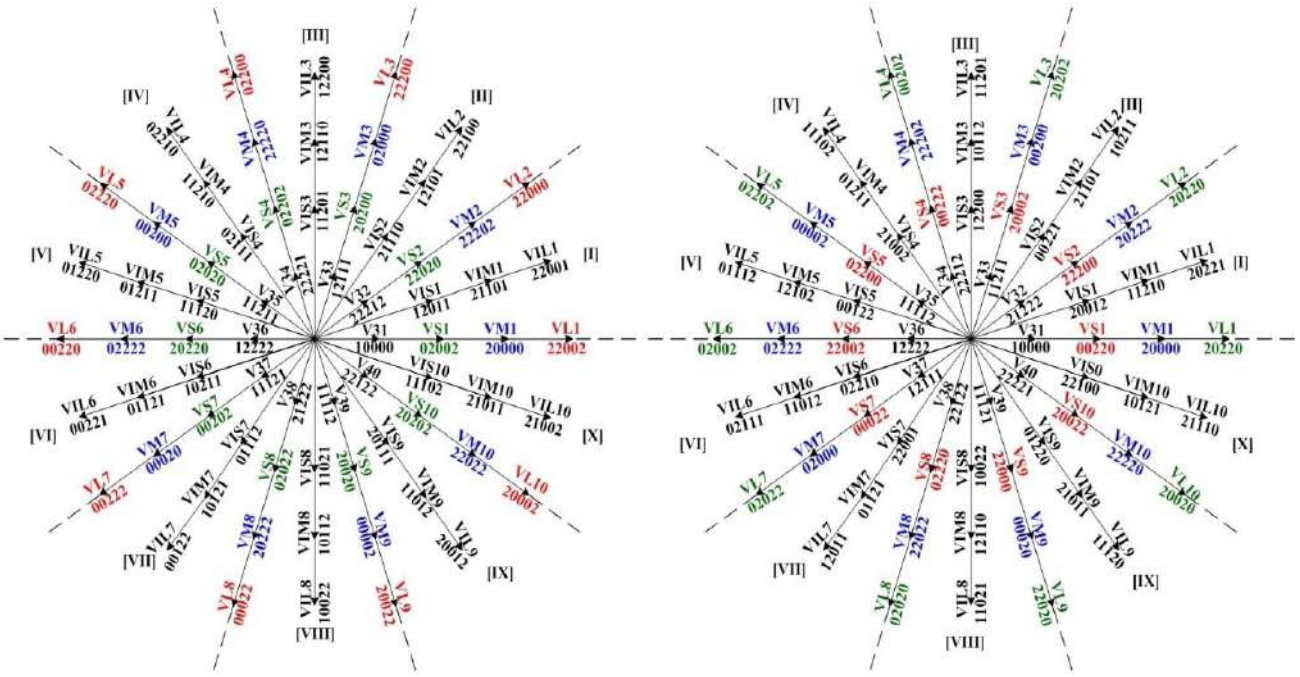

(a) (b)

Figure 1.14: Mapping of the VVs: (a) $\alpha\beta_1$ plane, (b) $\alpha\beta_2$ plane.

The amplitudes of the THL-FP-VSI's vertex and non-vertex VVs are given in Tables 1.4 and 1.5 in both $\alpha\beta_1$ and $\alpha\beta_2$ planes, respectively. For simplicity purposes not all the VVs are illustrated in Figure 1.14, [56] reports all the 243 VVs mapping in in both $\alpha\beta_1$ and $\alpha\beta_2$ planes.

Table 1.4: Vertex VVs amplitudes.

VVs	$\alpha\beta_1$ plane	$\alpha\beta_2$ plane
VL1 – VL10	$0.6472V_{dc}$	$0.076V_{dc}$
V1 - V10	$0.524V_{dc}$	$0.124V_{dc}$
V11 - V20	$0.447V_{dc}$	$0.247V_{dc}$
VM1 – VM10	$0.4V_{dc}$	$0.324V_{dc}$
V21 – V30	$0.324V_{dc}$	$0.4V_{dc}$
VS1- VS10	$0.247V_{dc}$	$0.447V_{dc}$
V31 - V40	$0.124V_{dc}$	$0.524V_{dc}$
V41 – V50	$0.076V_{dc}$	$0.6472V_{dc}$
V0, V100, V243	$0V_{dc}$	$0V_{dc}$

Table 1.5: Non-vertex VVs amplitudes.

VVs	$\alpha\beta_1$ plane	$\alpha\beta_2$ plane
VIL1 – VIL10	$0.615V_{dc}$	$0.145V_{dc}$
VIM1 – VIM10	$0.38V_{dc}$	$0.235V_{dc}$
VILM – VIM10	$0.235V_{dc}$	$0.38V_{dc}$
VI1 – VI10	$0.145V_{dc}$	$0.615V_{dc}$

1.5. Modeling of the two parallel-connected multi-phase machines drive

1.5.1. Introduction

In general, the industrial sectors require the use of multiple electrical drives. Thus, the engineers have three possible choices to discuss:

- First, multiple independent machines drives.
- Second, multiple VSI for each machine with a common DC-link.
- Third, parallel/series connection of multiple machines to a single VSI.

As illustrated in Figure 1.15. Where the first and second choices increase the drive's overall size, cost, and complexity to maintain.

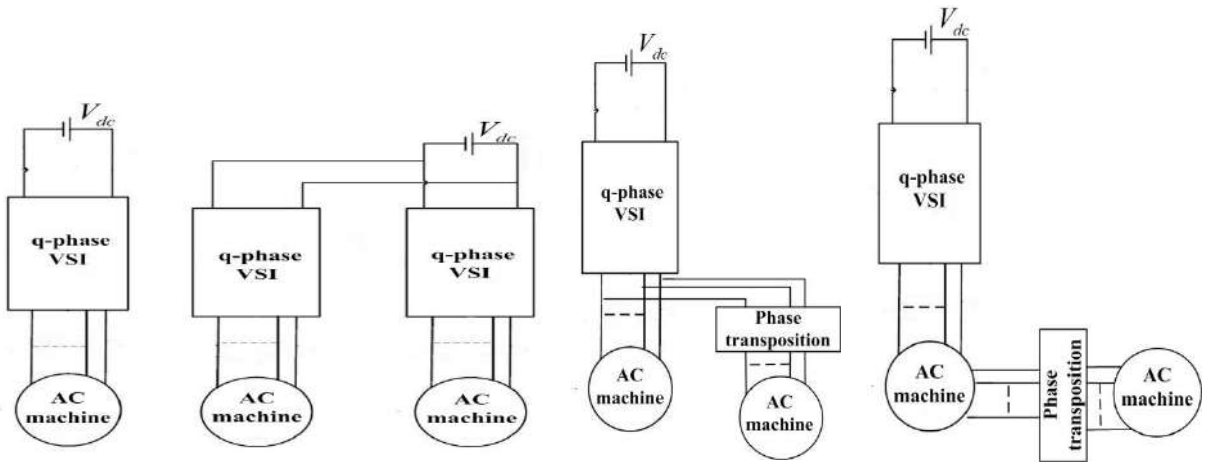

Figure 1.15: Possible configurations of ASD: (a) independent one machine drive, (b) multiple VSI with shared DC-link, (c) parallel-connected multi-machine drive, and (d) series-connected multi-machine drive.

Moreover, in the case of the parallel/series connection of multiple three-phase machines to a single VSI, the control algorithm does not ensure independent control between the machines [32].

However, the multi-phase system provides an interesting solution for multiple machines with parallel/series connected drives controlled independently regardless of the working scenario (load and speed) fed by a single VSI due to the additional DOFs. These two configurations have the benefits of diminutiveness, weightlessness, and economy [42].

Nevertheless, the series connection results in a complex drive's structure because both stator windings must be brought out to the machine's terminal box. In addition, the high current causes a higher loss, reducing the drive's efficiency [42].

1.5.2. parallel-connected multi-phase machines drive's advantages

The multi-machine drive system parallel-connected has some significant advantages over the traditional three-phase systems:

The reduction of the VSI legs: In the case of the independence of two FPIMs, the VSI legs are reduced by one since the three-phase requires six legs.

The reduction of the switches in use results in a reduction in the VSI's components (firing and protection circuits), which in turn results in a more reliable drive system.

In addition, the discussed approach retains the advantages of the existing concepts of multi-machine drive, such as the use of different multi-phase AC machines (IM, PMSM, etc.) connected in parallel.

Thus, the parallel connection of the multi-phase AC machines is more suitable for industrial applications such as electronic differential for HEV and EV, HVAC, and drilling operations.

1.5.3. multi-phase machines parallel- connectivity

The parallel connection of the multi-phase AC machines refers to the machines' stator windings being connected in parallel to a single VSI in a proper arrangement to enable independent control of the drive system. Where the cornerstone of the independent control of the considered drive is based on two factors:

- **First:** The current components producing the flux and torque of the first machine must not contribute to producing the flux and torque for the other machines in the drive and vice versa. This is ensured due to the applied phase transposition. This latter is deduced from the decoupling matrix and allows a complete decoupling between the flux and torque-generating current components of the two-machine drive.

  For even phase number "q" multi-phase AC machines, the decoupling matrix is expressed as follows [42]:

$$[C]=\sqrt{\frac{2}{q}}\begin{bmatrix}
1 & \cos(\alpha) & \cos(2\alpha) & \cos(3\alpha) & \cos(4\alpha) & .... & \cos((q-1)\alpha)\\
0 & \sin(\alpha) & \sin(2\alpha) & \sin(3\alpha) & \sin(4\alpha) & .... & \sin((q-1)\alpha)\\
1 & \cos(2\alpha) & \cos(4\alpha) & \cos(6\alpha) & \cos(8\alpha) & .... & \cos 2((q-1)\alpha)\\
0 & \sin(2\alpha) & \sin(4\alpha) & \sin(6\alpha) & \sin(8\alpha) & .... & \sin 2((q-1)\alpha)\\
1 & \cos(3\alpha) & \cos(6\alpha) & \cos(9\alpha) & \cos(12\alpha) & .... & \cos 3((q-1)\alpha)\\
0 & \sin(3\alpha) & \sin(6\alpha) & \sin(9\alpha) & \sin(12\alpha) & .... & \sin 3((q-1)\alpha)\\
.... & .... & .... & .... & .... & .... & ....\\
1 & \cos\left(\left(\frac{q-2}{2}\right)\alpha\right) & \cos 2\left(\left(\frac{q-2}{2}\right)\alpha\right) & \cos 3\left(\left(\frac{q-2}{2}\right)\alpha\right) & \cos 4\left(\left(\frac{q-2}{2}\right)\alpha\right) & .... & \cos(q-1)\left(\left(\frac{q-2}{2}\right)\alpha\right)\\
0 & \sin\left(\left(\frac{q-2}{2}\right)\alpha\right) & \sin 2\left(\left(\frac{q-2}{2}\right)\alpha\right) & \sin 3\left(\left(\frac{q-2}{2}\right)\alpha\right) & \sin 4\left(\left(\frac{q-2}{2}\right)\alpha\right) & .... & \sin(q-1)\left(\left(\frac{q-2}{2}\right)\alpha\right)\\
\sqrt{1/2} & \sqrt{1/2} & \sqrt{1/2} & \sqrt{1/2} & \sqrt{1/2} & \sqrt{1/2} & \sqrt{1/2}\\
\sqrt{1/2} & \sqrt{1/2} & \sqrt{1/2} & \sqrt{1/2} & \sqrt{1/2} & \sqrt{1/2} & \sqrt{1/2}
\end{bmatrix}$$

(1.35)

For the case of an odd phase number "q", the decoupling matrix is expressed as follows [42]:

$$[C]=\sqrt{\frac{2}{q}}\begin{bmatrix} 1 & \cos(\alpha) & \cos(2\alpha) & \cos(3\alpha) & \cos(4\alpha) & .... & \cos((q-1)\alpha) \\ 0 & \sin(\alpha) & \sin(2\alpha) & \sin(3\alpha) & \sin(4\alpha) & .... & \sin((q-1)\alpha) \\ 1 & \cos(2\alpha) & \cos(4\alpha) & \cos(6\alpha) & \cos(8\alpha) & .... & \cos 2((q-1)\alpha) \\ 0 & \sin(2\alpha) & \sin(4\alpha) & \sin(6\alpha) & \sin(8\alpha) & .... & \sin 2((q-1)\alpha) \\ 1 & \cos(3\alpha) & \cos(6\alpha) & \cos(9\alpha) & \cos(12\alpha) & .... & \cos 3((q-1)\alpha) \\ 0 & \sin(3\alpha) & \sin(6\alpha) & \sin(9\alpha) & \sin(12\alpha) & .... & \sin 3((q-1)\alpha) \\ .... & .... & .... & .... & .... & .... & \\ 1 & \cos\left(\left(\frac{q-1}{2}\right)\alpha\right) & \cos 2\left(\left(\frac{q-1}{2}\right)\alpha\right) & \cos 3\left(\left(\frac{q-1}{2}\right)\alpha\right) & \cos 4\left(\left(\frac{q-1}{2}\right)\alpha\right) & .... & \cos(q-1)\left(\left(\frac{q-1}{2}\right)\alpha\right) \\ 0 & \sin\left(\left(\frac{q-1}{2}\right)\alpha\right) & \sin 2\left(\left(\frac{q-1}{2}\right)\alpha\right) & \sin 3\left(\left(\frac{q-1}{2}\right)\alpha\right) & \sin 4\left(\left(\frac{q-1}{2}\right)\alpha\right) & .... & \sin(q-1)\left(\left(\frac{q-1}{2}\right)\alpha\right) \\ \sqrt{1/2} & \sqrt{1/2} & \sqrt{1/2} & \sqrt{1/2} & \sqrt{1/2} & \sqrt{1/2} & \sqrt{1/2} \end{bmatrix}$$

(1.36)

In a general way, Tables 1.6 and 1.7 summarize the phase transposition rules for the even and odd phase number multi-phase AC machines, respectively [32].

Table 1.6: Phase transposition rules for even phase number.

		The VSI's phases														
		V_A^{inv}	V_B^{inv}	V_C^{inv}	V_D^{inv}	V_E^{inv}	V_F^{inv}	V_G^{inv}	V_H^{inv}	V_I^{inv}	V_J^{inv}	V_K^{inv}	V_L^{inv}	V_M^{inv}	V_N^{inv}	V_O^{inv}
Machine's phases connection order	M 1	1	2	3	4	5	6	7	8	9	10	11	12	13	14	15
	M 2	1	3	5	7	9	11	13	15	2	4	6	8	10	12	14
	M 3	1	4	7	10	13	1	4	7	10	13	1	4	7	10	13
	M 4	1	5	9	13	2	6	10	14	3	7	11	15	4	8	12
	M 5	1	7	13	4	10	1	7	13	4	10	1	7	13	4	10
	M 6	1	8	15	7	14	6	13	5	12	4	11	3	10	2	9
	M 7	1	6	11	1	6	11	1	6	11	1	6	11	1	6	11

Table 1.7: Phase transposition rules for odd phase number.

		The VSI's phases											
		V_A^{inv}	V_B^{inv}	V_C^{inv}	V_D^{inv}	V_E^{inv}	V_F^{inv}	V_G^{inv}	V_H^{inv}	V_I^{inv}	V_J^{inv}	V_K^{inv}	V_L^{inv}
Machine's phases connection order	M1	1	2	3	4	5	6	7	8	9	10	11	12
	M2	1	3	5	7	9	11	1	3	5	7	9	11
	M3	1	4	7	10	1	4	7	10	1	4	7	10
	M4	1	5	9	1	5	9	1	5	9	1	5	9
	M5	1	6	11	4	9	2	7	12	5	10	3	8

- **Second:** The VC of the AC machines requires controlling only the current components that contribute to the flux and torque generation. This condition is ensured by exploiting the additional current components provided by the additional DOFs of the multi-phase AC machines. This latter provides (q-1)⁄2 and (q-2)⁄2 sets of current components in the case of the odd and even phase numbers, respectively, to ensure the optimum performance of the VC.

1.5.4. Two parallel-connected FPIMs' modelling

Figure 1.16 shows the considered two-machine drive, which consisted of the n-level VSI feeding two parallel-connected FPIMs. Subsection 1.3 describes the two machines.

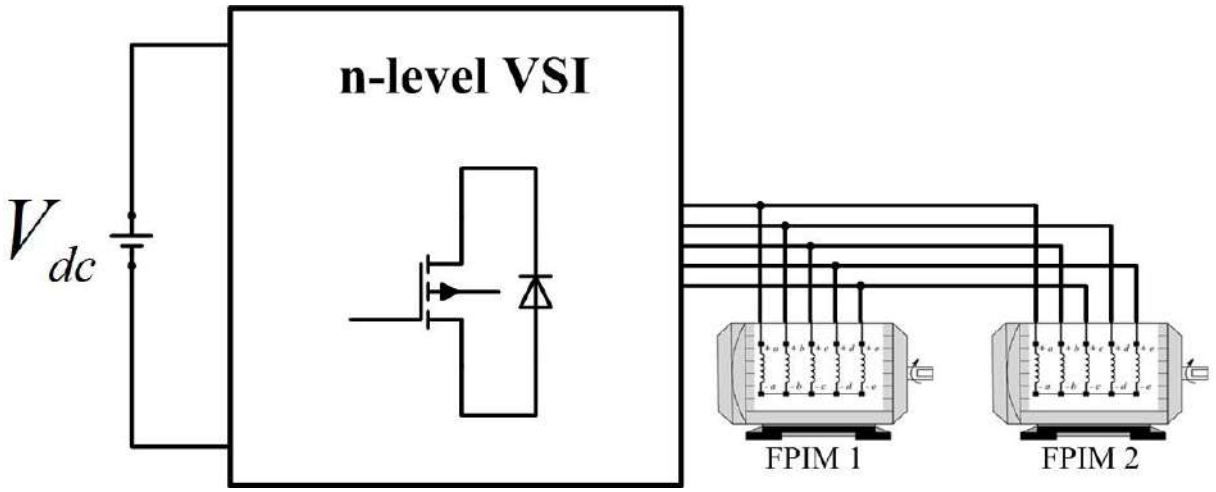

Figure 1.16: Schematic diagram of two-machine drive.

Table 1.8 gives the phase transposition rule for the two FPIMs drive deduced from $[C_s]$ in (1.8) and shown in Figure 1.16.

Table 1.8: Phase transposition rules.

FPIM	Inverter phase				
	A	B	C	D	E
1	1	2	3	4	5
2	1	4	2	5	3

The combination of the aforementioned criterion, it allows access to both of the five-phase VSI planes by aligning the first FPIM windings with the $\alpha\beta_1$ plane and the second with the $\alpha\beta_2$ plane, ensuring the independent control over the two-machine drive fed by a single VSI [56].

From Figure 1.16, the relationship between the VSI and the two-machines stator voltages and the VSI voltages are defined as:

$$V_{ABCDE} = \begin{bmatrix} V_{AN}^{inv} \\ V_{BN}^{inv} \\ V_{CN}^{inv} \\ V_{DN}^{inv} \\ V_{EN}^{inv} \end{bmatrix} = \begin{bmatrix} V_{S_{A1}} = V_{S_{A2}} \\ V_{S_{B1}} = V_{S_{C2}} \\ V_{S_{C1}} = V_{S_{E2}} \\ V_{S_{D1}} = V_{S_{B2}} \\ V_{S_{E1}} = V_{S_{D2}} \end{bmatrix} \tag{1.37}$$

From Figure 1.16, the relationship between the VSI and the two-machines stator currents and the VSI currents are defined as:

$$i_{ABCDE} = \begin{bmatrix} i_{AN}^{inv} \\ i_{BN}^{inv} \\ i_{CN}^{inv} \\ i_{DN}^{inv} \\ i_{EN}^{inv} \end{bmatrix} = \begin{bmatrix} i_{S_{A1}} + i_{S_{A2}} \\ i_{S_{B1}} + i_{S_{C2}} \\ i_{S_{C1}} + i_{S_{E2}} \\ i_{S_{D1}} + i_{S_{B2}} \\ i_{S_{E1}} + i_{S_{D2}} \end{bmatrix} \tag{1.38}$$

Where: $j = 1 \; or \; 2$

$V_{sabcdej}$: stator voltages.

$i_{sabcdej}$: stator currents.

The stator voltages and VSI voltages relationship can be described in the two orthogonal subspaces $\alpha\beta_1$ and $\alpha\beta_2$ using the transformation matrix $[C_S]$ defined in equation (1.8) as follows:

$$V_{ABCDE}=\begin{bmatrix} v_{\alpha 1}^{inv} \\ v_{\beta 1}^{inv} \\ v_{\alpha 2}^{inv} \\ v_{\beta 2}^{inv} \\ v_{0}^{inv} \end{bmatrix}=[C]V_{ABCDE}^{inv}\begin{bmatrix} v_{s1\alpha 1}=v_{s2\alpha 2} \\ v_{s1\beta 1}=-v_{s2\beta 2} \\ v_{s1\alpha 2}=v_{s2\alpha 1} \\ v_{s1\beta 2}=v_{s2\beta 1} \\ 0 \end{bmatrix} \tag{1.39}$$

The stator currents and VSI currents relationship can be described in the two orthogonal subspaces $\alpha\beta_1$ and $\alpha\beta_2$ using the transformation matrix $[C_S]$ defined in equation (1.8) as follows:

$$i_{ABCDE}=\begin{bmatrix} i_{\alpha 1}^{inv} \\ i_{\beta 1}^{inv} \\ i_{\alpha 2}^{inv} \\ i_{\beta 2}^{inv} \\ i_{0}^{inv} \end{bmatrix}=[C]i_{ABCDE}^{inv}\begin{bmatrix} i_{s1\alpha 1}+i_{s2\alpha 2} \\ i_{s1\beta 1}-i_{s2\beta 2} \\ i_{s1\alpha 2}+i_{s2\alpha 1} \\ i_{s1\beta 2}+i_{s2\beta 1} \\ 0 \end{bmatrix} \tag{1.40}$$

Where:

$V_{sj\alpha\beta j}$ and $i_{sj\alpha\beta j}$ are the two machines stator voltages and currents in the two subspaces $\alpha\beta_1$ and $\alpha\beta_2$.

The mathematical model of the two parallel-connected FPIMs in the $\alpha\beta_1$ and $\alpha\beta_2$ frame is given as [53]:

$$\begin{cases} v_{s1\alpha 1}^{inv}=R_{s1}i_{s1\alpha 1}+L_{sl1}\dfrac{di_{s1\alpha 1}}{dt}+M_{sr1}\dfrac{di_{r1}}{dt}=R_{s2}i_{s2\alpha 2}+L_{sl2}\dfrac{di_{s2\alpha 2}}{dt} \\ v_{s1\beta 1}^{inv}=R_{s1}i_{s1\beta 1}+L_{sl1}\dfrac{di_{s1\beta 1}}{dt}+M_{sr1}\dfrac{di_{r1}}{dt}=R_{s2}i_{s2\beta 2}+L_{sl2}\dfrac{di_{s2\beta 2}}{dt} \\ v_{s2\alpha 2}^{inv}=R_{s2}i_{s2\alpha 2}+L_{sl2}\dfrac{di_{s2\alpha 2}}{dt}+M_{sr2}\dfrac{di_{r2}}{dt}=R_{s1}i_{s1\alpha 1}+L_{sl1}\dfrac{di_{s1\alpha 1}}{dt} \\ v_{s2\beta 1}^{inv}=R_{s2}i_{s2\beta 2}+L_{sl2}\dfrac{di_{s2\beta 2}}{dt}+M_{sr2}\dfrac{di_{r2}}{dt}=R_{s1}i_{s1\beta 1}+L_{sl1}\dfrac{di_{s1\beta 1}}{dt} \\ 0=R_{rj}i_{rj}+L_{rj}\dfrac{di_{rj}}{dt}+M_{rsj}\dfrac{di_{sj\alpha\beta j}}{dt}-j\omega(M_{rsj}i_{sj\alpha\beta j}+L_{rj}i_{rj}) \end{cases} \tag{1.41}$$

The stator flux linkages, position, and magnitude are expressed as follows:

$$\begin{cases} \phi_{sj\alpha j} = \int (v_{s\alpha j} - R_{sj} i_{sj\alpha j}) dt \\ \phi_{sj\beta j} = \int (v_{s\beta j} - R_{sj} i_{sj\beta j}) dt \\ \phi_{sj} = \sqrt{\phi_{sj\alpha j}{}^2 + \phi_{sj\beta j}{}^2} \\ \theta_{sj} = \tan^{-1}\left(\dfrac{\phi_{sj\beta j}}{\phi_{sj\alpha j}}\right) \end{cases} \quad (1.42)$$

The dynamic equation and electromagnetic torque of the two FPIMs are given as:

$$\begin{cases} J_j \dfrac{d\omega_{mj}}{dt} = T_{emj} - T_{Lj} - f_j \omega_{mj} \\ T_{emj} = \dfrac{5p_j}{2} (\phi_{sj\alpha j} i_{sj\beta j} - \phi_{sj\beta j} i_{sj\alpha j}) \end{cases} \quad (1.43)$$

1.6. Simulation results

To validate the mathematical model of the two-machine drive described herein, a simulation study is made in MATLAB/Simulink. To evaluate their performance, a comparative study between the FP-VSI and the THL-FP-VSI is considered. The drive is constituted by two identical FPIMs whose parameters are given in Table 1.9.

Table 1.9: Parameters of the two FPIMs.

1 HP; 200 V; 5 A; 50 Hz; 1400 rpm								
R_s [Ω]	R_r [Ω]	L_s [H]	L_r [H]	L_m [H]	J [$Kg.m^2$]	f [$\frac{Nm.s^{-1}}{rad}$]	T_{em} [$N.m$]	p
10	6.3	0.4642	0.4612	0.4212	0.03	0.0001	8	2

Table 1.10 summarizes the two machines' testing conditions.

Table 1.10: Testing scenario.

Time [s]	$0 \rightarrow 1$	$1 \rightarrow 2$	$2 \rightarrow 3$	$3 \rightarrow 4$
T_{L1}	0	8		4
T_{L2}	8	4	8	0

Figures 1.17 and 1.18 group the simulation results for the FP-VSI fed drive and the THL-FP-VSI fed drive, respectively.

The present results illustrate the independence of the two-machine drive, where the transient state of one machine in the drive does not affect the regular operation of the other machine in the drive. Thus, it is demonstrated that the $\alpha\beta_1$ component of the VSI controls the FPIM1's flux/torque, while the $\alpha\beta_2$ component of the VSI controls the FPIM2's flux/torque.

The THL-FP-VSI illustrates a better performance when compared to the FP-VSI in terms of flux and torque ripples and current THD.

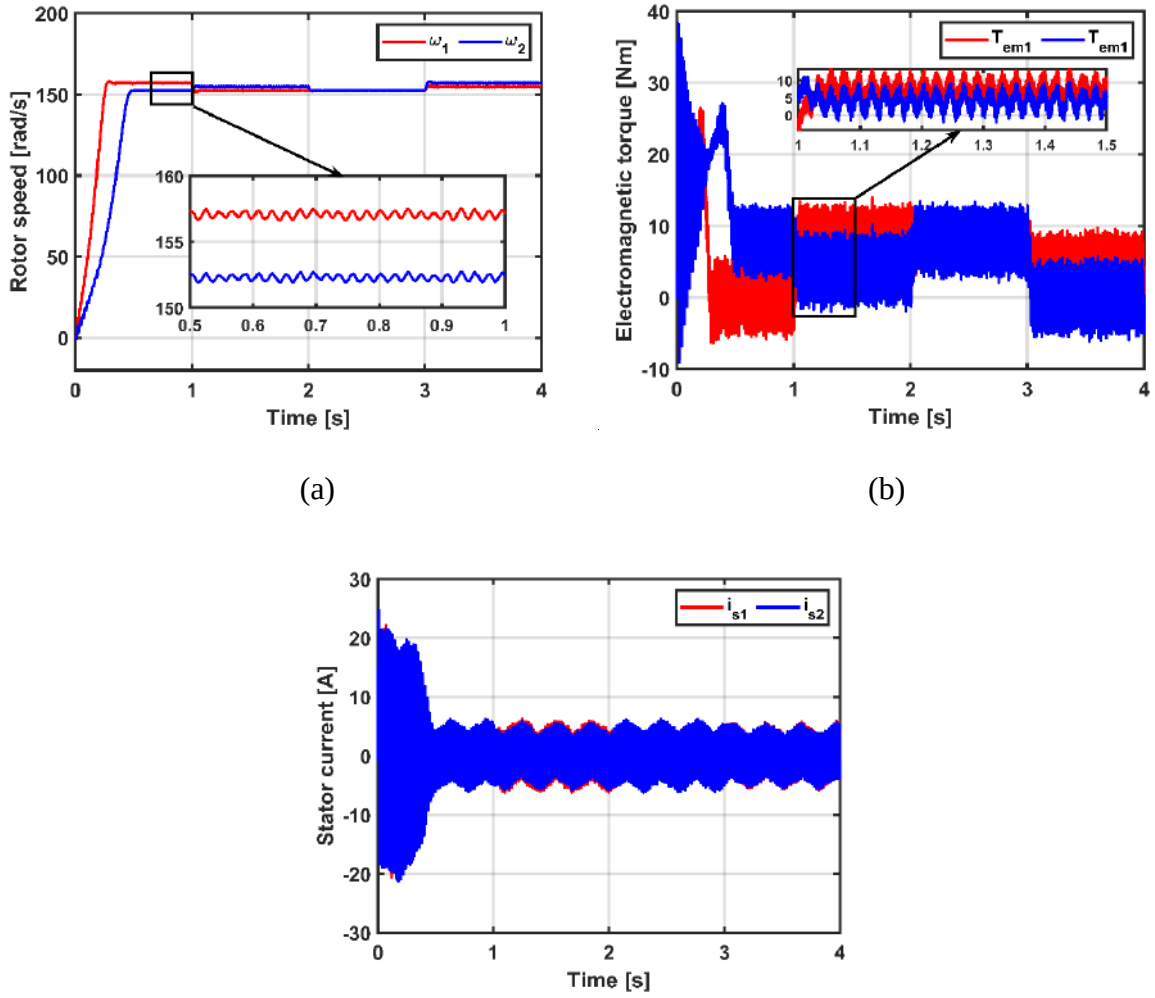

(a) (b)

(c)

Figure 1.17: Two parallel-connected FPIMs drive response's fed by FP-VSI: (a) mechanical rotor speed, (b) electromagnetic torque, and (c) stator current.

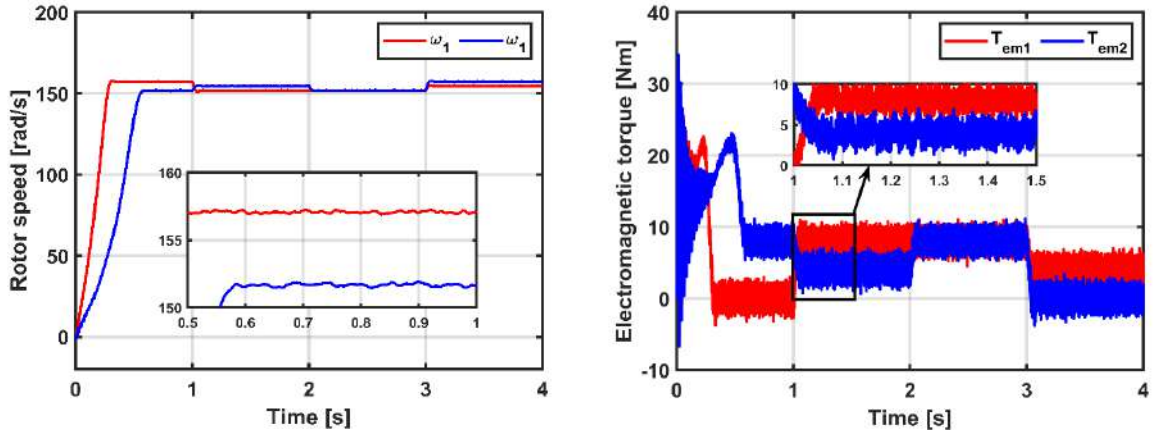

(a)

(b)

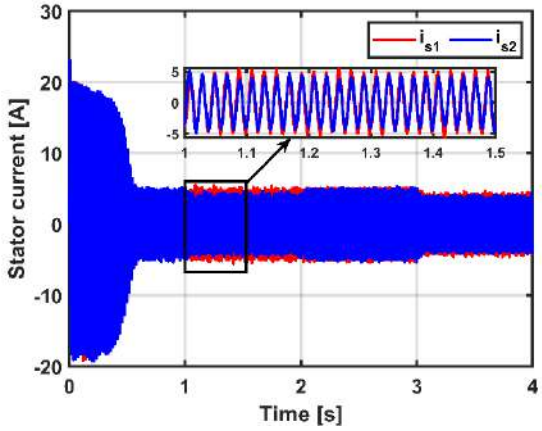

(c)

Figure 1.18: Two parallel-connected FPIMs drive response's fed by THL-FP-VSI: (a) mechanical rotor speed, (b) electromagnetic torque, and (c) stator current.

1.7. Conclusion

The first chapter of this thesis presents the types of multi-phase machines, the mathematical modelling of the FPIMs, multi-level VSI, and the Parallel-connected two-machine drive while discussing the simplifying theories. The complex model of the FPIMs has been simplified through the use of a transformation matrix to the αβ plane and further clarifies the coupled model of the machine.

Based on the fact that only the stator $\alpha\beta_1$ current component is required to control the FPIMs' flux and torque, in addition to the remaining DOF, $\alpha\beta_2$ current component, a second FPIM can be independently controlled while being fed by the same VSI and connected in parallel. Such configuration requires a phase transposition to be introduced for the second machine to ensure

that the current components producing flux and torque for one machine do not contribute to producing the flux and torque for the machine in the drive.

The next chapter of this thesis will discuss the independent two-level and three-level direct torque control of the two parallel-connected FPIMs drive.

Chapter2

Multi-level DTC of two-machine drive

2.1. Introduction

In the last decades, DC machines have been preferred due to their natural decoupled control of the machine's flux and torque [57]. However, with the introduction of the VFDs, the IM garnered due to their advantages over the DC machines considering the required performance in the industrial sector by means of VC.

The DTC is one significant method of VC strategies. This provides a decoupled control of the electromagnetic torque and stator flux linkage by controlling one set of current components, in addition to being less sensitive to parameter variations, eliminating the need for the internal current regulator, PWM modulator, and coordinate transformation; therefore, the DTC scheme has a robust and fast dynamic performance in addition to a simple structure. Nevertheless, this strategy suffers from drawbacks such as high stator flux and electromagnetic torque ripple content, acoustic noise, and inconstant switching frequency. This control strategy applies directly to the VVs based on the machine's requirements; hence, the error between the reference and computed values of the flux and torque [58].

The FPIMs offer two sets of current components offered by the DOFs of the multi-phase structure. In addition, the VC of the FPIMs requires the control of only one set of current components; thus, the multi-machine drive independently controlled by the DTC strategy is possible.

Therefore, this chapter considers the independent control of the two parallel-connected FPIMs driven by two-level and three-level conventional DTC, referred to as 2L-DTC and 3L-DTC, respectively. It is structured as follows: first, the basic principle of DTC is detailed; second, the DTC of the parallel-connected drive is introduced; and third, a simulation and comparative study is made to evaluate the two schemes' performance.

2.2. Conventional DTC

The DTC scheme appeared in the middle of the 1980s, and it was presented by Takahashi, Noguchi, and Depenbrock [19]. The ABB group's MAK DE 502 first introduced the diesel-electric traction system driven by the DTC [59]. Figure 2.1 presents the MAK locomotive.

Figure 2.1: MAK DE502 introduced by ABB and controlled by DTC scheme.

2.2.1. DTC's principals

The basic idea of the DTC is to directly control the VSI's semiconductor switching states by the use of a predefined table without the intermediate current control loops. The VVs selection is made on the basis of the machine's electromagnetic state [60]. This latter can be determined from the machine's mathematical model and the stator voltages/currents utilizing an open-loop estimator. This estimator results, at each sampling period, in the estimation of:

- The machine's stator flux linkage.
- The machine's electromagnetic torque.

Figure 2.2 gives the basic block diagram of the conventional DTC.

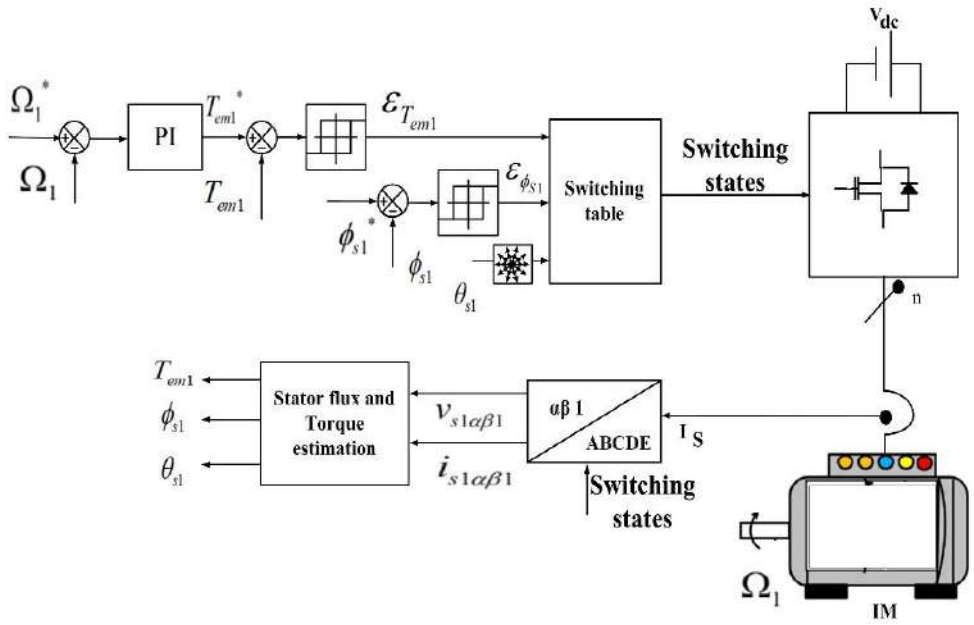

Figure 2.2: Block diagram of DTC.

2.2.1.1. Stator flux control

The stator flux estimation is based on the machine's model in the stationary reference frame, and the stator voltage expression is given from (1.7) and (1.22) as follows [61]:

$$\begin{cases} \phi_{s\alpha} = \int_0^{Ts} (V_{s\alpha} - R_s I_{s\alpha}) dt \\ \phi_{s\beta} = \int_0^{Ts} (V_{s\beta} - R_s I_{s\beta}) dt \end{cases} \quad (2.1)$$

In a defined time interval limited to the sampling time Ts, the stator voltages are considered constant, and if the term $R_s I_{s\alpha\beta}$ is neglected compared to the stator voltage $V_{s\alpha\beta} >> R_s I_{s\alpha\beta}$, the stator flux expression becomes given as:

$$\begin{cases} \phi_{s\alpha} \cong \phi_{s\alpha 0} + V_{s\alpha} Ts \\ \phi_{s\beta} \cong \phi_{s\beta 0} + V_{s\beta} Ts \end{cases} \quad (2.2)$$

Where: $\phi_{s\alpha\beta 0}$ is the stator flux at instant (t=0).

From equation (2.2), if the active VV is applied, the stator flux vector is oriented toward the applied VV. Figure 2.3 illustrates the stator flux control principle.

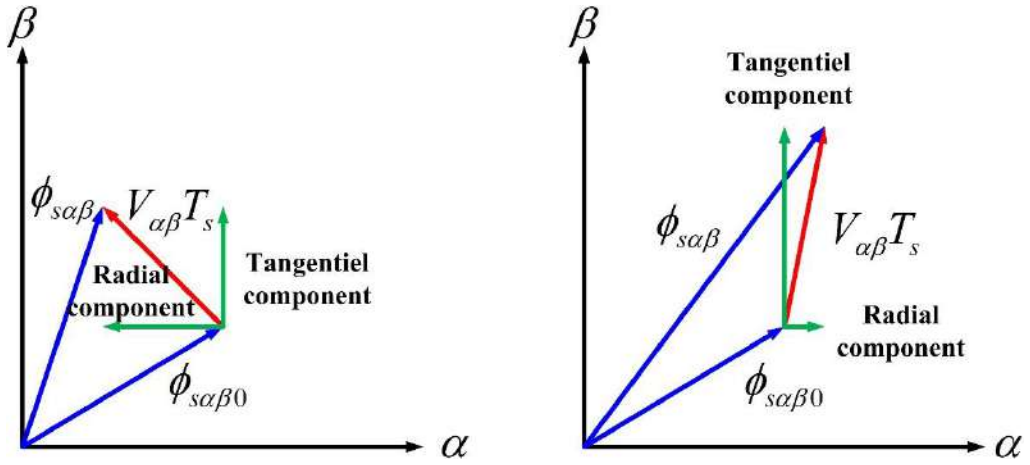

(a) (b)

Figure 2.3: Stator flux control: (a) VV applied to reduce the flux amplitude, (b) VV applied to increase the flux amplitude.

The VSI's VVs are constituted of two components as follows:

- The radial component that affects the stator flux vector amplitude.
- The tangential component that orient the stator flux direction and position.

In a defined sampling time, where the stator's time constant is less than the rotor's time constant, by the selection of the optimum VV to apply, the stator flux is oriented in the desired circular trajectory with a nearly constant amplitude, as illustrated in Figure 2.4.

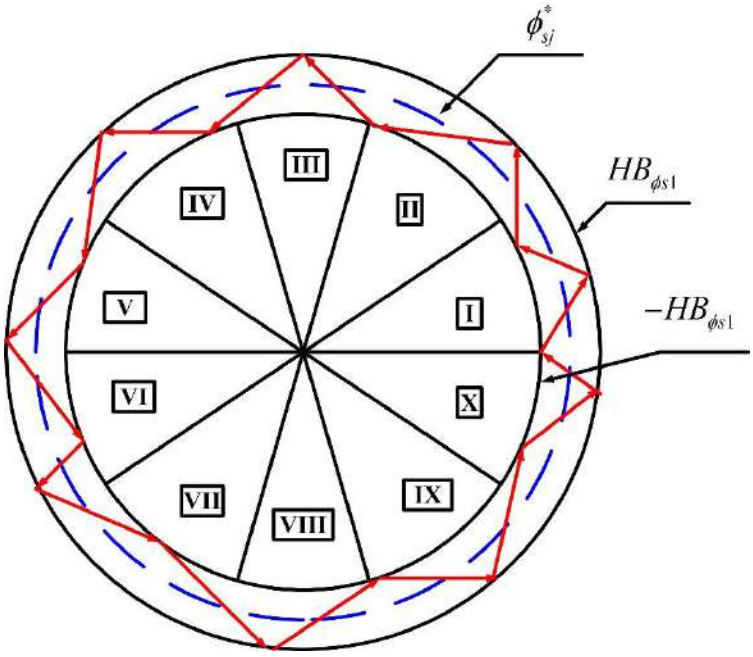

Figure 2.4: Stator flux circular trajectory.

2.2.1.2. Electromagnetic torque control

The stator flux/current and the rotor's speed are the most considered state variables in the mathematical modelling of the IM. The DTC utilizes the described model in the stationary reference frame as follows [62]:

The stator and rotor voltage equations are given as follows:

$$\begin{cases} V_{s\alpha} = R_s I_{s\alpha} + d\phi_{s\alpha}/dt \\ V_{s\beta} = R_s I_{s\beta} + d\phi_{s\beta}/dt \\ V_{r\alpha} = R_r I_{r\alpha} + d\phi_{r\alpha}/dt - j\omega_r \phi_{r\alpha} \\ V_{r\beta} = R_r I_{r\beta} + d\phi_{r\beta}/dt - j\omega_r \phi_{r\beta} \end{cases} \quad (2.3)$$

The stator and rotor flux equations are given as follows:

$$\begin{cases} \phi_{s\alpha} = L_s I_{s\alpha} + M_{sr} I_{r\alpha} \\ \phi_{s\beta} = L_s I_{s\beta} + M_{sr} I_{r\beta} \\ \phi_{r\alpha} = L_r I_{r\alpha} + M_{rs} I_{s\alpha} \\ \phi_{r\beta} = L_r I_{r\beta} + M_{rs} I_{s\beta} \end{cases} \quad (2.4)$$

By extracting the $I_{s\alpha\beta}$ expression from the stator flux equation in (2.4), and by substituting it in the rotor flux equation, the rotor current expression is given as:

$$\begin{cases} I_{r\alpha} = 1/\sigma \left(\phi_{r\alpha}/L_r - M_{rs}/L_r L_s \, \phi_{s\alpha} \right) \\ I_{r\beta} = 1/\sigma \left(\phi_{r\beta}/L_r - M_{rs}/L_r L_s \, \phi_{s\beta} \right) \end{cases} \quad (2.5)$$

Where: σ is the coefficient of dispersion.

In addition, by substituting (2.5) in (2.3), the model expression is given as:

$$\begin{cases} V_{s\alpha} = R_s I_{s\alpha} + d\phi_{s\alpha}/dt \\ V_{s\beta} = R_s I_{s\beta} + d\phi_{s\beta}/dt \\ d\phi_{r\alpha}/dt + \left(1/\sigma T_r - j\omega_r\right)\phi_{r\alpha} = M_{rs}/\sigma T_r L_s \, \phi_{s\alpha} \\ d\phi_{r\beta}/dt + \left(1/\sigma T_r - j\omega_r\right)\phi_{r\beta} = M_{rs}/\sigma T_r L_s \, \phi_{s\beta} \end{cases} \quad (2.6)$$

Where: T_r is the rotor's time constant.

From the model in (2.6), one can notice that;

- If the resistive voltage drop is neglected, the stator flux can be controlled via the stator VV.
- The stator flux variations are followed by the rotor flux variations with a difference of σT_r. Hence, this latter determines variations in time response of the angle between the machine's two fluxes; the rotor flux is given as:

$$\begin{cases} \phi_{r\alpha} = \left(M_{rs}/L_r\right)\left(\phi_{s\alpha}/1 - j\omega_r \sigma T_r\right) \\ \phi_{r\beta} = \left(M_{rs}/L_r\right)\left(\phi_{s\beta}/1 - j\omega_r \sigma T_r\right) \end{cases} \quad (2.7)$$

The electromagnetic torque expression, taking into consideration the angle variation, is as follows:

$$T_{em} = \left(pM_{rs}/L_r L_s\right)\left(\phi_{s\alpha\beta}\phi_{r\alpha\beta}\right) = \left(pM_{rs}/L_r L_s\right)\left\|\overrightarrow{\phi_{s\alpha\beta}}\right\|\left\|\overrightarrow{\phi_{r\alpha\beta}}\right\|\sin\delta \quad (2.8)$$

Where: $\left\|\overrightarrow{\phi_{s\alpha\beta}}\right\|$, $\left\|\overrightarrow{\phi_{r\alpha\beta}}\right\|$ and δ are the stator rotor flux module, respectively, and the angle between them.

Therefore, the machine's electromagnetic torque is controlled through the optimum control of the machine's stator flux module and position, as well as the angle between the stator and rotor fluxes via the applied VV. This control is possible only if the sampling time is less than the time constant σT_r. Figure 2.5 illustrates the electromagnetic torque.

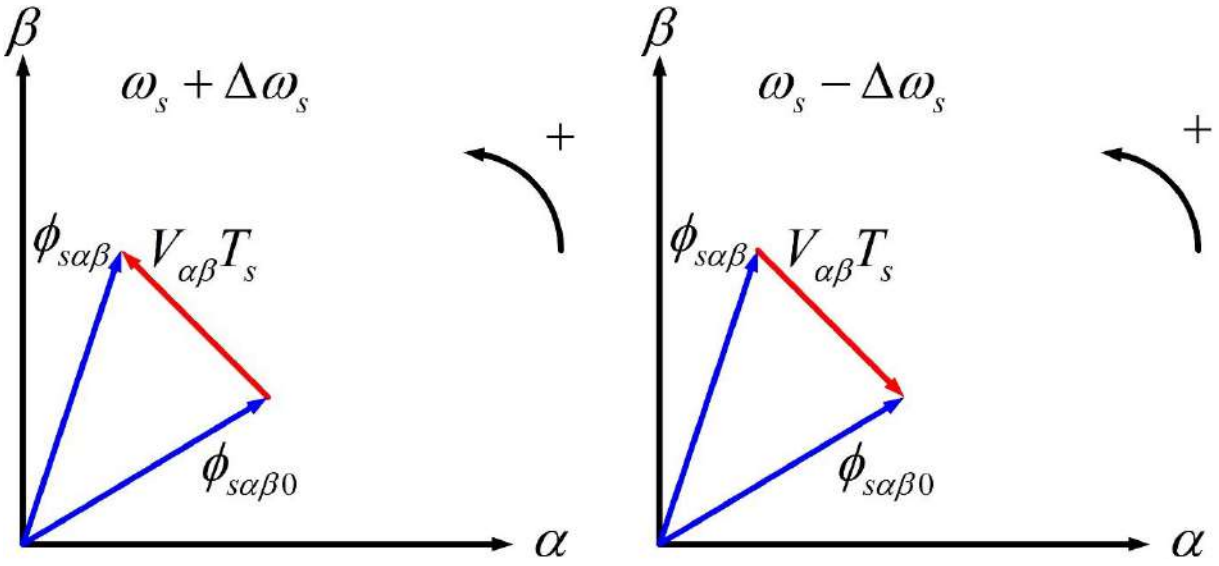

(a) (b)

Figure 2.5: Electromagnetic torque: (a) torque variation for a positive change in the speed, (b) torque variation for a negative change in the speed.

2.2.2. DTC's merits and demerits [63]

2.2.2.1. DTC's merits

- The DTC utilizes a simplified mode of the FPIM in stationary reference, eliminating the need for the coordinate transformation.
- Discard the PWM modulator.
- Fast dynamic response.
- Robustness to parameter variations.

2.2.2.2. DTC's demerits

- Torque and flux ripples.
- Inconstant switching frequency.
- Need for a robust flux and torque estimation.
- The resistive voltage drop influences the low-speed operation.

2.3. Two-machines drive's DTC

The DTC of the two parallel-connected machine drive is illustrated in figure 2.6.

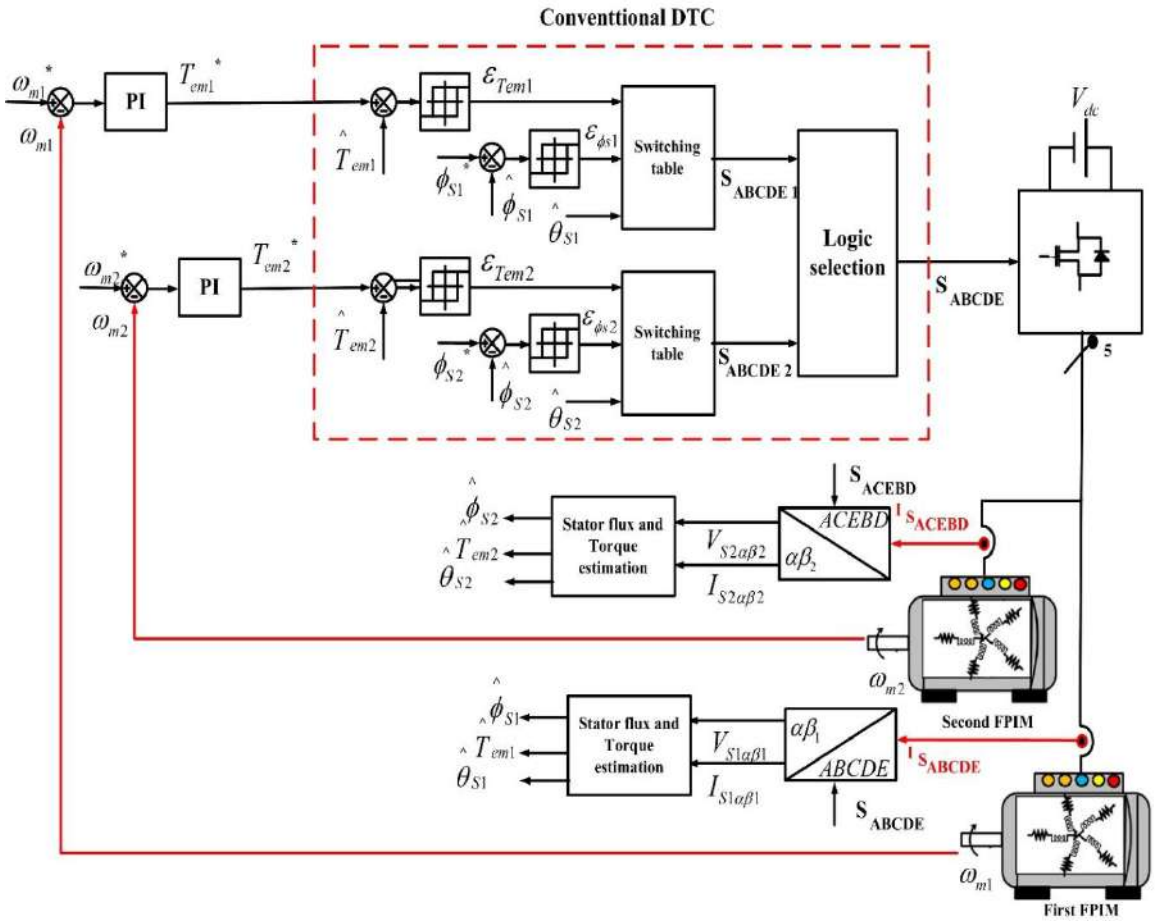

Figure 2.6: Schematic diagram of the two-machine drive's multi-level DTC.

The DTC of the two-machine drive follows the same aforementioned principle for both machines with respect to the fact that the flux/torque generating currents components for one machine do not contribute to the production of any rotating field of the other machine to enable the independent control with the appropriate phase transposition shown in Figure 1.13. Thus, two independent DTC controllers are required for the drive, which follows four basic steps.

2.3.1. Variable state estimation

2.3.1.1. Stator flux estimation

From the information on the applied VV and the measured stator currents, the stator flux can be expressed as follows [64]:

$$\begin{cases} \phi_{sj\alpha j} = \int_0^t (V_{sj\alpha j} - R_{sj} I_{sj\alpha j}) dt \\ \phi_{sj\beta j} = \int_0^t (V_{sj\beta j} - R_{sj} I_{sj\beta j}) dt \end{cases} \quad (2.9)$$

The flux vector is computed from the flux of two components in the stationary reference frame:

$$\phi_{sj} = \phi_{sj\alpha j} + j\phi_{sj\beta j} \tag{2.10}$$

The currents components in the $\alpha\beta j$ axis are obtained from the measured currents as follows [9]:

$$\begin{cases} I_{s\alpha} = 2/5\left(i_a + \cos\left(2\pi/5\right)(i_b + i_e) + \cos\left(4\pi/5\right)(i_c + i_d)\right) \\ I_{s\beta} = 2/5\left(\sin\left(2\pi/5\right)(i_e - i_b) + \sin\left(4\pi/5\right)(i_d - i_c)\right) \end{cases} \tag{2.11}$$

As for the voltage components in the $\alpha\beta j$ axis are obtained from the VV's switching states and the DC-link voltage as follows [65]:

$$\begin{cases} V_{s\alpha} = 2V_{dc}/5\left(S_a + \cos\left(2\pi/5\right)(S_b + S_e) + \cos\left(4\pi/5\right)(S_c + S_d)\right) \\ V_{s\beta} = 2V_{dc}/5\left(\sin\left(2\pi/5\right)(S_e - S_b) + \sin\left(4\pi/5\right)(S_d - S_c)\right) \end{cases} \tag{2.12}$$

Thus, the stator flux vector and position expressions are given as:

$$\begin{cases} \phi_{sj} = \sqrt{\phi_{sj\alpha j}^2 + j\phi_{sj\beta j}^2} \\ \theta_{sj} = \tan^{-1}\left(\phi_{sj\beta j}/\phi_{sj\alpha j}^2\right) \end{cases} \tag{2.13}$$

2.3.1.2. Electromagnetic torque estimation

From the estimated stator flux components in (2.9) and the stator currents components in the $\alpha\beta j$ plane in (2.11), the electromagnetic torque of the machine is expressed as:

$$T_{emj} = p_j(\phi_{sj\alpha j} I_{sj\beta j} - \phi_{sj\beta j} I_{sj\alpha j}) \tag{2.14}$$

3.2.2. State variables controller

As mentioned above, the DTC basic idea is to keep the flux and torque in a predefined hysteresis band (HB).

3.2.2.1. Two-level stator flux HC

The purpose of the two-level HC (2L-HC) is to control the flux variations and restrain it inside the HB with a circular trajectory, as shown in Figure 2.4. The controller's digital response depends upon the difference between the imposed reference command and the estimated values

of the stator flux to determine the action required for the stator flux to either increase or decrease, as expressed in (2.15) [64].

$$\begin{cases} HB_{\phi s1} >= \phi_{sj}^{*} - \hat{\phi}_{sj} & \varepsilon_{\phi sj} = 1 \\ -HB_{\phi s1} <= \phi_{sj}^{*} - \hat{\phi}_{sj} & \varepsilon_{\phi sj} = -1 \end{cases} \tag{2.15}$$

Figure 2.7 depicts the 2L-HC's structure and the illustration of the flux behaviour.

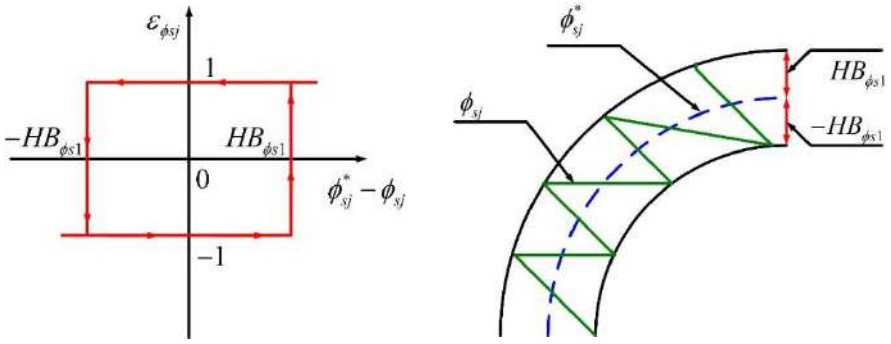

(a) (b)

Figure 2.7: (a) Two-level HC's structure (b) flux behaviour.

2.3.2.2. Seven-level electromagnetic torque HC

The seven-level HC (7L-HC) structure is adopted to enable precise control over the developed torque of the machine for the four quadrants of operation. The 7L-HC controls the torque either by increasing or decreasing it based on the information from the error between the reference and estimated values of the torque as expressed in (2.16) [66].

$$\begin{cases} HB_{Tem3} > T_{emj}^{*} - \hat{T}_{emj} & \varepsilon_{Temj} = 3 \\ HB_{Tem2} < T_{emj}^{*} - \hat{T}_{emj} <= HB_{Tem3} & \varepsilon_{Temj} = 2 \\ HB_{Tem1} < T_{emj}^{*} - \hat{T}_{emj} <= HB_{Tem2} & \varepsilon_{Temj} = 1 \\ -HB_{Tem1} < T_{emj}^{*} - \hat{T}_{emj} <= HB_{Tem1} & \varepsilon_{Temj} = 0 \\ -HB_{Tem2} < T_{emj}^{*} - \hat{T}_{emj} <= -HB_{Tem1} & \varepsilon_{Temj} = -1 \\ -HB_{Tem3} < T_{emj}^{*} - \hat{T}_{emj} <= -HB_{Tem2} & \varepsilon_{Temj} = -2 \\ -HB_{Tem3} <= T_{emj}^{*} - \hat{T}_{emj} & \varepsilon_{Temj} = -3 \end{cases} \tag{2.16}$$

Figure 2.8 depicts the schematic diagram of the 7L-HC.

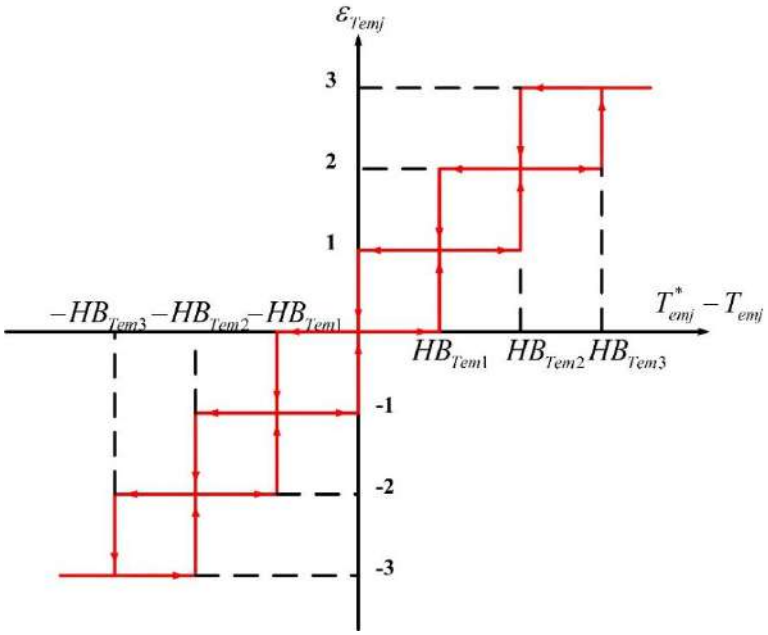

Figure 2.8: Seven-level HC's structure.

2.3.3. VV's selection

As mentioned before, the DTC controls the magnitude of the flux to keep it within a pre-set HB with the precise selection of the proper VV based on the predefined Switching Table (ST). This latter is constituted based on the action required for the machine's flux and torque obtained from the two HCs described in sections 2.3.2.1 and 2.3.2.2, respectively, and the sector's location (S) [66]. The VSI's space vector is divided into 10 sectors, as given in Table 2.1 and shown in Figures 1.17 and 1.11, as for the as for the sector location is decided from the stator flux angle.

Table 2.1: Sector numbers and boundaries.

S	θ_{sj}	S	θ_{sj}
I	$0° < \theta_{sj} \leq 36°$	VI	$-180° < \theta_{sj} \leq -144°$
II	$36° < \theta_{sj} \leq 72°$	VII	$-144° < \theta_{sj} \leq -108°$
III	$72° < \theta_{sj} \leq 108°$	VIII	$-108° < \theta_{sj} \leq -72°$
IV	$108° < \theta_{sj} \leq 144°$	IX	$-72° < \theta_{sj} \leq -36°$
V	$144° < \theta_{sj} \leq 180°$	X	$-36° < \theta_{sj} \leq 0°$

Thus, the selected VV is defined based on the combined information between the two HCs and the sector location following a set of rules, as shown in Figure 2.9 [42]:

- If the flux and torque are to be increased, then the VV to be selected is V(S+1).
- If the flux and torque are to be decreased, then the VV to be selected is V(S-4).
- If the flux is to be decreased and torque is to be increased, then the VV to be selected is V(S+4).
- If the flux is to be increased and torque is to be decreased then the VV to be selected is V(S-1).
- If the torque is to be maintained, a null error, then the VV to be selected is the zero VV.

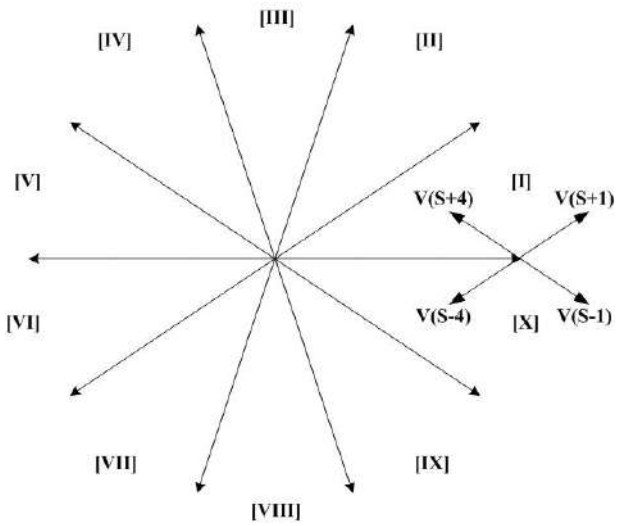

Figure 2.9: Selection rules of the VVs in the first sector.

2.3.3.1. Two-level DTC's ST

Based upon the aforementioned criterion, the optimum ST for the VV selection is elaborated for the 2L-DTC grouping the flux/torque HCs output and the sector location, as given in Table 2.2.

For further explanation, if the first machine's stator flux is to be increased, based on the 2L-HC's response ($\varepsilon_{\phi s1} = 1$) and the torque to decreased, where the 7L-HC's response is ($\varepsilon_{Tem1} = -3$), in addition to the information that the stator flux is located in sector X. thus, the VV to be selected is VL9 with a switching sequence of 10011, from $\alpha\beta_1$ plane in Figure 1.10.a. Moreover, if the second machine's in the drive stator flux is to be decreased ($\varepsilon_{\phi s2} = -1$) and the torque to be increased ($\varepsilon_{Tem2} = 1$) in sector V, then the VV VS9 with a switching sequence of 00010 is selected from $\alpha\beta_2$ plane in Figure 1.10.b.

Table 2.2: Two-level DTC's ST.

$\varepsilon_{\phi sj}$	ε_{Temj}	Sectors									
		[I]	[II]	[III]	[IV]	[V]	[VI]	[VII]	[VIII]	[IX]	[X]
1	3	VL2	VL3	VL4	VL5	VL6	VL7	VL8	VL9	VL10	VL1
	2	VM2	VM3	VM4	VM5	VM6	VM7	VM8	VM9	VS10	VS1
	1	VS2	VS3	VS4	VS5	VS6	VS7	VS8	VS9	VS10	VS1
	0	V0	V0	V0	V0	V0	V0	V0	V0	V0	V0
	-1	VS10	VS1	VS2	VS3	VS4	VS5	VS6	VS7	VS8	VS9
	-2	VM10	VM1	VM2	VM3	VM4	VM5	VM6	VM7	VM8	VM9
	-3	VL10	VL1	VL2	VL3	VL4	VL5	VL6	VL7	VL8	VL9
-1	3	VL5	VL6	VL7	VL8	VL9	VL10	VL1	VL2	VL3	VL4
	2	VM5	VM6	VM7	VM8	VM9	VM10	VM1	VM2	VM3	VM4
	1	VS5	VS6	VS7	VS8	VS9	VS10	VS1	VS2	VS3	VS4
	0	V0	V0	V0	V0	V0	V0	V0	V0	V0	V0
	-1	VS7	VS8	VS9	VS10	VS1	VS2	VS3	VS4	VS5	VS6
	-2	VM7	VM8	VM9	VM10	VM1	VM2	VM3	VM4	VM5	VM6
	-3	VL7	VL8	VL9	VL10	VL1	VL2	VL3	VL4	VL5	VL6

2.3.3.2. Three-level DTC's ST

Based upon the aforementioned criterion the optimum ST for the VV selection is elaborated for the 3L-DTC grouping the flux/torque HCs output and the sector location as given in Table 2.3.

Table 2.3: Three-level DTC's ST.

$\varepsilon_{\phi sj}$	ε_{Temj}	Sectors									
		[I]	[II]	[III]	[IV]	[V]	[VI]	[VII]	[VIII]	[IX]	[X]
1	3	VL2	VL3	VL4	VL5	VL6	VL7	VL8	VL9	VL10	VL1
	2	VM2	VM3	VM4	VM5	VM6	VM7	VM8	VM9	VS10	VS1
	1	VS2	VS3	VS4	VS5	VS6	VS7	VS8	VS9	VS10	VS1
	0	V0	V0	V0	V0	V0	V0	V0	V0	V0	V0
	-1	VS10	VS1	VS2	VS3	VS4	VS5	VS6	VS7	VS8	VS9
	-2	VM10	VM1	VM2	VM3	VM4	VM5	VM6	VM7	VM8	VM9
	-3	VL10	VL1	VL2	VL3	VL4	VL5	VL6	VL7	VL8	VL9
-1	3	VL5	VL6	VL7	VL8	VL9	VL10	VL1	VL2	VL3	VL4
	2	VM5	VM6	VM7	VM8	VM9	VM10	VM1	VM2	VM3	VM4
	1	VS5	VS6	VS7	VS8	VS9	VS10	VS1	VS2	VS3	VS4
	0	V0	V0	V0	V0	V0	V0	V0	V0	V0	V0
	-1	VS7	VS8	VS9	VS10	VS1	VS2	VS3	VS4	VS5	VS6
	-2	VM7	VM8	VM9	VM10	VM1	VM2	VM3	VM4	VM5	VM6
	-3	VL7	VL8	VL9	VL10	VL1	VL2	VL3	VL4	VL5	VL6

For further explanation, if the first machine's stator flux is to be decreased, based on the 2L-HC's response ($\varepsilon_{\phi s1} = -1$) and the torque to increased, where the 7L-HC's response is ($\varepsilon_{Tem1} = 2$), in addition to the information that the stator flux is located in sector X. thus, the VV to be selected is VM4 with a switching sequence of 20000, from $\alpha\beta_1$ plane in Figure 1.14.a. Moreover, if the second machine's in the drive stator flux in to be increased ($\varepsilon_{\phi s2} = 1$) and the torque to be increased ($\varepsilon_{Tem2} = 3$) in sector V, then the VV VL4 with a switching sequence of 00202 is selected from $\alpha\beta_2$ plane in Figure 1.14.b.

2.3.4. Logic selection

The two VVs, selected by the two DTC controllers, are alternatively applied to the VSI by the logic selection block, as shown in Figure 2.10, each for a whole sampling period.

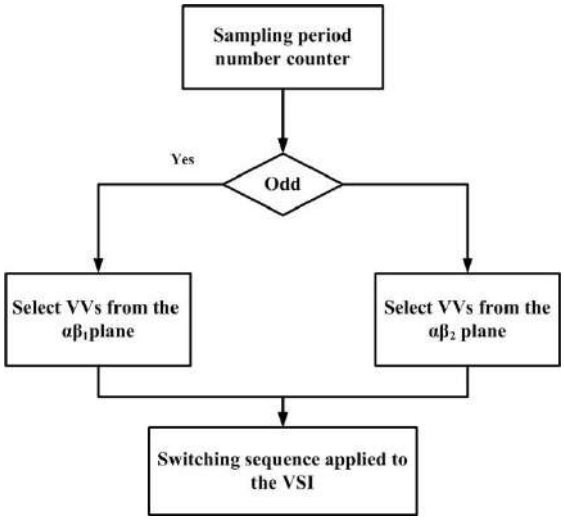

Figure 2.10: Logic selection block's structure.

2.4 Simulation results

The performance of the two-machine drive controlled by the conventional DTC scheme is evaluated through multitudinous simulation studies, and a comparison between the 2L-DTC and 3L-DTC is made. The drive is constituted by two identical FPIMs whose parameters are given in Table 1.9 section 1.6.

2.4.1. First simulation scenario

Figures 2.11 to 2.14 show the dynamic response of the two-machine drive, where the two FPIMs operate in the opposite direction with a speed reversion under constant loading conditions. Tables 2.5 and 2.6 summarize the first test scenario.

Table 2.5: First test scenario of the FPIM1.

Time [s]	$0 \rightarrow 0.5$	$0.5 \rightarrow 1.5$	$1.5 \rightarrow 2.5$	$2.5 \rightarrow 3$
Ω $[rad/s]$	$0 \rightarrow 100$	100	$100 \rightarrow -100$	-100
$T_L[Nm]$	8			

Table 2.6: First test scenario of the FPIM2.

Time [s]	$0 \rightarrow 0.5$	$0.5 \rightarrow 1.5$	$1.5 \rightarrow 2.5$	$2.5 \rightarrow 3$
Ω $[rad/s]$	$0 \rightarrow -100$	-100	$-100 \rightarrow 100$	100
$T_L[Nm]$	-8			

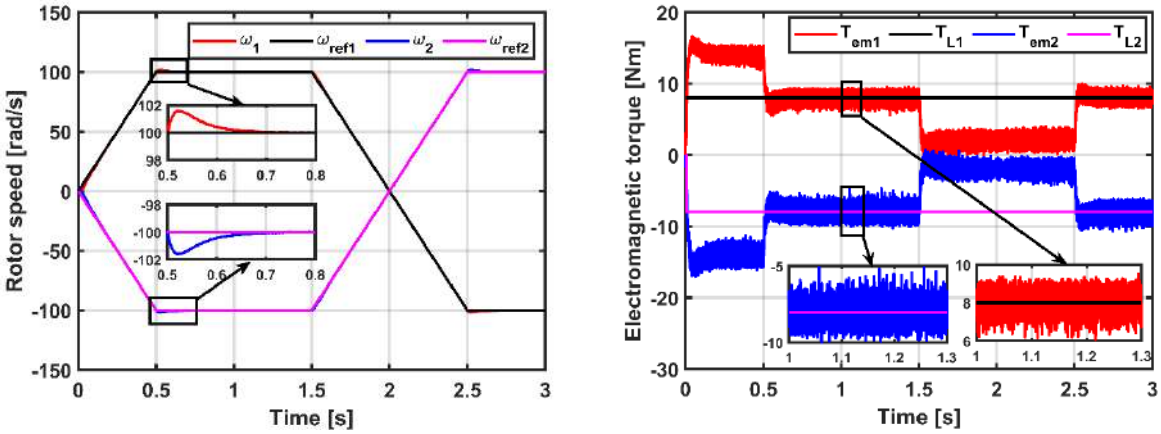

(a) (b)

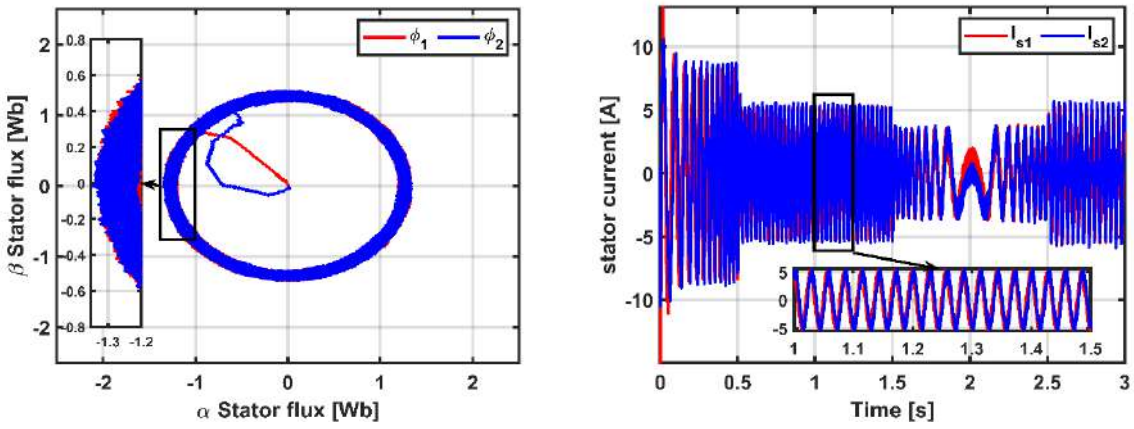

(c) (d)

Figure 2.11: Two-level DTC's response: (a) mechanical rotor speed, (b) electromagnetic torque, (c) stator flux, and (d) stator currents.

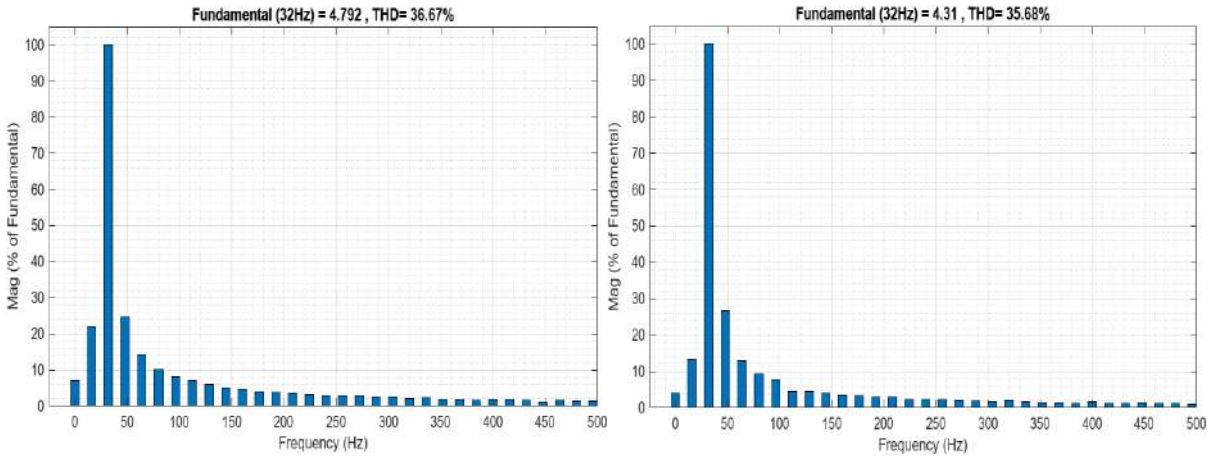

(a) (b)

Figure 2.12: Two-level DTC's currents THD: (a) FPIM1 and (b) FPIM2.

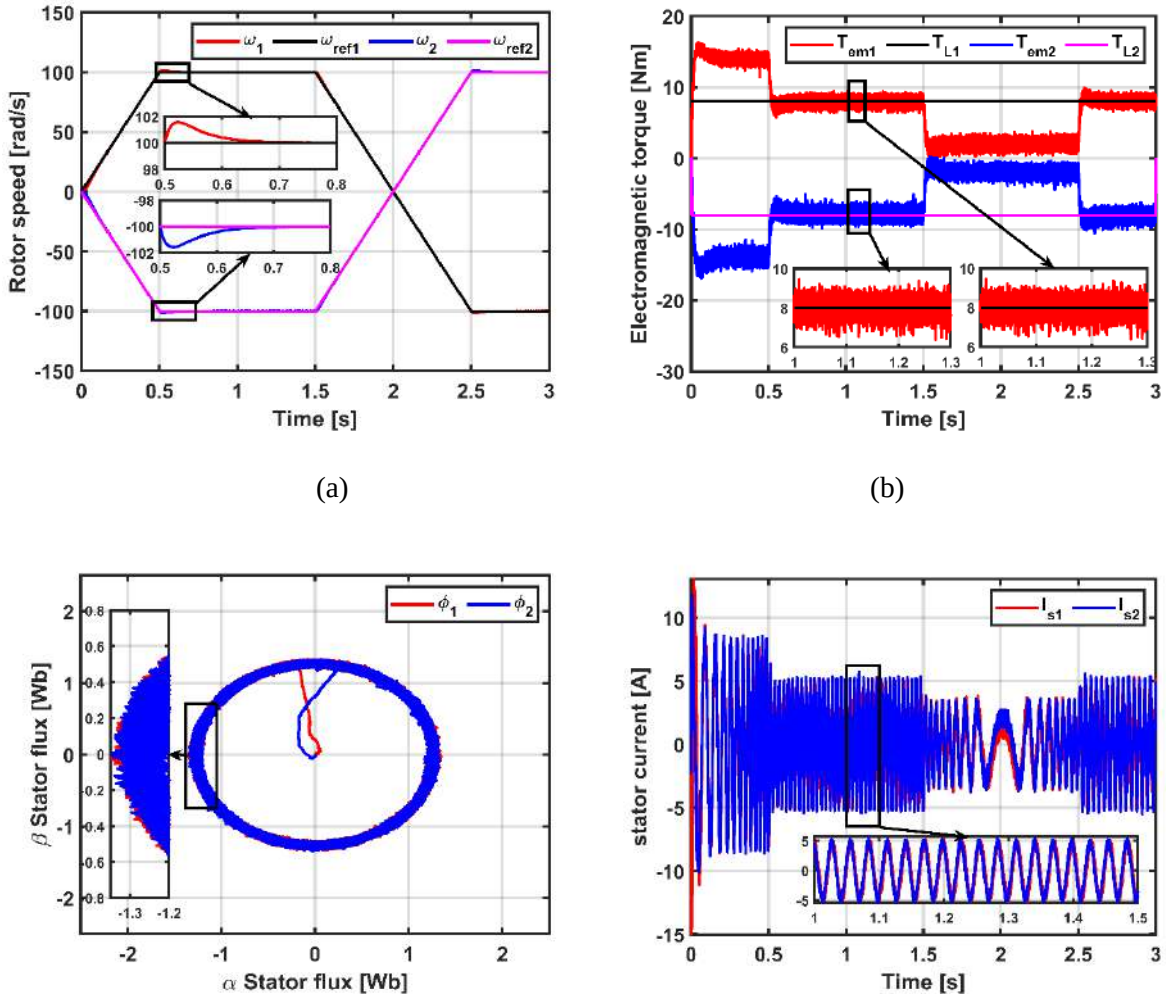

(a) (b)

(c) (d)

Figure 2.13: Three-level DTC's response: (a) mechanical rotor speed, (b) electromagnetic torque, (c) stator flux, and (d) stator currents.

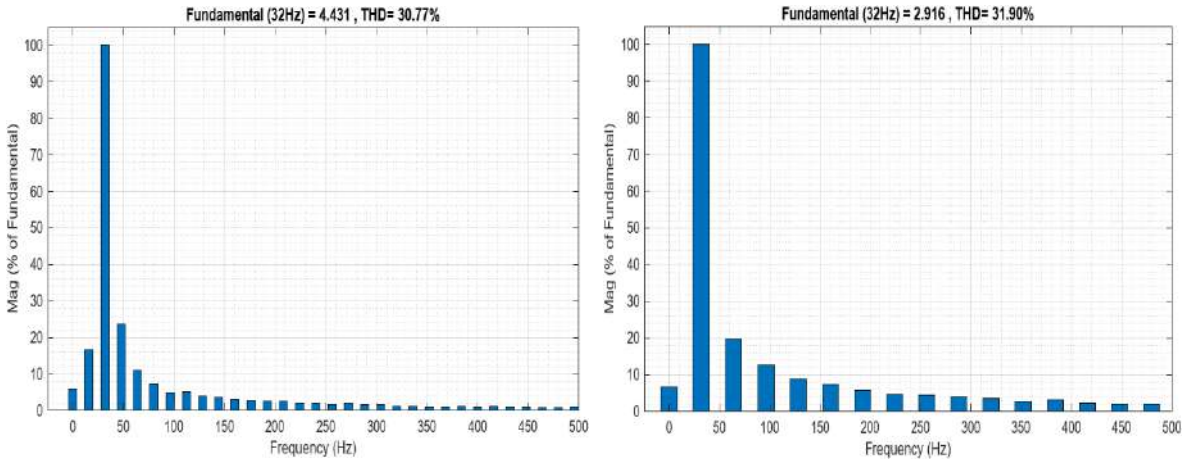

(a) (b)

Figure 2.14: Three -level DTC's currents THD: (a) FPIM1 and (b) FPIM2.

2.4.1. Second simulation scenario

In this test, both machines run in the same direction following a constant speed reference command under variable loading conditions. The two machines' responses are in Figures 2.15 and 2.16. Table 2.7 summarizes the second test scenario.

Table 2.7: Second test scenario.

$Time[s]$	$\omega_m[rad/s]$	$T_{L1}[Nm]$	$T_{L2}[Nm]$
$0 \rightarrow 0.5$	$0 \rightarrow 100$	8	-2
$0.5 \rightarrow 1$	100		
$1 \rightarrow 2$		0	8
$2 \rightarrow 3$		-4	0

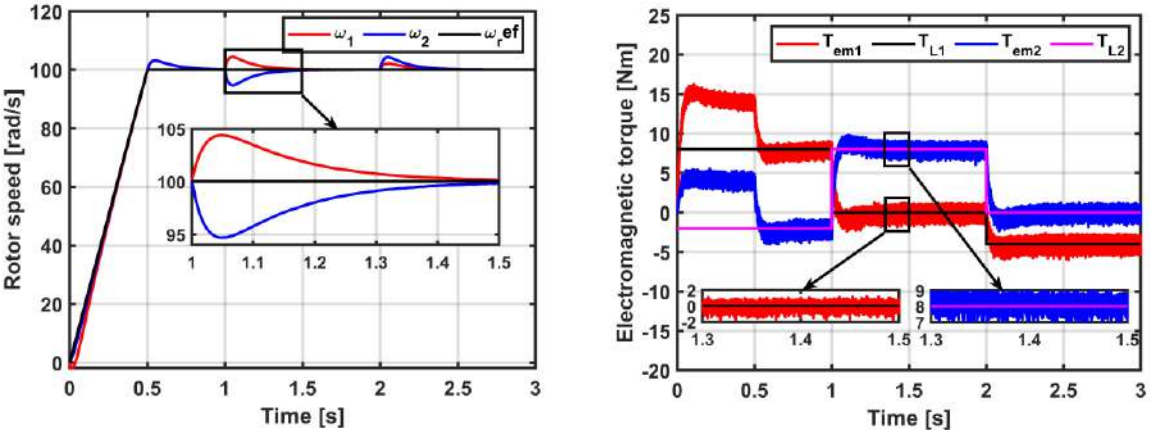

(a) (b)

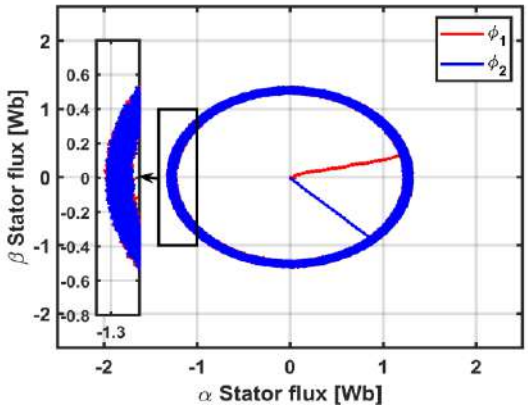

(c)

Figure 2.15: Two-level DTC's response: (a) mechanical rotor speed, (b) electromagnetic torque, and (c) stator flux.

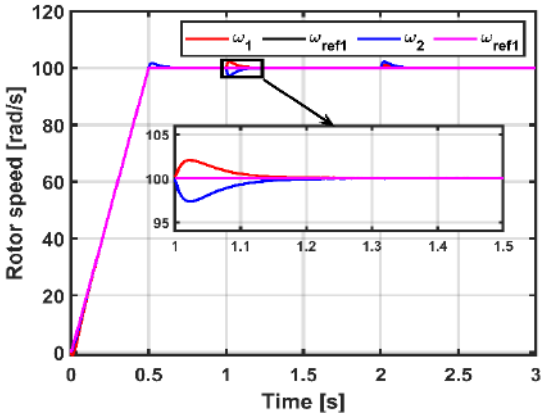

(a)

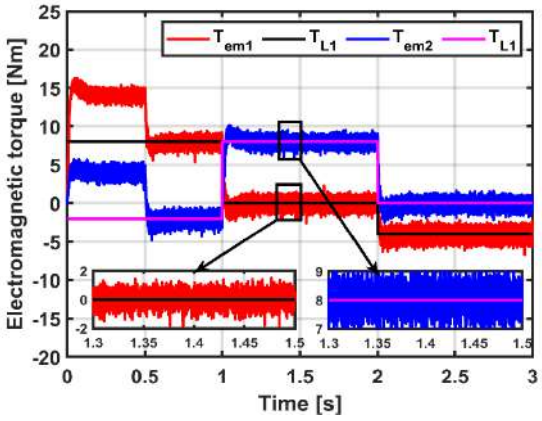

(b)

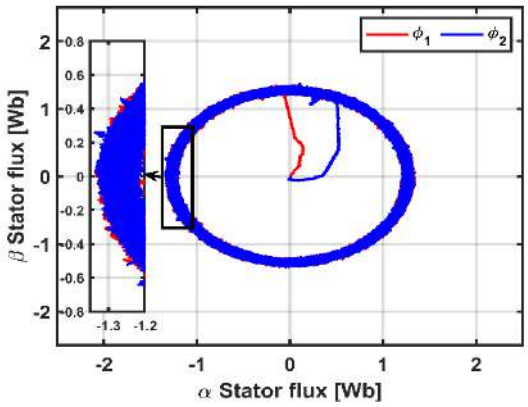

(c)

Figure 2.16: Three-level DTC's response: (a) mechanical rotor speed, (b) electromagnetic torque, and (c) stator flux.

2.4.3. Results interpretation

The reference and actual rotors' mechanical speeds of both machines are shown in Figures 2.11.a, 2.13.a, 2.15.a and 2.16.a for different reference speed command and loading conditions. It can be noticed that regardless of the operating conditions both machines follow their reference commands accordingly with an over/undershot due to the applied/removed load torque.

The electromagnetic torque response of the drive is illustrated in Figures 2.11.b, 2.13.b, 2.15.b and 2.16.b. It is shown that for both control schemes, the developed electromagnetic torque changes in response to the variations of the speed commands and loading conditions in the transient mode of operation and equal to the load torque in the steady state of the drive.

Figures 2.11.c, 2.13.c, 2.15.c and 2.16.c show the two FPIMs' stator flux trajectory in the $\alpha\beta_j$ plane following a circular trajectory accordingly with its reference commands with no over/undershot. Figures 2.11.d and 2.13.d depict the phase "a" stator currents for both, machines showing a distorted waveform, where the THD content is presented in Figures 2.12 and 2.14.

2.4.4. Comparative study

From the present results, it is clear that the control scheme preserves the decoupling control between the flux and torque for both FPIMs in both the transient and steady states, in addition to the independent control between the machines in both motoring and generating modes.

Furthermore, the present results illustrate the effect of VSI's level on the DTC scheme. Where the 2L-DTC dynamic response presents a higher ripple content in the case of the torque, flux, and current waveform compared to the 3L-DTC scheme, this latter can be noticed in the harmonic content presented in the stator current, as shown in Figures 2.12 and 2.14, where the THD is reduced by 5% in the 3L-DTC compared to 2L-DTC.

Moreover, the 3L-DTC presents a better dynamic performance for the drive operation. Table 2.8 gives a general comparison between the two control schemes.

2.5. Conclusion

This chapter presents the conventional direct torque control of the two FPIMs parallel-connected to a single two-level and three-level VSI. The independence of the control scheme is demonstrated, and that the $\alpha\beta_1$ component of the VSI controls the first FPIM's flux/torque, while the second component $\alpha\beta_2$,of the inverter controls the second FPIM's flux/torque.

The performance of the two-level and three-level DTC of the two-machine drive have been the prominent part where the simulation results illustrate the superior performance of the 3L-DTC in terms of the flux and torque ripples and faster dynamic response compared to the 2L-DTC.

However, the conventional DTC is based on the HCs, which have a non-linear nature, cause several drawbacks to the control scheme such as ripples and variable switching frequencies.

Thus, an artificial intelligence technique based on the artificial neural network is combined with the DTC to overcome the above-mentioned drawbacks and improve the drive's performance.

Table 2.8: Comparative study between the 2L-DTC and 3L-DTC techniques.

Performance	Assessment parameters	2L-DTC	3L-DTC
ω_m	Recovery time (s)	0.5	0.3
	Overshoot (rad/s)	5	2
	Undershoot (rad/s)	5	2
T_{em}	Ripples (%)	57	50
ϕ_s	Ripples (%)	16	12
i_{sa}	THD (%)	35	30

Chapter 3

Multi-level intelligent DTC of two-machine drive

3.1. Introduction

The electrical engineering community is knowledgeable about the accelerating rate of the development of artificial intelligence (AI) techniques. Especially after the introduction of the artificial neural network controllers (ANN) to mimic the stator currents controllers of the three-phase PWM VSI in 1989 [67]. In addition to the application of several AI techniques, such as regression or classification, in ASD for fault diagnosis and condition monitoring [68, 69].

ANNs are an approach fundamentally considered for data treatment and classification. These structures are adaptive and parallel distributed systems designed to imitate the biological neural networks of the human brain. The cornerstone of these networks is the artificial neurons. These last-mentioned units are heavily interconnected to reproduce the optimum response for the network's data sets [70].

Recently, with the potential of power electronics and signal processing technologies, ANNs are the most recognized technique among the known AI techniques for the identification, control, and estimation of complex systems of electrical machine drives.

Among the disadvantages of the conventional DTC scheme, discussed in Chapter 2, are the high flux and torque ripples, high level of current harmonic content, and the complexity of the ST due to the use of multi-level HCs and their non-linear nature.

For the purpose of improving the performance of the DTC scheme, several approaches based on AI are introduced, such as Fuzzy-DTC [71 - 73] and ANN-based DTC (DTC-ANN) [74 - 76]. This chapter's scope is multi-level DTC-ANN and is organized as follows: first, a brief introduction to the ANNs is given, then the DTC based on ANN is discussed, and afterwards, a comparative study is made based on the simulation results.

3.2. Artificial neural networks

The idea of ANNs can be traced back to 1943 when Mac Culloch and Pitts first tried to mathematically model the biological NNs of the human brain. Their first concept was based on the consideration that the nervose impulse results from the interconnected NNs effect of the human brain [77].

ANNs are considered computational models inspired by the biological human brain. They are capable of learning to perform non-preprogrammed tasks just from a set of data examples.

3.2.1. Biological neuron

The human brain, with a weight of less than two kg, is constituted of 2000 billion cells, and the NNs are deemed to be half of these cells. These nerve cells can be categorized into four types, as illustrated in Figure 3.1.

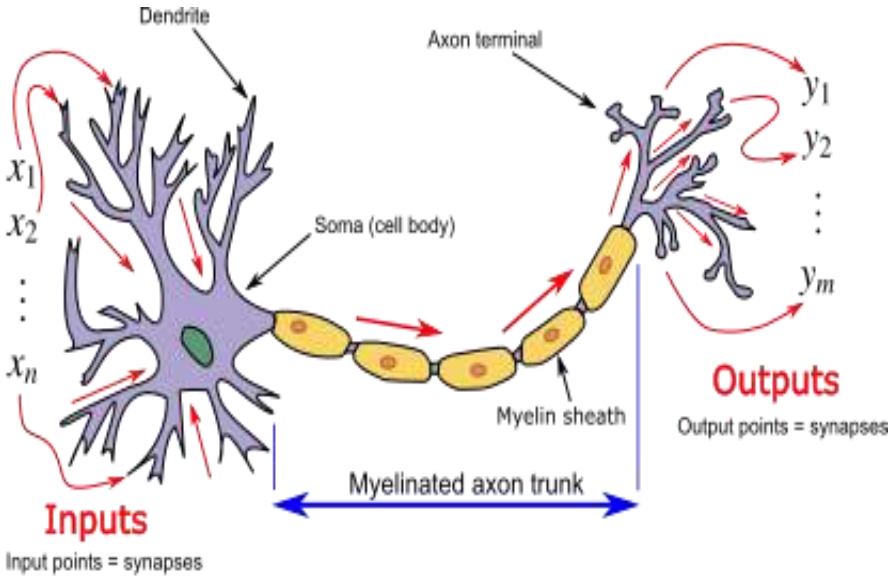

Figure 3.1: The neuron cell.

- The first type is the dendrites, which are responsible for synaptic contact and receiving signals.
- The second type is the soma, the cell body, which is considered the processing unit.
- The third type is the axons, which are responsible for the transmission of nerve messages.
- The last type is the synapse, which is considered as the communication cells between the NNs.

An action potential is generated when an electrical impulse is sent by a stimulated neuron to their threshold, along the axon cells, to the NNs through chemical signals.

3.2.2. Formal neuron

The artificial neuron which is the simplified mathematical model of the human brain's biological neuron and is considered as the elementary processing unit of ANNs. The schematics of Mac Culloch and Pitts' model of the artificial neuron is given in Figure 3.2 [78].

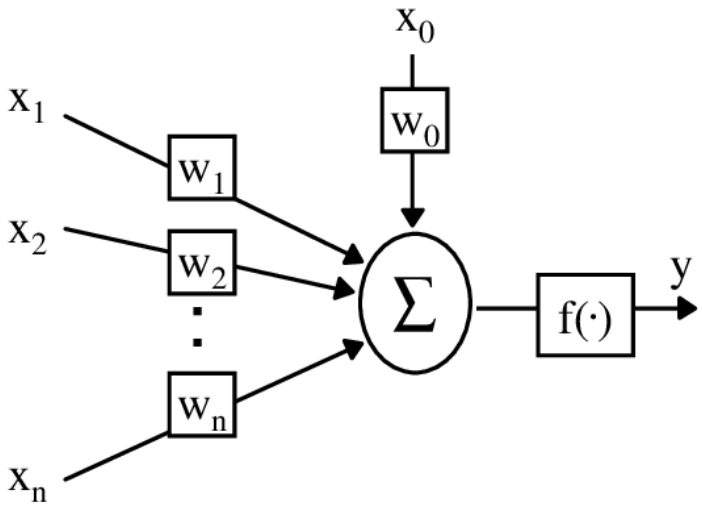

Figure 3.2: Mac Culloch and Pitts' model of the artificial neuron.

The model, illustrated in Figure 3.2, is constituted of:

- n inputs $x_i; i = 1,2, \dots, n.$
- Weighting parameters w_{ij}.
- Activation function.
- The neuron output.

Where the formal neuron output is expressed as follows:

$$netj = \sum_{j=0}^{N} w_{ij} x_j \tag{3.1}$$

From the result of Equation (3.1), the artificial neuron output can be computed through the activation function and transmitted to the other neurons in the network.

$$y_i = \gamma(netj) \tag{3.2}$$

Figure 3.3 illustrates some of the most selected activation functions in use.

Active Function Name	Formula	2D Graphical Representation	3D Graphical Representation	Description
Linear	$f(x) = x,$ *for all* x	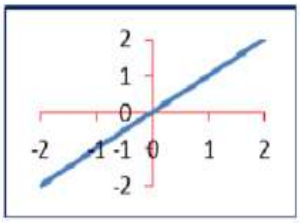	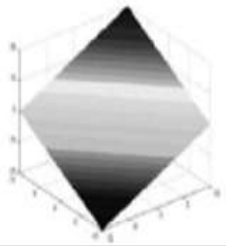	The activation of the neuron is passed on directly as the output
Logistic (or sigmoid)	$f(x) = \frac{1}{1+e^{-x}}$	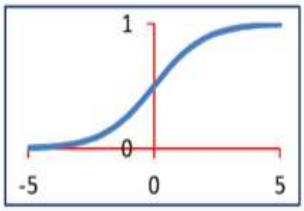	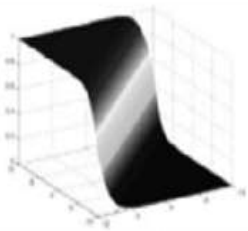	A S-shaped curve, very popular because it is Monotonous and has a simple derivative, Range of logistic or sigmoid function is from 0 to 1
Hyperbolic Tangent	$f(x) = tanh(x)$ $f(x) = \frac{1+e^{-2x}}{1+e^{2x}}$	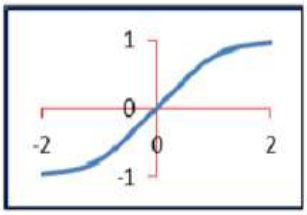	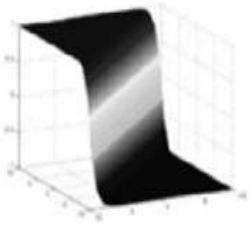	A sigmoid curve similar to the logistic function. Often performs better than the logistic function because of its symmetry. Ideal for multilayer Perceptrons, particularly the hidden layers. Output value is between -1 and +1

Figure 3.3: The most selected activation functions.

3.2.3. ANNs architecture types

Several architecture types of the ANNs are discussed in the literature. This architecture refers to the network's structure or the type and number of layers that depend on the desired application complexity and characteristics, which can be categorized as follows:

3.2.3.1. Feedforward ANNs

The simple and most basic form of multi-layered ANNs is where the input data are fed forward from the input layer to the output layer with no loops or cycles, as illustrated in Figure 3.4. It can be used for pattern recognition and data analysis [79].

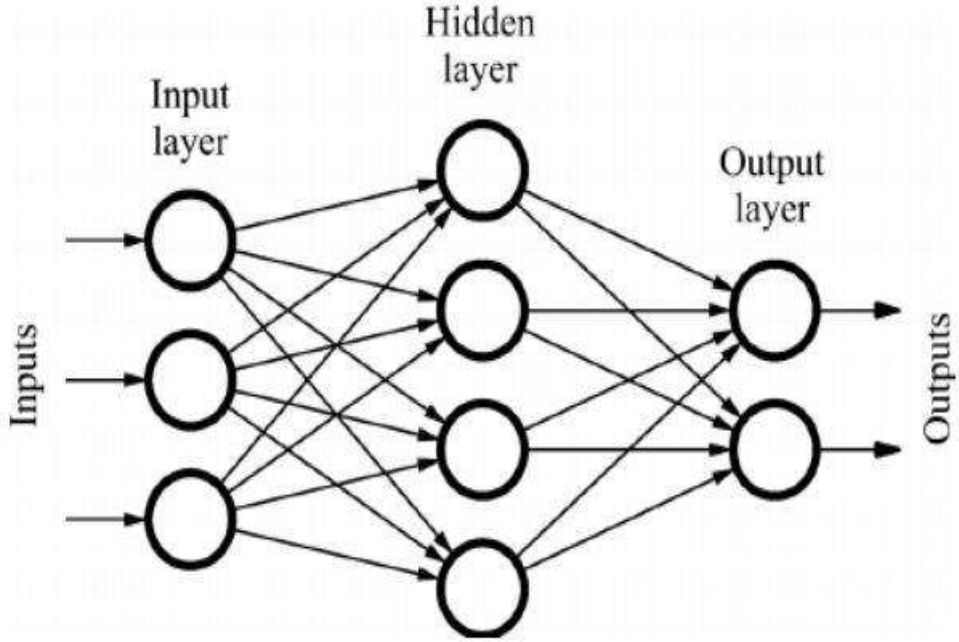

Figure 3.4: Feedforward ANNs.

The feedforward ANNs have a bestrewn application in various industrial domains such as:

- Facial recognition.
- Natural language processing.
- Computer vision.

Nevertheless, this structure has some limitation that restricts its use, such as:

- Lack of feedback connections.
- Difficulty in capturing temporal sequence information.
- Risk in overfitting.

3.2.3.2. Recurrent ANNs

This ANN architecture type is founded on feedforward ANNs with a hidden layer, as shown in Figure 3.5. The main feature of this type is its memory, which is constituted based on the loop that returns the feedback information of the ANN output so that the network learns how to predict the future output [80].

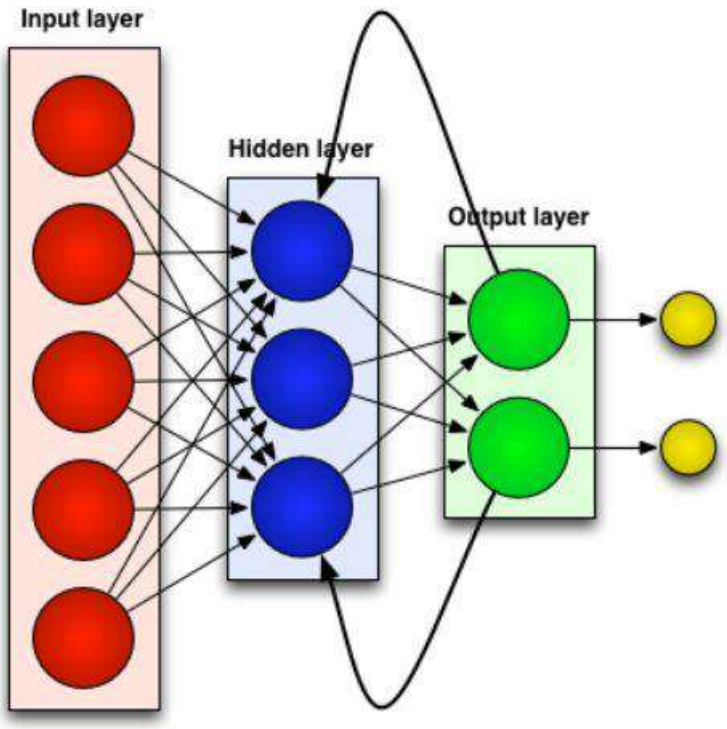

Figure 3.5: Recurrent ANNS.

The recurrent ANNs have a bestrewn application in processing sequential data for:

- Speech recognition.
- Natural language processing.
- Time series prediction.

Nevertheless, this structure has some limitation that restricts its use, such as:

- Vanishing gradient problem.
- High computational burden.
- Difficulty in parallelization.

3.2.3.3. Convolutional ANNs

A specialized structure of ANNs for grid-like data processing, like images for instants. This type utilizes a convolutional mathematical model, which is a specialized type of linear operation, to recognize patterns with different classes of extreme variability and abstraction. Figure 3.6 shows the convolutional ANNs [81].

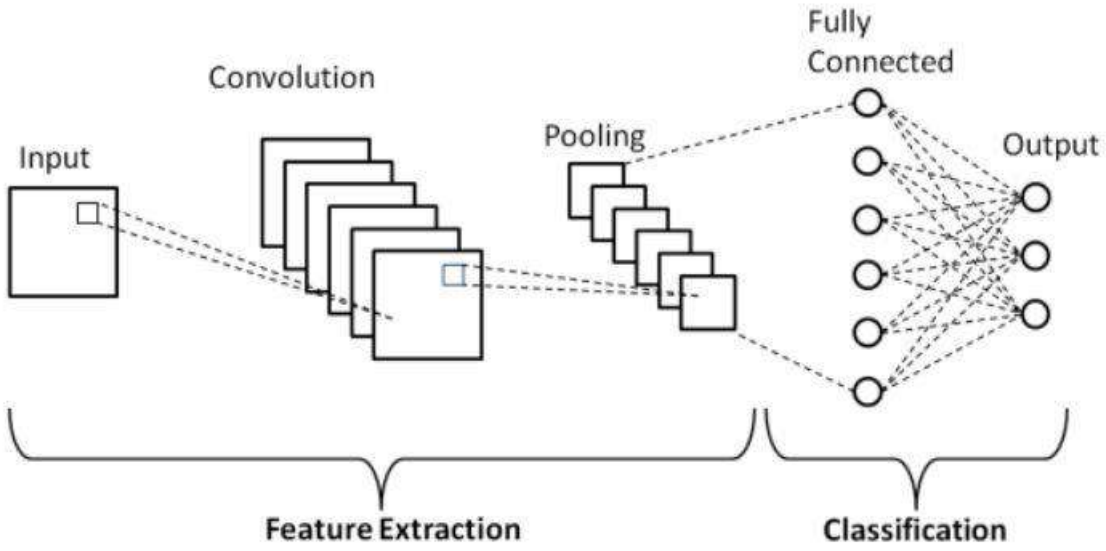

Figure 3.6: Convolutional ANNs.

The convolutional ANNs have a bestrewn application in various domains such as:

- Automated driving.
- Facial recognition.
- Agriculture.
- Medical image analysis.

Nevertheless, this structure has some limitation that restricts its use, such as:

- High complexity.
- Expensive computation.
- Overfitting risk.
- Limited to grid-like data.

3.2.3.4 Generative adversarial ANNs (GAN)

This type is an unsupervised learning ANN that uses an adversarial training process based on two components: the generator network and the discriminator network, as shown in Figure 3.7 [82].

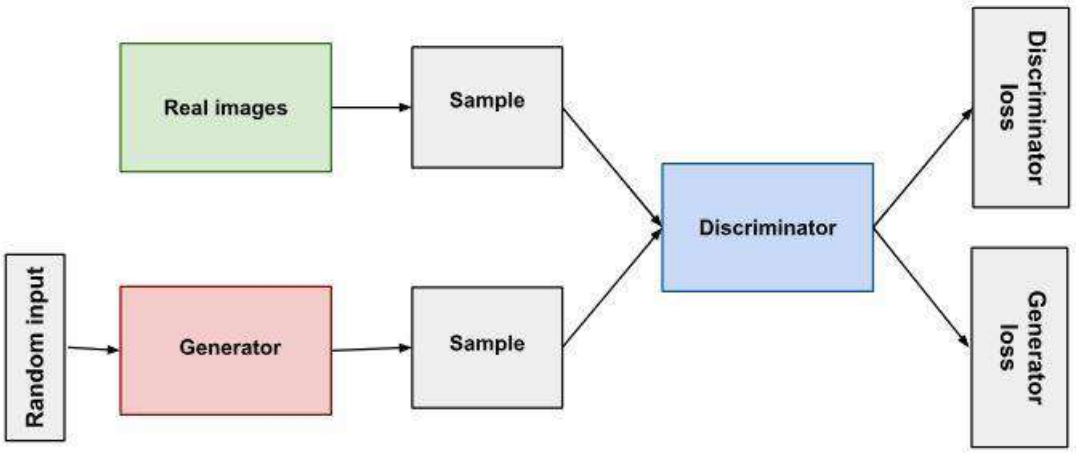

Figure 3.7: Generative adversarial ANNs structure.

The GAN have a bestrewn application in various domains such as:

- Entertainment and media.
- Fashion and design.
- Medical imaging.

Nevertheless, this structure has some limitation that restricts its use, such as:

- Training difficulty.
- Mode collapse.
- Evaluation challenges.

3.2.4. ANNs learning

The ANNs have two main features, which are the learning and the adaptation capability. Where in the learning phase, the weights for each connection are set. Afterwards, the network can adapt and handle various input scenarios that it has not learned. The learning rules can be distinguished as supervised and non-supervised learning algorithms.

3.2.4.1. Supervised learning

Supervised learning is a class of machine learning algorithms. Where in this method, a set of labelled inputs/outputs data are provided to the ANNS. The learning is done using techniques such as a back-propagation algorithm where the outputs of the ANNs are compared with the given ones, and the learning is complete when the error between the two outputs is negligible [83]. Figure 3.8 illustrates the supervised learning technique.

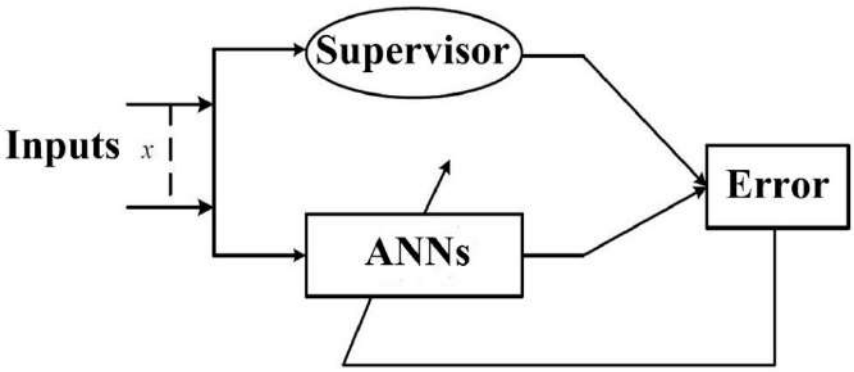

Figure 3.8: Supervised learning.

3.2.4.2. Unsupervised leaning

Unsupervised learning is a class of machine learning algorithms. Where in this method, only a set of unlabelled inputs are provided to the ANNs, with no desirable outputs. Afterwards, the ANNs start to learn to uncover the relationship and pattern between the provided data. Kohonen's self-organizing ANNs are a good example of unsupervised learning ANNs [84]. Figure 3.9 illustrates the unsupervised learning technique.

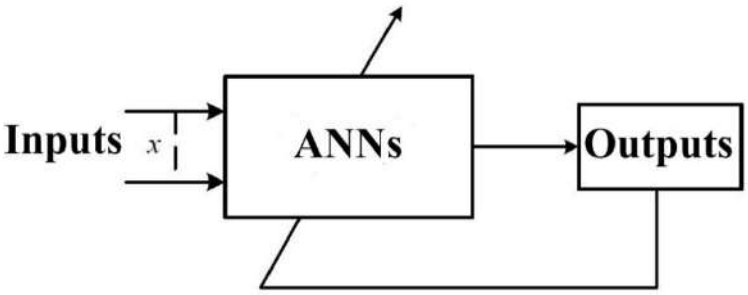

Figure 3.9: Unsupervised learning.

3.3. ANN based DTC

The introduced computational structure, known as ANNs, is used to improve the DTC performance and solve the problem of high ripple content.

ANN controllers, based on the feed-forward back-propagation technique, are used as a complex systems' universal approximator to imitate the working principle of the two HCs and ST of the conventional DTC scheme [85]. Thus, the constructed ANNs shall decide the action required on the flux and torque based on the computed error between the reference and actual values and determine the optimum VV to be applied [86].

The training process of the ANNs' controllers is based on the backpropagation algorithm, which is a supervised technique [86]. Figure 3.10 shows the training process flowchart.

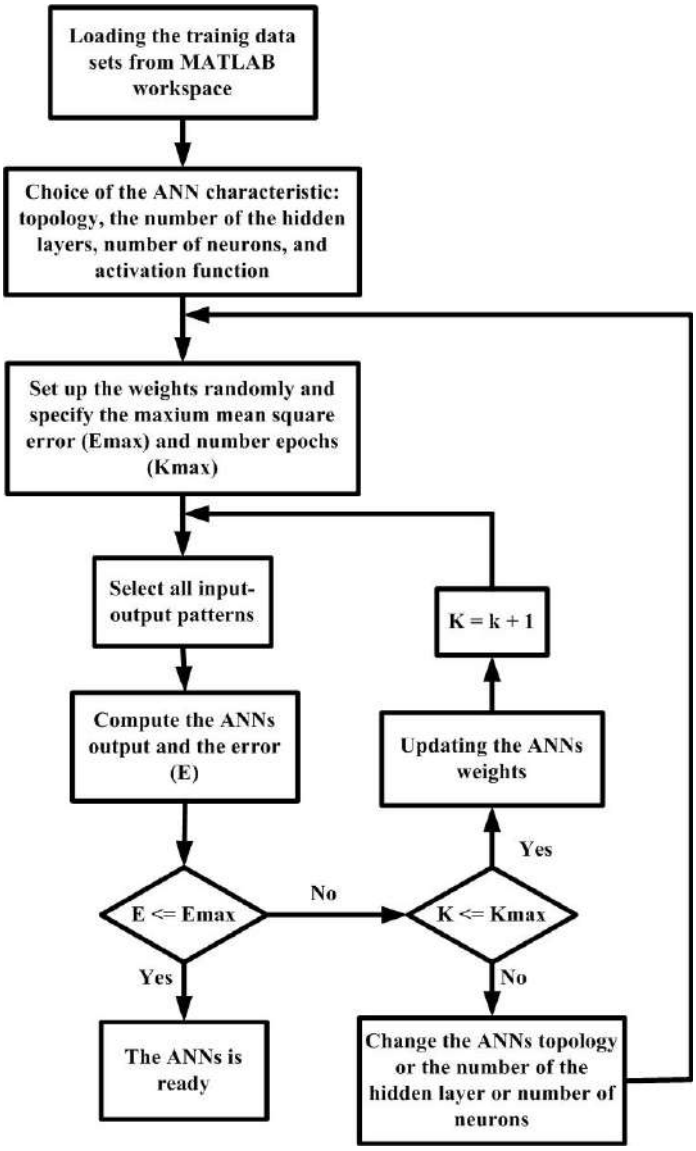

Figure 3.10: Training process flowchart.

In the considered offline learning algorithm, here in, the three ANN controllers are located in parallel to the conventional HCs and the ST, as shown in Figure 3.11. This technique has two main features, which are as follows [87]:

- The first benefit is that the intensive computation burden of the backpropagation algorithm is not executed in real-time. Thus, allowing for the implementation of a more complex network.
- The Online training might result in inefficient results compared to the offline training.

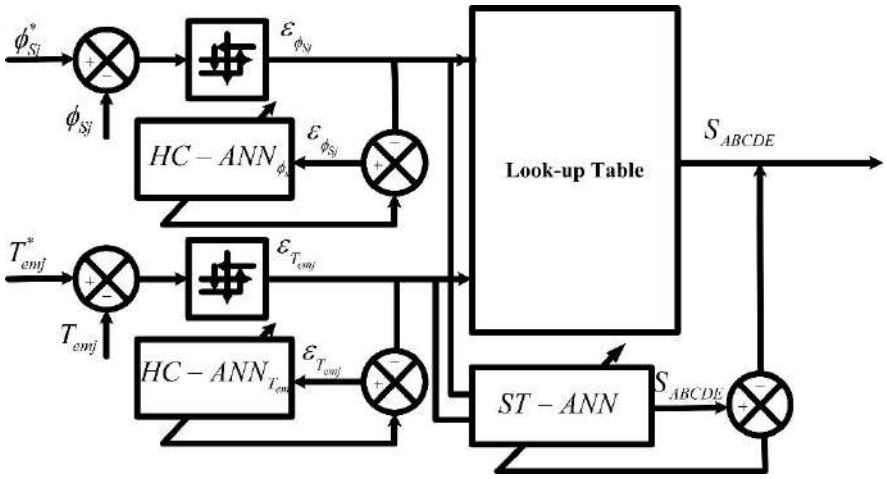

Figure 3.11: Off-line training technique.

3.3.1. Two-level DTC-ANN

The three trained ANN controllers' schematic diagrams are illustrated in Figure 3.12 and applied to the 2L-DTC [85].

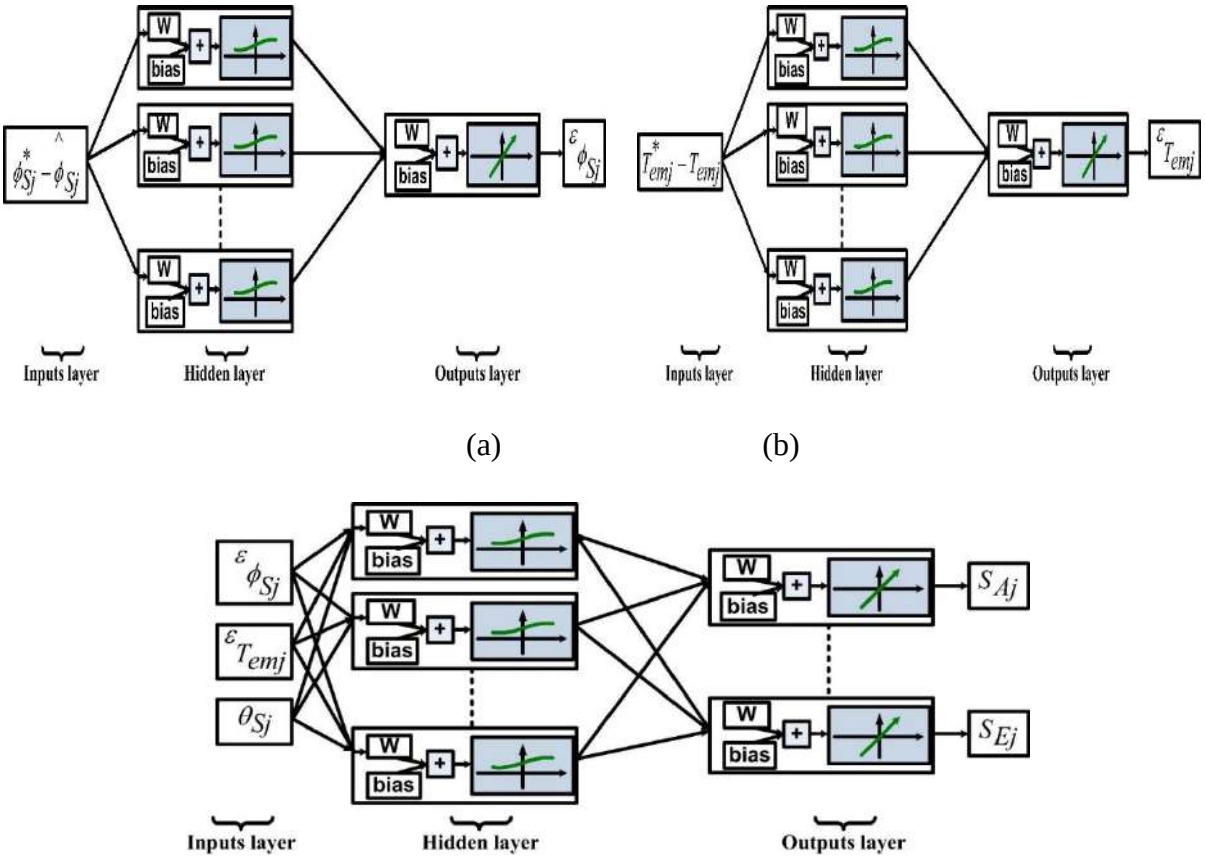

(a) (b)

(c)

Figure 3.12: Two-level DTC-ANN ANNs controllers: (a) $ANN-HC_{\phi_s}$, (b) $ANN-HC_{T_{em}}$, and (c) $ANN-ST$.

Tables 3.1 summarize the technical characteristics and parameters of the three proposed ANN controllers for the two-level DTC-ANN (2L-DTC-ANN).

Table 3.1: Two-level DTC-ANN ‘s controllers characteristics.

ANN controller parameters		Methods and values details		
		$ANN-HC_{\phi_s}$	$ANN-HC_{T_{em}}$	$ANN-ST$
ANN type		Feed-forward neural network		
ANN training algorithm		BACKPROPAGATION		
Adaptation learning function		Trainlm		
Activation function		Logsig	Logsig	Logsig
Learning rate		0.5	0.5	0.5
ANN architecture	Input layer	1	1	3
	Hidden layer	10	17	40
	Output layer	1	1	5
Training data sets		The data sets, five million samples, utilized during the training process were collected from the simulation results of DTC in MATLAB environments.		

3.3.2. Three-level DTC-ANN

The three trained ANNs controllers’ schematic diagrams are illustrated in Figure 3.13 applied to the 3L-DTC [88].

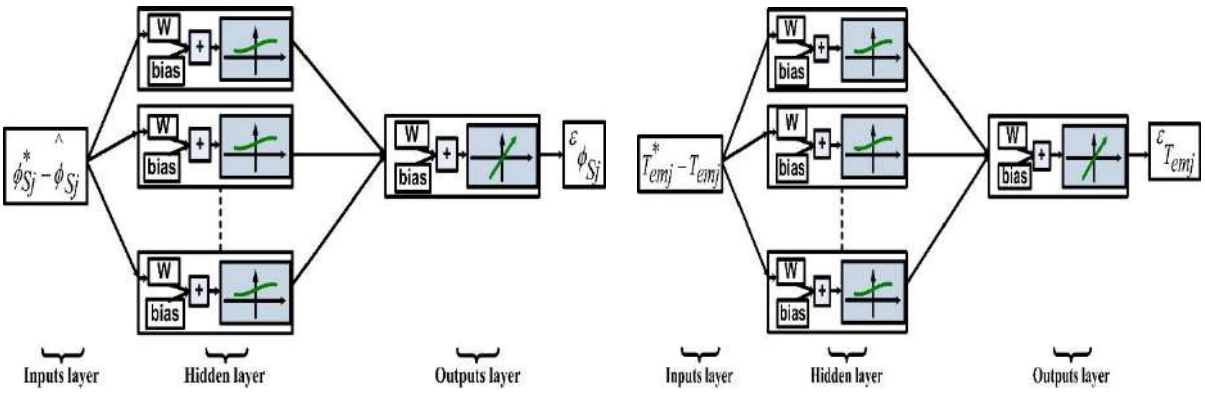

(a) (b)

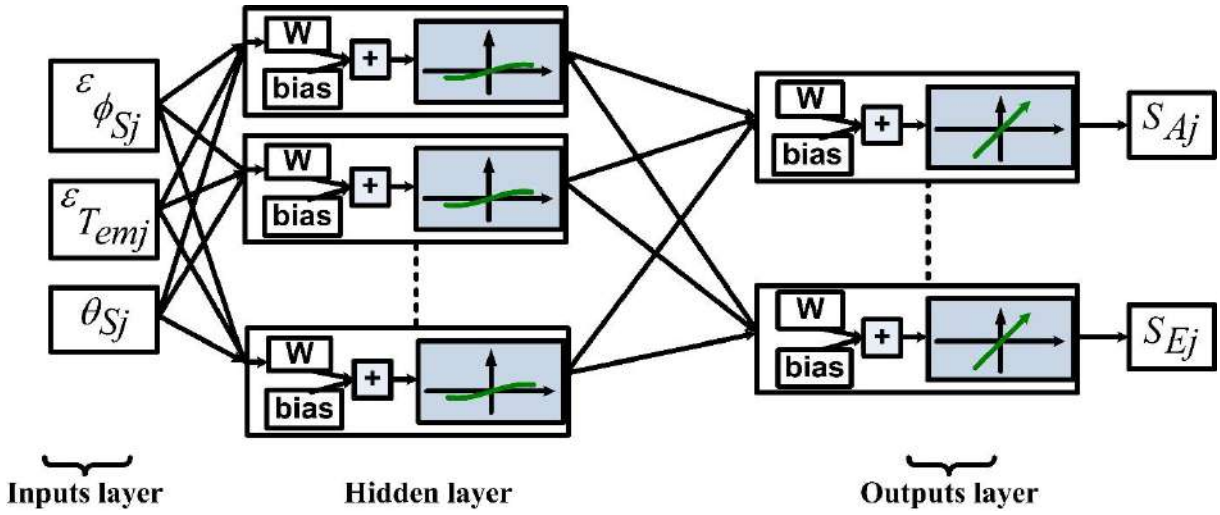

(c)

Figure 3.13: Three-level DTC-ANN ANNs controllers: (a) $ANN-HC_{\phi_s}$, (b) $ANN-HC_{T_{em}}$, and (c) $ANN-ST$.

Tables 3.2 summarize the technical characteristics and parameters of the three proposed ANN controllers for the three-level DTC-ANN (3L-DTC-ANN).

Table 3.2: Three-level DTC-ANN ‘s controllers characteristics.

ANN controller parameters		Methods and values details		
		$ANN-HC_{\phi_s}$	$ANN-HC_{T_{em}}$	$ANN-ST$
ANN type		Feed-forward neural network		
ANN training algorithm		BACKPROPAGATION		
Adaptation learning function		Trainlm		
Activation function		Logsig	Logsig	Tansig
Learning rate		0.5	0.5	0.5
ANN architecture	Input layer	1	1	3
	Hidden layer	12	17	35
	Output layer	1	1	5
Training data sets		The data sets, five million samples, utilized during the training process were collected from the simulation results of DTC in MATLAB environments.		

3.4. Simulation results

The two parallel-connected FPIMs fed by multi-level VSI controlled by DTC-ANN performance are evaluated through multitudinous simulation studies and compared to the conventional scheme. The machines' parameters are the same as in section 1.6, Table 1.9.

Figure 3.14 presents the schematic diagram of the multi-level DTC-ANN of the two parallel-connected FPIMs drive.

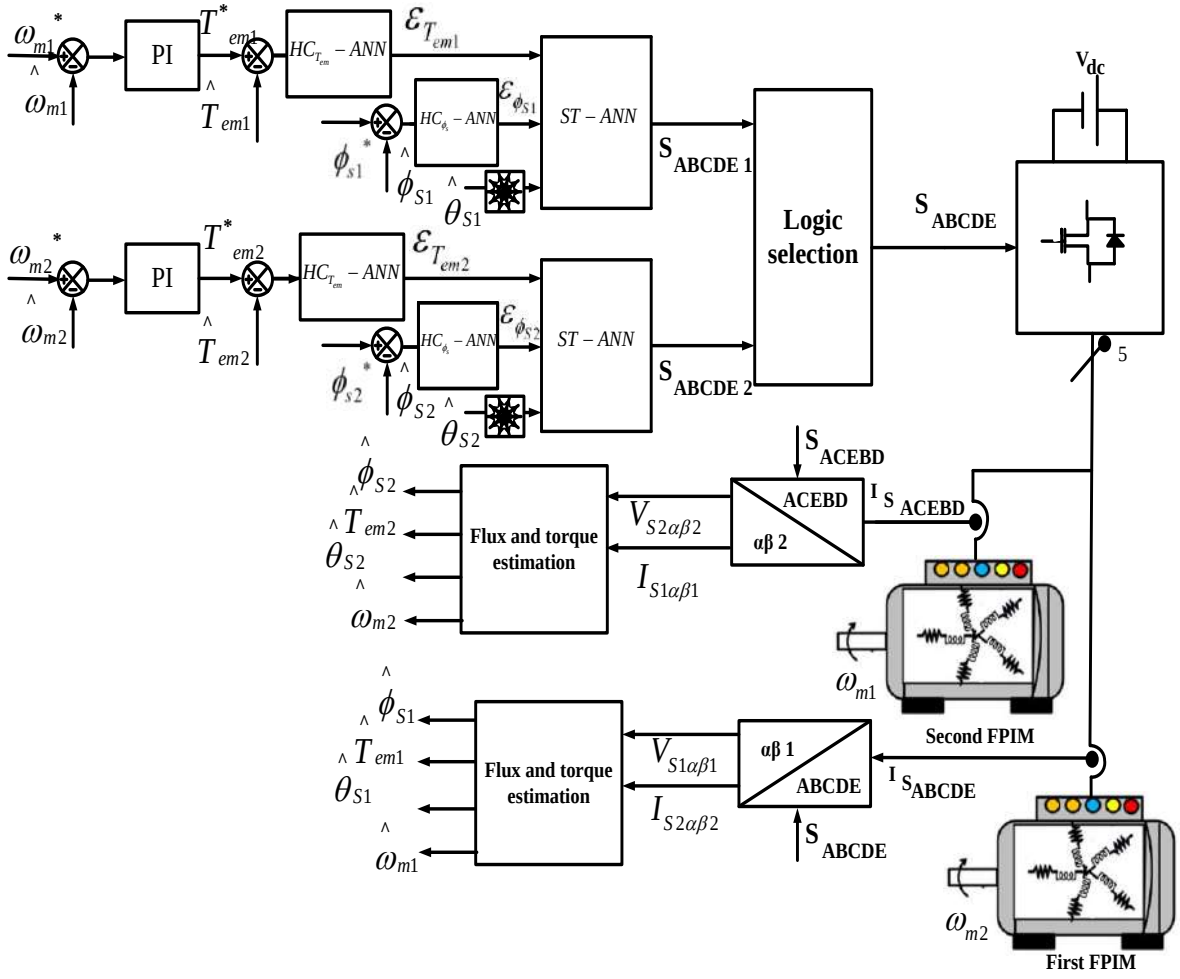

Figure 3.14: Multi-level DTC-ANN of the two parallel-connected FPIMs' drive.

3.4.1. First simulation scenario

The dynamic response of the two FPIMs is illustrated in Figures 3.15 And 3.16, where the two machines run in the opposite direction with a speed reversion under constant loading conditions. Table 3.3 summarizes the first test scenario.

Table 3.3: First test scenario.

Time [s]	ω_{m1} [rad/s]	T_{L1} [Nm]	ω_{m2} [rad/s]	T_{L2} [Nm]	Time [s]	ω_{m1} [rad/s]	T_{L1} [Nm]	ω_{m2} [rad/s]	T_{L2} [Nm]
$0 \rightarrow 0.25$	$0 \rightarrow 50$		$0 \rightarrow -50$		$2.75 \rightarrow 3.25$	-50		50	
$0.25 \rightarrow 0.75$	50		-50		$3.25 \rightarrow 3.5$	$-50 \rightarrow -100$		$50 \rightarrow 100$	
$0.75 \rightarrow 1$	$50 \rightarrow 100$		$-50 \rightarrow -100$		$3.5 \rightarrow 4$	-100		100	
$1 \rightarrow 1.5$	100	8	-100	-8	$4 \rightarrow 4.25$	$-100 \rightarrow -50$	8	$100 \rightarrow 50$	-8
$1.5 \rightarrow 1.75$	$100 \rightarrow 50$		$-100 \rightarrow -50$		$4.25 \rightarrow 4.75$	-50		50	
$1.75 \rightarrow 2.25$	50		-50		$4.75 \rightarrow 5$	$-50 \rightarrow 0$		$50 \rightarrow 0$	
$2.25 \rightarrow 2.75$	$50 \rightarrow -50$		$-50 \rightarrow 50$						

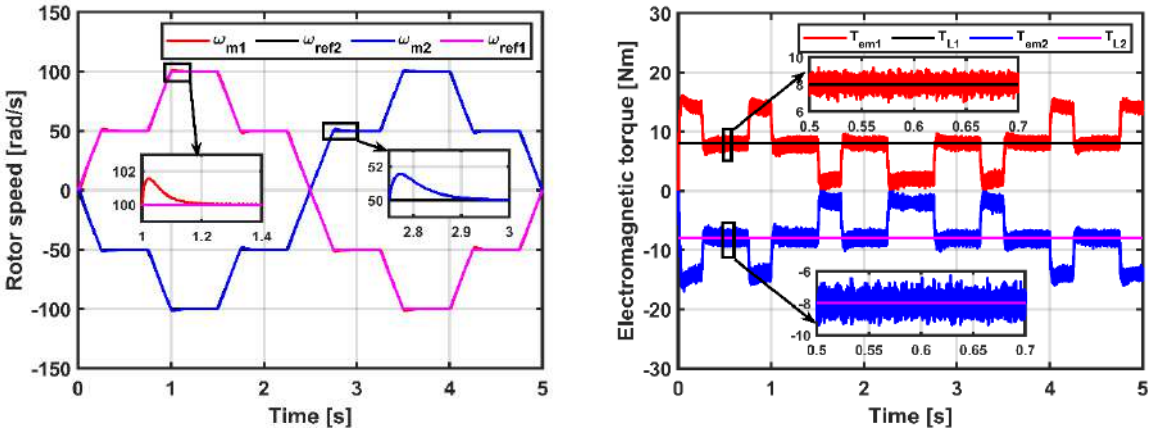

(a)

(b)

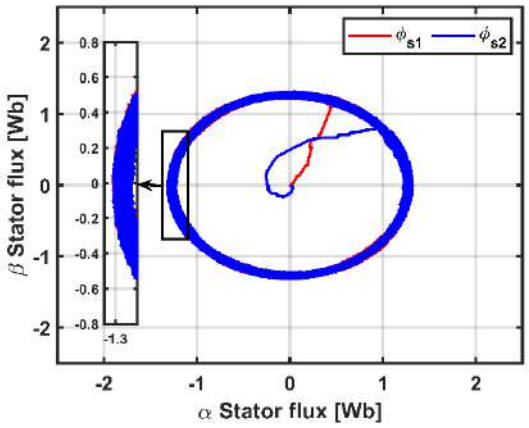

(c)

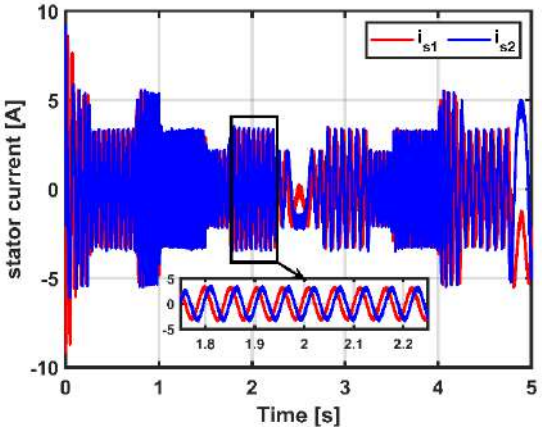

(d)

Figure 3.15: Two-level DTC-ANN's response: (a) rotor's mechanical speed, (b) electromagnetic torque, (c) stator flux, (d) stator current.

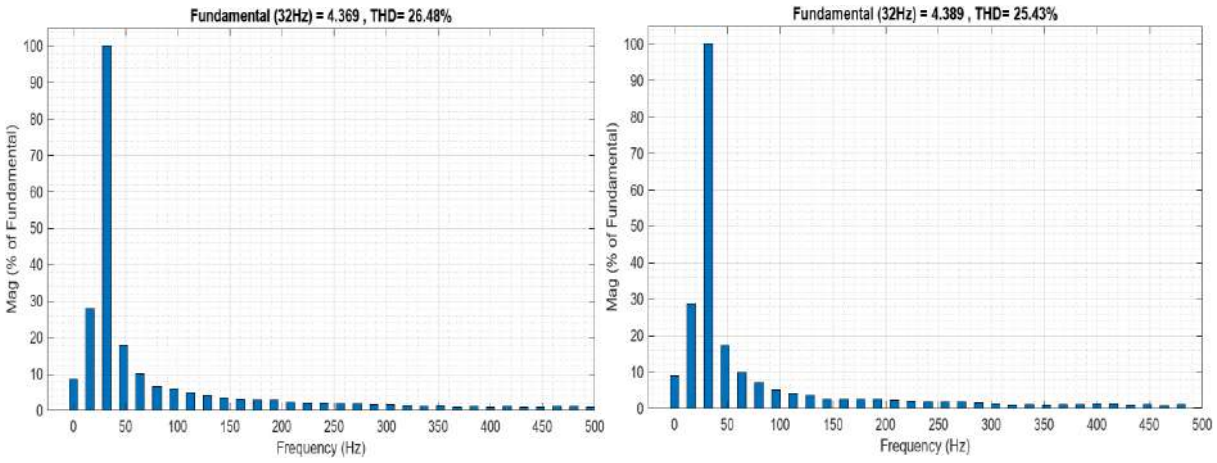

(a) (b)

Figure 3.16: Two-level DTC-ANN's currents' THD: (a) FPIM1, (b) FPIM2.

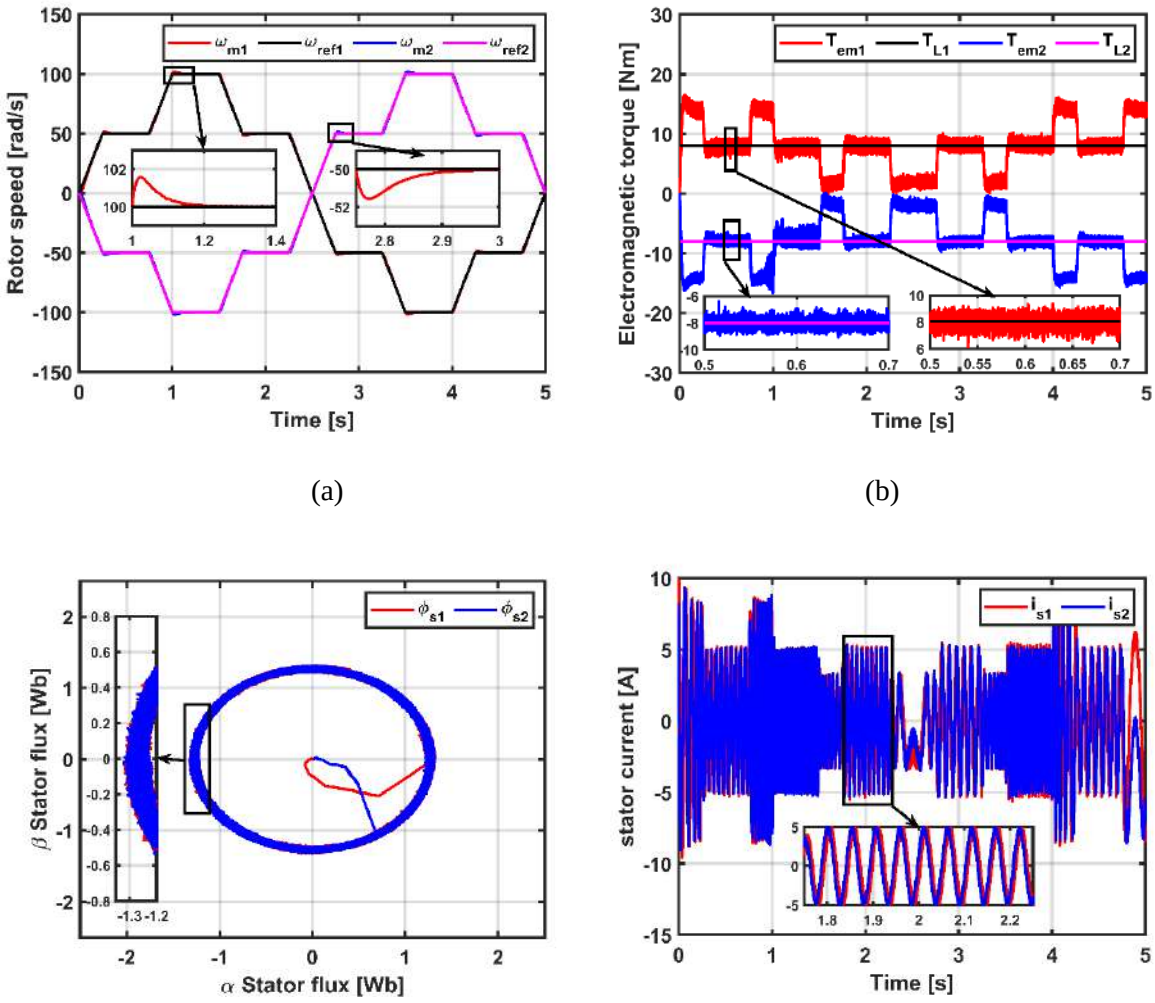

(a) (b)

(c) (d)

Figure 3.17: Three-level DTC-ANN's response: (a) rotor's mechanical speed, (b) electromagnetic torque, (c) stator flux, (d) stator current.

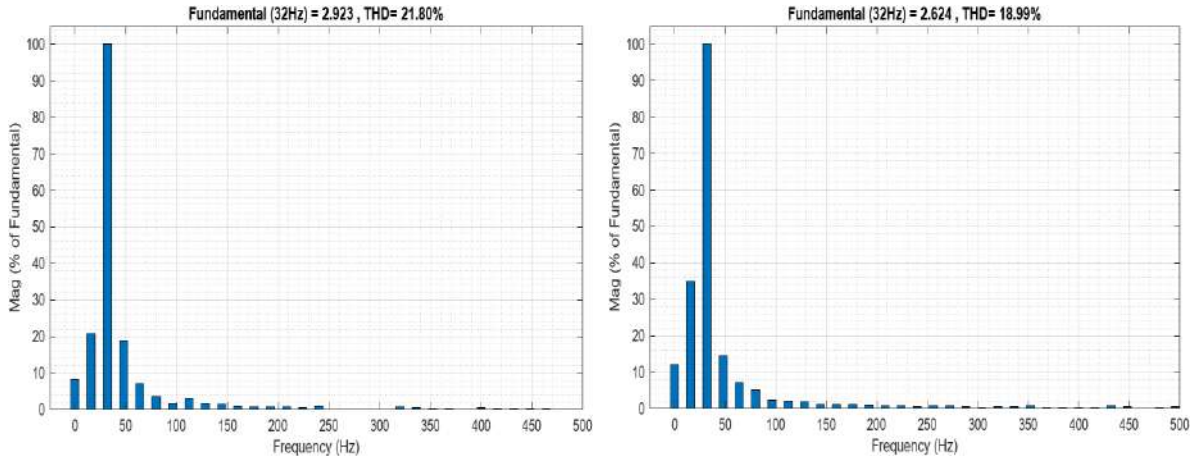

(a) (b)

Figure 3.18: Three-level DTC-ANN's currents' THD: (a) FPIM1, (b) FPIM2.

3.4.2. Second test scenario

For this test, both machines run with a constant speed command and a variable loading profile. The drive's response is given in Figures 3.17 and 3.18. Table 3.4 summarizes the second test scenario.

Table 3.4: Second test scenario.

$Time[s]$	$\omega_m[rad/s]$	$T_{L1}[Nm]$	$T_{L2}[Nm]$
$0 \rightarrow 0.5$	$0 \rightarrow 100$	8	-2
$0.5 \rightarrow 1$	100		
$1 \rightarrow 2$		0	8
$2 \rightarrow 3$		-4	0

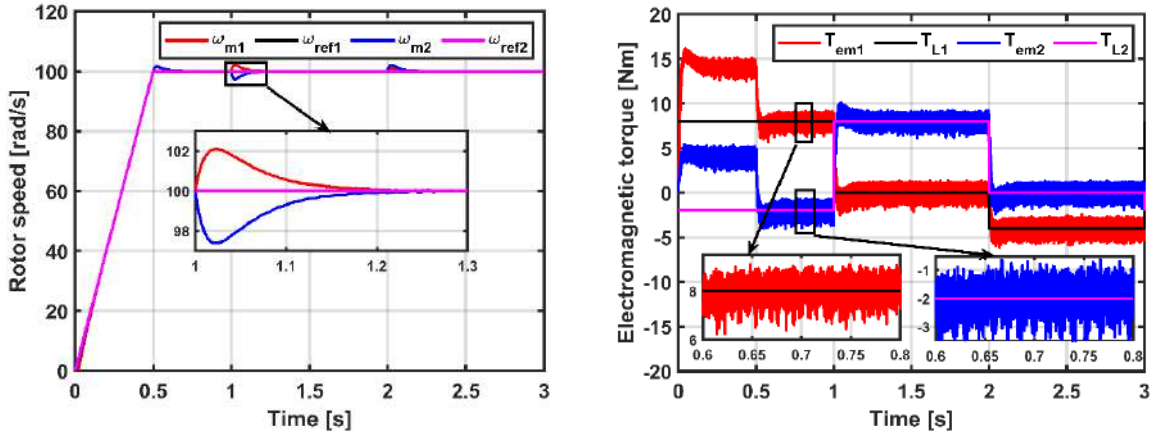

(a) (b)

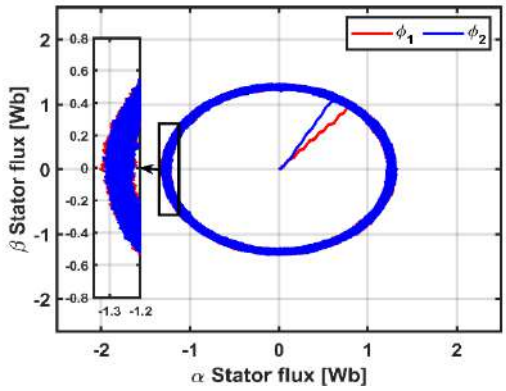

(c)

Figure 3.19: Two-level DTC-ANN's response: (a) rotor's mechanical speed, (b) electromagnetic torque, (c) stator flux.

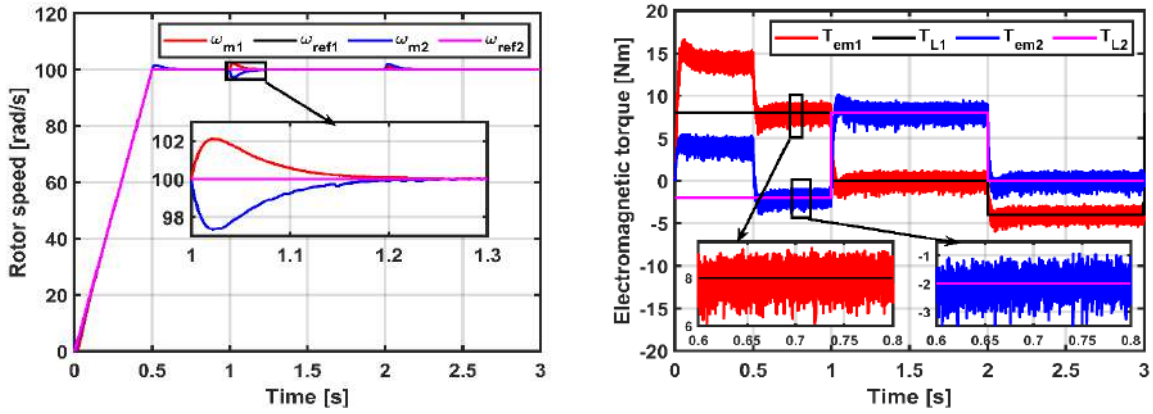

(a) (b)

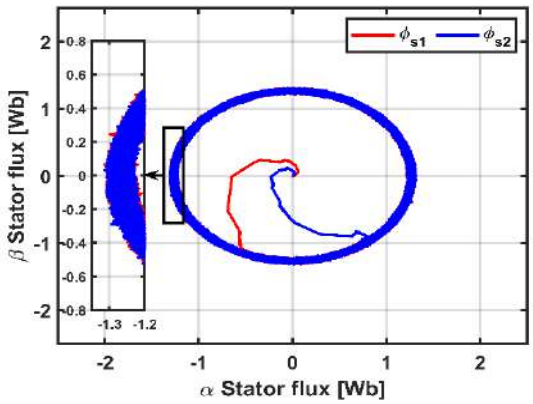

(c)

Figure 3.20: Three-level DTC-ANN's response: (a) rotor's mechanical speed, (b) electromagnetic torque, (c) stator flux.

3.4.3. Results interpretation

From the present results, illustrated to provide a comparative study between the conventional and the intelligent DTC method in Figures 2.11 to 2.14 and Figures 3.15 to 3.20, respectively, one can notice:

The two FPIMs' rotor mechanical speeds follow precisely their reference command with a minor over/undershot, as shown in Figures 3.15.a, 3.17.a, 3.19.a, and 3.20.a, regardless of the operating conditions applied to the drive in Figures 2.11.a, 2.13.a, 2.15.a, and 2.16.a.

The electromagnetic torque shows a faster response controlled via DTC-ANN, in Figures 3.15.b, 3.16.b, 3.19.b, and 3.20.b, with less torque ripple by 5% when compared to the response of conventional DTC in Figures 2.11.b, 2.13.b, 2.15.b, and 2.16.b. Furthermore, the 3L-DTC-ANN presents a superior performance regarding the ripple content and drives response.

The flux module, illustrated in Figures 3.15.c, 3.17.c, 3.19.c, and 3.20.c, presents a constant circular trajectory in the $\alpha\beta_j$ plane independent of the electromagnetic torque variations. Moreover, the DTC-ANN presents less ripple content by 4% when compared to the conventional scheme in Figures 2.11.c, 2.13.c, 2.15.c, and 2.16.c.

The DTC-ANN controlled drive presents a better stator currents waveform and less distortion in Figures 3.15.d and 3.17.d when compared to the DTC scheme from Figures 2.11.d and 2.13.d.

The THD analysis of the intelligent DTC stator currents waveform is given in Figures 3.16 and 3.17, where it can be deduced that that the DTC-ANN significantly reduced the content of current harmonics by 5% when compared to the DTC, from Figures 2.12 and 2.14.

3.4.4. Comparative study

From the analysis of the above interpretation, it is noticed that the DTC-ANN improved the drive's performance while preserving the advantages of the conventional method. The three-level DTC-ANN presents remarkable performance for all the possible operating modes of the drive while ensuring the independent and decoupled control of the drive. Table 3.5 gives an analytical comparison between the two control schemes.

3.5. Conclusion

In this chapter, the basis of the ANNs inspired by the evolution of neurobiology studies to imitate the human brain, especially with the introduction of the backpropagation algorithm, is briefly introduced. These structures are discussed for their ability to learn and are applied to

improve the DTC scheme performance of the two-machine drive by replacing the conventional HCs and STs with ANN controllers. The intelligent multi-level DTC based on the ANNs shows a remarkable reduction of the machines' flux/torque ripples and current THD, and furthermore, by improving the FPIMs' dynamic performances.

Nevertheless, the DTC still suffers from estimation problems, especially during low-speed operation, which affect the drive's performance. Thus, in the next chapter, sensorless control based on Machine-Model methods is introduced to address this problem.

Table 3.5: Analytical study between the 2L-DTC and 2L-DTC-ANN.

Performance	Assessment parameters	2L-DTC	2L-DTC-ANN
ω_m	Recovery time (s)	0.5	0.3
	Overshoot (rad/s)	5	2
	Undershoot (rad/s)	5	2
ϕ_s	Ripples (%)	16	13
T_{em}	Ripples (%)	57	52
I_S	THD (%)	35	25

Table 3.6: Analytical study between the 3L-DTC and 3L-DTC-ANN.

Performance	Assessment parameters	3L-DTC	3L-DTC-ANN
ω_m	Recovery time (s)	0.3	0.3
	Overshoot (rad/s)	2	3
	Undershoot (rad/s)	2	3
ϕ_s	Ripples (%)	12	8
T_{em}	Ripples (%)	50	46
I_S	THD (%)	30	20

Chapter 4

Sensorless multi-level intelligent DTC of two-machine drive

4.1. Introduction

In the domain of ASA of the FPIMs drives, several speed and flux transducers are used for the optimum performance of the VC schemes, such as resolvers, tacho-generators, digital encoders, and hall effect sensors. However, the use of these sensors results in several disadvantages [89, 90]:

- Increases the system's overall cost, complexity, and volume.
- Some sensors require a unique design for the machine.
- In aggressive, hazardous, and defective environments, the implemented sensors represent the weakest part of the system.
- Sensitivity to EMI, temperature, and vibrations.

The aforementioned disadvantages result, in turn, in reliability issues and reduce the advantages and performance of the FPIMs drives and the VC schemes, respectively. For this purpose, and in addition to the recent development of high-speed processors required for real-time applications, several sensorless VC methods have been developed. These methods are usually based on the machine's mathematical model and the measured electrical quantities, such as the stator voltages/currents, to estimate the machine's state variables. Moreover, the conventional DTC relies on the use of an open-loop estimator to estimate the electromagnetic variables based on the measurements of the stator currents and DC link voltage; however, this method suffers from initial values and DC drift problems [91].

Thus, this chapter discusses the sensorless direct torque control of the two parallel-connected FPIMs drive. For this reason, three different Machine-Model based (MM) state observers are proposed: Model reference Adaptive System (MRAS), Sliding Mode Observer (SMO), and Virtual Current Sensor (VCS).

4.2. MM sensorless control

The common definition of MM-based sensorless control methods is that the electromagnetic and mechanical state variables are not measured [92], such as speed and torque, and can be classified into two categories.

4.2.1. Estimators

The state estimators are employed in an open-loop configuration that exploits the machine's model. However, this approach is sensitive to modeling errors and parameter variation due to the absence of feedback connections; hence, the perturbation errors are not considered [93, 94]. Figure 4.1 represents the basic structure of the estimator.

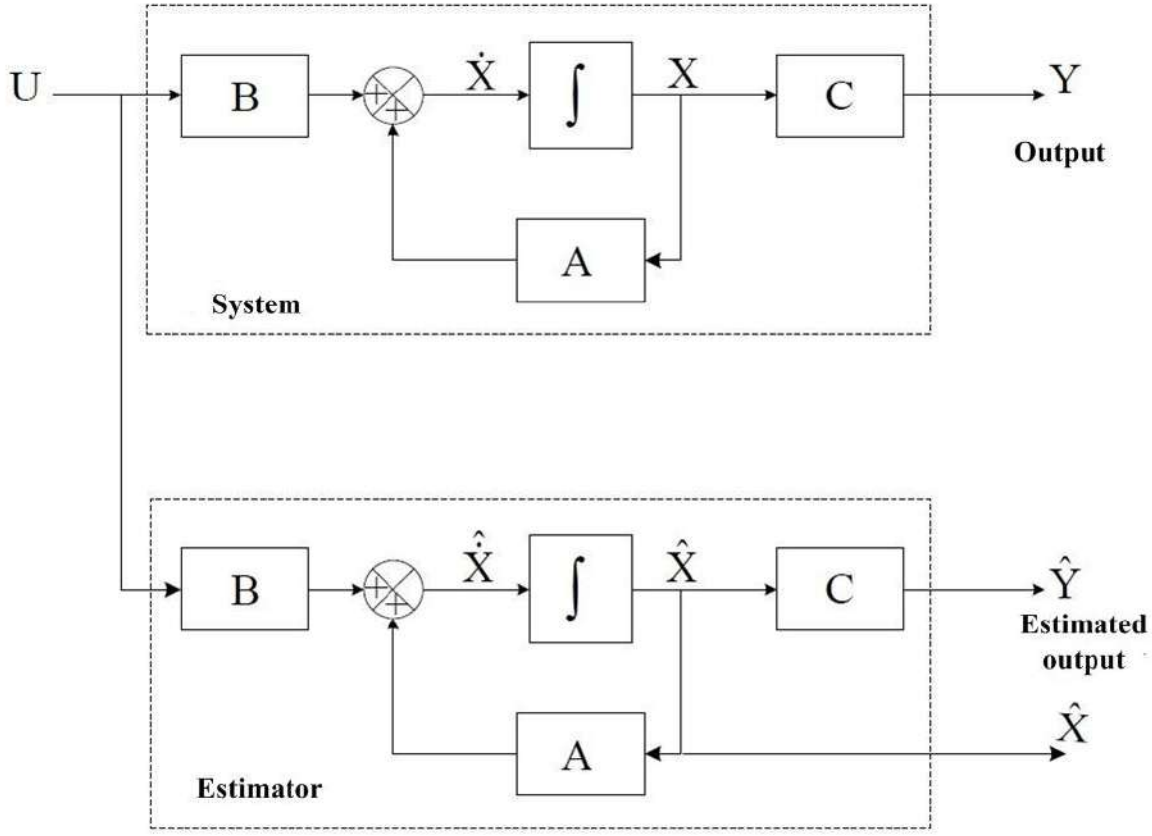

Figure 4.1: Basic structure of estimators.

4.2.2. Observers

The state observers are employed in a closed-loop configuration. This approach has an independent dynamic from the system, offering an estimation of a physical quantity from the measured or known information of the studied system with feedback on the error between the estimated and real output values. With the help of the gain matrices K, the dynamic of the

observer is adjusted so that the error converges to zero [94, 95]. Figure 4.2 represents the basic structure of a state observer.

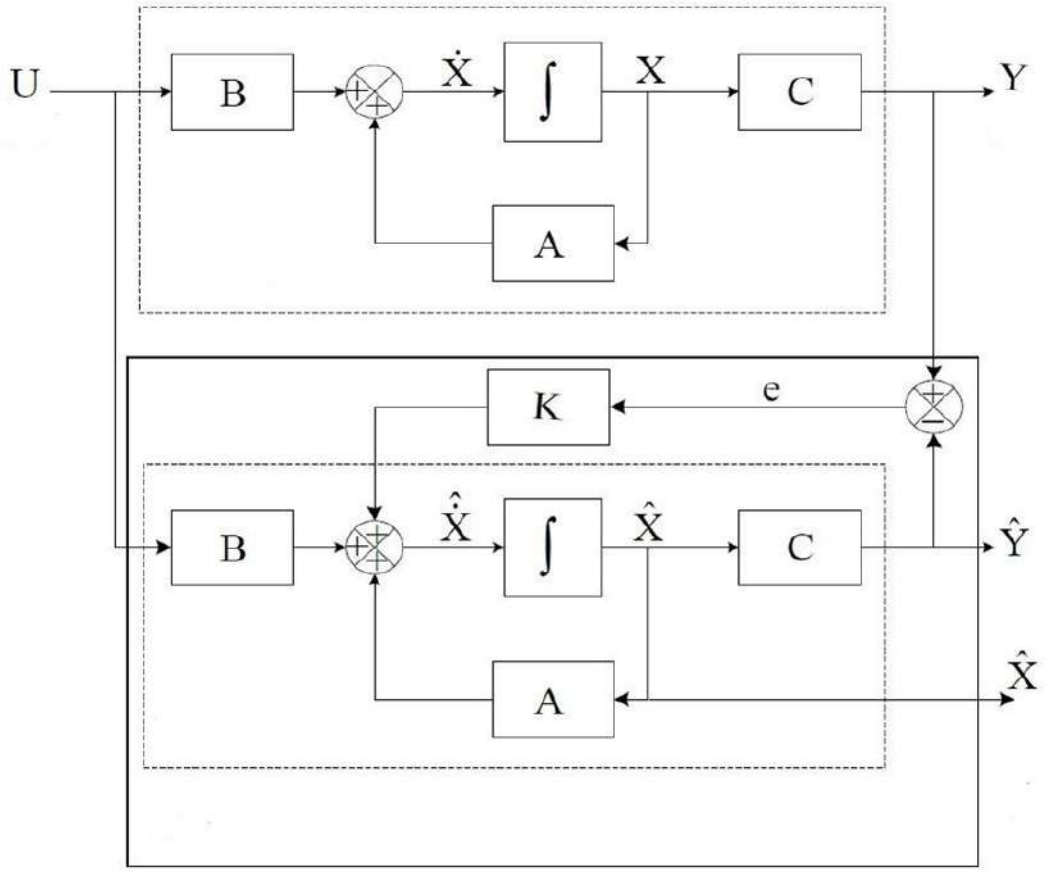

Figure 4.2: Basic structure of observer.

4.3. Sensorless DTC-ANN based on MRAS

4.3.1. Model Reference Adaptive System (MRAS)

The observer approach of the MRAS was originally proposed in [96], and Figure 4.3 represents the basic structure of the MRAS technique.

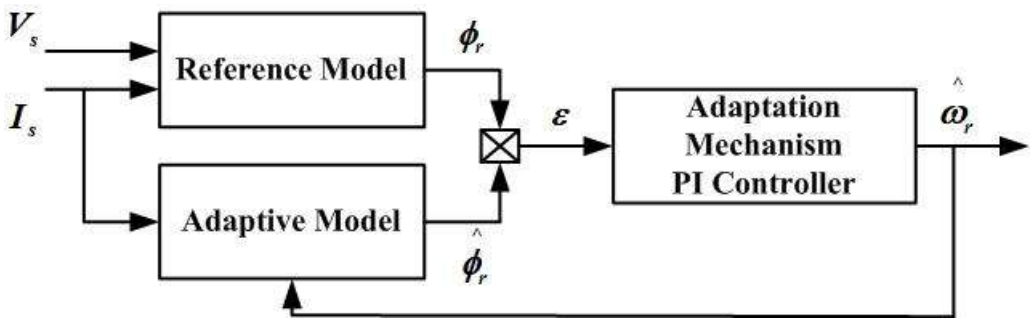

Figure 4.3: The structure of the MRAS observer.

The main objective of the MRAS technique is to accurately estimate the rotor speed and flux based on the available measured quantities, the supplied stator voltages, and currents.

4.3.1.1. Estimation of the rotor flux

The MRAS observer utilizes two models to estimate the rotor flux, which are as follows [97, 98]:

- **The reference model**

The stator voltage mathematical model of the FPIM is used in the reference model due to its independence of the estimated quantity and the rotor speed. The reference model expression is given as:

$$\frac{d}{dt}\begin{bmatrix}\phi_{rj\alpha j}\\ \phi_{rj\beta j}\end{bmatrix}=\frac{L_{rj}}{L_{mj}}\left(\begin{bmatrix}V_{sj\alpha j}\\ V_{sj\beta j}\end{bmatrix}-R_{sj}\begin{bmatrix}I_{sj\alpha j}\\ I_{sj\beta j}\end{bmatrix}-\sigma_j L_{sj}\begin{bmatrix}I_{sj\alpha j}\\ I_{sj\beta j}\end{bmatrix}\right) \tag{4.1}$$

- **The adaptive model**

The stator current mathematical model of the FPIM is used in the adaptive model, which utilizes the estimated quantity and the rotor speed to adjust the observer dynamics. The adaptive model mathematical expression is given as:

$$\frac{d}{dt}\begin{bmatrix}\hat{\phi}_{rj\alpha j}\\ \hat{\phi}_{rj\beta j}\end{bmatrix}=\frac{L_{mj}}{T_{rj}}\begin{bmatrix}I_{sj\alpha j}\\ I_{sj\beta j}\end{bmatrix}-\frac{1}{T_{rj}}\begin{bmatrix}\hat{\phi}_{rj\alpha j}\\ \hat{\phi}_{rj\beta j}\end{bmatrix}+\omega_r\begin{bmatrix}-\hat{\phi}_{rj\alpha j}\\ \hat{\phi}_{rj\beta j}\end{bmatrix} \tag{4.2}$$

4.3.1.2. The rotor's speed estimation

The rotor mechanical speed is computed from the error signals of the two models as follows:

$$\varepsilon_{estj}=\hat{\phi}_{rj}\otimes\phi_{rj}=\phi_{rj\beta j}\hat{\phi}_{rj\alpha j}-\phi_{rj\alpha j}\hat{\phi}_{rj\beta j} \tag{4.3}$$

Where: $\otimes$ is the cross product of the two vectors.

The error signal between the two models is obtained and inputted to the PI controller to adjust the dynamic of the MRAS observer. The rotor's mechanical speed expression is given as:

$$\hat{\omega}_{rj}=K_{pj}\varepsilon_{estj}+K_{ij}\int\varepsilon_{estj}dt \tag{4.4}$$

Figure 4.4 gives the block diagram of the MRAS observer.

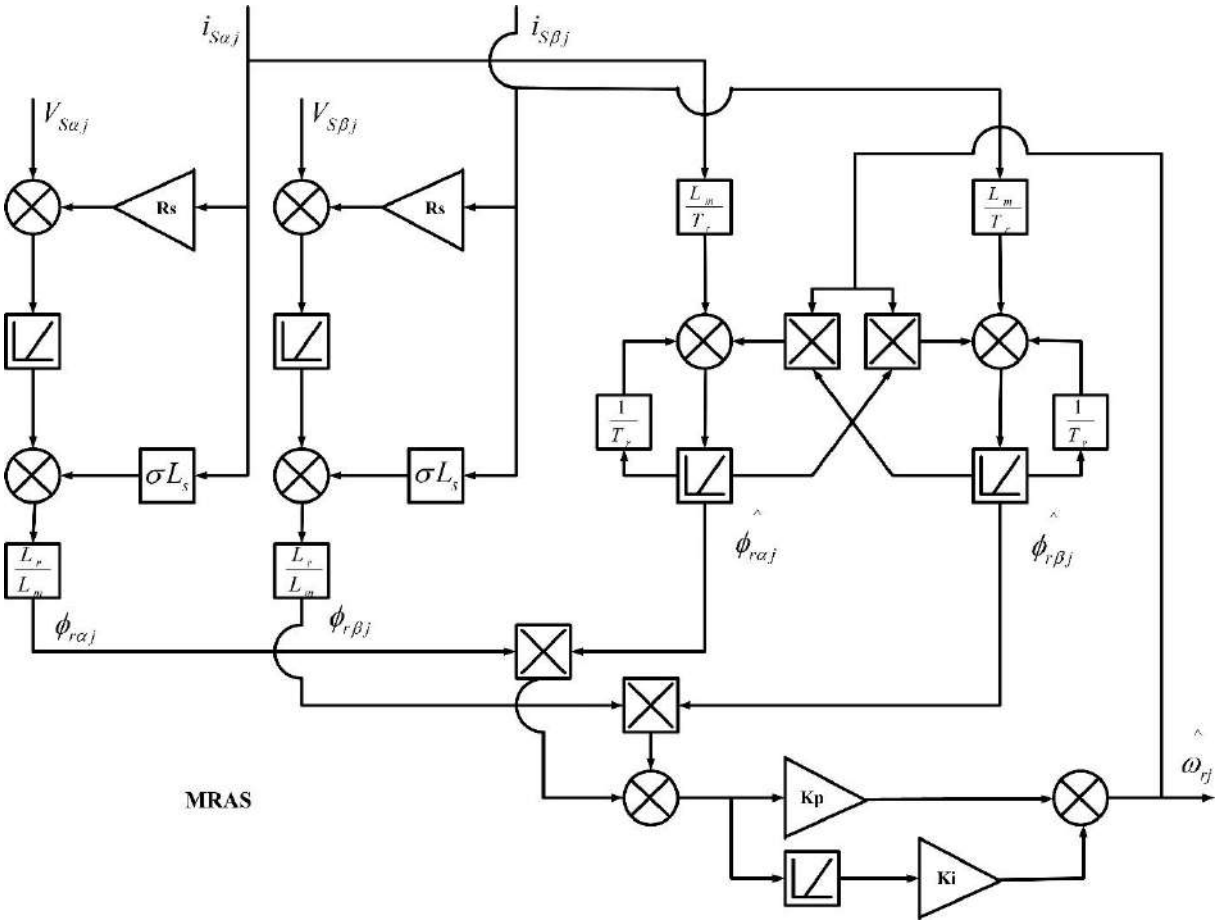

Figure 4.4: The schematic diagram of the MRAS observer.

4.3.1.3. Stator flux and electromagnetic torque estimation

The estimated flux and electromagnetic torque expression are given as:

$$\begin{cases} \hat{\phi}_{sj\alpha j} = \dfrac{L_{mj}}{L_{rj}}\hat{\phi}_{rj\alpha} + \dfrac{L_{sj}L_{rj} - L_{mj}^2}{L_{rj}} i_{sj\alpha j} \\ \hat{\phi}_{sj\beta j} = \dfrac{L_{mj}}{L_{rj}}\hat{\phi}_{rj\beta} + \dfrac{L_{sj}L_{rj} - L_{mj}^2}{L_{rj}} i_{sj\beta j} \\ \hat{\phi}_{sj} = \sqrt{\hat{\phi}_{sj\alpha j}^{\ 2} + \hat{\phi}_{sj\beta j}^{\ 2}} \\ \theta_{sj} = \tan^{-1}\left(\dfrac{\hat{\phi}_{sj\beta j}}{\hat{\phi}_{sj\alpha j}}\right) \\ \hat{T}_{emj} = \dfrac{5p_j}{2}(\hat{\phi}_{sj\alpha j} i_{sj\beta j} - \hat{\phi}_{sj\beta j} i_{sj\alpha j}) \end{cases} \tag{4.5}$$

4.3.2. Simulation results

This part will consider the simulation study of the MM sensorless approach to the DTC-ANN based on the MRAS of the two parallel-connected FPIMs. For study purposes, the 3L-DTC-ANN scheme is adopted. Figure 4.5 depicts the block diagram of the sensorless DTC-ANN of the two-machine drive.

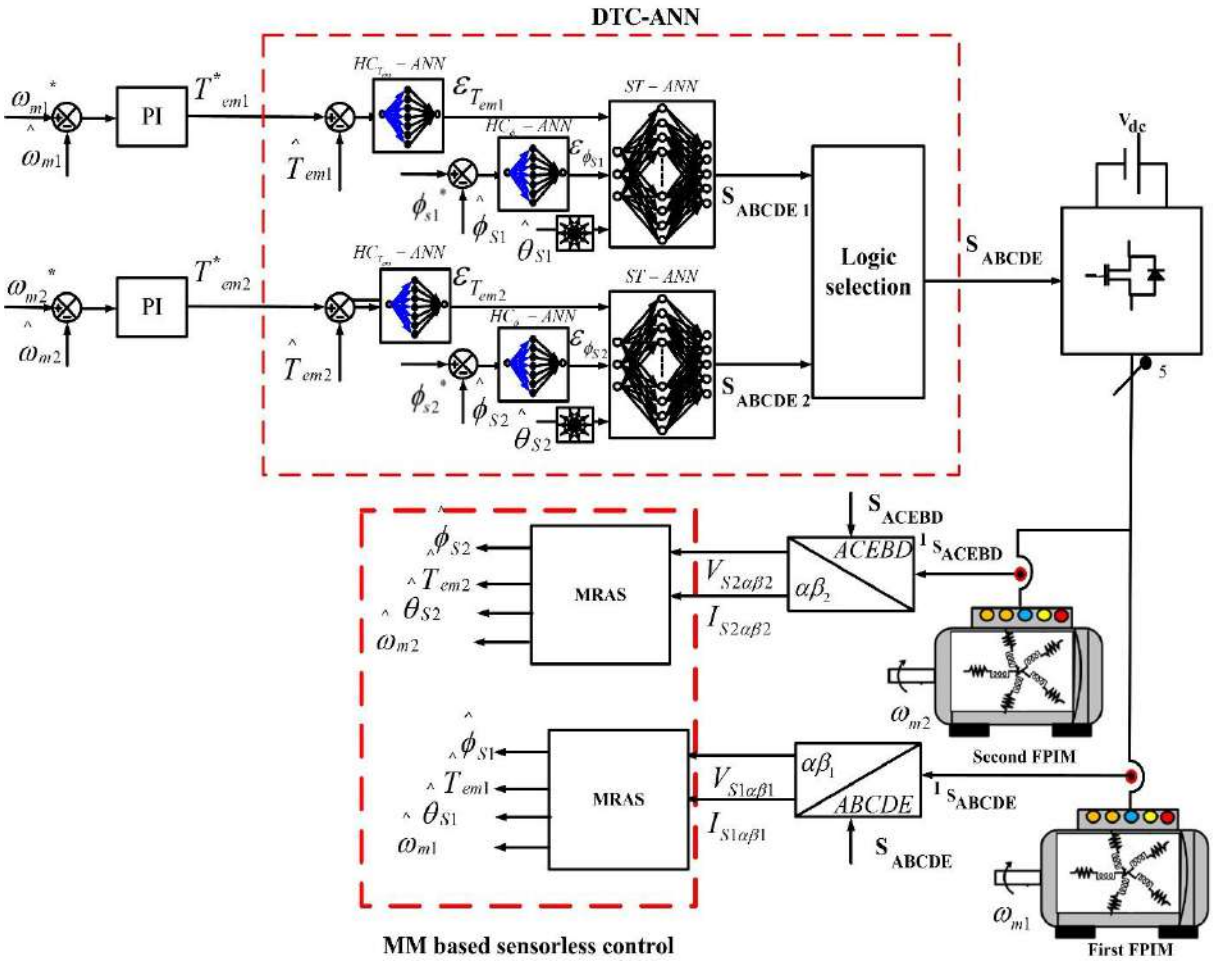

Figure 4.5: Sensorless DTC-ANN based on MRAS.

Two different test scenarios are created in the Matlab/Simulink environment to test and compare the performance of the sensorless method. The machine's parameters are the same as those in section 1.6, Table 1.9.

4.3.2.1. Test one

This test considers the application of different speed reference commands, reversion, and low-speed operation under constant loading conditions. Tables 4.1 and 4.2 summarize the first test scenario.

Table 4.1: First test scenario for the FPIM1.

Time [s]	$0 \rightarrow 0.1$	$0.1 \rightarrow 1$	$1 \rightarrow 1.3$	$1.3 \rightarrow 2$	$2 \rightarrow 2.2$	$2.2 \rightarrow 3$	$3 \rightarrow 4$	$4 \rightarrow 4.5$
$\omega_m[rad/s]$	$0 \rightarrow 20$	20	$20 \rightarrow 60$	60	$60 \rightarrow 100$	100	$100 \rightarrow -100$	-100
$T_L[Nm]$	8							

Table 4.2: First test scenario for the FPIM2.

Time [s]	$0 \rightarrow 0.5$	$0.5 \rightarrow 2$	$2 \rightarrow 2.6$	$2.6 \rightarrow 3.4$	$3.4 \rightarrow 3.7$	$3.7 \rightarrow 4.2$	$4.2 \rightarrow 4.4$	$4 \rightarrow 4.5$
$\omega_m[rad/s]$	$0 \rightarrow -100$	-100	$-100 \rightarrow 20$	20	$20 \rightarrow 60$	60	$60 \rightarrow 100$	100
$T_L[Nm]$	-8							

The following Figure illustrates the simulation results for the first test scenario.

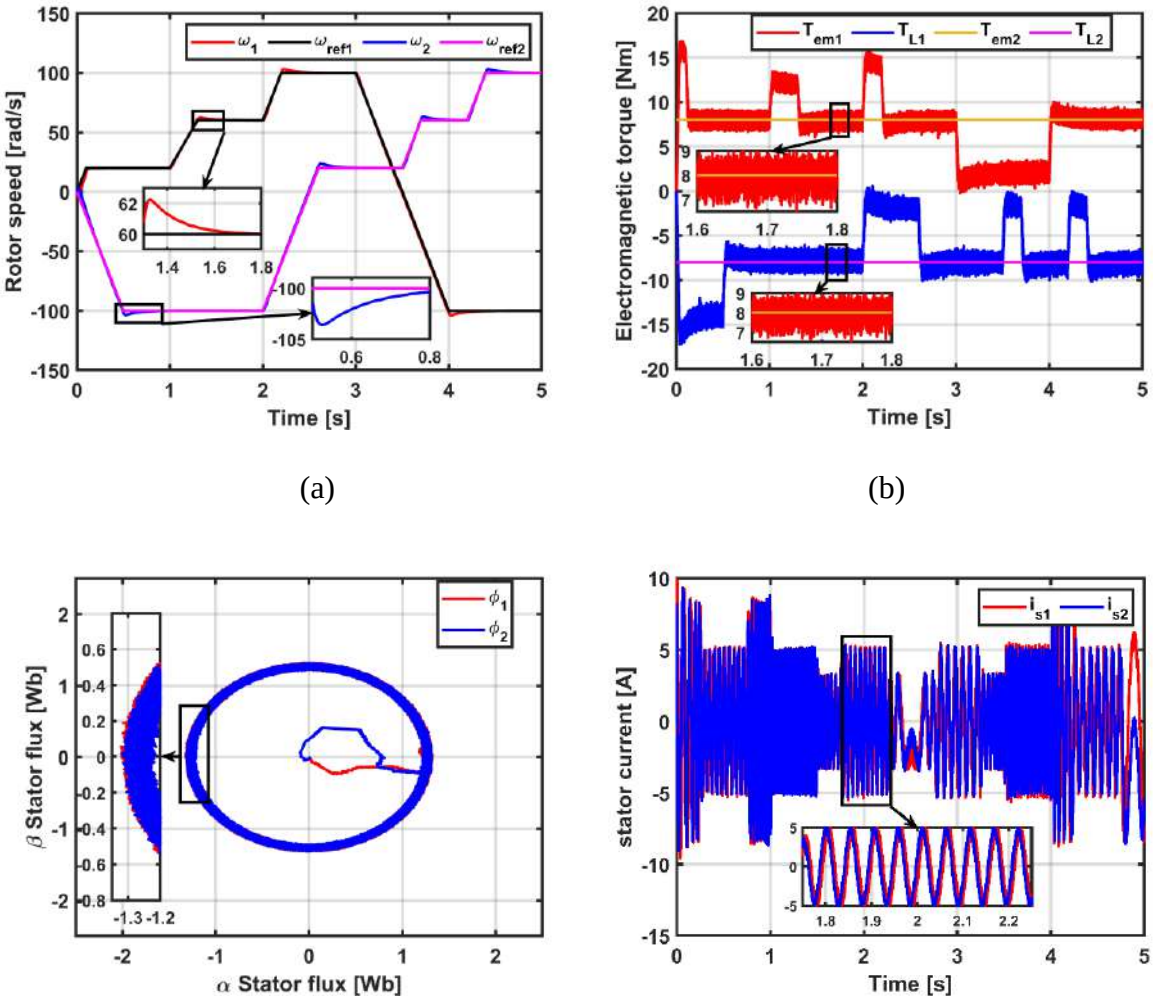

(a) (b)

(c) (d)

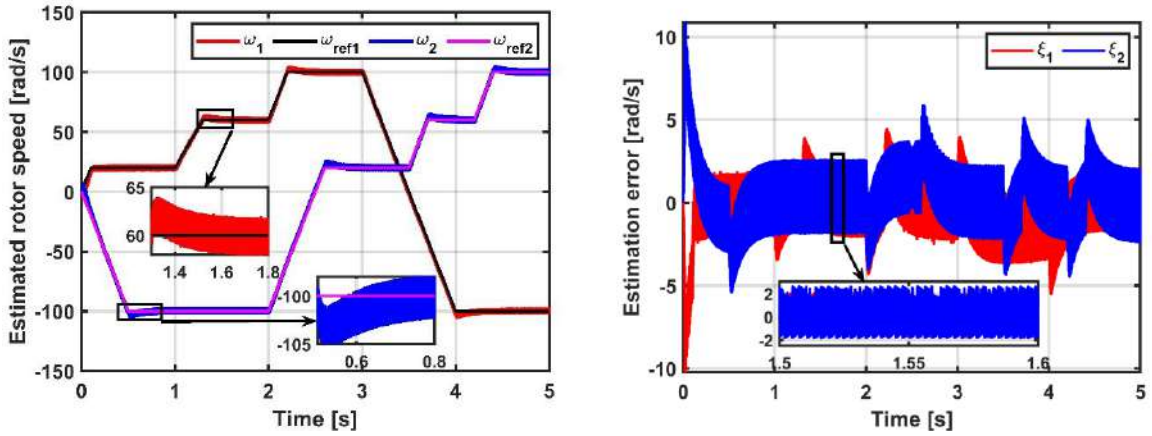

(e) (f)

Figure 4.6: Sensorless DTC-ANN based on MRAS: (a) mechanical rotor speed, (b) electromagnetic torque, (c) stator flux, (d) stator current, (e) estimated rotor speed, and (f) estimation error of rotor speed.

4.3.2.2. Test two

The second test scenario considers the application of different torque load profiles under a constant speed reference command. It is summarized in Table 4.3.

Table 4.3: Second test scenario for the two machines.

$Time[s]$	$\omega_m[rad/s]$	$T_{L1}[Nm]$	$T_{L2}[Nm]$
$0 \rightarrow 0.5$	$0 \rightarrow 100$	8	-2
$0.5 \rightarrow 1$	100		
$1 \rightarrow 2$		0	8
$2 \rightarrow 3$		-4	0

The following Figure illustrates the simulation results for the second test scenario.

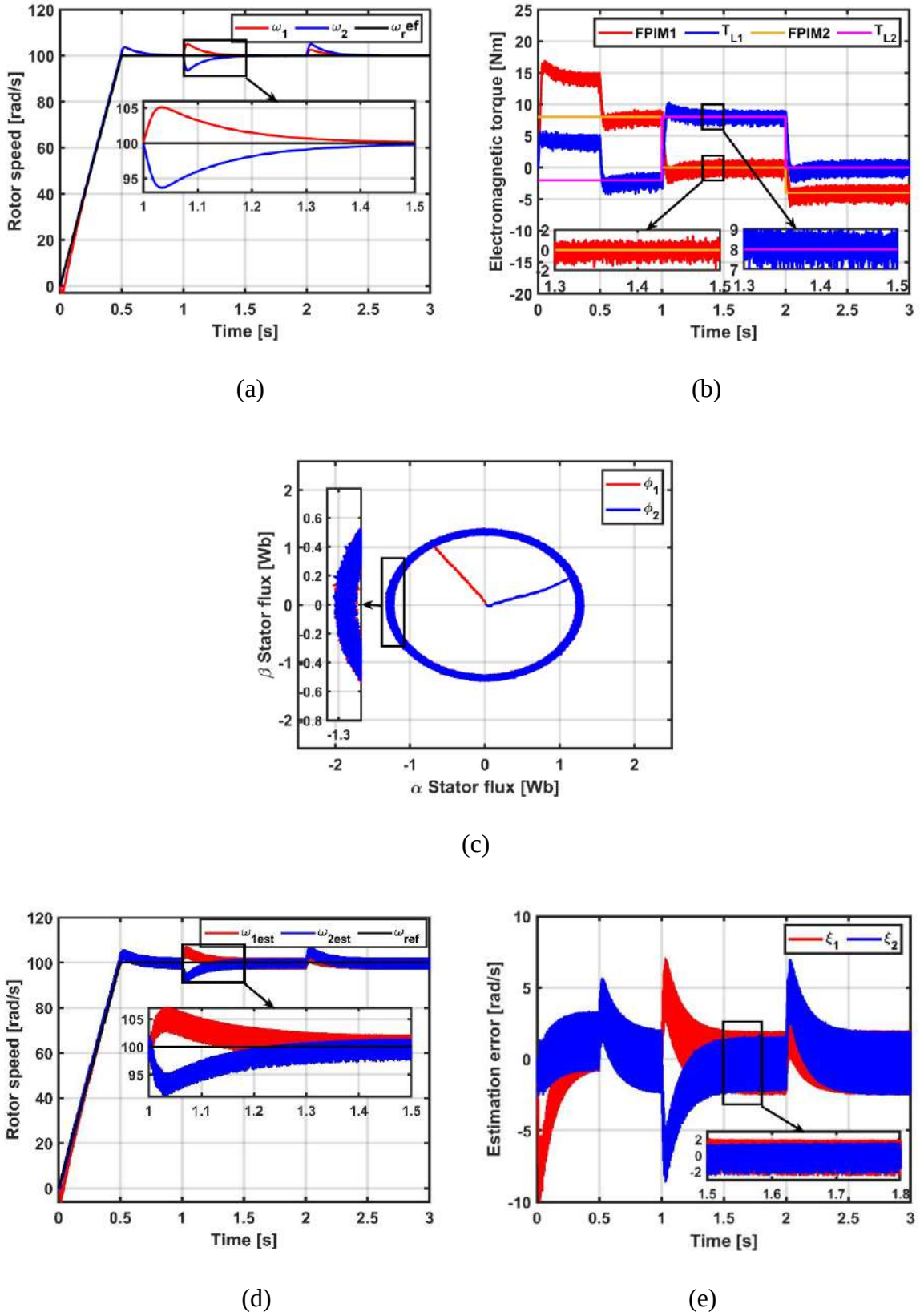

(a) (b)

(c)

(d) (e)

Figure 4.7: Sensorless DTC-ANN based on MRAS: (a) mechanical rotor speed, (b) electromagnetic torque, (c) stator flux, (d) estimated rotor speed, and (e) estimation error of rotor speed.

4.3.2.3. Results discussion

The simulative results of the MM sensorless DTC-ANN based on MRAS are presented and evaluated for different operating conditions.

First, the MRAS technique does not affect the independent control of the two-machine drive, ensuring complete decoupled control between the two machines and the stator flux/electromagnetic torque for each of them.

The rotor's mechanical speed response of the drive from Figures 4.6.a and 4.7.a. It can be noticed that both the transient and steady-state operation of the two-machine drive shows a high dynamic response to the speed reference command changes with negligible over/undershot due to the change in the loading condition or the reference command of ±4 rad/s.

The generated electromagnetic torque of both machines exhibits comparable performance to the 3L-DTC-ANN scheme for different loading and speed reference profiles, with a ripple rate of 50% (Figures 4.6.b and 4.7.b).

Figures 4.6.c and 4.7.c show the two FPIMs' stator flux, which depicts a fast response with a circular trajectory and accurate response to the reference command, with a ripple rate of 10%.

Moreover, Figure 4.6.d shows the stator current of phase "a" waveform for both machines and THD analysis. The stator current has a distorted sinusoidal waveform corresponding to the ripple content in the stator flux and electromagnetic torque responses. The current harmonic content for the sensorless DTC-ANN is 19.93%.

The estimated rotor's mechanical speed and the corresponding estimation error for the MRAS technique are illustrated in Figures 4.6.e, 4.6.f, 4.7.d and 4.7.e. The observer accurately estimates the rotor's mechanical speed with a negligible estimation error of ±4 rad/s during the transient and steady-state and regardless of the loading conditions.

4.4. Sensorless DTC-ANN based on SMO

4.4.1. Sliding Mode Observer (SMO)

The SMO is based on the theory of variable system structures. From the measured stator voltages/currents and the FPIM's current mathematical model, the SMO estimates the state variable of the FPIM [50], Figure 4.8 illustrates the basic diagram of the SMO.

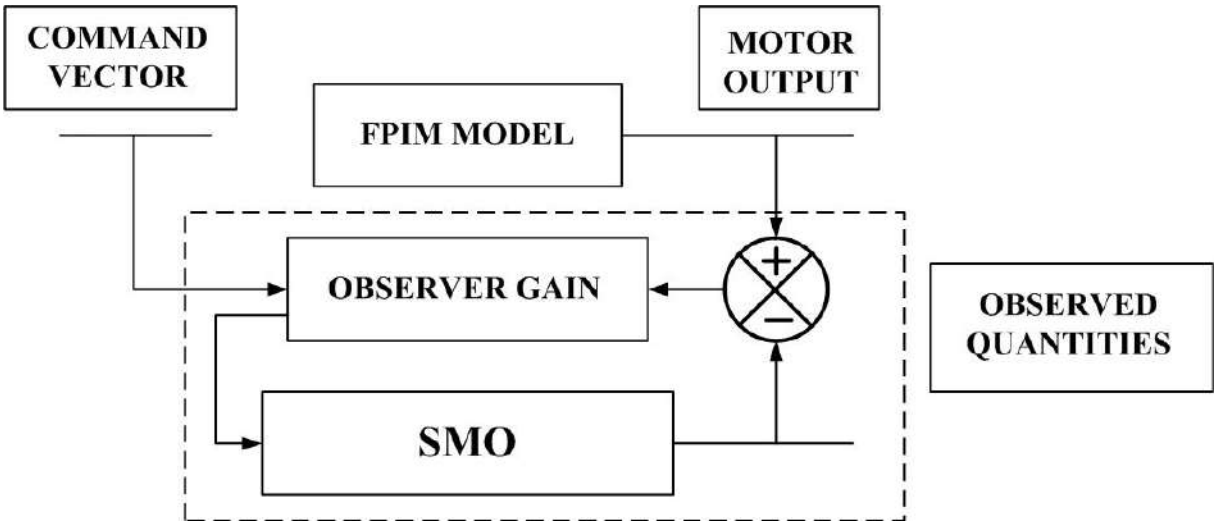

Figure 4.8: Basic structure of SMO.

The basic idea of the SMO is to compare the measured outputs of the system to the estimated ones and then define a sliding surface to control the observer's behavior. The sign of the difference between the two outputs on this surface is multiplied by the gain matrices to ensure a null estimation error. The advantages of this approach are:

- The rotor's speed and time constant are not used.
- High dynamic performance for a wide speed range of operation.
- Robustness to external perturbation.

4.4.1.1. Stator flux and electromagnetic torque estimation

The stator flux expression is derived from the FPIM's model in the stationary reference frame as follows [85]:

$$\begin{cases} \dfrac{d}{dt}\begin{bmatrix} i_{s\alpha j} \\ i_{s\beta j} \end{bmatrix} = \begin{bmatrix} -(\dfrac{R_s+R_r}{\sigma L_s}) & -\omega_r \\ \omega_r & -(\dfrac{R_s+R_r}{\sigma L_s}) \end{bmatrix}\begin{bmatrix} i_{s\alpha j} \\ i_{s\beta j} \end{bmatrix} + \begin{bmatrix} \dfrac{R_r}{\sigma L_s L_r} & \dfrac{\omega_r}{\sigma L_s} \\ -\dfrac{\omega_r}{\sigma L_s} & \dfrac{R_r}{\sigma L_s L_r} \end{bmatrix}\begin{bmatrix} \varphi_{s\alpha j} \\ \varphi_{s\beta j} \end{bmatrix} + \begin{bmatrix} \dfrac{1}{\sigma L_s} & 0 \\ 0 & \dfrac{1}{\sigma L_s} \end{bmatrix}\begin{bmatrix} V_{s\alpha j} \\ V_{s\beta j} \end{bmatrix} \\ \dfrac{d}{dt}\begin{bmatrix} \varphi_{s\alpha j} \\ \varphi_{s\beta j} \end{bmatrix} = \begin{bmatrix} -R_s & 0 \\ 0 & -R_s \end{bmatrix}\begin{bmatrix} i_{s\alpha j} \\ i_{s\beta j} \end{bmatrix} + \begin{bmatrix} 1 & 0 \\ 0 & 1 \end{bmatrix}\begin{bmatrix} V_{s\alpha j} \\ V_{s\beta j} \end{bmatrix} \end{cases} \quad (4.6)$$

Since the stator flux is not measured, in addition to the rotor speed in this work, the observer can be expressed as follows:

$$\begin{cases} \dfrac{d}{dt}\begin{bmatrix} \hat{i}_{s\alpha j} \\ \hat{i}_{s\beta j} \end{bmatrix} = \begin{bmatrix} -(\dfrac{R_s+R_r}{\sigma L_s}) & -\omega_r \\ \omega_r & -(\dfrac{R_s+R_r}{\sigma L_s}) \end{bmatrix}\begin{bmatrix} \hat{i}_{s\alpha j} \\ \hat{i}_{s\beta j} \end{bmatrix} + \begin{bmatrix} \dfrac{R_r}{\sigma L_s L_r} & \dfrac{\omega_r}{\sigma L_s} \\ -\dfrac{\omega_r}{\sigma L_s} & \dfrac{R_r}{\sigma L_s L_r} \end{bmatrix}\begin{bmatrix} \hat{\varphi}_{s\alpha j} \\ \hat{\varphi}_{s\beta j} \end{bmatrix} + \begin{bmatrix} \dfrac{1}{\sigma L_s} & 0 \\ 0 & \dfrac{1}{\sigma L_s} \end{bmatrix}\begin{bmatrix} V_{s\alpha j} \\ V_{s\beta j} \end{bmatrix} + \begin{bmatrix} A_{i1} & A_{i2} \\ A_{i3} & A_{i4} \end{bmatrix}\begin{bmatrix} I_{s1} \\ I_{s2} \end{bmatrix} \\ \dfrac{d}{dt}\begin{bmatrix} \hat{\varphi}_{s\alpha j} \\ \hat{\varphi}_{s\beta j} \end{bmatrix} = \begin{bmatrix} -R_s & 0 \\ 0 & -R_s \end{bmatrix}\begin{bmatrix} \hat{i}_{s\alpha j} \\ \hat{i}_{s\beta j} \end{bmatrix} + \begin{bmatrix} 1 & 0 \\ 0 & 1 \end{bmatrix}\begin{bmatrix} V_{s\alpha j} \\ V_{s\beta j} \end{bmatrix} + \begin{bmatrix} A_{\varphi 1} & A_{\varphi 2} \\ A_{\varphi 3} & A_{\varphi 4} \end{bmatrix}\begin{bmatrix} I_{s1} \\ I_{s2} \end{bmatrix} \end{cases}$$

(4.7)

Where: $\hat{i}_{s\alpha}$, $\hat{i}_{s\beta}$, $\hat{\phi}_{s\alpha}$, and $\hat{\phi}_{s\beta}$ are the estimated stator currents and flux components, respectively.

In addition to:

$$I_s = \begin{bmatrix} I_{s1} \\ I_{s2} \end{bmatrix} = \begin{bmatrix} sign(S1) \\ sign(S2) \end{bmatrix} \tag{4.8}$$

A_{ij} and $A_{\phi j}$ represents the SMO's gains.

S1 And S2 are the sliding surfaces.

I_s is the sign vector of the chosen sliding vector, defined by:

εi the current's observation error.

$\varepsilon\phi$ the flux observation error.

$$\varepsilon i = \begin{bmatrix} \varepsilon i_\alpha \\ \varepsilon i_\beta \end{bmatrix} = \begin{bmatrix} i_{s\alpha} - \hat{i}_{s\alpha} \\ i_{s\beta} - \hat{i}_{s\beta} \end{bmatrix}; \varepsilon\phi = \begin{bmatrix} \varepsilon\phi_\alpha \\ \varepsilon\phi_\beta \end{bmatrix} = \begin{bmatrix} \phi_{s\alpha} - \hat{\phi}_{s\alpha} \\ \phi_{s\beta} - \hat{\phi}_{s\beta} \end{bmatrix} \tag{4.9}$$

On the basis of equations (4.6), (4.7), (4.9), the equation controlling the observation errors is expressed as follows:

$$\begin{cases} d\varepsilon i_\alpha / dt = -\left(R_s / \sigma L_s + R_r / \sigma L_r\right)\varepsilon i_\alpha - \omega_r \varepsilon i_\beta + R_r / \sigma L_r L_s \, \varepsilon\phi_\alpha + \omega_r / \sigma L_s \, \varepsilon\phi_\beta - (A_{i1} * sign(S1) + A_{i2} * sign(S2)) \\ d\varepsilon i_\beta / dt = -\left(R_s / \sigma L_s + R_r / \sigma L_r\right)\varepsilon i_\beta + \omega_r \varepsilon i_\alpha + R_r / \sigma L_r L_s \, \varepsilon\phi_\beta - \omega_r / \sigma L_s \, \varepsilon\phi_\alpha - (A_{i3} * sign(S1) + A_{i4} * sign(S2)) \\ d\varepsilon\phi_\alpha / dt = -R_s \varepsilon i_\alpha - (A_{\phi 1} * sign(S1) + A_{\phi 2} * sign(S2)) \\ d\varepsilon\phi_\beta / dt = -R_s \varepsilon i_\beta - (A_{\phi 3} * sign(S1) + A_{\phi 4} * sign(S2)) \end{cases}$$

(4.10)

Considering the determination of the stator currents' gain matrix, the sliding surface is linked to the stator currents' errors as follows:

$$S = \begin{bmatrix} S1 \\ S2 \end{bmatrix} = D^{-1} \begin{bmatrix} i_{s\alpha} - \hat{i}_{s\alpha} \\ i_{s\beta}\, \hat{i}_{s\beta} \end{bmatrix} \tag{4.11}$$

Where:

$$D = \begin{bmatrix} \dfrac{R_r}{\sigma L_s L_r} & \dfrac{\omega_r}{\sigma L_s} \\ -\dfrac{\omega_r}{\sigma L_s} & \dfrac{R_r}{\sigma L_s L_r} \end{bmatrix} \tag{4.12}$$

When the stator currents' errors are null ($i_{s\alpha} = \hat{i}_{s\alpha}$ and $i_{s\beta} = \hat{i}_{s\beta}$) then S=0.

The matrix S allows to determine the dynamic performance of the observer since it depends on the mechanical and electrical parameters of the FPIM. The precise measurement of stator currents and estimation of the rotor's mechanical speed ensures the consideration of a null observation error. The stator currents' gain matrix is given as [99]:

$$A_i = \begin{bmatrix} A_{i1} & A_{i2} \\ A_{i3} & A_{i4} \end{bmatrix} = D \begin{bmatrix} \delta_1 & 0 \\ 0 & \delta_2 \end{bmatrix} \tag{4.13}$$

With δ_1 and δ_2 are constants determined based on the stability analysis conditions of Lyapunov to assure the convergence of the sliding surface.

On the other hand, the determination of the stator flux gain matrix is based on the convergence of the sliding surface (S=0). From Equation (4.10), by neglecting the S and $\dot{S}$ terms, which is translated by the annulment of the stator currents' error and its derivative ($\varepsilon i_\alpha = \varepsilon i_\beta = \varepsilon \dot{i}_\alpha = \varepsilon \dot{i}_\beta = 0$), as follows:

$$\begin{cases} R_r / \sigma L_r L_s \; \varepsilon\phi_\alpha + \omega_r / \sigma L_s \; \varepsilon\phi_\beta = (A_{i1} * sign(S1) + A_{i2} * sign(S2)) \\ R_r / \sigma L_r L_s \; \varepsilon\phi_\beta - \omega_r / \sigma L_s \; \varepsilon\phi_\alpha = (A_{i3} * sign(S1) + A_{i4} * sign(S2)) \end{cases} \tag{4.14}$$

By the use of Equation (4.12), the sign vector is given as:

$$I_s = \begin{bmatrix} I_{s1} \\ I_{s2} \end{bmatrix} = \begin{bmatrix} sign(S1) \\ sign(S2) \end{bmatrix} = \begin{bmatrix} A_{i1} & A_{i2} \\ A_{i3} & A_{i4} \end{bmatrix}^{-1} D \begin{bmatrix} \varepsilon\phi_\alpha \\ \varepsilon\phi_\beta \end{bmatrix} \tag{4.15}$$

By substituting Equation (4.13) in (4.9) of the stator flux errors, it results in:

$$d\varepsilon\phi/dt = \left[-\begin{bmatrix} A_{\phi1} & A_{\phi2} \\ A_{\phi3} & A_{\phi4} \end{bmatrix} \begin{bmatrix} A_{i1} & A_{i2} \\ A_{i3} & A_{i4} \end{bmatrix}^{-1} D \right] \tag{4.16}$$

Since the dynamic response of the SMO is based on the exponential convergence of the stator flux error, then the stator flux error can be imposed as:

$$d\varepsilon\phi/dt = -Q\varepsilon\phi \tag{4.17}$$

With:

$$Q = \begin{bmatrix} q_1 & 0 \\ 0 & q_2 \end{bmatrix} \tag{4.18}$$

Where: q_1 and q_2 are positive constants.

By substitution of Equation (4.17) in (4.16), the stator flux gain matrix is expressed as follows:

$$A_\phi = \begin{bmatrix} A_{\phi1} & A_{\phi2} \\ A_{\phi3} & A_{\phi4} \end{bmatrix} = \begin{bmatrix} q_1\delta_1 & 0 \\ 0 & q_2\delta_2 \end{bmatrix} \tag{4.19}$$

The observer's dynamic response must be as quick as the system's response; thus, the constants δ_1, δ_2, q_1, and q_2 must be adequately chosen.

The SMO's stability depends on its convergence towards its sliding surface by the optimum selection of the δ_1 and δ_2. Thus, the SMO's stability is verified as follows [100]:

First, the Lyapunov function is given as:

$$V = \frac{1}{2} S^T S \tag{4.20}$$

Therefore, to ensure the convergence towards the sliding surface, the derivative of V must be negative:

$$\dot{V} = \frac{1}{2} S^T \dot{S} < 0 \tag{4.21}$$

Then:

$$\begin{cases} \dot{V} = [S1 \quad S2]^T D^{-1} d\varepsilon i / dt \\ \dot{V} = [S1 \quad S2]^T \left(\begin{bmatrix} R_r / \sigma L_r L_s & -\omega_r / \sigma L_s \\ \omega_r / \sigma L_s & R_r / \sigma L_r L_s \end{bmatrix} \begin{bmatrix} \varepsilon\phi_\alpha \\ \varepsilon\phi_\beta \end{bmatrix} - \begin{bmatrix} A_{i1} & A_{i2} \\ A_{i3} & A_{i4} \end{bmatrix} \begin{bmatrix} sign(S1) \\ sign(S2) \end{bmatrix} \right) \\ \dot{V} = [S1 \quad S2]^T \left(\begin{bmatrix} \varepsilon\phi_\alpha \\ \varepsilon\phi_\beta \end{bmatrix} - \begin{bmatrix} \delta_1 & 0 \\ 0 & \delta_2 \end{bmatrix} \begin{bmatrix} sign(S1) \\ sign(S2) \end{bmatrix} \right) \end{cases} \tag{4.22}$$

Thus, the SMO's stability is ensured if and only if the inequality is verified:

$$\begin{cases} \delta_1 \geq \left| \varepsilon_{\phi\alpha} \right| \\ \delta_2 \geq \left| \varepsilon_{\phi\beta} \right| \end{cases} \tag{4.23}$$

The stator flux vector and position, in addition to the electromagnetic torque, can be calculated as follows:

$$\begin{cases} \hat{\phi}_{sj} = \sqrt{\hat{\phi}_{s\alpha j}^{\ 2} + \hat{\phi}_{s\beta j}^{\ 2}} \\ \hat{\phi}_{sj} = \sqrt{\hat{\phi}_{s\alpha j}^{\ 2} + \hat{\phi}_{s\beta j}^{\ 2}} \\ \hat{\theta}_{sj} = \tan^{-1}\left(\hat{\phi}_{s\beta j} / \hat{\phi}_{s\alpha j} \right) \\ \hat{T}_{emj} = \dfrac{5 p_j}{2} (\hat{\phi}_{s\alpha j} i_{s\beta j} - \hat{\phi}_{s\beta j} i_{s\alpha j}) \end{cases} \tag{4.24}$$

Figure 4.9 gives the block diagram of the SMO.

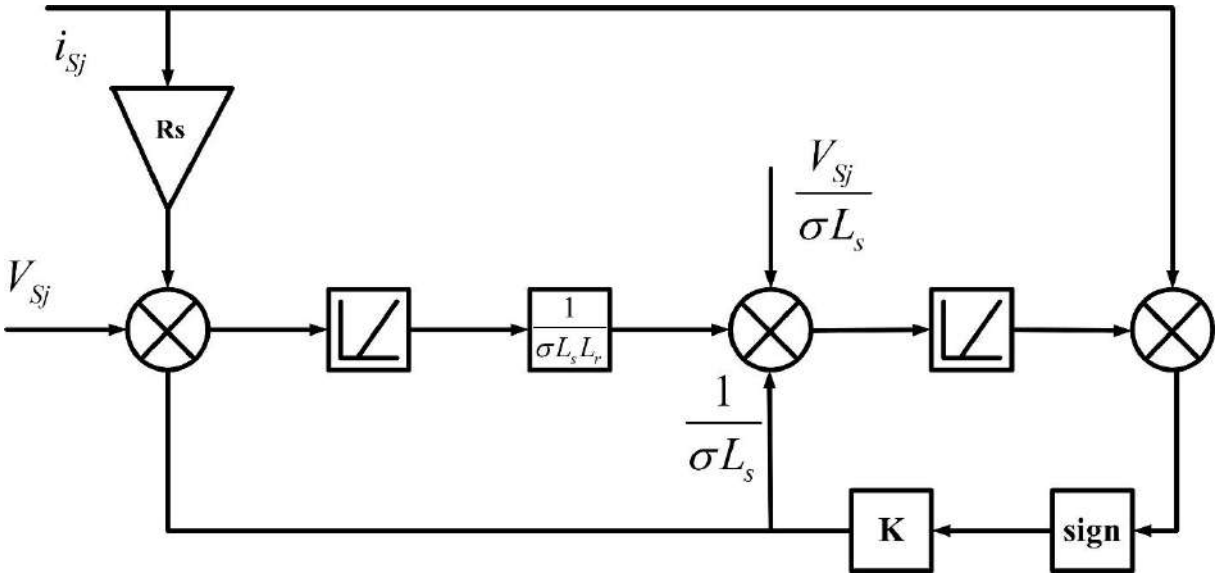

Figure 4.9: Schematic diagram of SMO.

4.4.1.2. The rotor's mechanical speed estimation

From the estimated stator flux components and measured stator currents and load torque, the rotor's mechanical speed can be estimated as follows:

$$\frac{d\,\hat{\omega}_{mj\,j}}{dt} = 1/J_j(p_j(\hat{\phi}_{s\alpha j}\, i_{s\beta j} - \hat{\phi}_{s\beta j}\, i_{s\alpha j}) - T_{Lj} - f_j\,\hat{\omega}_{mj}) \tag{4.25}$$

4.4.2. Simulation results

The MM sensorless DTC-ANN based on the SMO of the two-parallel-connected FPIMs performance is evaluated in this part. For the study purposes, the 3L-DTC-ANN scheme is adopted, Figure 4.10 depicts the block diagram of the sensorless DTC-ANN of the two-machine drive.

In order to test and compare the performance of the sensorless method two different test scenarios are made in Matlab/Simulink environment. The machine's parameters are the same as in section 1.6 Table 1.9.

4.4.2.1. Test one

This test considers the application of different speed reference commands, reversion and low-speed operation, under constants loading conditions. The first test scenario is summarized in Tables 4.4 and 4.5.

Table 4.4: First test scenario for the FPIM1.

Time [s]	$0 \rightarrow 0.1$	$0.1 \rightarrow 1$	$1 \rightarrow 1.3$	$1.3 \rightarrow 2$	$2 \rightarrow 2.2$	$2.2 \rightarrow 3$	$3 \rightarrow 4$	$4 \rightarrow 4.5$
$\omega_m[rad/s]$	$0 \rightarrow 20$	20	$20 \rightarrow 60$	60	$60 \rightarrow 100$	100	$100 \rightarrow -100$	-100
$T_L[Nm]$	8							

Table 4.5: Second test scenario for the FPIM2.

Time [s]	$0 \rightarrow 0.5$	$0.5 \rightarrow 2$	$2 \rightarrow 2.6$	$2.6 \rightarrow 3.4$	$3.4 \rightarrow 3.7$	$3.7 \rightarrow 4.2$	$4.2 \rightarrow 4.4$	$4 \rightarrow 4.5$
$\omega_m[rad/s]$	$0 \rightarrow -100$	-100	$-100 \rightarrow 20$	20	$20 \rightarrow 60$	60	$60 \rightarrow 100$	100
$T_L[Nm]$	-8							

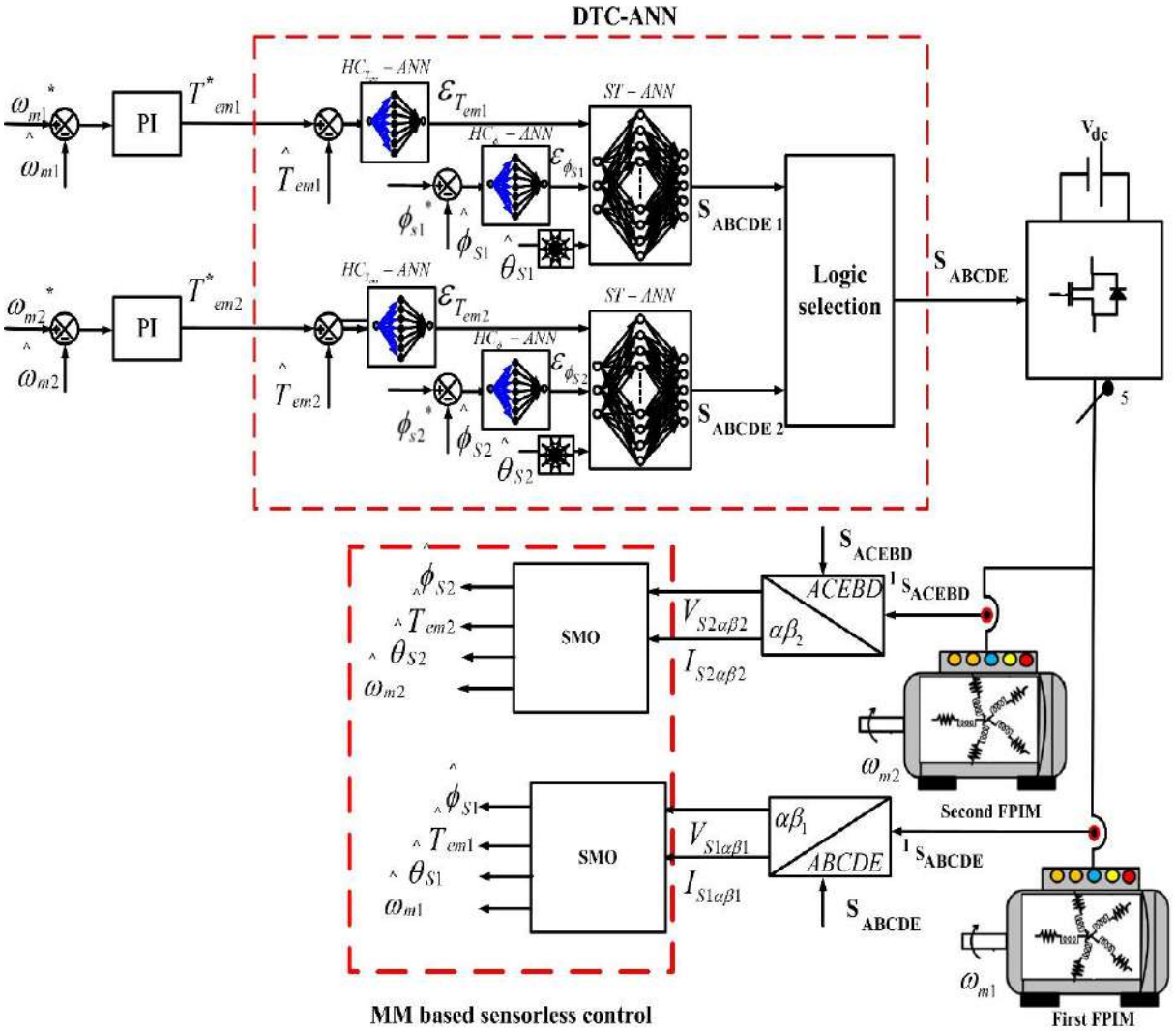

Figure 4.10: Sensorless DTC-ANN based on SMO.

The simulation results for the first test scenario are illustrated in Figure 4.11.

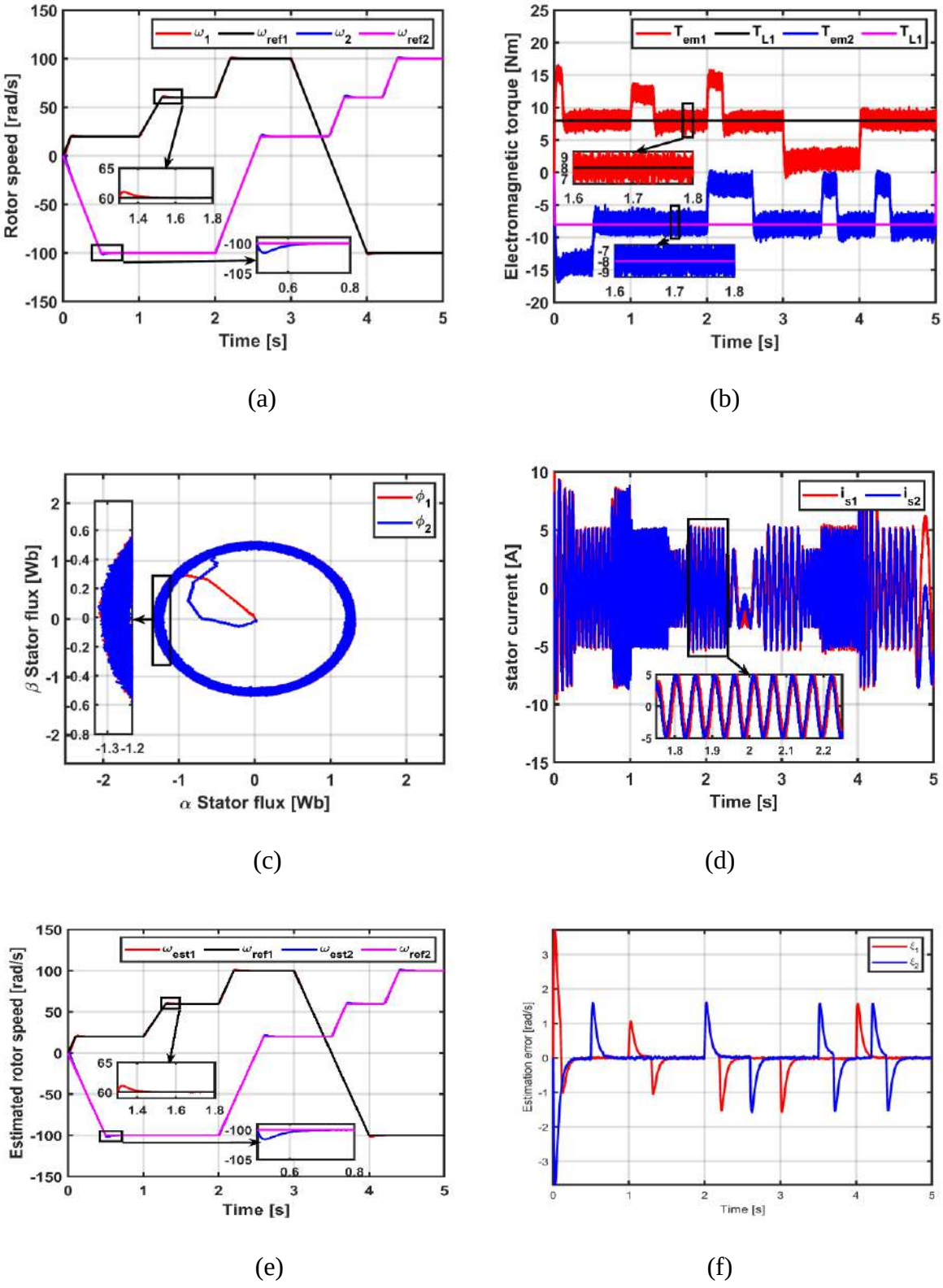

(a) (b)

(c) (d)

(e) (f)

Figure 4.11: Sensorless DTC-ANN based on SMO: (a) mechanical rotor speed, (b) electromagnetic torque, (c) stator flux, (d) stator current, (e) estimated rotor speed, and (f) estimation error of rotor speed.

4.4.2.2. Test two

The second test scenario considers the application of different torque load profiles under a constant speed reference command. It is summarized in Table 4.6.

Table 4.6: Second test scenario for the two machines.

$Time[s]$	$\omega_m[rad/s]$	$T_{L1}[Nm]$	$T_{L2}[Nm]$
$0 \rightarrow 0.5$	$0 \rightarrow 100$	8	-2
$0.5 \rightarrow 1$	100		
$1 \rightarrow 2$		0	8
$2 \rightarrow 3$		-4	0

The simulation results for the second test scenario are illustrated in Figure 4.12.

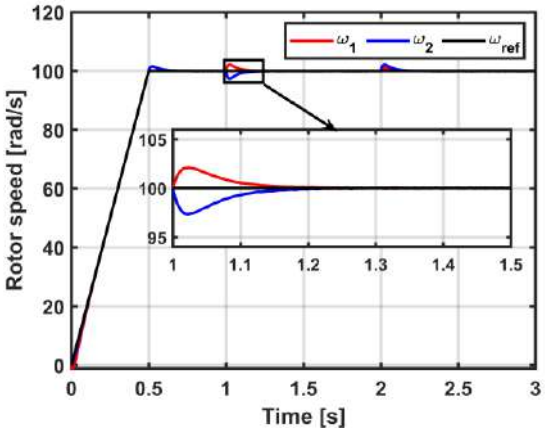

(a)

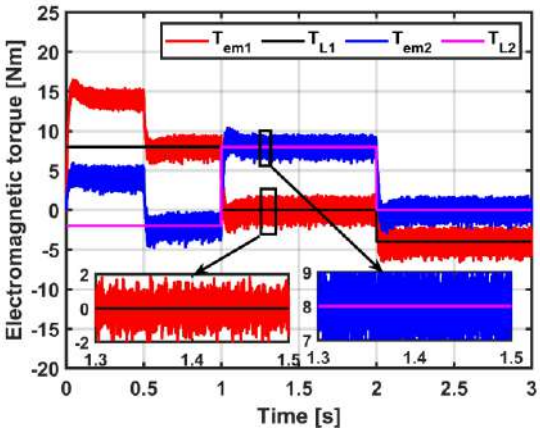

(b)

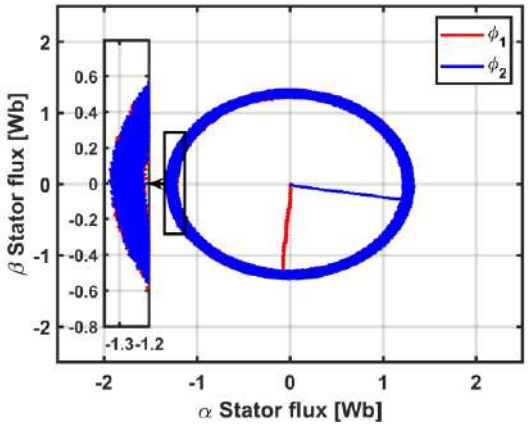

(c)

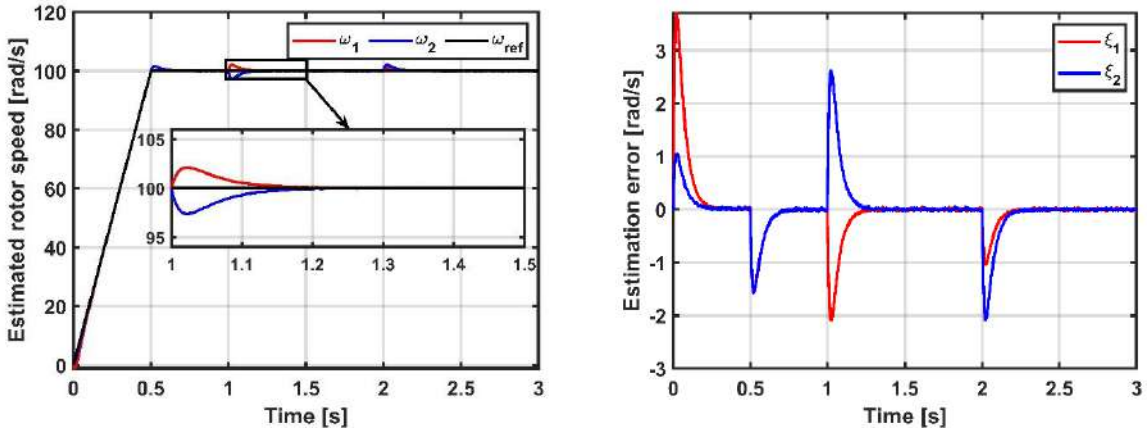

(d) (e)

Figure 4.12: Sensorless DTC-ANN based on SMO: (a) mechanical rotor speed, (b) electromagnetic torque, (c) stator flux, (d) estimated rotor speed, and (e) estimation error of rotor speed.

4.4.2.3. Results discussion

The simulation results for the MM sensorless DTC-ANN are presented based on SMO for a different operating scenario.

First, the independent control of the two-machine drive is ensured with a complete decoupled control between the two FPIMs and for the stator flux/electromagnetic torque for each machine; thus, the SMO technique does not affect the drive's performance.

The rotor's mechanical speed response of the drive, in Figures 4.11.a and 4.12.a, shows that during both the transient and steady state operation of the drive, the machines show a high dynamic response to the changes in the speed reference command with negligible over/undershot due to the loading condition or the reference command of ± 3 rad/s.

The generated electromagnetic torque of the two FPIMs exhibits comparable performance to the 3L-DTC-ANN scheme with a ripple content of 44% for different loading and speed reference scenarios, as shown in Figures 4.11.b and 4.12.b.

The two FPIMs' stator flux, shown in Figures 4.11.c and 4.12.c, depicts a fast response with a circular trajectory following the reference command accurately, with a ripple rate of 5%.

Moreover, Figure 4.11.d shows the stator current of phase "a" waveform of two FPIMs and THD analysis. It is illustrated that the stator current has a distorted sinusoidal waveform

corresponding to the ripple content in the stator flux and electromagnetic torque responses. The current harmonic content for the sensorless DTC-ANN is 20%.

Figures 4.11.e, 4.11.f, 4.12.d, and 4.12.e show the estimated rotor's mechanical speed and the corresponding estimation error for the SMO. The observer accurately estimates the rotor's mechanical speed with a negligible estimation error during the transient and steady-state, regardless of loading conditions, of ±4 rad/s.

4.5. Sensorless DTC-ANN based on stator currents reconstruction

4.5.1. Introduction

Current sensor (CS) failure, such as LEM-type transducers, in modern ASD, especially in hazardous conditions, constitutes a major and one of the most frequent problems for the control algorithm [101 - 103]. This is because an accurate measurement of the stator currents for estimating state variables, such as the stator flux and electromagnetic torque for the DTC scheme, is required to achieve the optimum performance. Several current fault-tolerant control (FTC) sensors can be found in the literature and grouped as hardware and software solutions. Due to the additional implemented equipment, such as redundant CS or shunt resistors, the hardware solution is associated with high cost, size, and complexity [103]. Conversely, software solutions are the most attractive methods for stator current reconstruction based on the Virtual Current Sensor.

4.5.2. Virtual Current Sensor (VCS)

Real-time accurate stator currents' measurement is essential information for ASD performance. The stator five-phase currents are reconstructed in the postfault operation of the two-machine drive based on the VCS algorithm from the VSI switching states and the DC-link voltage [103]. The discussed approach is based on three sets of equations of the fundamental and harmonic components of the stator currents and the rotor flux components from the FPIM's model in the stationary reference frame as follows:

The estimated rotor flux expression:

$$\begin{cases} \dfrac{d}{dt}\hat{\phi}_{rj\alpha} = \dfrac{R_{rj}}{L_{rj}}(L_{mj}\,\hat{i}_{sj\alpha} - \hat{\phi}_{rj\alpha}) - \omega_{mj}\,\hat{\phi}_{rj\beta} \\ \dfrac{d}{dt}\hat{\phi}_{rj\beta} = \dfrac{R_{rj}}{L_{rj}}(L_{mj}\,\hat{i}_{sj\beta} - \hat{\phi}_{rj\beta}) + \omega_{mj}\,\hat{\phi}_{rj\alpha} \end{cases} \tag{4.26}$$

The estimated rotor current expression:

$$\begin{cases} \dfrac{d}{dt}\hat{i}_{sj\alpha j} = \dfrac{1}{L_{sj}\sigma_j}(V_{sj\alpha j} - R_{sj}\hat{i}_{sj\alpha j} - \dfrac{L_{mj}}{L_{rj}}\hat{\phi}_{rj\alpha}) \\ \dfrac{d}{dt}\hat{i}_{sj\beta j} = \dfrac{1}{L_{sj}\sigma_j}(V_{sj\beta j} - R_{sj}\hat{i}_{sj\beta j} - \dfrac{L_{mj}}{L_{rj}}\hat{\phi}_{rj\beta}) \end{cases} \tag{4.27}$$

The estimated stator flux and currents of the harmonic component's expression:

$$\begin{cases} \dfrac{d}{dt}\hat{\phi}_{sj\alpha\beta j} = V_{sj\alpha\beta j} - R_s\hat{i}_{sj\alpha\beta j} \\ \hat{i}_{sj\alpha\beta j} = \dfrac{\hat{\phi}_{sj\alpha\beta j}}{L_s} \end{cases} \tag{4.28}$$

4.5.3. Stator flux and electromagnetic torque estimation

The VCS algorithm adopts the indirect method to estimate the stator flux module and position based on the information of the reconstructed currents and estimated rotor flux with the advantage of eliminating the direct method drawback of using a pure integrator. The estimated stator flux module and position and electromagnetic torque expressions are given as follows:

$$\begin{cases} \hat{\phi}_{sj\alpha j} = \dfrac{L_{mj}}{L_{rj}}\hat{\phi}_{rj\alpha} + \dfrac{L_{sj}L_{rj} - L_{mj}^2}{L_{rj}}\hat{i}_{sj\alpha j} \\ \hat{\phi}_{sj\beta j} = \dfrac{L_{mj}}{L_{rj}}\hat{\phi}_{rj\beta} + \dfrac{L_{sj}L_{rj} - L_{mj}^2}{L_{rj}}\hat{i}_{sj\beta j} \\ \hat{\phi}_{sj} = \sqrt{\hat{\phi}_{sj\alpha j}^{\,2} + \hat{\phi}_{sj\beta j}^{\,2}} \\ \theta_{sj} = \tan^{-1}\left(\dfrac{\hat{\phi}_{sj\beta j}}{\hat{\phi}_{sj\alpha j}}\right) \end{cases} \tag{4.29}$$

$$\hat{T}_{emj} = \frac{5p_j}{2}(\hat{\phi}_{sj\alpha j}\hat{i}_{sj\beta j} - \hat{\phi}_{sj\beta j}\hat{i}_{sj\alpha j}) \tag{4.30}$$

Figure 4.13 represents the block diagram of the current reconstruction algorithm.

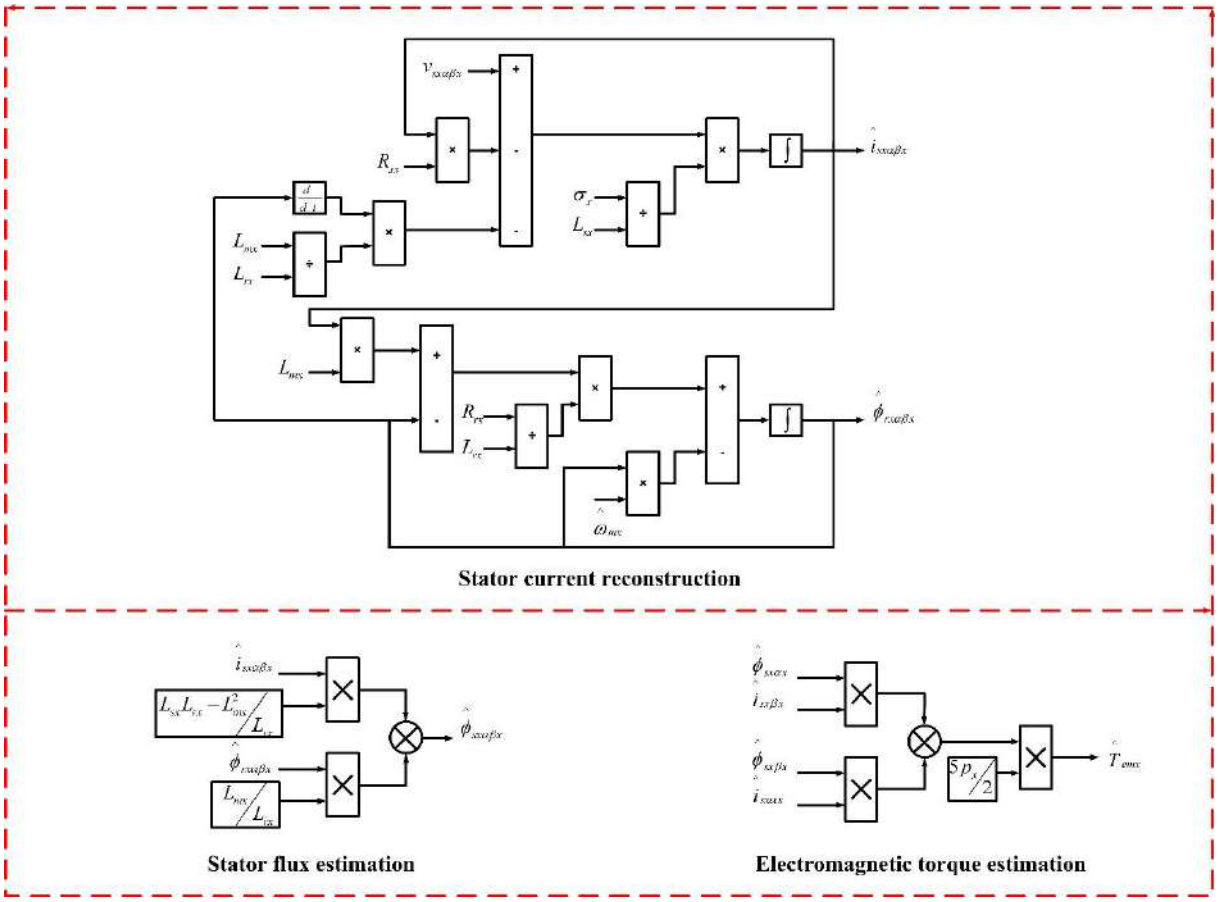

Figure 4.13: Schematic diagram of VCS.

4.5.4. Simulation results

This part considers the stator current reconstruction sensorless DTC-ANN based on VCS, where the 3L-DTC-ANN is adopted. Figure 4.14 depicts the block diagram of the sensorless DTC-ANN of the two-machine drive.

In order to test and compare the performance of the sensorless method, two different test scenarios were used in the Matlab/Simulink environment. The stator currents presented in this study are the estimated currents based on the VCS. The machine's parameters are the same as in section 1.6, Table 1.9.

4.5.4.1. Test one

This test considers the application of different speed reference commands, reversion, and low-speed operation under constant loading conditions. The first test scenario is summarized in Tables 4.7 and 4.8.

Table 4.7: First test scenario for the FPIM1.

Time [s]	$0 \rightarrow 0.1$	$0.1 \rightarrow 1$	$1 \rightarrow 1.3$	$1.3 \rightarrow 2$	$2 \rightarrow 2.2$	$2.2 \rightarrow 3$	$3 \rightarrow 4$	$4 \rightarrow 4.5$
$\omega_m[rad/s]$	$0 \rightarrow 20$	20	$20 \rightarrow 60$	60	$60 \rightarrow 100$	100	$100 \rightarrow -100$	-100
$T_L[Nm]$	8							

Table 4.8: First test scenario for the FPIM2.

Time [s]	$0 \rightarrow 0.5$	$0.5 \rightarrow 2$	$2 \rightarrow 2.6$	$2.6 \rightarrow 3.4$	$3.4 \rightarrow 3.7$	$3.7 \rightarrow 4.2$	$4.2 \rightarrow 4.4$	$4 \rightarrow 4.5$
$\omega_m[rad/s]$	$0 \rightarrow -100$	-100	$-100 \rightarrow 20$	20	$20 \rightarrow 60$	60	$60 \rightarrow 100$	100
$T_L[Nm]$	-8							

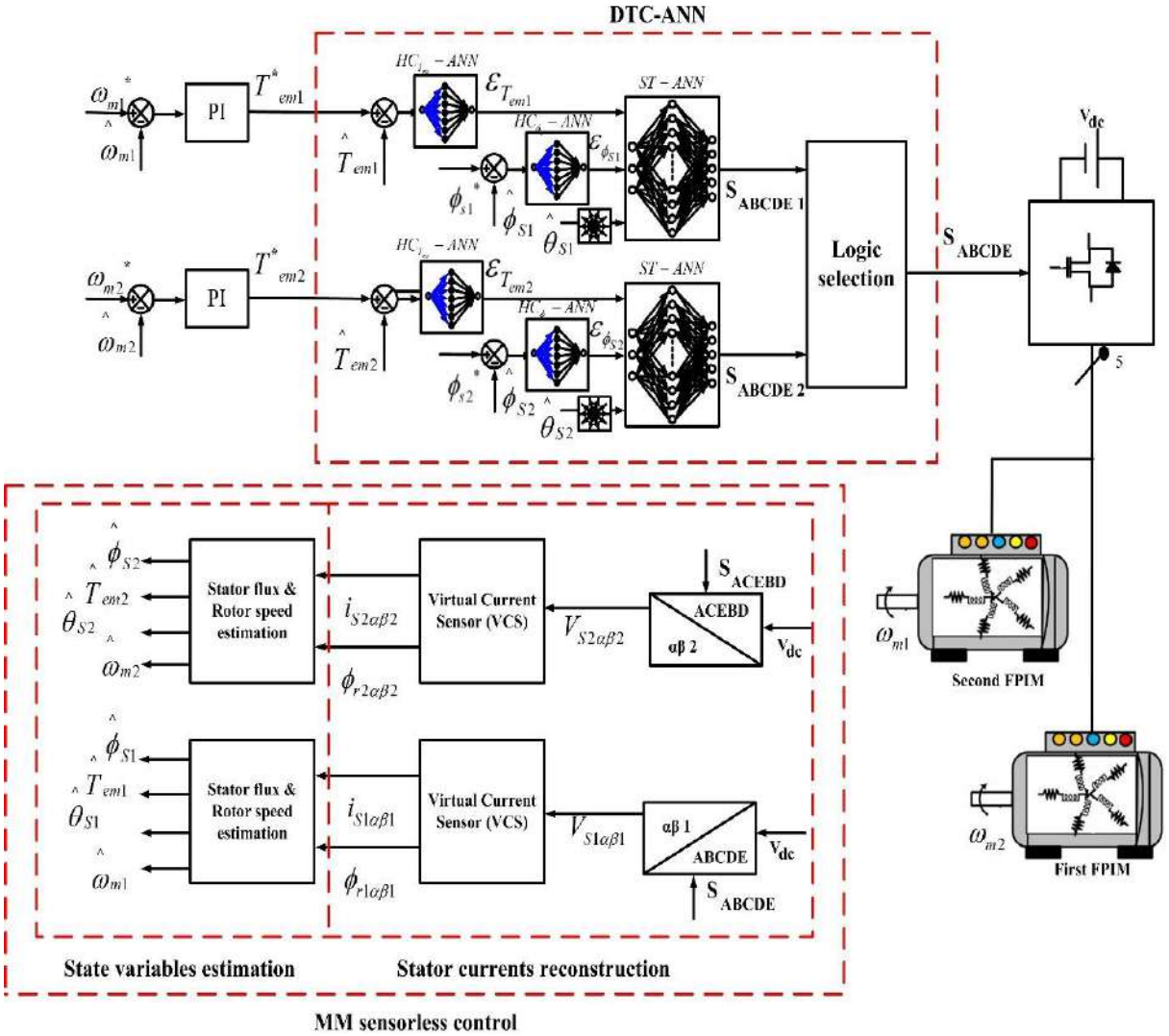

Figure 4.14: Sensorless DTC-ANN based on VCS.

The first test scenario's simulation results are presented in Figure 4.15.

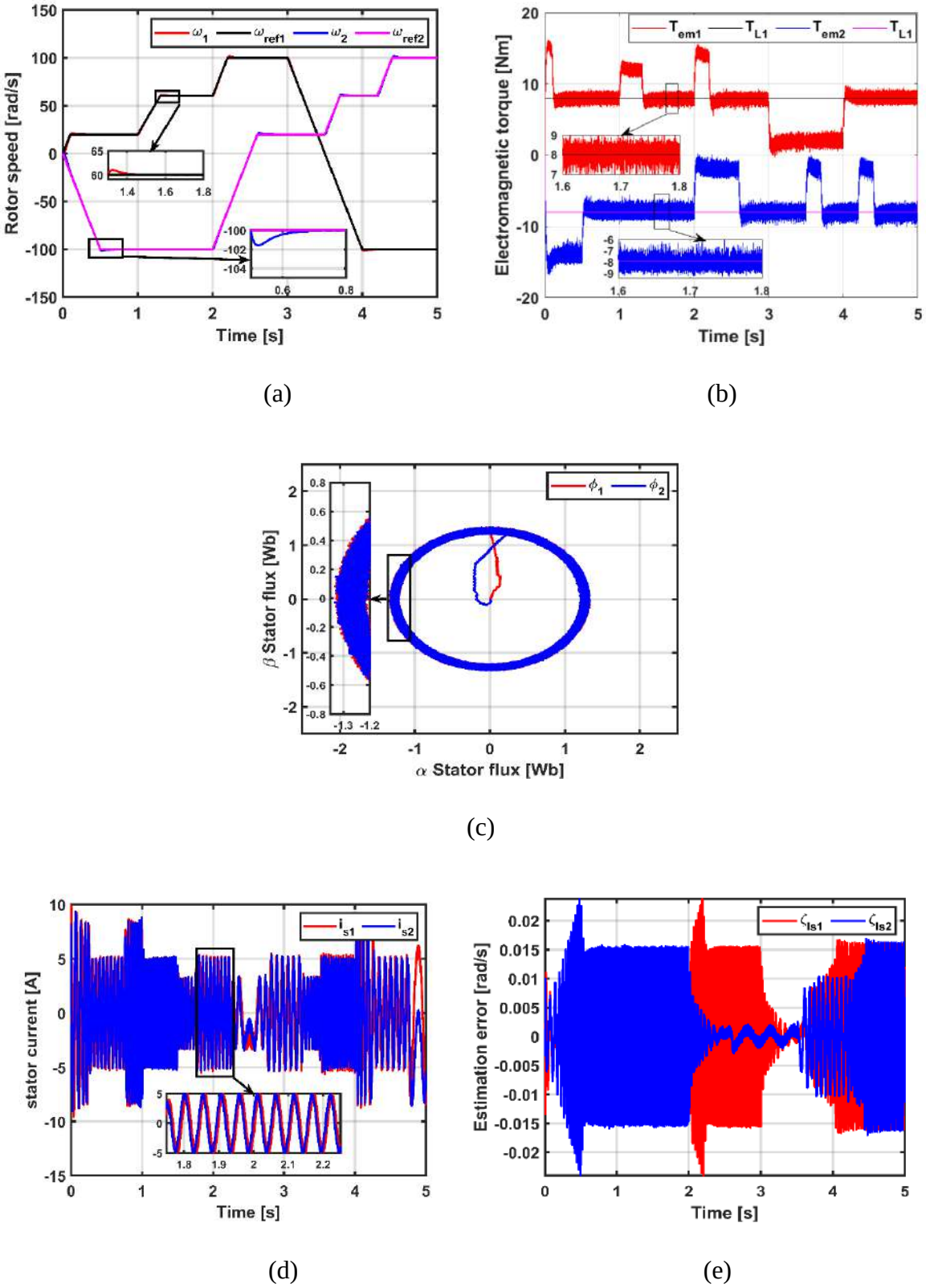

(a) (b)

(c)

(d) (e)

Figure 4.15: Sensorless DTC-ANN based on VCS: (a) mechanical rotor speed, (b) electromagnetic torque, (c) stator flux, (d) stator current, (e) estimated stator current.

4.5.4.2. Test two

The second test scenario considers the application of a different torque load profile under a constant speed reference command. It is summarized in Table 4.9.

Table 4.9: Second test scenario for the two machines.

$Time[s]$	$\omega_m[rad/s]$	$T_{L1}[Nm]$	$T_{L2}[Nm]$
$0 \rightarrow 0.5$	$0 \rightarrow 100$	8	-2
$0.5 \rightarrow 1$	100		
$1 \rightarrow 2$		0	8
$2 \rightarrow 3$		-4	0

The second test scenario's simulation results are presented in Figure 4.16.

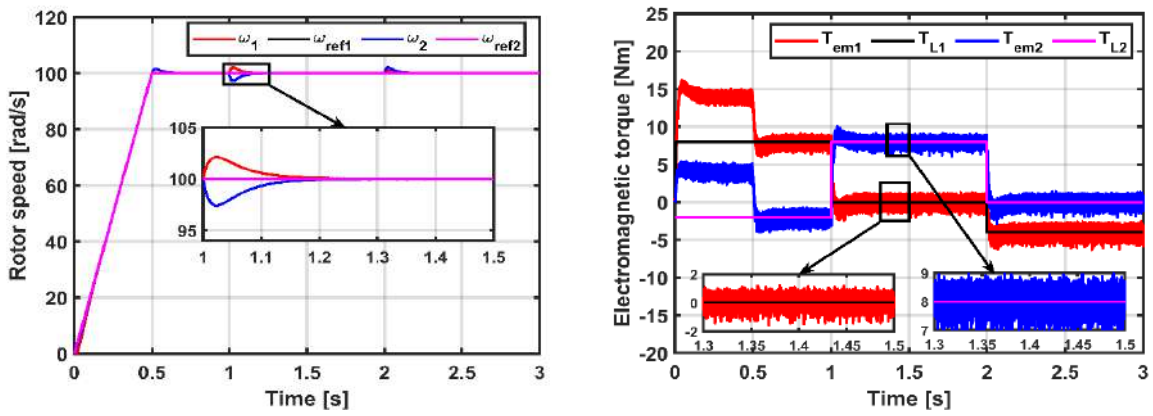

(a) (b)

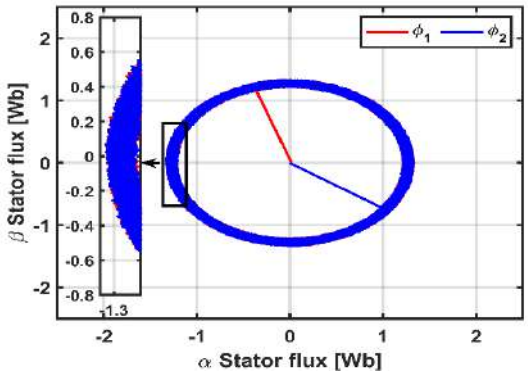

(c)

Figure 4.16: Sensorless DTC-ANN based on VCS: (a) mechanical rotor speed, (b) electromagnetic torque, (c) stator flux.

4.5.4.3. Results discussion

The simulative results of the MM sensorless DTC-ANN-based VCS are presented and evaluated for different operating conditions.

First, the three methods do not affect the independent control of the two-machine drive, ensuring complete decoupled control between the two machines and the stator flux/electromagnetic torque for each of them.

Figures 4.15.a and 4.16.a illustrate the rotor's mechanical speed response of the VCS-based sensorless controlled drive. It can be noticed that during both the transient and steady-state operation of the two-machine drive, the rotor's speed shows a high dynamic response to the speed reference command changes with negligible over/undershot of 2 rad/s due to the change in the loading condition or the reference command.

The generated electromagnetic torque of both machines for the three sensorless schemes is presented in Figures 4.15.b and 4.16.b. The electromagnetic torque presents a comparable performance to the 3L-DTC-ANN scheme, with a ripple rate of 47%, for different loading and speed reference profiles.

Figures 4.15.c and 4.16.c illustrates the response of the two FPIMs' stator flux depicting a fast response with a circular trajectory and accurate response to the reference command, with a ripples content of 7.3%.

Moreover, the stator current of phase "a" waveform for two machines and THD analysis are shown in Figures 4.15.d and 4.16.d. It is shown that the stator current has a distorted sinusoidal waveform corresponding to the ripple content in the stator flux and electromagnetic torque responses. The THD is 19%.

Finally, phase "a" reconstructed currents by the VCS method. for both machines. They show an accurate estimation of the phase current of both FPIMs in the motoring and generating mode with an estimation error of ±0.025 A, as shown in Figure 4.15.e.

4.6. Comparative study

Table 4.10 summarizes the comparison study between the three MM methods and the conventional scheme in terms of toque/flux ripples, reference tracking performance, and estimation error.

Table 4.10: Comparative analysis of the performance of DTC and DTC-ANN.

Assessment parameters		3L-DTC-ANN	DTC-MRAS	DTC-SMO	DTC-VCS
ω_m	Recovery time (s)	0.3	0.5	0.2	0.2
	Overshoot (rad/s)	2	4	3	2
	Undershoot (rad/s)	2	4	3	2
	Estimation error (rad/s)	-	±4	±3	-
ϕ_s	Ripples (%)	8	10	44	7.3
T_{em}	Ripples (%)	46	50	5	47
I_S	THD (%)	20	22	20	19
	Estimation error (A)	-	-	-	±0.025

Table 4.11 summarizes a comparative study between the proposed sensorless methods merits and demerits based on selected performance criterions.

Table 4.11: Performance comparison of the three MM sensorless methods.

	Steady-state error	Dynamic behaviour	Low-speed operation	Complexity	Computation time
MRAS	Very good	Good	Satisfactory	Very good	Good
SMO	Excellent	Excellent	Very good	Complex	Very good
VCS	Very good	Good	Satisfactory	Excellent	Very good

4.7. Conclusion

In this chapter, an independent sensorless DTC of two FPIMs connected in parallel fed by a single VSI based on MRAS, SMO, and VCS is discussed. The three proposed approaches use an MM-based method to estimate the machine's state variables, enhancing the control scheme performance by overcoming the conventional open-loop estimator drawbacks.

The MRAS observer is considered for the rotor's mechanical speed estimation because of its simple yet robust structure. In addition, the stator flux module, position, and electromagnetic torque can be estimated from the estimated rotor flux information. However, this method has drawbacks, such as the PI controller tuning problem and the reduced starting at full load.

The SMO is proposed to tackle the MRAS technique's starting problem and provide a more robust and accurate estimation of the machine's state variables, improving the control scheme's dynamic performance. Nevertheless, this approach also has the drawback of tuning the observer gain matrix by eight coefficients to determine.

Another MM method is proposed to estimate the FPIM's state variables and replace the CS. The VCS accurately reconstructs the stator phase currents regardless of the operating conditions, giving a fault-tolerant operating advantage to the drive and addressing the parameters tuning drawback of the previous methods. Finally, the simulation results demonstrate a complete decoupled control between the FPIMs' stator flux and torque both in the steady/transient state and motoring/generating mode, improving the dynamic performance of the drive and adding the value of fault-tolerant operation to the drive during the sensors downtime.

The next chapter tackles one of the most frequent tracks of the PWM-controlled VSI, which is the Common Mode voltage, which affects the drive's performance through a preventive control scheme.

Chapter 5

Multi-level DTC with CMV mitigation for two-machine drive

5.1. Introduction

In the ASA industries, where the use of the PWM-controlled VFD concept is required to obtain an adjustable AC in terms of voltages and frequency to control the machine's speed and torque, the recurring drawback of the Common-Mode Voltage (CMV) is faced [104]. This latter is a PWM's inherited drawback, which is translated in a voltage difference between the VSI's neutral point and the ground through the capacitive coupling. Moreover, with the introduction of the VFDs ranging from several kHz to MHz, this voltage plays a crucial role in potential problems in AC machine drives, affecting their lifespan and correct operation [95, 96], especially with the upcoming introduction of wide bandgap semiconductors technology that allows reaching a high operating frequency [105].

On this basis, multi-level VSIs have proven to be a key point in solving this drawback over the last decades since these topologies present DOF compared to the two-level VSIs [104].

Thus, this chapter discusses a proposed preventive method to mitigate the CMV in the five-phase two-machine drive. This latter is an extension of the mitigation technique introduced in [106] presented by TATTE, exploiting the concept of virtual voltage vectors (VVV).

This chapter provides a state-of-the-art assessment of the CMV impacts and the mitigation approaches discussed in the literature. It then discusses the proposed preventive technique based on DTC. The simulative results illustrate the effectiveness of the control scheme.

5.2. Common-Mode Voltage

In applications that require a high power demand and fault tolerance, for instant electromobility applications, multiphase star-connected AC machines are highly considered. Nevertheless, as with the three-phase drives, the CMV presents a prominent issue for the multiphase drives as well [105].

5.2.1. Definition of CMV

The CMV is elucidated as the potential difference between the star point with respect to the mid-point of the DC link of the VSI, as shown in Figure 5.1. The analytical expression considered for the generated CMV by the VSI's phase voltage is [107]:

$$U_{CM}(t) = \frac{1}{q}\sum_{i=1}^{q} V_{io} \approx V_{No}(t) \tag{5.1}$$

Where: q is the phase number, V_{io} is the VSI's i-th pole voltage.

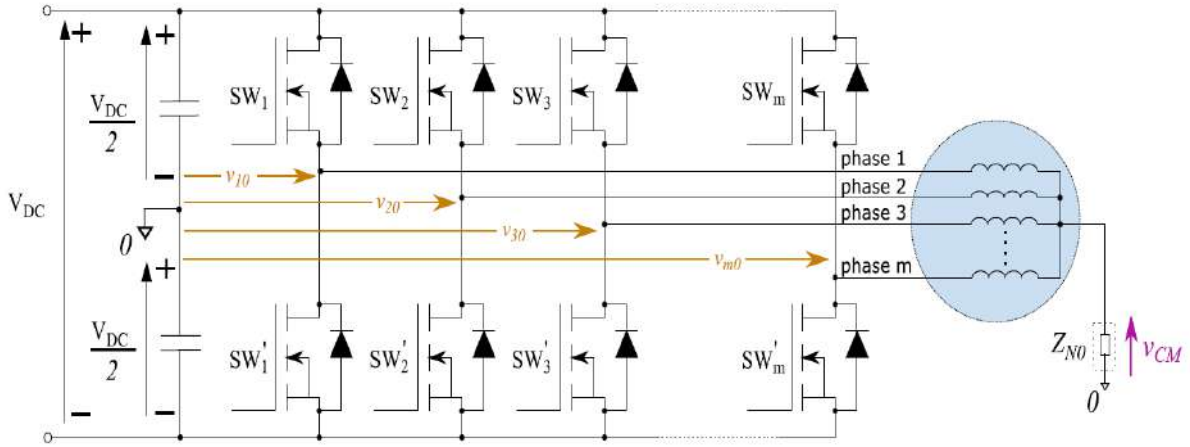

Figure 5.1: The path of the CMV in generalized schematic of the multi-phase VSI [107].

This phenomenon is the natural outcome of the PWM-controlled VSI due to the fact that this latter does not generate a sinusoidal voltage waveform but a discrete voltage at the terminal output. Thus, depending on the VSI switching states, the CMV peak-to-peak value may vary between 0V to $\pm V_{dc}/2$.

5.2.2. Impact of CMV

The generated CMV has several adverse effects that reduce the electric drive's reliability. Among them:

- **Electromagnetic interference (EMI):** The radiated and/or conducted EMI that results from the VSI's voltage waveforms and the parasitic impedances of the machine. Due to the CM impedance paths, highlighted in Figure 5.2, this EMI can further affect the other parts of the ASD [108, 109].

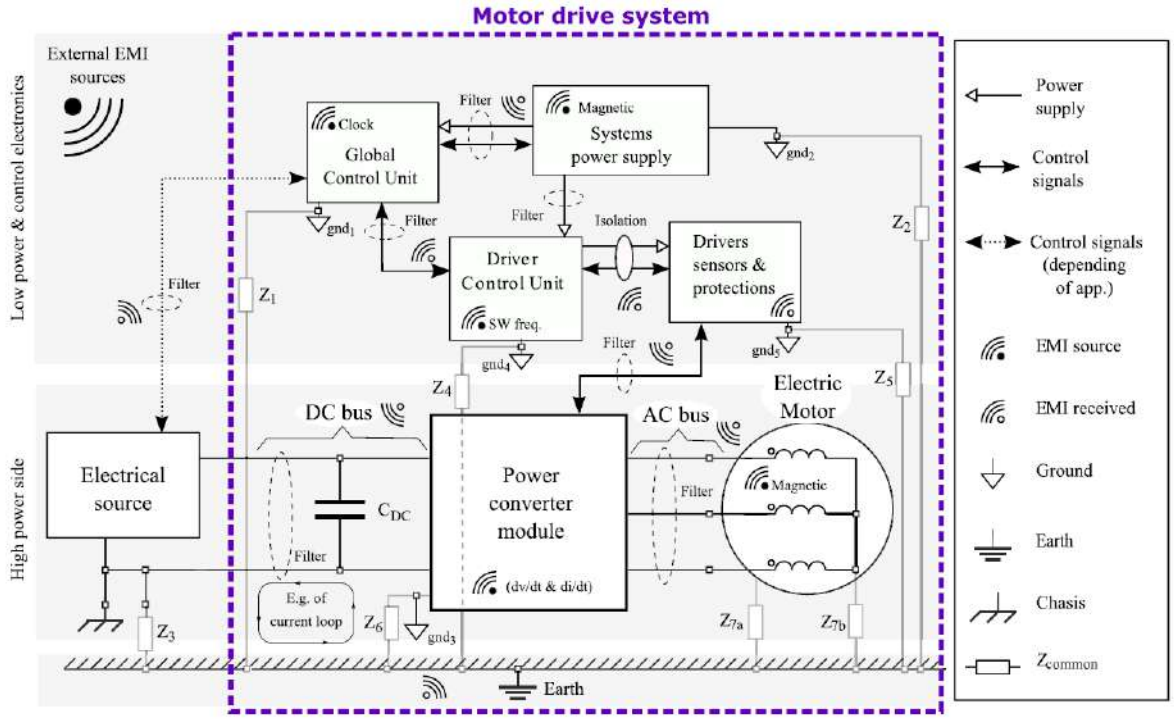

Figure 5.2: Sources of EMI in the ASD [104].

- **Winding insulation damage:** The large $^{dv}/_{dt}$ produced by the PWM technique at the input terminals of the stator's windings creates a significant stress that degrades the windings' insulations, as shown in Figure 5.3 [110, 111].

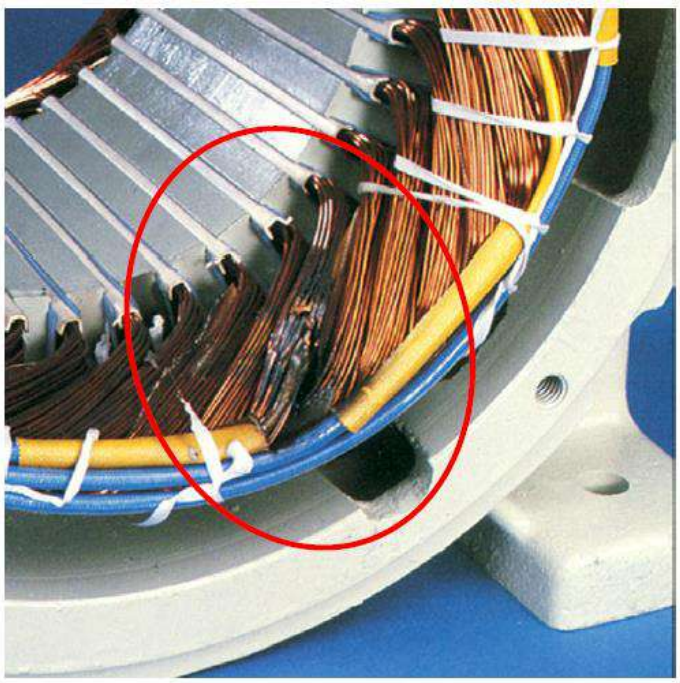

Figure 5.3: The effect of the voltage surge on the machine's windings insulation.

- **Induced voltage shaft:** The high-frequency CMV resulting from the PWM technique induces a voltage on the machine's shaft. This latter, when it exceeds the bearings' insulation's capability, it results in circulating currents through the machine's parasitic capacitance that cause a bearing failure, as shown in Figure 5.4 [112, 113].

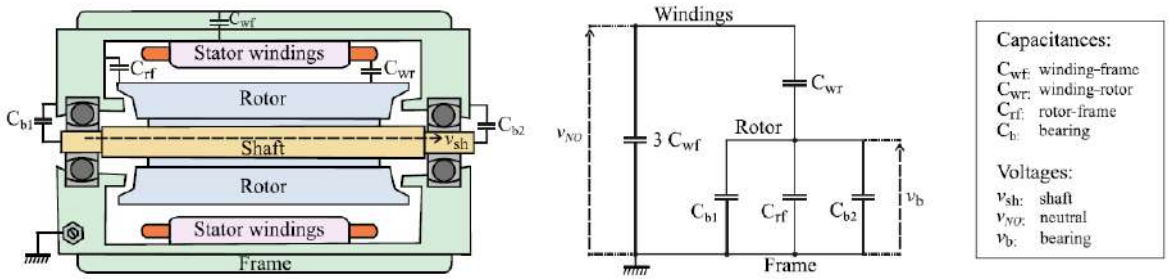

Figure 5.4: Voltages generated in the AC machines due to the parasitic capacitances and the simplified equivalent circuit [107].

- **Bearing currents:** Aside from the shaft voltage, the CMV variations cause a leakage current through the machine's bearings combined with parasitic capacitance, as illustrated in Figure 5.5 [107]. Four types of bearing currents can be distinguished as follows:
  1. Capacitances currents.
  2. Electric discharge machining currents.
  3. Circulating currents.
  4. Rotor to the ground currents.

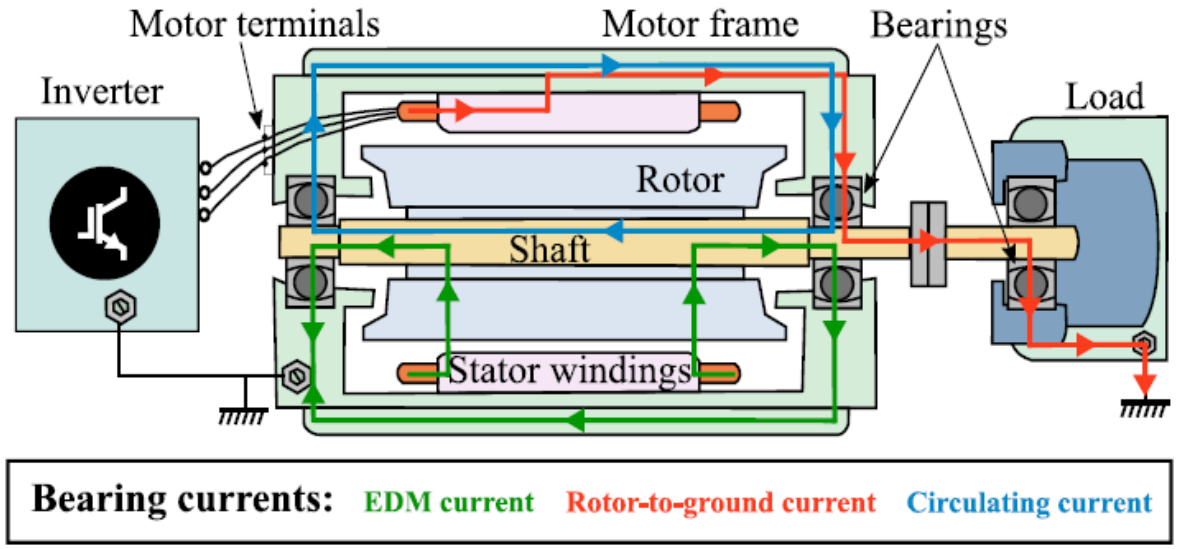

Figure 5.5: Paths of the bearing's currents [107].

5.2.3. Techniques for CMV mitigation

The CMV mitigation techniques can be classified into two families: corrective and preventive solutions. Figure 5.6 summarizes the CMV effects and solutions as follows [107]:

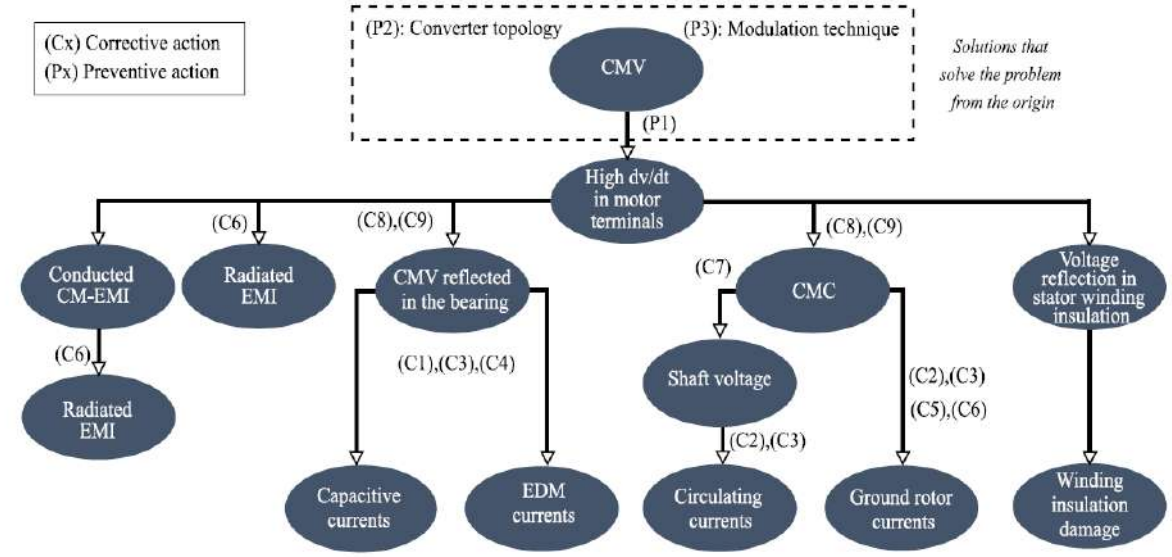

(a)

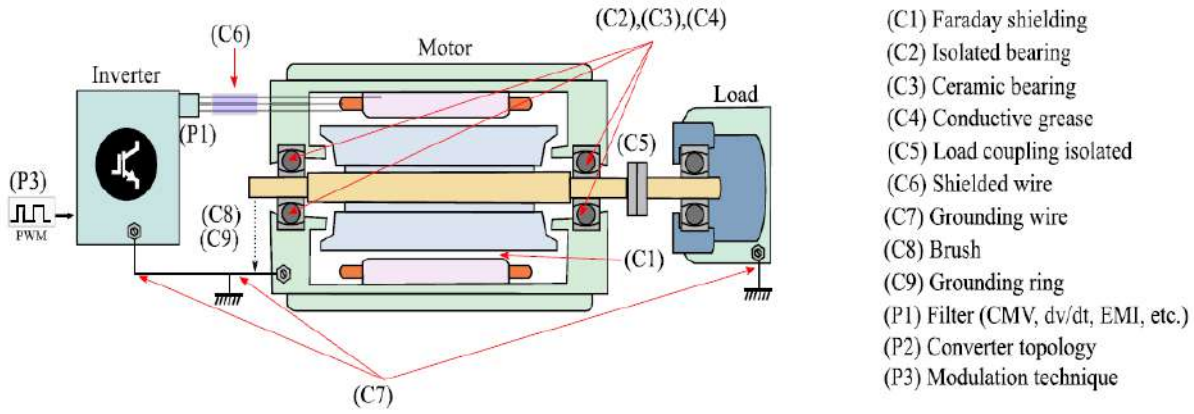

(b)

Figure 5.6: (a) Causes of the CMV, effects and their respective solutions, (b) The solution location on the drive [107].

5.2.3.1. Corrective methods

It can be considered a countermeasure to the effects of the CMV by encompassing additional specially designed hardware and procedures (‘Cx’ tags).

- **(C1) Faraday shielding:** The cornerstone of this solution is inserting a conductive shield between the stator and rotor to block the flow of the current generated from the VSI and further prevent it from being induced in the shaft [115]. This method is seldom utilized in practice and presents a high implementation cost and difficulties [116]. Figure 5.7 illustrates (C1) the Faraday shielding.

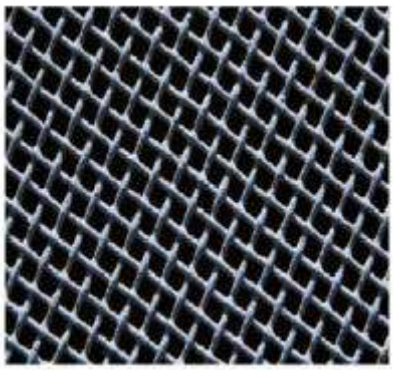

Figure 5.7: (C1) Faraday shielding.

- **(C2) Insulated bearings:** This type of bearings has the capability to prevent the shaft current from discharging through them into the machine's stator frame [117]. Generally, a layer of ceramic or a non-conductive resin is used in this type of bearing. Nevertheless, this solution increases the cost of implementation since it requires modifying the machine. Figure 5.8 illustrates (C2) the insulated bearings.

Figure 5.8: (C2) Insulated bearings.

- **(C3) Ceramic or hybrid bearings:** In this solution, and to prevent the flow of the shaft current through the bearings by the use of either ceramic rolling material and steel track or by the use of only ceramic elements, and it is particularly effective in small machines. Nevertheless, it presents a cost-ineffective solution since it is more expensive and

diverts the problem to other parts of the drive [107, 116]. Figure 5.9 (C3) ceramic or hybrid bearings.

Figure 5.9: (C3) Ceramic or hybrid bearings.

- **(C4) Conductive grease:** This solution considers the reduction of the harmful discharge due to the shaft voltage by creating a continuous conductive path through the bearings using grease containing a conductive particle. Nevertheless, this latter shortens the service lifetime of the bearings due to ineffective lubrication [116]. Figure 5.10 illustrates (C4) the conductive grease.

Figure 5.10: (C4) Conductive grease.

- **(C5) Insulated mechanical load coupling:** This solution considers the protection of the driven load against any potential damage by isolating the coupling path to prevent the flow of any leakage currents [107]. Figure 5.11 illustrates (C5) the insulated mechanical load coupling.

Figure 5.11: (C5) Insulated mechanical load coupling.

- **(C6) Shielded cables:** This solution considers the creation of an alternative electric path characterized by a low impedance for the Common-Mode Currents generated by the VSI through symmetrical ground cable protection [107]. Thus, it results in a reduction of the EMI and near elimination of the rotor-to-ground currents. Nevertheless, the downside of this solution is that it generates an overvoltage at the machine's terminals, resulting in premature failure of the windings insulation due to the length of these cables and the high switching frequencies. Figure 5.12 illustrates (C6) the shielded cables.

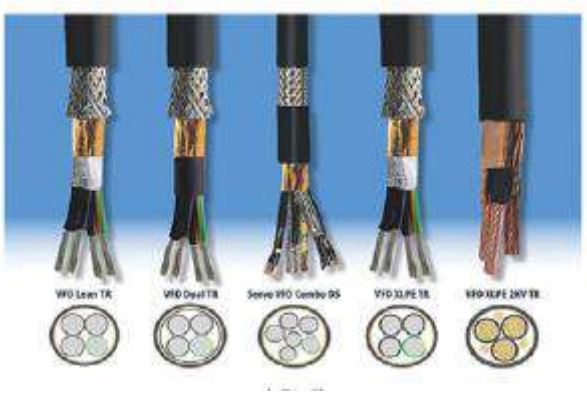

Figure 5.12: (C6) Shielded cables.

- **(C7) Grounding cables:** This solution considers the use of thin-film twisted cable to provide a decreased impedance path to the ground from the machine for the currents to flow through. These cables are placed either on the VSI or machine's sides [118, 119]. Figure 5.13 illustrates (C7) the grounding cables.

Figure 5.13: (C7) Grounding cables.

- **(C8) Brushes:** This solution considers the use of brushes based on metal or carbon material to provide a parallel connection from the machine's frame to the shaft aside from the bearings. Nevertheless, the material selection must be made based on the machine's size and use [120]. Figure 5.14 illustrates (C8) the brushes.

Figure 5.14: (C8) Brushes.

- **(C9) Shaft grounding ring:** This solution considers the same approach as the brushes to redirect the discharge aside from the machines by incorporating a micro-conductor fiber-based ring between the machine's frame and the shaft. This solution is cost-effective and utilized by multiple machine manufacturers [121]. Figure 5.15 illustrates (C9) the shaft grounding rings.

Figure 5.15: (C9) Shaft grounding ring.

5.2.3.2. Preventive methods

This solution considers the mitigation technique to be applied to the control scheme of the inverter to directly eliminate or reduce the CMV [107]. Thus, this thesis considers a preventive mitigation method combined with the DTC, discussed in the next section ('Px' tags).

5.3. Preventive DTC method (DTC_{CMV})

In the conventional DTC, the $\alpha\beta_1$ and $\alpha\beta_2$ planes are utilized to independently control the two five-phase machines, respectively. Nevertheless, this method has several drawbacks, as mentioned earlier. Thus, an implementation of the concept of VVVs is described to mitigate the generated CMV and further improve the overall performance of the drive. Therefore, for the purpose of synthesizing the proposed control scheme, an analysis study on the VSI's space vector is required (Step 1), the VVVs synthesize (Step 2), the VVVs selection (Step 3), and the actual VVs selection (Step 4).

5.3.1. Step 1

As mentioned above, the CMV is directly related to the VSI's switching states voltage phase, as summarized in Table 1.3, which determines the CMV waveform peak-to-peak value, as the equation (5.2) indicates [106]:

$$U_{cm} = \frac{U_{az} + U_{bz} + U_{cz} + U_{dz} + U_{ez}}{5} \tag{5.2}$$

Figure 5.16, illustrates the CMV's path in the two-machine drive [122].

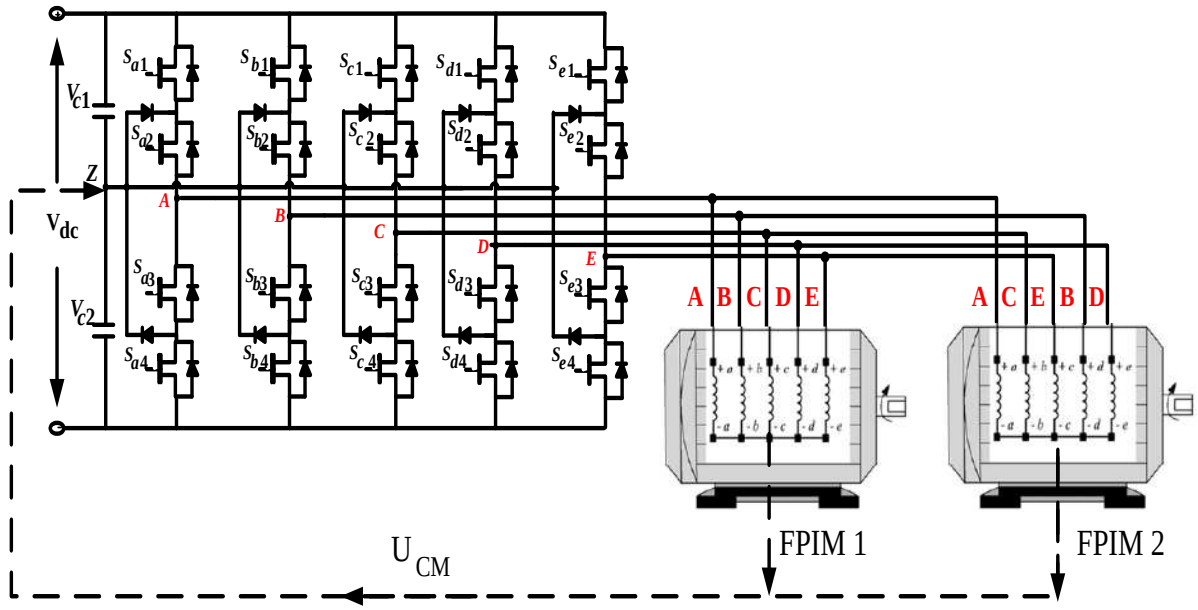

Figure 5.16: The path of CMV in the two-machine drive.

5.3.1.1. Three-level DTC's CMV status

In the conventional 3L DTC, for instance the two zero VVs utilized have the switching sequence of [00000] and [22222], where each sequence generates a $\pm V_{dc}/_2$ phase voltage. Thus, by substituting in (5.2) yields to $\pm V_{dc}/_2$ peak-to-peak CMV values.

Therefore, the direct extension of the DTC to the THL-VSI results in several potential problems due to the generated CMV. Table 5.1 illustrates the CMV values and waveforms of the selected THL-VSI's VVs [122].

Table 5.1: Peak-to-peak CMV and the theoretical waveforms.

Reported strategies	VV	CMV	Theoretical waveform of CMV	Peak-peak CMV
3L-DTC	$V1$ -$V10$	$\pm V_{dc}/10$	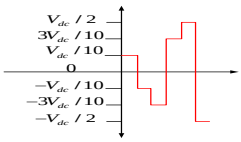	$\pm V_{dc}/2$
	$V21$ -$V30$	$\pm 3V_{dc}/10$		
	$V31$ -$V40$	$\pm V_{dc}/10$		
	$V0$	$\pm V_{dc}/2$		
DTC_{CMV}	$V1$ - $V10$	$\pm V_{dc}/10$	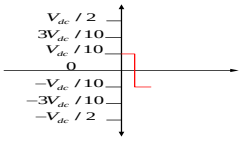	$\pm V_{dc}/10$
	$V11$ -$V20$	$\pm V_{dc}/10$		
	$V31$ -$V40$	$\pm V_{dc}/10$		
	$V0$	$0V_{dc}$		

5.3.1.2. Status of CMV for the mitigation technique DTC_{CMV}

Contrary to the conventional method, the DTC_{CMV} selects the VVs based on their generated CMV peak-to-peak status [106]. Where 31 VVs are chosen, where the CMV values and waveforms are given in Table 5.1 and presented in Figure 5.17, as follows:

- 10 large VVs (V1-V10).
- 10 small VVs (V31-V40).
- 10 medium VVs (V11-V20).
- 1 zero VVs [11111].

For instants, the VV V20, from Figure 5.17.a, with a switching state of [21012] having a phase voltage of $+V_{dc}/2$, 0, $-V_{dc}/2$, 0, and $+V_{dc}/2$, respectively, and by substituting in (5.2) the generated CMV peak-to-peak value is equal to $\pm V_{dc}/10$. These VVs are utilized to synthesize the VVVs in the next step.

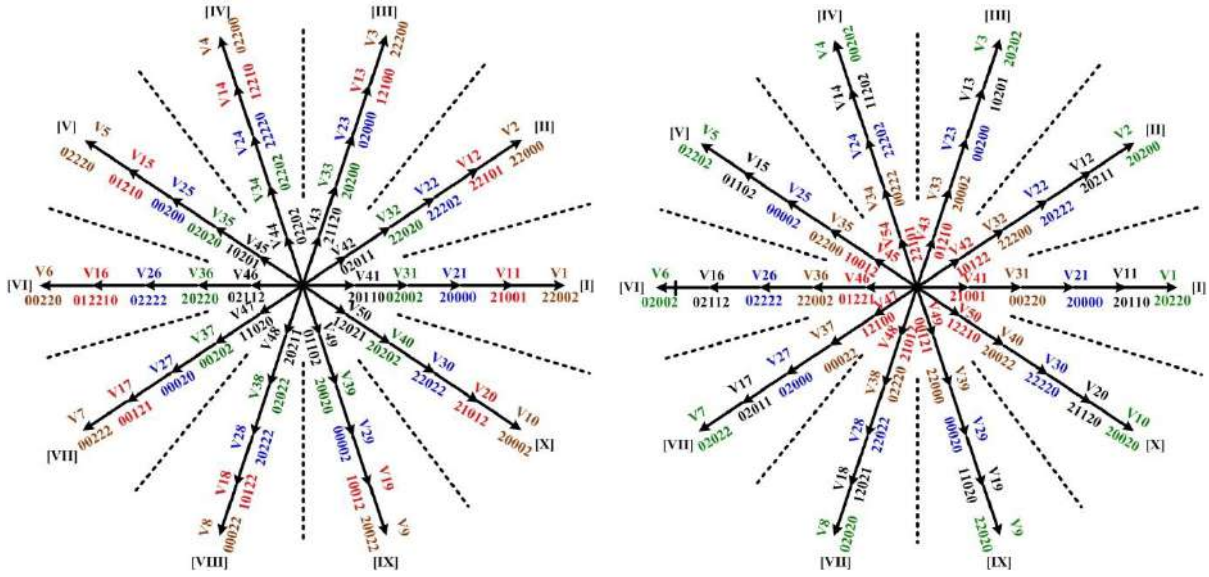

(a) (b)

Figure 5.17: Mapping of the VVs: (a) $\alpha\beta_1$ plane, (b) $\alpha\beta_2$ plane.

5.3.2. step 2

The THL-VSI's space vector, illustrated in Figure 5.17, exhibits a peculiarity for mapping the collinear VVs between the $\alpha\beta_1$ and $\alpha\beta_2$ planes. For instance, the VVs V, V13, V23, V33, and V43 in the $\alpha\beta_1$ plane have the opposite direction and different locations in the $\alpha\beta_2$ plane and vice-versa, as shown in Figure 5.18.a [122].

By exploiting the benefit of this verity, 21 VVVs are synthesized from the 31 actual VVs, defined in Step 1, in a manner that their application results in the annulation of one of the $\alpha\beta_1/\alpha\beta_2$ planes [106].

Thus, the VVVs are obtained from the combination of the 21 VVs as follows:

- The zero VV [11111] is used the ZVV.
- The 10 large VVVs (VVLx) are synthesized from the large and medium VVs.
- The 10 small VVVs (VVSx) are synthesized from the small and medium VVs.

The mapping of these VVVs is illustrated in Figure 5.18.b.

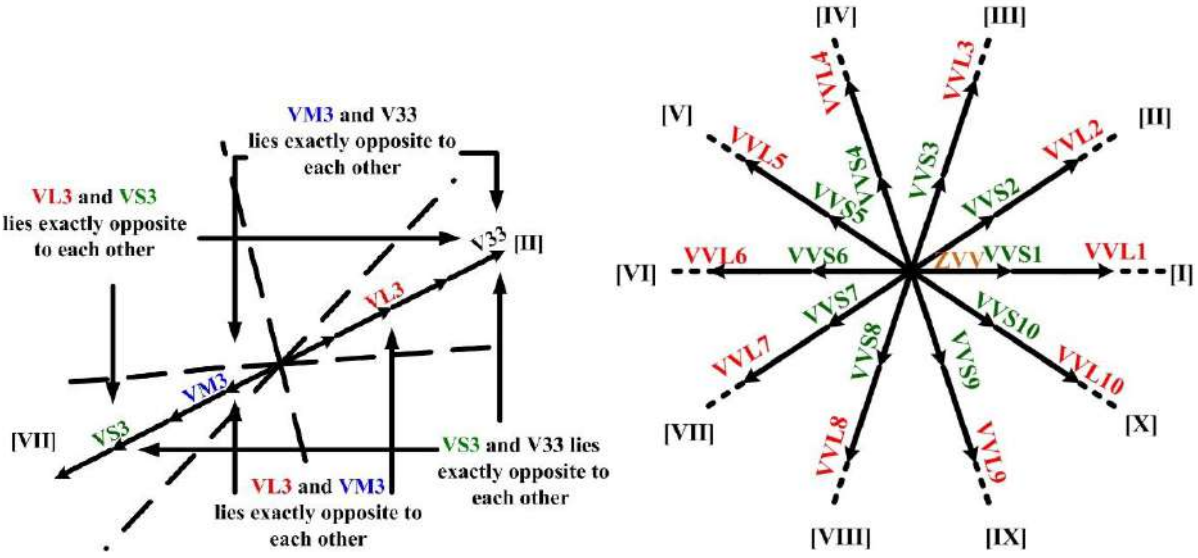

(a) (b)

Figure 5.18: (a) Peculiarities of the VVs, (b) Mapping of the VVVs.

5.3.3. step 3

As in the conventional DTC scheme, the optimum VVV is selected from a predefined ST constructed based on the digital response of the two-level and five-level HCs of the flux and torque, respectively, and the sector location [122]. Table 5.2 depicts the VVVs ST.

For instance, if the first machine's stator flux is located in the sector I and the digital response of the flux and torque HCs are ($\varepsilon_{\emptyset s} = 1\ and\ \varepsilon_{Tem} = -1$), respectively, the selected VVV is VVS9. Moreover, if the second machine's stator flux is located in sector V and the digital response of the flux and torque HCs are ($\varepsilon_{\emptyset s} = -1\ and\ \varepsilon_{Tem} = 2$), respectively, the selected VVV is VVL8.

Table 5.2: The ST of VVVs.

		Sector									
$\varepsilon_{\emptyset sj}$	ε_{Temj}	I	II	III	IV	V	VI	VII	VIII	IX	X
1	2	VVL3	VVL4	VVL5	VVL6	VVL7	VVL8	VVL9	VVL10	VVL1	VVL2
	1	VVS3	VVS4	VVS5	VVS6	VVS7	VVS8	VVS9	VVS10	VVS1	VVS2
	0	ZVV	ZVV	ZVV	ZVV	ZVV	ZVV	ZVV	ZVV	ZVV	ZVV
	-1	VVS9	VVS10	VVS1	VVS2	VVS3	VVS4	VVS5	VVS6	VVS7	VVS8
	-2	VVL9	VVL10	VVL1	VVL2	VVL3	VVL4	VVL5	VVL6	VVL7	VVL8
0	2	VVL4	VVL5	VVL6	VVL7	VVL8	VVL9	VVL10	VVL1	VVL2	VVL3
	1	VVS4	VVS5	VVS6	VVS7	VVS8	VVS9	VVS10	VVS1	VVS2	VVS3
	0	ZVV	ZVV	ZVV	ZVV	ZVV	ZVV	ZVV	ZVV	ZVV	ZVV
	-1	VVS8	VVS9	VVS10	VVS1	VVS2	VVS3	VVS4	VVS5	VVS6	VVS7
	-2	VVL8	VVL9	VVL10	VVL1	VVL2	VVL3	VVL4	VVL5	VVL6	VVL7

Where: ZVV=11111

5.3.4. Step 4

The actual VV to be applied is selected based on the selected VVV and the location of the machine's auxiliary stator flux, as illustrated in Table 5.3 [106].

Table 5.3: Actual VV's ST.

Large VVV	VVL1	VVL2	VVL3	VVL4	VVL5	VVL6	VVL7	VVL8	VVL9	VVL10
Location of stator flux of auxiliary plane	IX-III	II-VI	V-IX	VIII-II	I-V	IV-VIII	VII-I	X-IV	VIII-II	I-IV
Actual large VV	V1	V2	V3	V4	V5	V6	V7	V8	V9	V10
Location of stator flux of auxiliary plane	IV-VIII	VII-I	X-IV	III-VII	VI-X	IX-III	II-VI	V-IX	VIII-II	I-V
Actual medium VV	V11	V12	V13	V14	V15	V16	V17	V18	V19	V20
Small VVV	VVS1	VVS2	VVS3	VVS4	VVS5	VVS6	VVS7	VVS8	VVS9	VVS10
Location of stator flux of auxiliary plane	IX-III	II-VI	V-IX	VIII-II	I-V	IV-VIII	VII-I	X-IV	VIII-II	I-IV
Actual small VV	V31	V32	V33	V34	V35	V36	V37	V38	V39	V40
Location of stator flux of auxiliary plane	IV-VIII	VII-I	X-IV	III-VII	VI-X	IX-III	II-VI	V-IX	VIII-II	I-V
Actual medium VV	V11	V12	V13	V14	V15	V16	V17	V18	V19	V20

For example, if the VVV VVS9 is elected and the auxiliary stator flux of the FPIM1 is located in sector 3, then the VV to be applied is V39. Moreover, if the VVV VVL8 is selected and the auxiliary stator flux of the FPIM2 is located in sector V, then the VV to be applied is V18. Figure 5.19 depicts the block diagram of the DTC_{CMV}.

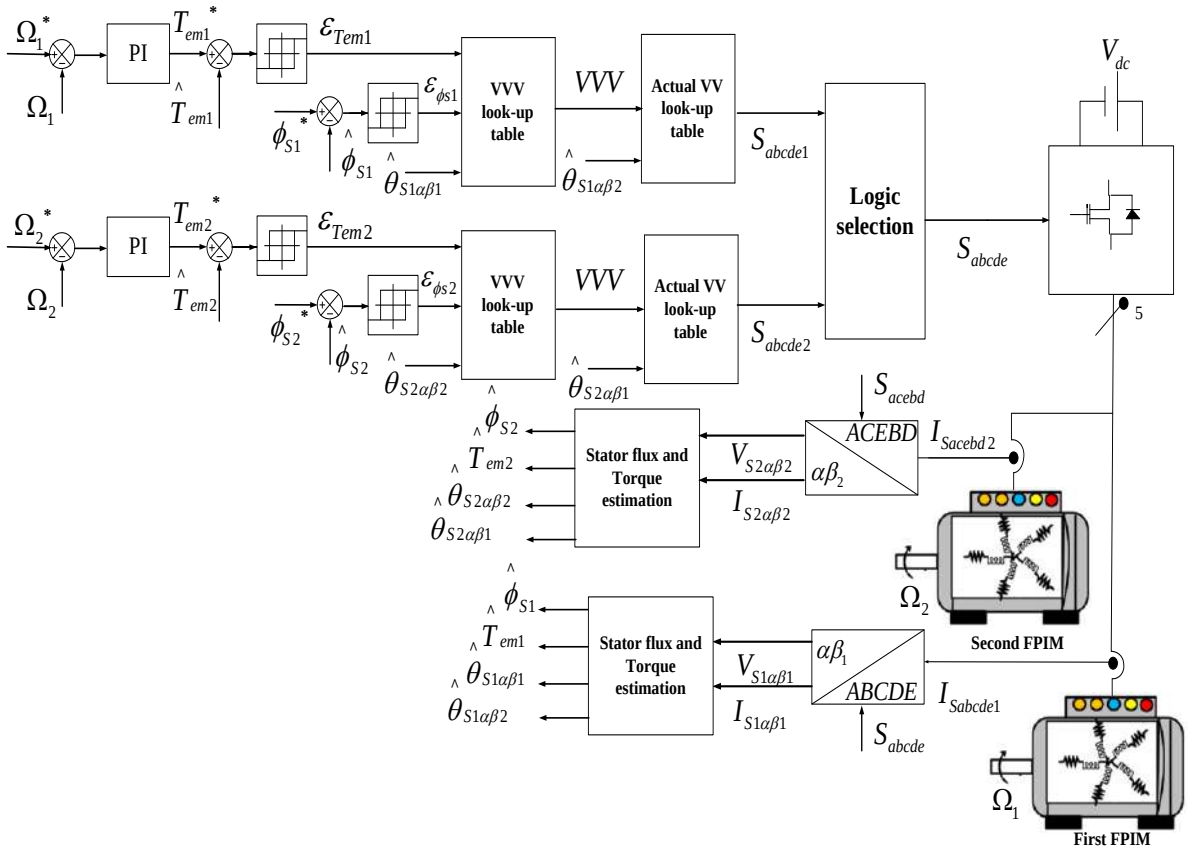

Figure 5.19: Schematics of DTC_{CMV} for the two-machine drive.

5.4. Simulation results

The mitigation technique DTC_{CMV} performance discussed herein is evaluated and compared to the intelligent 3L-DTC in MATLAB/Simulink. The FPIM's parameters are the same as those defined in Table 1.9, section 1.6. Tables 5.4 and 5.5 Summarize the testing conditions and the obtained results, which are illustrated in Figures 5.20 to 5.25.

Table 5.4: First test scenario for the FPIM1.

Time [s]	$0 \rightarrow 0.5$	$0.5 \rightarrow 1.5$	$1.5 \rightarrow 2.5$	$2.5 \rightarrow 3$
$\Omega\ [rad/s]$	$0 \rightarrow 100$	100	$100 \rightarrow -100$	-100
$T_L[Nm]$	8			

Table 5.5: First test scenario for the FPIM2.

Time [s]	$0 \rightarrow 0.5$	$0.5 \rightarrow 1.5$	$1.5 \rightarrow 2.5$	$2.5 \rightarrow 3$
$\Omega\ [rad/s]$	$0 \rightarrow -100$	-100	$-100 \rightarrow 100$	100
$T_L[Nm]$	-8			

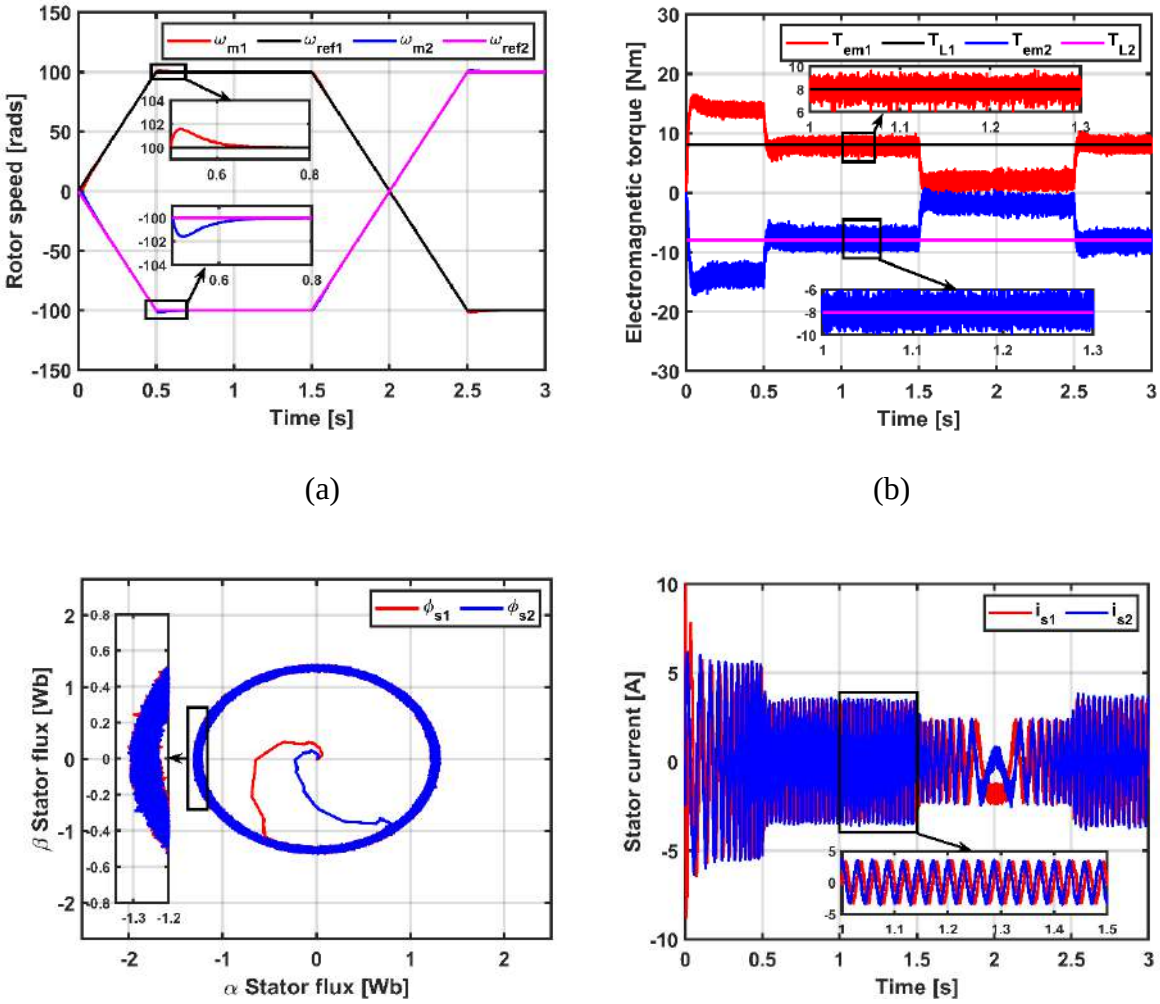

(a) (b)

(c) (d)

Figure 5.20: Three-level DTC-ANN response: (a) rotor's mechanical speed, (b) electromagnetic torque, (c) stator flux, (d) stator currents.

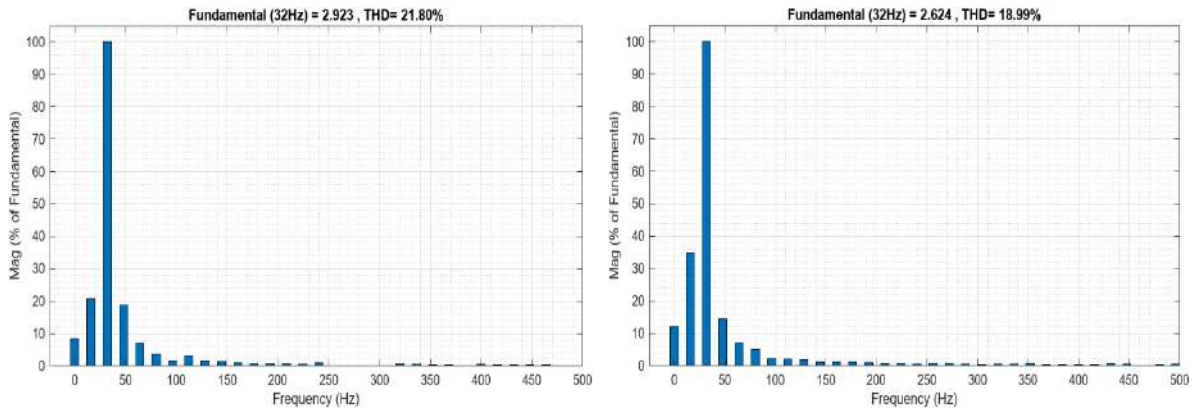

(a) (b)

Figure 5.21: Stator currents' THD of Three-level DTC-ANN: (a) FPIM1, (b) FPIM2.

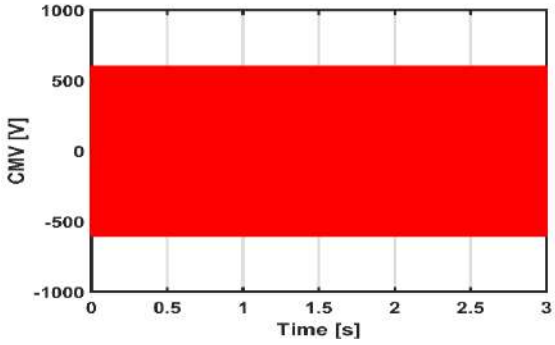

Figure 5.22: Generated CMV in three-level DTC-ANN.

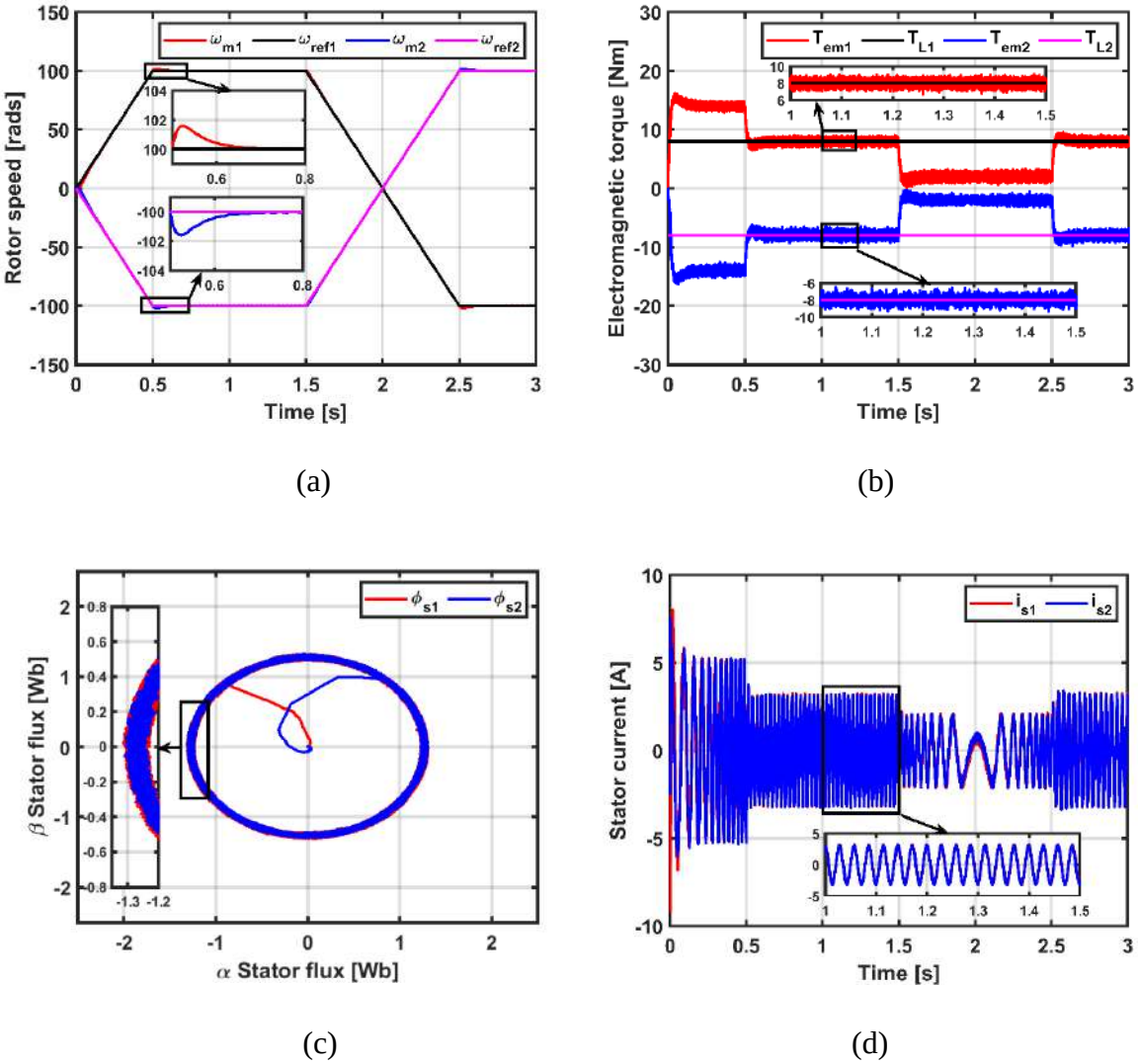

(a) (b)

(c) (d)

Figure 5.23: Response Of DTC_{CMV}: (a) rotor's mechanical speed, (b) electromagnetic torque, (c) stator flux, (d) stator currents.

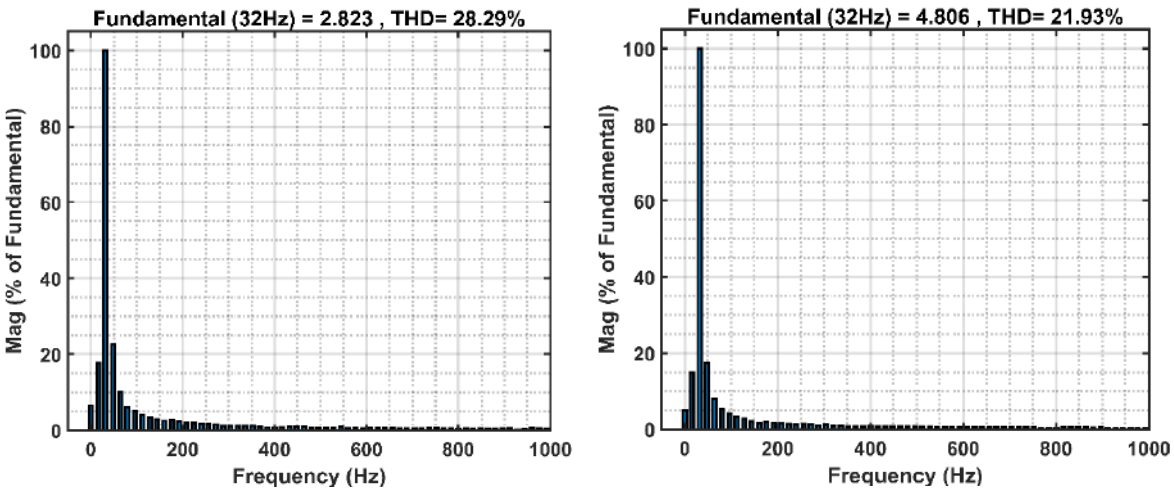

(a) (b)

Figure 5.24: Stator currents' THD of DTC_{CMV}: (a) FPIM1, (b) FPIM2.

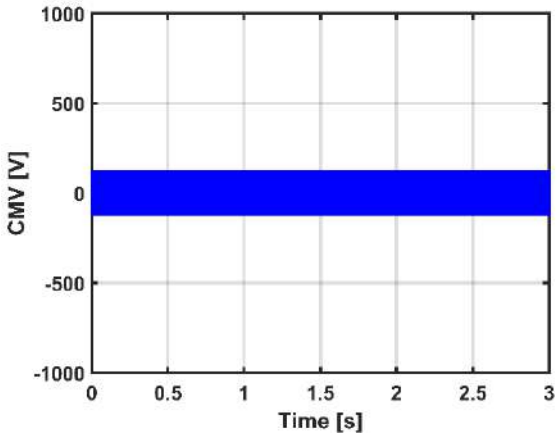

Figure 5.25: Generated CMV in DTC_{CMV}.

First, the rotor's mechanical speed of the two machines are given in Figures 5.20.a and 5.23.a. It can be interrupted that the two FPIMs successfully followed their speed reference commands with nearly the same performance.

Second, Figures 5.20.b and 5.23.b, show the two FPIMs' electromagnetic torque responses. It is observable that this latter accurately complies with the changes in the rotor's speed and loading conditions. Furthermore, a reduction rate of 3% in the torque ripples is noticed in the DTC_{CMV} compared to 3L-DTC-ANN.

Third, the two five-phase machines' stator flux responses are given in Figures 5.20.c and 5.23.c, in $\alpha\beta_1$ and $\alpha\beta_2$ planes. Where the adopted control method has illustrated a better and faster

dynamic response when compared to the 3L-DTC-ANN scheme with 2.5% reduction in the flux ripples content.

Fourth, the two FPIMs' stator currents and the THD analysis are given in Figures 5.21 and 5.24, respectively. Where the 3L-DTC-ANN method exhibits a better current waveform with less current THD by 4% compared to the discussed method DTC_{CMV}, as shown in Figures 5.20.d and 5.23.d.

Fifth, Figures 5.22 and 5.23 Depicts the generated CMV. The DTC_{CMV} has successfully reduced the generated CMV peak-to-peak value to $\pm V_{dc}/_{10}$ compared to $\pm V_{dc}/_{2}$ in the intelligent 3L DTC.

Finally, from the presented simulation results, the DTC_{CMV} shows a superior performance while preserving the decoupled control between the machine's torque/flux and the control independence of the drive, regardless of the working conditions. Table 5.6 Summarizes a comparative study between the control schemes.

Table 5.6: Comparative analysis.

Performance	Assessment parameters	3L-DTC-ANN	DTC_{CMV}
ω_m	Recovery time (s)	0.3	0.3
	Overshoot (rad/s)	2	1.6
	Undershoot (rad/s)	2	1.6
T_{em}	Ripples (%)	46	43
ϕ_s	Ripples (%)	8	5.5
i_{sa}	THD (%)	20	24
CMV	Peak-to-peak value (V)	600	120

5.5. Conclusion

The first part of this chapter discusses CMV and its relative potential problems affecting AC machines' drives, in addition to the corrective and preventive methods to mitigate the generated CMV. The second part has given a theoretical evaluation and analysis of the CMV generated by the conventional DTC fed by the THL-FP-VSI. Where in the last part the extended mitigation approach for the two-machine drive is introduced and applied to the 3L-DTC based

on the concept of the VVVs control technique. The simulative results demonstrate the effectiveness of the mitigation technique of the CMV while preserving the simplicity and the advantages of the conventional scheme and further enhancing the torque and flux ripples, reduced by 3% and 2.5%, respectively, compared to the DTC.

General conclusion

In the context of research on the independent control of the two multiphase machines connected in parallel drive fed by a multi-level voltage source inverter, this thesis is made. Where the main objective is to study the five-phase induction machines controlled via the direct torque control scheme, which in turn gives a fair trade-off between the system's merits/demerits and cost; thus, this thesis has dealt with selected adverse downsides of the drive's system. This is achieved by several amendments, either by the combination of AI techniques such as ANNs and machine-model sensorless control methods or by modifying the conventional scheme.

The first chapter gives a brief state of the art in which the merits/demerits of the multiphase topology and the two-machine parallel-connected drive are highlighted. The modelling of the FPIMs, multi-level VSI, and the two parallel-connected FPIMs is explained, in addition to the transformation matrix to the arbitrary reference frame. Where, the principle points that can be highlighted in the first chapter are:

- The discussed multi-machine drive system presents a reduction in the number of the VSI's phases, which can be translated into cost's reduction of the system.
- The control of the FPIM requires only the control of one set of current components, that is responsible for the flux/torque generation, while the remaining components are not used.
- Through an introduction of an appropriate phase transposition of the stator windings, the other set of the current's component can be exploited to independently control another FPIM connected in parallel to the same VSI, resulting in a current component that is flux/torque generating for one machine and non-generating for the other, and vice-versa.

The second chapter presents the independent direct torque control of the two parallel-connected FPIMs drive and states the scheme's working principle in the case of a two-machine drive fed by multi-level VSI. Where, the principle points that can be highlighted in the first chapter, based on the theoretical and simulation study, are:

- The conventional DTC has successfully maintained an independent control over the two-machine drive, while preserving a decoupled control over the flux/torque.

- The DTC has a better performance and simple structure compared to the conventional control methods. However, it suffers from the flux/torque ripples due to the HC's nature and the poor performance of open-loop estimation in low-speed operation.

For this reason, an AI and sensorless approaches are discussed to address these drawbacks, respectively.

The third chapter is dedicated to the artificial intelligent control design using the artificial neural networks-based DTC to address the conventional scheme drawback and further improve the performance and robustness of the drive. Where, the principle points that can be highlighted in the first chapter, based on the theoretical and simulation study, are:

- The non-linear capability of the ANNs is a method to further improve the performance of the two-machine drive, through the enhancement of the DTC's structure.
- Reduction of the drive's flux/torque ripples content.
- Improving both the steady and transient state response of the drive.

The fourth chapter presents the sensorless control of the two-machine drive based on the Machine-Model based methods to estimate the machine's state variables from the information of the measured quantities using the MRAS, SMO, and VCS. Where, the principle points that can be highlighted in the first chapter, based on the theoretical and simulation study, are:

- Reduction of the system's overall cost and size due to the reduction of the implemented sensors' numbers.
- The MRAS approach presents a simple yet a robust sensorless method to estimate the machine's state variable. Nevertheless, it suffers from low performance during speed operation and difficulties to tune the PI controller.
- The SMO approach presents a better rotor speed tracking during both the transient and steady state operation, with neglected estimation error. However, the major drawback of this approach is the high number of coefficients to tune.
- The VCS approach gives a simple yet robust MM based observer to enhance the drive's fault-tolerant capability, reducing the sensors' number to only one (DC-link voltage sensor).

The fifth chapter deals with the Common-Mode Voltage drawback of the PWM-controlled VSI and discusses the mitigation technique based on corrective and preventive approaches. Where,

the principle points that can be highlighted in the first chapter, based on the theoretical and simulation study, are:

- Reducing the effect of the inherited drawback of the multi-level VSI.
- Enhancing the drive's reliability and performance.
- Reducing the down time due to the side effects of the CMV.

Finally, based on the presented work in this thesis, a new axis of research can be suggested as a future work as follows:

- Development of multi-level space vector modulation for the two-machine drive and further improvement by applying Sliding Mode Control, Input/output linearization control, and Model Reference Adaptive Control.
- Study the behavior of the two-machine drive under faulty conditions.
- Developing and improving the direct torque control to balance the neutral point voltage in the multi-level inverter topologies.

With regards

References

[1] Mansouri, A. et al. (2023) 'Wind Energy based Conversion topologies and Maximum Power Point Tracking: A Comprehensive Review and Analysis', e-Prime, 6, pp. 100351–100351. Available at: https://doi.org/10.1016/j.prime.2023.100351.

[2] Liu, C. et al. (2020) 'A Critical Review of Advanced Electric Machines and Control Strategies for Electric Vehicles', Proceedings of the IEEE, 109(6), pp. 1–25. Available at: https://doi.org/10.1109/jproc.2020.3041417.

[3] Frikha, M.A. et al. (2023) 'Multiphase Motors and Drive Systems for Electric Vehicle Powertrains: State of the Art Analysis and Future Trends', Energies, 16(2), p. 768. Available at: https://doi.org/10.3390/en16020768.

[4] N. Arish, Kamper, M.J. and Wang, R.J. (2024) 'Advancements in electrical marine propulsion technologies: A comprehensive overview', SAIEE Africa Research Journal, 116(1), pp. 14–29. Available at: https://doi.org/10.23919/saiee.2025.10755059.

[5] Paolo Pescetto et al. (2023) 'Active Control of Variable DC-Link for Maximum Efficiency of Traction Motor Drives', IEEE Transactions on Industry Applications, 59(4), pp. 4120–4129. Available at: https://doi.org/10.1109/tia.2023.3267770.

[6] Gholamian, M., Beik, O. and Arshad, M. (2024) 'A Review of State-of-the-Art Multiphase and Hybrid Electric Machines', Electronics, 13(18), p. 3636. Available at: https://doi.org/10.3390/electronics13183636.

[7] Mokhtar Nesri et al. (2024) 'Robust Adaptive Speed Control for the DC Motor Based on a Modified MRAC', Communications - Scientific letters of the University of Zilina, 26(4), pp. C38–C46. Available at: https://doi.org/10.26552/com.c.2024.055.

[8] Aktas, M. et al. (2020) 'Direct torque control versus indirect field-oriented control of induction motors for electric vehicle applications', Engineering Science and Technology, an International Journal, 23(5), pp. 1134–1143. Available at: https://doi.org/10.1016/j.jestch.2020.04.002.

[9] Gaikwad, S.A. and Shinde, S.M. (2020) 'Review on Five-phase Induction Motor fed by Five-phase Voltage Source Inverter with different Conduction Mode', 2020 International

Conference on Industry 4.0 Technology (I4Tech), pp. 199–202. Available at: https://doi.org/10.1109/I4Tech48345.2020.9102695.

[10] Ward, E.E. and HärerH. (1969) 'Preliminary investigation of an invertor-fed 5-phase induction motor', Proceedings of the Institution of Electrical Engineers, 116(6), p. 980. Available at: https://doi.org/10.1049/piee.1969.0182.

[11] ZELECHOWSKI, Marcin. Space vector modulated–direct torque controlled (dtc–svm) inverter–fed induction motor drive. Warsaw University of Technology Faculty of Electrical Engineering Institute of Control and Industrial Electronics, 2005.

[12] Jasiński, M. (2005) Direct power and torque control of AC/DC/AC converter-fed induction motor drives. PhD Thesis. Available at: https://repo.pw.edu.pl/info/phd/WUT283632/.

[13] Jisha, L.K. and Powly Thomas, A.A. (2013) 'A comparative study on scalar and vector control of Induction motor drives', 2013 International conference on Circuits, Controls and Communications (CCUBE) [Preprint]. Available at: https://doi.org/10.1109/ccube.2013.6718554.

[14] Chenchireddy, K., Kumar, V., & Sreejyothi, K. R. (2021, March). Investigation of performance vector control single-phase induction motor. In 2021 7th International Conference on Advanced Computing and Communication Systems (ICACCS) (Vol. 1, pp. 887-891). IEEE.

[15] Barış Çavuş and Mustafa Aktaş (2024) 'A New Adaptive Terminal Sliding Mode Speed Control in Flux Weakening Region for DTC Controlled Induction Motor Drive', IEEE transactions on power electronics, 39(1), pp. 449–458. Available at: https://doi.org/10.1109/tpel.2023.3326383.

[16] Ho, S. D., Brandstetter, P., Palacky, P., Kuchar, M., Dinh, B. H., & Tran, C. D. (2021). Current sensorless method based on field-oriented control in induction motor drive. Journal of Electrical Systems, 17(1).

[17] Ambrish Devanshu, Singh, M. and Kumar, N. (2020) 'Nonlinear flux observer-based feedback linearisation control of IM drives with ANN speed and flux controller', International Journal of Electronics, 108(1), pp. 139–161. Available at: https://doi.org/10.1080/00207217.2020.1765416.

[18] Wang, F., Guiying, L. and He, Y.-J. (2021) 'Passivity-Based Model Predictive Control of Three-Level Inverter-Fed Induction Motor', IEEE Transactions on Power Electronics, 36(2), pp. 1984–1993. Available at: https://doi.org/10.1109/tpel.2020.3008915.

[19] Takahashi, I. and Ohmori, Y. (1989) 'High-performance direct torque control of an induction motor', IEEE Transactions on Industry Applications, 25(2), pp. 257–264. Available at: https://doi.org/10.1109/28.25540.

[20] Messaoudi, M., Kraiem, H., Hamed, M. B., Sbita, L., & Abdelkrim, M. N. (2008). A robust sensorless direct torque control of induction motor based on MRAS and extended Kalman filter. Leonardo Journal of Sciences, 12(1), 35-56.

[21] Reza, C.M.F.S., Islam, Md.D. and Mekhilef, S. (2014) 'A review of reliable and energy efficient direct torque controlled induction motor drives', Renewable and Sustainable Energy Reviews, 37, pp. 919–932. Available at: https://doi.org/10.1016/j.rser.2014.05.067.

[22] Kumar, R.H., Iqbal, A. and Lenin, N.C. (2018) 'Review of recent advancements of direct torque control in induction motor drives – a decade of progress', IET Power Electronics, 11(1), pp. 1–15. Available at: https://doi.org/10.1049/iet-pel.2017.0252.

[23] El Ouanjli, N. et al. (2019) 'Modern improvement techniques of direct torque control for induction motor drives - a review', Protection and Control of Modern Power Systems, 4(1). Available at: https://doi.org/10.1186/s41601-019-0125-5.

[24] Mohan, H., Pathak, M.K. and Dwivedi, S.K. (2019) 'Sensorless Control of Electric Drives – A Technological Review', IETE Technical Review, 37(5), pp. 504–528. Available at: https://doi.org/10.1080/02564602.2019.1662738.

[25] Holtz, J. (2006) 'Sensorless Control of Induction Machines—With or Without Signal Injection?', IEEE Transactions on Industrial Electronics, 53(1), pp. 7–30. Available at: https://doi.org/10.1109/tie.2005.862324.

[26] Zine, W. et al. (2018) 'Interests and Limits of Machine Learning-Based Neural Networks for Rotor Position Estimation in EV Traction Drives', IEEE Transactions on Industrial Informatics, 14(5), pp. 1942–1951. Available at: https://doi.org/10.1109/tii.2017.2765398.

[27] Joshi, B.M. and Chandorkar, M.C. (2014) 'Vector Control of Two-motor Single-inverter Induction Machine Drives', Electric Power Components and Systems, 42(11), pp. 1158–1171. Available at: https://doi.org/10.1080/15325008.2014.921949.

[28] Hossein Mohktari and Abdollah Alizadeh (2007) 'A new multi-machine control system based on Direct Torque Control algorithm', 2007 7th Internatonal Conference on Power Electronics, pp. 1103–1108. Available at: https://doi.org/10.1109/icpe.2007.4692551.

[29] Levi, E. (2008) 'Multiphase Electric Machines for Variable-Speed Applications', IEEE Transactions on Industrial Electronics, 55(5), pp. 1893–1909. Available at: https://doi.org/10.1109/tie.2008.918488.

[30] M. Osama and T. A. Lipo, "A magnetic relief scheme for four pole induction motors," in Proc. ElectrIMACS, Lisbon, Portugal, 1999, pp. 115–121.

[31] S. Gataric, "A polyphase Cartesian vector approach to control of polyphase AC machines," in Conf. Rec. IEEE IAS Annu. Meeting, Rome, Italy, 2000, pp. 1648–1654.

[32] JONES, M. (2005) 'A Novel Concept of Series Connected Multi-Phase, Multi-Motor Drive Systems. PhD Thesis, John Moores University.

[33] LEVI, Emil, JONES, Martin, VUKOSAVIC, Slobodan N., et al. Steady-state modeling of series-connected five-phase and six-phase two-motor drives. IEEE Transactions on industry applications, 2008, vol. 44, no 5, p. 1559-1568.

[34] YAHIA, Chedni, DJAMEL, Boudana, et al. Direct Torque Control of Two Series Connected Six-Three phases Motor Fed by Single Six Phases VSI Based on Optimum Vectors Selection. Journal of Renewable Energies, 2020, vol. 23, no 2, p. 304-317.

[35] NEZLI, Lazhari et ZOUAID, Omar. Sliding mode control of a five-phase series-connected two-motor drive. Algerian Journal of Signals and Systems, 2016, vol. 1, no 1, p. 59-68.

[36] Khan, M.R. and Iqbal, A. (2009) 'Extended Kalman filter based speeds estimation of series-connected five-phase two-motor drive system', Simulation Modelling Practice and Theory, 17(7), pp. 1346–1360. Available at : https://doi.org/10.1016/j.simpat.2009.05.007.

[37] Abjadi, N.R. (2014) 'Sliding-mode control of a six-phase series/parallel connected two induction motors drive', ISA Transactions, 53(6), pp. 1847–1856. Available at: https://doi.org/10.1016/j.isatra.2014.09.001.

[38] Tir, Z., Malik, O.P. and Eltamaly, A.M. (2016) 'Fuzzy logic based speed control of indirect field oriented controlled Double Star Induction Motors connected in parallel to a single six-phase inverter supply', Electric Power Systems Research, 134, pp. 126–133. Available at: https://doi.org/10.1016/j.epsr.2016.01.013.

[39] Kellner, J. and Praženica, M. (2021) 'Two five-phase induction motors used as an electronic differential', 55, pp. 896–903. Available at: https://doi.org/10.1016/j.trpro.2021.07.058.

[40] Kamel, T., Abdelkader, D., Said, B., Al-Hitmi, M., & Iqbal, A. (2018). Sliding mode control based DTC of sensorless parallel-connected two five-phase PMSM drive system. Journal of Electrical Engineering & Technology, 13(3), 1185-1201.

[41] Saadeh, O., Dalbah, M. and Dalala, Z. (2018) 'Control of two Five-Phase Parallel Connected Single Source Motor Drives under Balanced and Unbalanced Conditions', 2018 9th IEEE International Symposium on Power Electronics for Distributed Generation Systems (PEDG), pp. 1–6. Available at: https://doi.org/10.1109/pedg.2018.8447807.

[42] TOUNSI, K. (2019) Decoupled Control of AC Machines Connected in Parallel. PhD Thesis. Available at: http://dspace.univ-chlef.dz/handle/123456789/1335.

[43] Huy Luong-Gia et al. (2024) 'Modeling and Control of Multi-phase Motor Fed by Multi-level Inverter for Electric Vehicles', pp. 1–6. Available at: https://doi.org/10.1109/vppc63154.2024.10755490.

[44] Hadiouche, D. (2001) Contribution à l'étude de la machine asynchrone double étoile : modélisation, alimentation et structure. PhD Thesis, Université Henri Poincaré. Available at: https://hal.univ-lorraine.fr/tel-01746497.

[45] SADOUNI, R. (2010) Commande par mode glissant flou d'une machine asynchrone à double étoile. PhD Thesis, University of Sidi Bel Abbes Djillali Liabes.

[46] Klingshirn, E.A. (1983) 'High Phase Order Induction Motors - Part I-Description and Theoretical Considerations', IEEE Transactions on Power Apparatus and Systems, PAS-102(1), pp. 47–53. Available at: https://doi.org/10.1109/tpas.1983.317996.

[47] Toliyat, H.A., Lipo, T.A. and White, J.C. (1991) 'Analysis of a concentrated winding induction machine for adjustable speed drive applications. II. Motor design and performance', IEEE Transactions on Energy Conversion, 6(4), pp. 684–692. Available at: https://doi.org/10.1109/60.103642.

[48] KALLIO, S. (2014) 'Modeling and parameter estimation of double-star permanent magnet synchronous machines. PhD Thesis, Lappeenranta University.

[49] Tessarolo, A. (2011). 'Modeling and analysis of multiphase electric machines for high-power applications. PhD Thesis, Trieste University.

[50] Bermudez, M. et al. (2017) 'Open-Phase Fault-Tolerant Direct Torque Control Technique for Five-Phase Induction Motor Drives', IEEE Transactions on Industrial Electronics, 64(2), pp. 902–911. Available at: https://doi.org/10.1109/tie.2016.2610941.

[51] ZOUAID, O. (2009) 'Commande vectorielle de deux machines asynchrones pentaphasées en série. PhD Thesis, Ecole Nationale Polytechnique.

[52] IQBAL, A. (2005) 'Modelling and control of series-connected five-phase and six-phase two-motor drives. PhD Thesis, Liverpool John Moores University.

[53] Boussiala, B. (2010) 'Commande vectorielle d'une machine asynchrone polyphasée alimentée par onduleur à trois niveaux. PhDThesis, Ecole Nationale Polytechnique.

[54] Kang, J.-W. et al. (2020) 'A Novel Zero Dead-Time PWM Method to Improve the Current Distortion of a Three-Level NPC Inverter', Electronics, 9(12), p. 2195. Available at: https://doi.org/10.3390/electronics9122195.

[55] Tatte, Y.N. and Aware, M.V. (2017) 'Torque Ripple and Harmonic Current Reduction in a Three-Level Inverter-Fed Direct-Torque-Controlled Five-Phase Induction Motor', IEEE Transactions on Industrial Electronics, 64(7), pp. 5265–5275. Available at: https://doi.org/10.1109/tie.2017.2677346.

[56] Liliang Gao and Fletcher, J.E. (2010) 'A Space Vector Switching Strategy for Three-Level Five-Phase Inverter Drives', IEEE Transactions on Industrial Electronics, 57(7), pp. 2332–2343. Available at: https://doi.org/10.1109/tie.2009.2033087.

[57] WARNES, L. A. A. (1994) 'DC machines. Electronic and Electrical Engineering: Principles and Practice, p. 239-266.

[58] El Ouanjli, N. et al. (2019) 'Modern improvement techniques of direct torque control for induction motor drives - a review', Protection and Control of Modern Power Systems, 4(1). Available at: https://doi.org/10.1186/s41601-019-0125-5.

[59] HECHELEF, M. (2017) 'Commande directe du couple d'une machine asynchrone double étoile sans capteur mécanique par les techniques de l'intelligence artificielle. PhD Thesis, University of Sidi Bel Abbes Djillali Liabes.

[60] Wang, F. et al. (2018) ‘Advanced Control Strategies of Induction Machine: Field Oriented Control, Direct Torque Control and Model Predictive Control’, Energies, 11(1), p. 120. Available at: https://doi.org/10.3390/en11010120.

[61] MELIANI, S. (2013) ‘Modélisation et Simulation d’une Commande Directe du Couple (DTC) appliquée à la Machine asynchrone sans capteur de vitesse. PhD Thesis, University of Mohamed Boudiaf - M'sila.

[62] Yousfi, M. et al. (2007) ‘Commande directe du couple de la machine synchrone double étoile alimentée par deux types d’onduleurs. Projet fin d’étude de l’école Nationale Polytechnique.

[63] CHAPUIS, Y.A. (1996) Contrôle direct du couple d’une machine asynchrone par l’orientation de son flux statorique. PhD Thesis, Grenoble INPG.

[64] Tatte, Y.N. and Aware, M.V. (2015) ‘Torque ripple minimization in five-phase three-level inverter fed direct torque control induction motor drive’, pp. 1–6. Available at: https://doi.org/10.1109/epe.2015.7309400.

[65] Azib, A. and Ziane, D. (2023) ‘A Highly Effective Modified Direct Torque Control for Five Phase Induction Motor without AC Phase Current Sensors’, Periodica Polytechnica Electrical Engineering and Computer Science, 67(1), pp. 1–9. Available at: https://doi.org/10.3311/ppee.20384.

[66] Bıçak, A. and Gelen, A. (2021) ‘Sensorless direct torque control based on seven-level torque hysteresis controller for five-phase IPMSM using a sliding-mode observer’, Engineering Science and Technology, an International Journal, 24(5), pp. 1134–1143. Available at: https://doi.org/10.1016/j.jestch.2021.02.004.

[67] Kazmierkowski, M.P. and Malesani, L. (1998) ‘Current control techniques for three-phase voltage-source PWM converters: a survey’, IEEE Transactions on Industrial Electronics, 45(5), pp. 691–703. Available at: https://doi.org/10.1109/41.720325.

[68] Husari, F. and Jeevanand Seshadrinath (2021) ‘Incipient Interturn Fault Detection and Severity Evaluation in Electric Drive System Using Hybrid HCNN-SVM Based Model’, IEEE Transactions on Industrial Informatics, 18(3), pp. 1823–1832. Available at: https://doi.org/10.1109/tii.2021.3067321.

[69] Fantin, E. and Balaji, M. (2020) 'Analysis and Classification of Faults in Switched Reluctance Motors Using Deep Learning Neural Networks', Arabian Journal for Science and Engineering, 46(2), pp. 1313–1332. Available at: https://doi.org/10.1007/s13369-020-05051-y.

[70] Mijwel, M.M. (2021) 'Artificial Neural Networks Advantages and Disadvantages', Mesopotamian Journal of Big Data, 2021, pp. 29–31. Available at: https://doi.org/10.58496/MJBD/2021/006.

[71] Geeta Kamalapur et al. (2022) 'A Novel Neuro Fuzzy Method DTC of Induction Motor Drive for Efficient Torque Response', 2022 3rd International Conference for Emerging Technology (INCET), 39, pp. 1–7. Available at: https://doi.org/10.1109/incet54531.2022.9824324.

[72] Chaymae Fahassa et al. (2022) 'Induction Motor DTC Performance Improvement by Inserting Fuzzy Logic Controllers and Twelve-Sector Neural Network Switching Table', Mathematics, 10(9), pp. 1357–1357. Available at: https://doi.org/10.3390/math10091357.

[73] Massoum, S. et al. (2021) 'DTC based on SVM for induction motor sensorless drive with fuzzy sliding mode speed controller', International Journal of Electrical and Computer Engineering (IJECE), 11(1), p. 171. Available at: https://doi.org/10.11591/ijece.v11i1.pp171-181.

[74] Banda, G. and Kolli, S.G. (2021) 'Comparison of ANN- and GA-based DTC eCAR', Journal of Power Electronics, 21(9), pp. 1333–1342. Available at: https://doi.org/10.1007/s43236-021-00273-1.

[75] Yaichi, I. et al. (2021) 'An Improved DTC Strategy for a DFIG using an Artificial Neural Network Controller', 2021 9th International Conference on Smart Grid (icSmartGrid), pp. 231–237. Available at: https://doi.org/10.1109/icsmartgrid52357.2021.9551251.

[76] Benyoussef, E. and Barkat, S. (2022) 'Five-level DTC-ANN with Balancing Strategy of DSIM', International Journal of Energy, 16, pp. 52–59. Available at: https://doi.org/10.46300/91010.2022.16.8.

[77] Dumitru, F.-S. et al. (2024) 'Graphene Nanoribbon Based McCulloch-Pitts Neural Network', 2024 IEEE 24th International Conference on Nanotechnology (NANO), pp. 592–597. Available at: https://doi.org/10.1109/nano61778.2024.10628801.

[78] Makarov, V.A. et al. (2022) 'Toward Reflective Spiking Neural Networks Exploiting Memristive Devices', Frontiers in Computational Neuroscience, 16. Available at: https://doi.org/10.3389/fncom.2022.859874.

[79] Sharkawy, A.-N. (2020) 'Principle of Neural Network and Its Main Types: Review', Journal of Advances in Applied & Computational Mathematics, 7(1), pp. 8–19. Available at: https://doi.org/10.15377/2409-5761.2020.07.2.

[80] Hewamalage, H., Bergmeir, C. and Bandara, K. (2021) 'Recurrent Neural Networks for Time Series Forecasting: Current status and future directions', International Journal of Forecasting, 37(1), pp. 388–427. Available at: https://doi.org/10.1016/j.ijforecast.2020.06.008.

[81] Abdolrasol, M.G.M. et al. (2021) 'Artificial Neural Networks Based Optimization Techniques: A Review', Electronics, 10(21), p. 2689. Available at: https://doi.org/10.3390/electronics10212689.

[82] Jabbar, R., Jabbar, R. and Kamoun, S. (2022) 'Recent progress in generative adversarial networks applied to inversely designing inorganic materials: A brief review', Computational Materials Science, 213, p. 111612. Available at: https://doi.org/10.1016/j.commatsci.2022.111612.

[83] Tiwari, A. (2022) 'Supervised learning: From theory to applications', Elsevier eBooks, pp. 23–32. Available at: https://doi.org/10.1016/b978-0-12-824054-0.00026-5.

[84] Tyagi, K. et al. (2022) 'Unsupervised learning', Artificial Intelligence and Machine Learning for EDGE Computing, pp. 33–52. Available at: https://doi.org/10.1016/b978-0-12-824054-0.00012-5.

[85] BENZAOUI, K.M.S., Benyoussef, E. and Kouache, A.Z. (2024) 'Artificial neural network sensorless direct torque control of two parallel-connected five-phase induction machines', DOAJ (DOAJ: Directory of Open Access Journals) [Preprint]. Available at: https://doi.org/10.57647/j.mjee.2024.180348.

[86] Mahfoud, S. et al. (2022) 'Enhancement of the Direct Torque Control by using Artificial Neuron Network for a Doubly Fed Induction Motor', Intelligent Systems with Applications, 13, p. 200060. Available at: https://doi.org/10.1016/j.iswa.2022.200060.

[87] MEHROTRA, P. (1999) Artificial neural networks in induction motor speed estimation and control. PhD Thesis, Memorial University of Newfoundland.

[88] BENZAOUI, K.M.S. et al. (2024) 'Sensorless DTC Based on Artificial Neural Network for Independent Control of Dual 5-Phase Induction Machine Fed by a Three-Level NPC Inverter', Advances in Electrical and Electronic Engineering, 22(3). Available at: https://doi.org/10.15598/aeee.v22i3.5738.

[89] ZAKY, M.S. et al. (2008) 'Speed-Sensorless Control of Induction Motor Drives (Review Paper)', ACTA ELECTROTEHNICA, 49(3), pp. 251–268.

[90] Boulmane, A. et al. (2020) 'Design of Robust Adaptive Observer against Measurement Noise for Sensorless Vector Control of Induction Motor Drives', Journal of Electrical and Computer Engineering, 2020, pp. 1–12. Available at: https://doi.org/10.1155/2020/6570942.

[91] Ammar, A., Bourek, A. and Benakcha, A. (2016) 'Sensorless SVM-Direct Torque Control for Induction Motor Drive Using Sliding Mode Observers', Journal of Control, Automation and Electrical Systems, 28(2), pp. 189–202. Available at: https://doi.org/10.1007/s40313-016-0294-7.

[92] AKIN, B. (2003) State estimation techniques for speed sensorless field oriented control of induction motors. PhD Thesis, Middle East Technical University.

[93] Xu, Z. and Rahman, M.F. (2012) 'Comparison of a Sliding Observer and a Kalman Filter for Direct-Torque-Controlled IPM Synchronous Motor Drives', IEEE Transactions on Industrial Electronics, 59(11), pp. 4179–4188. Available at: https://doi.org/10.1109/tie.2012.2188252.

[94] BENYOUSSEF, E. (2015) Commande directe du couple floue et neuronale d'un moteur synchrone à double étoile sans capteur mécanique alimenté par onduleurs multiniveaux. PhD Thesis, University of Sidi Bel Abbes Djillali Liabes.

[95] Cao, X. and Fan, L. (2009) 'New DTC scheme based-on SVM with sliding-mode observer for induction motors', 2009 IEEE International Conference on Automation and Logistics, pp. 1484–1488. Available at: https://doi.org/10.1109/ical.2009.5262733.

[96] Sugimoto, H. and Tamai, S. (1987) 'Secondary Resistance Identification of an Induction-Motor Applied Model Reference Adaptive System and Its Characteristics', IEEE transactions on industry applications, IA-23(2), pp. 296–303. Available at: https://doi.org/10.1109/tia.1987.4504905.

[97] Guedida, S. et al. (2024) 'Novel Speed Sensorless DTC Design for a Five-Phase Induction Motor with an Intelligent Fractional Order Controller Based-MRAS Estimator', Power Electronics and Drives, 9(1), pp. 63–85. Available at: https://doi.org/10.2478/pead-2024-0005.

[98] Weam El Merrassi, Abdelouahed Abounada and Ramzi, M. (2021) 'Advanced speed sensorless control strategy for induction machine based on neuro-MRAS observer', Materials Today Proceedings, 45, pp. 7615–7621. Available at: https://doi.org/10.1016/j.matpr.2021.03.081.

[99] BENZAOUI, K.M.S., Elakhdar Benyoussef and Kouache, A.Z. (2023) 'Direct Torque Control of Sensorless Two FPIM Parallel Connected Using Slide Mode Observer', International Conference on Electrical Engineering and Advanced Technology (ICEEAT), 13, pp. 1–5. Available at: https://doi.org/10.1109/iceeat60471.2023.10425847.

[100] MEHAZZEM, F. (2010) Contribution à la commande d'un moteur asynchrone destiné à la traction électrique. PhD Thesis, Université Paris-Est.

[101] Orłowska-Kowalska, T., Kowalski, C.T. and Mateusz Dybkowski (2016) 'Fault-Diagnosis and Fault-Tolerant-Control in Industrial Processes and Electrical Drives', Studies in systems, decision and control, pp. 101–120. Available at: https://doi.org/10.1007/978-3-319-45735-2_5.

[102] Manohar, M. and Das, S. (2017) 'Current Sensor Fault-Tolerant Control for Direct Torque Control of Induction Motor Drive Using Flux-Linkage Observer', IEEE Transactions on Industrial Informatics, 13(6), pp. 2824–2833. Available at: https://doi.org/10.1109/tii.2017.2714675.

[103] Adamczyk, M. and Orlowska-Kowalska, T. (2022) 'Influence of the stator current reconstruction method on direct torque control of induction motor drive in current sensor postfault operation', Bulletin of the Polish Academy of Sciences Technical Sciences, pp. 140099–140099. Available at: https://doi.org/10.24425/bpasts.2022.140099.

[104] Robles, E. et al. (2022) 'Common-mode voltage mitigation in multiphase electric motor drive systems', Renewable and Sustainable Energy Reviews, 157, p. 111971. Available at: https://doi.org/10.1016/j.rser.2021.111971.

[105] Fernandez, M. et al. (2020) 'New Modulation Technique to Mitigate Common Mode Voltage Effects in Star-Connected Five-Phase AC Drives', Energies, 13(3), pp. 607–607. Available at: https://doi.org/10.3390/en13030607.

[106] Tatte, Y.N. and Aware, M.V. (2017) 'Direct Torque Control of Five-Phase Induction Motor With Common-Mode Voltage and Current Harmonics Reduction', IEEE Transactions on Power Electronics, 32(11), pp. 8644–8654. Available at: https://doi.org/10.1109/tpel.2016.2644988.

[107] Robles, E. et al. (2022) 'Common-Mode Voltage Elimination in Multilevel Power Inverter-Based Motor Drive Applications', IEEE Access, 10, pp. 2117–2139. Available at: https://doi.org/10.1109/access.2021.3137892.

[108] Han, D., Morris, C.T. and Sarlioglu, B. (2017) 'Common-Mode Voltage Cancellation in PWM Motor Drives With Balanced Inverter Topology', IEEE Transactions on Industrial Electronics, 64(4), pp. 2683–2688. Available at: https://doi.org/10.1109/tie.2016.2633234.

[109] Akagi, H. and Shimizu, T. (2008) 'Attenuation of Conducted EMI Emissions From an Inverter-Driven Motor', IEEE Transactions on Power Electronics, 23(1), pp. 282–290. Available at: https://doi.org/10.1109/tpel.2007.911878.

[110] Tallam, R.M. et al. (2012) 'Common-mode voltage reduction for regenerative AC drives', 2012 IEEE Energy Conversion Congress and Exposition (ECCE), pp. 3301–3308. Available at: https://doi.org/10.1109/ecce.2012.6342499.

[111] Jung, W. et al. (2018) 'H7 Inverter Using Zener Diode With Model Predictive Current Control for Common-Mode Voltage Reduction in PMSM Drive System', 2018 IEEE International Power Electronics and Application Conference and Exposition (PEAC), pp. 1–6. Available at: https://doi.org/10.1109/peac.2018.8590522.

[112] Park, J. et al. (2017) 'Mitigation Method of the Shaft Voltage According to Parasitic Capacitance of the PMSM', IEEE Transactions on Industry Applications, 53(5), pp. 4441–4449. Available at: https://doi.org/10.1109/tia.2017.2717378.

[113] Park, J.-K. et al. (2016) 'New Equivalent Circuit of the IPM-Type BLDC Motor for Calculation of Shaft Voltage by Considering Electric and Magnetic Fields', IEEE Transactions on Industry Applications, 52(5), pp. 3763–3771. Available at: https://doi.org/10.1109/tia.2016.2562009.

[114] Erdman, J.M. et al. (1996) ‘Effect of PWM inverters on AC motor bearing currents and shaft voltages’, IEEE Transactions on Industry Applications, 32(2), pp. 250–259. Available at: https://doi.org/10.1109/28.491472.

[115] Busse, D.F. et al. (1997) ‘An evaluation of the electrostatic shielded induction motor: a solution for rotor shaft voltage buildup and bearing current’, IEEE Transactions on Industry Applications, 33(6), pp. 1563–1570. Available at: https://doi.org/10.1109/28.649969.

[116] WILLIAM OH, H. and WILLWERTH, A. (2008) ‘Shaft Grounding— A Solution to Motor Bearing Currents’, ASHRAE Transactions, 114.

[117] Muetze, A. and Binder, A. (2006) ‘Calculation of influence of insulated bearings and insulated inner bearing seats on circulating bearing currents in machines of inverter-based drive systems’, IEEE Transactions on Industry Applications, 42(4), pp. 965–972. Available at: https://doi.org/10.1109/tia.2006.876083.

[118] Bearing currents application note AP040061E. Tech. rep., Eaton Corporation; 2014.

[119] AEGIS. Best practices for high-frequency grounding with AEGIS HFGS (high-frequency ground straps). 2016, Bearing Protection Best Practices.

[120] Willwerth A. To be considered ‘‘true inverter-duty’’, motors need bearing protection. Tech. rep., Electro Static Technology; 2016, Motors need bearing protection.

[121] Muetze, A. and Oh, H.W. (2010) ‘Current-Carrying Characteristics of Conductive Microfiber Electrical Contact for High Frequencies and Current Amplitudes: Theory and Applications’, IEEE Transactions on Power Electronics, 25(8), pp. 2082–2092. Available at: https://doi.org/10.1109/tpel.2010.2046499.

[122] BENZAOUI, K.M.S., et al. (2024) ‘Three-level direct torque control based on common mode voltage reduction strategy fed two parallel connected five-phase induction machine’, REVUE ROUMAINE DES SCIENCES TECHNIQUES — SÉRIE ÉLECTROTECHNIQUE ET ÉNERGÉTIQUE, 69(2), pp. 177–182. Available at: https://doi.org/10.59277/rrst-ee.2024.2.10.